Precision Calculations in the Dark Abelian Sector Model

Jonas Amadeo Rehberg

Dissertation

zur Erlangung des Doktorgrades

September 2024

Advisor: Prof. Dr. Stefan Dittmaier
Fakultät für Mathematik und Physik der
Albert-Ludwigs-Universität
Freiburg im Breisgau

Dekan: Prof. Dr. Michael Růžička
Erstgutachter: Prof. Dr. Stefan Dittmaier
Zweitgutachter: JProf. Dr. Stefan Vogl
Datum der mündlichen Prüfung: 25.11.2024

Abstract

We formulate and investigate the Dark Abelian Sector Model (DASM), which extends the gauge group of the Standard Model (SM) by an additional spontaneously broken $U(1)_\mathrm{d}$ gauge group of a possible hidden sector. The SM is assumed to be a singlet with respect to the $U(1)_\mathrm{d}$. Keeping the hidden sector rather generic, the DASM adds a neutral massive Z' boson corresponding to the $U(1)_\mathrm{d}$, a neutral Higgs boson and a Dirac fermion, which both only carry charge of the $U(1)_\mathrm{d}$, as well as right-handed SM-like neutrinos, to the SM. In this way, the DASM employs the only two possible SM operators (mass dimension < 4, gauge-invariant), namely the Higgs mass operator $\Phi^\dagger\Phi$ and the field-strength tensor of the weak hypercharge, to open up two portals to a possible dark sector. Additionally, the presence of the right-handed neutrinos allows for a third portal to the dark sector. We set up the theoretical framework for the DASM in terms of the masses $M_{h'}$, $M_{\mathrm{Z}'}$, and m_{ν_4} of the new Higgs boson, gauge boson, and fermion, respectively, the respective mixing angles α, γ, and θ_r of the Higgs, gauge, and fermion sectors, and the scalar self-coupling λ_{12}. Furthermore, we define on-shell and $\overline{\mathrm{MS}}$ renormalization schemes for the DASM at the 1-loop level. A first phenomenological analysis is performed using electroweak precision observables, namely the mass of the W boson derived from muon decay, the anomalous magnetic moment of the muon $(g-2)_\mu$, the leptonic effective weak mixing angle, and the leptonic partial decay width of the Z boson. For Z'-boson masses smaller than the Z-boson mass we find a wide range of the parameter space of the DASM that provides a significantly better agreement between measurements and the corresponding predictions for the investigated precision observables than the SM can provide.

Contents

1. Introduction

The field of high-energy physics (HEP) aims towards describing the fundamental constituents of matter as well as the fundamental interactions acting between them. To this end, roughly half a century ago the Standard Model of particle physics (SM) was developed. The SM is a quantum field theory based on the spontaneously broken

$$SU(3)_{\mathrm{C}} \times SU(2)_{\mathrm{W}} \times U(1)_{\mathrm{Y}}$$

gauge group. It describes the strong as well as the electroweak interactions. In the meantime countless results of high-precision collider experiments were found to agree precisely with their respective SM predictions, showcasing its remarkable predictive power. Furthermore, with the discovery of a Higgs boson [1, 2] at the Large Hadron Collider in 2012, that appears to have the properties of the Higgs boson proposed by the SM, it seems that all particles predicted by the SM have been found.

Despite this astonishing predictive power, there are several observations that clearly hint that the SM cannot be the ultimate theory of Nature. For one, no renormalizable quantum-field-theoretical description of the gravitational force is known today and, thus, gravity is not included in the SM. Additionally, the SM does not offer any explanation for the origin of neutrino masses. Furthermore, it can neither predict the matter–antimatter asymmetry observed in the visible universe, nor can it explain the origin of dark matter (DM) or the existence of dark energy.

There are also some precision measurements that show a tension with respect to their SM prediction. One of them is the measurement of the anomalous magnetic moment of the muon $(g-2)_\mu$ performed by the BNL and FNAL collaborations [3], that shows a 5.1σ deviation from the SM prediction [4]. However, recent developments in the field of lattice QCD allow for an alternative determination of the so-called hadronic vacuum polarization [5], which enters the prediction for $(g-2)_\mu$. Making use of this new lattice QCD result leads to a reasonably good agreement (1.7σ) between measurement and SM prediction for $(g-2)_\mu$. Thus, clarification on the result of the SM prediction is needed in the near future. Another measurement that shows a tension (7σ) with respect to its SM prediction [6] is the result for the W-boson mass obtained by the CDF collaboration [7]. Moreover, the CDF measurement is at variance with respect to the previous experimental world average,

and further clarification on the compatibility of the different results is needed (see also Ref. [8]).
As long as no further truly elementary particles are found by experiments, one promising option to obtain hints on the structure of possible physics beyond the SM (BSM) is to further increase the precision of measurements and predictions, i.e. to search for deviations between experimental results and SM predictions at an even higher level of accuracy. In parallel, it is of uttermost importance to investigate different possible BSM theories to learn more about their phenomenological implications. To this end, within the era of modern high-precision experiments, one has to ensure that the precision of any predictions calculated, even within these BSM theories, matches the accuracy of the respective measurements as far as possible.
In the pursuit of answering some of the open questions mentioned above, many interesting and possibly more complete theories, like Supersymmetric models (SUSY) or Grand Unifying Theories (GUTs), were developed. These more complete models often introduce several new parameters and predict many additional elementary particles. Despite the huge effort that was invested in countless analyses to test these models in the past decades, no significant evidence has been found hinting that one of them is realized in Nature. In addition, the large complexity of these theories makes it quite difficult to perform precision calculations within them.
This led to a shift of the focus of the HEP community towards more generic approaches, like effective field theories (EFTs) or simplified, generic extensions of the SM. Assuming the SM to be the low-energy limit of some more complete theory, EFTs, like the SM effective field theory (SMEFT) (for a detailed discussion on SMEFT see Ref. [9]) only consider the fields corresponding to the low-energy particle content of the full theory as dynamical degrees of freedom (d.o.f.). They parameterize the effects of possible new physics associated with the high-energy scale in terms of a perturbative series (in the inverse of the high-energy scale) using effective higher-order operators. Therefore, EFTs provide an effective framework for a widely model-independent approach to measure new-physics effects. At the same time their effective parameterization can—depending on the exact choice of EFT—be matched to a large amount of possible BSM theories. However, the very generic approach of EFTs tends to introduce a large number of effective operators with corresponding Wilson coefficients, already at lowest (non-trivial) order in the high-energy scale. This increases the complexity of any analysis drastically. Furthermore, the effective parameterization does not allow for an easy interpretation in case any BSM effects are found. Additionally, matching any BSM theory to the considered EFT is a non-trivial task, especially for high-precision calculations, i.e. when higher-order corrections in the perturbative expansion in the coupling constants are considered in the BSM predictions.
As a promising alternative to EFTs one can investigate generic extensions of the SM. In contrast to EFTs, these SM extensions are ultraviolet (UV) complete models that focus on extending specific subsectors of the SM in rather generic ways.

While these are not necessarily candidates for complete theories of Nature, they comprise generic building blocks for more complete models. Due to their reduced complexity and the moderate amount of newly introduced free parameters, they build a perfect basis to investigate and further understand the influence of such generic extensions on high-precision predictions. Therefore, they can contribute a crucial part to the search for new physics. One interesting class of these extensions investigates the exact structure of electroweak (EW) symmetry breaking. Probing the mechanism that is responsible for the mass generation of the particles at high precision is especially important since most of the more complete BSM theories (like SUSY or GUT models) predict some deviations compared to the SM case by introducing additional Higgs fields to the scalar sector. Some of the historically most prominent examples for generic Higgs-sector extensions are, e.g., the Singlet Extension of the SM (SESM) [10–13] or the Two Higgs Doublet Model (THDM) [14, 15]. These are known for several decades and numerous precision analyses (see e.g. Refs. [16, 17]) managed to set limits on the viable parameter space of these models. However, many of these generic Higgs-sector extensions (including the SESM and the THDM) are still viable.
A second class of generic SM extensions introduces an additional $U(1)$ gauge group or even more complex gauge symmetries [18–21] to the SM gauge structure. These models recently gained popularity since they might be able to loosen the tension observed in $(g-2)_\mu$. In the literature, many different ideas have been proposed on how to introduce such gauge-sector extensions to the SM without introducing any anomalies to the theory. These models can potentially solve some of the open questions like the origin of DM. For one, the global $B-L$ (baryon number minus lepton number) symmetry of the SM can be promoted to a, possibly spontaneously broken, gauge symmetry $U(1)_{B-L}$. Consequently a (massive) neutral Z'_{B-L} gauge boson that couples to the $B-L$ charge (see e.g. Refs. [22–24]) is added to the theory opening a portal to possible new physics carrying this charge. A possibly even more prominent class of generic $U(1)$ extensions are the so-called "dark photon" or Z' extensions. They introduce a dark sector with a non-trivial gauge structure of at least a, possibly broken, $U(1)_\mathrm{d}$ to the SM, without specifying the full matter content of this dark sector in detail [13, 25–34]. The presence of this additional abelian gauge group allows for kinetic mixing between the $U(1)_\mathrm{Y}$ of the SM and the $U(1)_\mathrm{d}$ introduced via their gauge-invariant field-strength tensors, as well as mass mixing for their respective gauge fields. This opens up a portal from the SM to the dark sector via the resulting massive neutral Z' gauge boson. A third class of generic SM extensions introduces generic building blocks to the neutrino sector of the SM. These types of extensions seem to provide promising DM candidates and propose several possible solutions for the mass generation of the SM neutrinos (see Refs. [35, 36] and references therein).

In this thesis, we formulate a model henceforth called the Dark Abelian Sector Model (DASM). The DASM is a quite generic extension of the SM that introduces

a dark sector to the theory. This dark sector resembles a large class of dark sectors with similar features that can be found in more fundamental models. It is assumed to be a singlet with respect to the SM gauge group, but features an additional "dark" $U(1)_\mathrm{d}$ gauge group. Thus, the gauge group of the DASM is given by

$$SU(3)_\mathrm{C} \times SU(2)_\mathrm{W} \times U(1)_\mathrm{Y} \times U(1)_\mathrm{d}.$$

This opens up the possibility of kinetic mixing between the SM $U(1)_\mathrm{Y}$ and the new $U(1)_\mathrm{d}$ (see e.g. Refs. [13, 26, 27] for similar models featuring kinetic mixing). Furthermore, a second complex Higgs field ρ is introduced in the dark sector, i.e. it is a singlet with respect to the SM but carries charge of the dark gauge group. This Higgs field ρ develops a non-vanishing vacuum expectation value (vev) which spontaneously breaks the $U(1)_\mathrm{d}$. Ultimately this leads to an additional massive neutral gauge boson as well as an additional neutral Higgs boson. The fermion sector of the DASM introduces right-handed, uncharged, partners to the SM neutrinos as well as a Dirac fermion that carries charge of the $U(1)_\mathrm{d}$.
Note that, keeping the charges of the SM fields unchanged, there are only two operators of the SM that are gauge-invariant and renormalizable by themselves. These are the Higgs mass operator $\Phi^\dagger\Phi$ and the field-strength tensors of the $U(1)_\mathrm{Y}$ gauge field. The Higgs- and gauge-sector extensions introduced by the DASM utilize both of them to employ possible portals to an abelian dark sector that is a singlet with respect to the SM gauge group. Further, the extension of the fermion sector by right-handed SM-like neutrinos as well as the additional fermion allows us to open up a third portal from the SM to the dark sector via Yukawa interactions. The existence of the additional gauge boson can have a significant impact on EW precision observables (POs) and potentially loosen the tension between the measurements and theory predictions for $(g-2)_\mu$ or even for the CDF measurement of the W-boson mass. Furthermore, the fermion sector of the DASM can accommodate neutrino masses, and some regions of the DASM parameter space allow for potential DM candidates. In recent times, models similar to the DASM that combine extensions of several subsectors in a generic way became more and more interesting and first analyses investigating their phenomenological implications were performed, e.g. by the authors of Ref. [37] on the Hidden Abelian Higgs Model, which is a model that features extensions of the Higgs and gauge sector that are similar to the ones of the DASM.
In this work, we set up the theoretical framework for the DASM and propose a set of intuitive and experimentally easily accessible input parameters that are well suited for phenomenological analyses at colliders. Further, being interested in next-to-leading order (NLO) BSM corrections, we give the complete NLO renormalization procedure for the DASM. To this end, we develop an on-shell (OS) renormalization scheme that is based on measurable quantities as far as possible, providing a well-suited setup to study Higgs and EW POs. Alternatively, we give the results for $\overline{\mathrm{MS}}$ renormalization conditions for the additional mixing angles introduced by the DASM. To the best of our knowledge, the discussion of suitable

renormalization schemes for gauge-boson mixing angles originating from kinetic mixing was not present in the literature beforehand. Thus, Ref. [38] (which anticipated some results of this thesis) might serve as a rather general proposal for the definition of OS renormalization conditions for such mixing angles. Having the renormalization set up, we derive predictions for four POs, namely the W-boson mass M_{W} derived from muon decay, the anomalous magnetic moment of the muon $(g-2)_\mu$, the effective weak mixing angle $s^2_{\mathrm{w,eff},l}$, and the leptonic partial decay width of the Z boson, $\Gamma_{\mathrm{Z}\to ll}$, at the 1-loop level in the BSM effects. Further, we combine these predictions in a global fit of the BSM d.o.f., to investigate the predictive power of the DASM and to get a first idea whether the DASM remains a promising candidate in the search for BSM physics.

This thesis is structured as follows:

- In Chapter 2 a brief overview of the SM is given. We conclude the summary of the SM with a brief discussion of its shortcomings that highlight the need for BSM physics.

- A detailed description of the theoretical setup of the DASM is given in Chapter 3. Further, we define a simplified version of the full fermion-sector extension that is well suited for our following analysis of collider phenomenology and $(g-2)_\mu$, and greatly reduces the amount of newly introduced free parameters. Finally, we define a set of intuitive and experimentally easily accessible input parameters for the DASM. To this end, we trade the original parameters of the theory in favour of the masses of the new particles and mixing angles which are directly connected to the coupling strengths of the respective particles.

- Chapter 4 gives a detailed description of the NLO renormalization of the DASM. In total, we give the results for the NLO renormalization constants in two different schemes, one being an on-shell scheme and a second one employing $\overline{\mathrm{MS}}$ renormalization conditions for the newly introduced mixing angles.

- In the first half of Chapter 5, we define different electroweak input schemes used in the following calculations. Further, we give a detailed discussion of the derivations and results for the POs M_{W}, $(g-2)_\mu$, $s^2_{\mathrm{w,eff},l}$, and $\Gamma_{\mathrm{Z}\to ll}$ investigated in the following phenomenological analysis. In the second half of the chapter, a global fit of the BSM parameters is performed using the predictions for these POs. This includes a detailed discussion of the fit setup and the fit results.

- In the final Chapter 6, we give a summary and our conclusions, as well as an outlook.

- The appendices contain explicit expressions of interesting quantum-field-theoretical quantities. In particular, we give the Feynman rules for the DASM in Appendix F.

2. The Standard Model

The SM is the current theory of particle physics. It is a relativistic quantum field theory based on the gauge group

$$SU(3)_{\mathrm{C}} \times SU(2)_{\mathrm{W}} \times U(1)_{\mathrm{Y}}. \tag{2.1}$$

The SM describes three of the four known fundamental interactions, namely the strong, the weak, and the electromagnetic forces, as well as the elementary particles that make up the fundamental constituents of matter. For the fourth fundamental interaction, the gravitational force, no fully consistent quantum-field-theoretical description is known. Thus, it cannot be included in the SM in a straightforward manner. However, the small value of its coupling strength makes the impact of the gravitational force on HEP measurements negligible compared to the remaining three fundamental interactions. Therefore, the SM is suitable to describe physics at energy scales of modern HEP experiments within the required bounds of accuracy.

In the SM, the strong interactions are governed by the theory of quantum chromodynamics (QCD) [39–41] described by the $SU(3)_{\mathrm{C}}$ part of the gauge group. The remaining $SU(2)_{\mathrm{W}} \times U(1)_{\mathrm{Y}}$ part of the SM gauge group describes the weak and electromagnetic forces via the Glashow-Salam-Weinberg (GSW) model [42–45] and combines them into the so-called electroweak (EW) interactions. In the GSW model, the Higgs–Kibble mechanism [46–50] is introduced to the SM, spontaneously breaking the $SU(2)_{\mathrm{W}} \times U(1)_{\mathrm{Y}}$ gauge group in order to consistently describe a gauge theory with massive force carriers. The spontaneous breaking of the SM gauge group is done such that only a $U(1)_{\mathrm{em}}$ part of the EW gauge group, describing quantum electrodynamics (QED), is left unbroken.

The so-called matter fields of the SM are spin $\mathcal{J} = \frac{1}{2}$ fermions. The force carriers are vector bosons with spin $\mathcal{J} = 1$, and the Higgs boson, whose existence is a consequence of the Higgs–Kibble mechanism, is the only scalar ($\mathcal{J} = 0$) boson of the SM. The force carriers of the strong interactions are the eight massless gluons. The EW force is mediated by two massive, charged bosons $\mathrm{W}^{\pm}$, the massive, neutral Z boson, and the massless photon.

The fermions described by the SM can further be classified into charged leptons l_i, neutrinos ν_i, up-type quarks u_i, and down-type quarks d_i. There are three gen-

erations, i.e. $i = 1, 2, 3$, of each of these fermion types. The charged leptons and neutrinos only carry charge of the EW gauge group and can appear as (asymptotically) free particles in Nature[1]. Up-type and down-type quarks additionally carry colour charge of the $SU(3)_{\mathrm{C}}$. They are subject to confinement and will only appear in bound states, the so-called hadrons, in Nature.
In the following, we discuss the SM in detail. It is convenient to split the Lagrangian of the SM

$$\mathcal{L}_{\mathrm{SM}} = \mathcal{L}_{\mathrm{EW}}^{\mathrm{SM}} + \mathcal{L}_{\mathrm{QCD}}^{\mathrm{SM}} \tag{2.2}$$

into its EW part $\mathcal{L}_{\mathrm{EW}}^{\mathrm{SM}}$ and its QCD part[2] $\mathcal{L}_{\mathrm{QCD}}^{\mathrm{SM}}$. Throughout this chapter, we follow Refs. [51–54] and adopt the conventions of Ref. [54] for quantum-field-theoretical quantities.

2.1. The Electroweak Lagrangian

The gauge structure of the EW part of the SM (EWSM) is given by the non-abelian gauge group $SU(2)_{\mathrm{W}} \times U(1)_{\mathrm{Y}}$. The $SU(2)_{\mathrm{W}}$ part describes the weak isospin. The generators of the weak isospin in the fundamental representation are given by $I_{\mathrm{W}}^{j} = \frac{\sigma_j}{2}$, with the three Pauli matrices σ_j, $j = 1, 2, 3$. The abelian $U(1)_{\mathrm{Y}}$ part of the gauge group describes the so-called weak hypercharge with corresponding quantum number Y_{W}. Thus, describing the EW interactions, the EWSM introduces the four EW gauge bosons $W^{\pm}$, Z, and the photon. While the latter one is massless, the $W^{\pm}$ and Z bosons are known to be massive. However, naively adding mass terms to the Lagrangian would break local gauge invariance, which is the fundamental guiding principle of the SM for the introduction of interactions. To solve this contradiction the Higgs mechanism is applied to the SM. It adds a scalar $SU(2)_{\mathrm{W}}$ doublet to the theory. This doublet carries weak hypercharge and develops a non-vanishing vev that breaks the $SU(2)_{\mathrm{W}} \times U(1)_{\mathrm{Y}}$ spontaneously, leaving only the $U(1)_{\mathrm{em}}$ which describes the electromagnetic interactions, unbroken. In this way, mass terms for the three massive EW gauge bosons are introduced in the EWSM without any violation of gauge invariance in the underlying Lagrangian (see Sect. 2.1.2 for details). The left-chiral up- and down-type quarks as well as the left-chiral charged leptons and neutrinos are combined into doublets of the weak isospin for each generation. In contrast, their right-chiral counterparts are singlets under the $SU(2)_{\mathrm{W}}$ gauge group. Consequently, adding simple mass terms for the corresponding fermion fields would break gauge invariance. Again, the Higgs mechanism is used to introduce mass terms for the respective fields via so-called Yukawa interactions. For a detailed discussion of these various parts we

[1] We give a detailed description of the exact quantum numbers of the different fermions in Sect. 2.1.3.
[2] We include the kinetic and mass terms for the quarks in $\mathcal{L}_{\mathrm{EW}}^{\mathrm{SM}}$.

split up the Lagrangian of the EWSM according to

$$\mathcal{L}_{\text{EW}}^{\text{SM}} = \mathcal{L}_{\text{YM}}^{\text{SM}} + \mathcal{L}_{\text{Higgs}}^{\text{SM}} + \mathcal{L}_{\text{Fermion}}^{\text{SM}} + \mathcal{L}_{\text{Yukawa}}^{\text{SM}} \tag{2.3}$$

and discuss them separately in detail in the following.

2.1.1. Gauge sector

The gauge sector of the EWSM introduces the kinetic terms for the gauge fields W_μ^i, $i = 1, 2, 3$, and B_μ of the $SU(2)_{\text{W}}$ and $U(1)_{\text{Y}}$ gauge groups, respectively, to the SM Lagrangian in a gauge-invariant way. The corresponding part of the EWSM Lagrangian reads

$$\mathcal{L}_{\text{YM}}^{\text{SM}} = -\frac{1}{4} W^{i,\mu\nu} W_{\mu\nu}^i - \frac{1}{4} B^{\mu\nu} B_{\mu\nu}, \tag{2.4}$$

with the field-strength tensors

$$W_{\mu\nu}^i = \partial_\mu W_\nu^i - \partial_\nu W_\mu^i + g_2 \epsilon^{ikl} W_\mu^k W_\nu^l, \qquad B_{\mu\nu} = \partial_\mu B_\nu - \partial_\nu B_\mu, \tag{2.5}$$

where g_2 and ϵ^{ikl}, $i, k, l = 1, 2, 3$, are the coupling constant and the totally anti-symmetric structure constants of the $SU(2)_{\text{W}}$, respectively.
Guided by the principle of local gauge invariance, the gauge fields B_μ and W_μ^i can be used to construct the covariant derivative

$$D^\mu = \partial^\mu + \mathrm{i} g_1 \frac{Y_{\text{W}}}{2} B^\mu - \mathrm{i} g_2 I_{\text{W}}^j W^{j,\mu}, \tag{2.6}$$

which rules the EW gauge interactions of the fermions and the Higgs doublet. Here g_1 is the coupling constant corresponding to the $U(1)_{\text{Y}}$. The gauge transformations of the gauge fields are given by

$$\delta W_\mu^i = \partial_\mu \delta\theta^i + g_2 f^{ikl} W_\mu^k \delta\theta^l, \qquad \delta B_\mu = \partial_\mu \delta\theta^{\text{Y}}, \tag{2.7}$$

where θ^l and θ^{Y} are the gauge-group parameters of the $SU(2)_{\text{W}}$ and $U(1)_{\text{Y}}$, respectively. Combining Eqs. (2.5) and (2.7) immediately yields the gauge invariance of the $U(1)_{\text{Y}}$ field-strength tensor

$$\delta B_{\mu\nu} = 0. \tag{2.8}$$

Note that Eq. (2.8) is true for the respective field-strength tensors of any abelian gauge group[3]. Due to the presence of the non-vanishing structure constants, reflecting the non-commutativity of the respective generators of the underlying Lie algebra, field-strength tensors of non-abelian gauge groups are not gauge invariant by themselves. Thus, in the non-abelian case the contraction of two field-strength tensors with identical transformation properties is needed to obey the gauge-invariance requirement.

[3]This will open up the possibility for so-called kinetic mixing in the DASM introduced in Chapter 3.

2.1.2. Higgs sector

The Higgs mechanism is used to introduce mass terms for the SM particles while keeping the Lagrangian gauge invariant. To this end, it adds a complex, scalar $SU(2)_{\mathrm{W}}$ doublet

$$\Phi = \begin{pmatrix} \phi^+ \\ \phi^0 \end{pmatrix} \tag{2.9}$$

to the theory. This doublet carries weak hypercharge $Y_{\mathrm{W}}^{\Phi} = 1$. With the help of the covariant derivative defined in Eq. (2.6) the Higgs part of the SM Lagrangian can be written as

$$\mathcal{L}_{\mathrm{Higgs}}^{\mathrm{SM}} = (D_\mu \Phi)^\dagger (D^\mu \Phi) - V^{\mathrm{SM}}(\Phi). \tag{2.10}$$

The first term contains the kinetic terms of the Higgs doublet as well as its gauge interactions. The most general, gauge-invariant, renormalizable Higgs potential is given by

$$V^{\mathrm{SM}}(\Phi) = -\mu_2^2 \Phi^\dagger \Phi + \frac{\lambda_2}{4} (\Phi^\dagger \Phi)^2. \tag{2.11}$$

The choice $\lambda_2, \mu_2^2 > 0$ ensures that the potential is bounded from below and has a non-vanishing vev. Choosing a ground state that minimizes the Higgs potential Eq. (2.11),

$$\Phi_0 = \begin{pmatrix} 0 \\ \frac{v}{\sqrt{2}} \end{pmatrix}, \qquad v \equiv 2\sqrt{\frac{\mu_2^2}{\lambda_2}}, \tag{2.12}$$

where we introduced the vev parameter v, spontaneously breaks both the weak isospin and the weak hypercharge, i.e.

$$I_{\mathrm{W}}^j \Phi_0 \neq 0, \qquad Y_{\mathrm{W}} \Phi_0 \neq 0. \tag{2.13}$$

The remaining combination

$$Q\Phi_0 \equiv \left(\frac{\sigma_3}{2} + \frac{Y_{\mathrm{W}}}{2} \right) \Phi_0 = 0, \tag{2.14}$$

that annihilates this ground state, defines the electric charge operator corresponding to the unbroken $U(1)_{\mathrm{em}}$ gauge group of electromagnetism.
For the following discussion it is useful to rewrite the Higgs doublet given in Eq. (2.9) in terms of component fields

$$\Phi = \begin{pmatrix} \phi^+ \\ \frac{1}{\sqrt{2}}(v + h + \mathrm{i}\chi) \end{pmatrix}, \tag{2.15}$$

which yield an expansion around the ground state Eq. (2.12). Here h corresponds to the neutral CP-even physical Higgs boson, χ represents a neutral CP-odd would-be Goldstone boson, and ϕ^+ and $\phi^- = (\phi^+)^\dagger$ describe the charged would-be Goldstone bosons.
While the three would-be Goldstone fields represent unphysical degrees of freedom, the Higgs field h introduces a physical Higgs boson with mass

$$M_\mathrm{h} = \sqrt{2\mu_2^2} \tag{2.16}$$

to the particle content of the SM. Combining Eqs. (2.10) and (2.15) yields the mass terms of the gauge bosons

$$\mathcal{L}^\mathrm{SM}_\mathrm{V,mass} = \frac{1}{4}\frac{v^2}{2}[g_2^2 W_\mu^1 W^{1,\mu} + g_2^2 W_\mu^2 W^{2,\mu} + (g_2 W_\mu^3 + g_1 B_\mu)(g_2 W^{3,\mu} + g_1 B^\mu)]. \tag{2.17}$$

The fields that correspond to mass and charge eigenstates are obtained by appropriate rotations,

$$W_\mu^\pm = \frac{1}{\sqrt{2}}\left(W_\mu^1 \mp \mathrm{i} W_\mu^2\right), \qquad \begin{pmatrix} B_\mu \\ W_\mu^3 \end{pmatrix} = \begin{pmatrix} c_\mathrm{w} & s_\mathrm{w} \\ -s_\mathrm{w} & c_\mathrm{w} \end{pmatrix} \begin{pmatrix} A_\mu \\ Z_\mu \end{pmatrix}, \tag{2.18}$$

where the so-called weak mixing angle θ_w is given by

$$c_\mathrm{w} \equiv \cos\theta_\mathrm{w} = \frac{g_2}{\sqrt{g_1^2 + g_2^2}}, \qquad s_\mathrm{w} \equiv \sin\theta_\mathrm{w}. \tag{2.19}$$

Finally, one ends up with a massless photon A as well as three massive physical gauge bosons Z and $\mathrm{W}^\pm$, with masses

$$M_\mathrm{A} = 0, \qquad M_\mathrm{Z} = \frac{v}{2}\sqrt{g_1^2 + g_2^2}, \qquad M_\mathrm{W} = \frac{g_2 v}{2}, \tag{2.20}$$

respectively. Further, identifying the coupling constant of the photon to charged particles to be the electric unit charge e one finds the relation

$$e = \frac{g_1 g_2}{\sqrt{g_1^2 + g_2^2}}, \tag{2.21}$$

between the coupling constants of the $SU(2)_\mathrm{W}$, $U(1)_\mathrm{Y}$, and the $U(1)_\mathrm{em}$. Finally, combining Eqs. (2.19) and (2.20) one finds the relation

$$c_\mathrm{w} = \frac{M_\mathrm{W}}{M_\mathrm{Z}}, \tag{2.22}$$

between the weak mixing angle and the gauge-boson masses in the SM.

2.1.2.1. Gauge-fixing and Ghost parts

Here we briefly discuss the gauge-fixing and ghost parts that have to be added when using the Faddeev–Popov method (FPM) to quantize the EWSM. A more detailed discussion on the FPM (within the DASM) is given in Sects. 3.2.2 and 3.2.3.
For the quantization of the EWSM a gauge has to be chosen to eliminate gauge-equivalent field configurations under the path integral. The most common choice is the so-called 't Hooft–Feynman gauge which is introduced by adding the gauge-fixing Lagrangian

$$\mathcal{L}^{\mathrm{SM}}_{\mathrm{EW,fix}} = -\frac{1}{2}\left(F^{A}\right)^{2} - \frac{1}{2}\left(F^{Z}\right)^{2} - F^{+}F^{-}, \tag{2.23}$$

with the gauge-fixing functionals

$$F^{A} = \partial^{\mu}A_{\mu}, \qquad F^{Z} = \partial^{\mu}Z_{\mu} - M_{\mathrm{Z}}\chi, \qquad F^{\pm} = \partial^{\mu}W^{\pm} \mp \mathrm{i}M_{\mathrm{W}}\phi^{\pm}, \tag{2.24}$$

to the EWSM. This choice leads to a cancelation between terms introduced by $\mathcal{L}^{\mathrm{SM}}_{\mathrm{Higgs}}$ that result in non-diagonal propagators in the gauge-boson–would-be Goldstone boson system and respective terms introduced by $\mathcal{L}^{\mathrm{SM}}_{\mathrm{EW,fix}}$. Furthermore, in 't Hooft–Feynman gauge the masses of the would-be Goldstone bosons coincide with the masses of their associated gauge bosons, $M_{\chi} = M_{\mathrm{Z}}$, $M_{\phi^{\pm}} = M_{\mathrm{W}}$.
To ensure the consistency of the gauge-fixing procedure under the functional integral the corresponding ghost part

$$\mathcal{L}^{\mathrm{SM}}_{\mathrm{EW,FP}} = -\int d^{4}y\, \bar{u}^{a}(x)\left(\frac{\delta F^{a}(x)}{\delta\theta^{b}(y)}\right)u^{b}(y), \tag{2.25}$$

with the ghost fields u^{a} and $\bar{u}^{a}$, $a = \mathrm{A}, \mathrm{Z}, \pm$, has to be added to the Lagrangian of the EWSM. Note that these Grassman-valued scalar ghost fields do not correspond to physical particles and, thus, will never represent external particle states in matrix elements.

2.1.3. Fermion sector

The matter content of the SM can be split up into up-type (u'_i) and down-type (d'_i) quarks, charged leptons (l'_i) , and neutrinos (ν'_i). Each of these classes consists of three fermions ($i = 1, 2, 3$) with identical internal quantum numbers but different masses. Note that in our notation primed fermion fields correspond to flavour eigenstates, while the respective fields without a prime correspond to mass eigenstates. Left-chiral up-type and down-type quarks as well as the left-chiral charged leptons and neutrinos are paired into the $SU(2)_{\mathrm{W}}$ doublets, L'^{L} and Q'^{L}, respectively. In contrast, their right-chiral counterparts are singlets with respect to the $SU(2)_{\mathrm{W}}$ gauge group,

$$L'^{\mathrm{L}}_{i} = \omega_{\mathrm{L}}L'_{i} = \begin{pmatrix}\nu'^{\mathrm{L}}_{i}\\ l'^{\mathrm{L}}_{i}\end{pmatrix}, \qquad Q'^{\mathrm{L}}_{i} = \omega_{\mathrm{L}}Q'_{i} = \begin{pmatrix}u'^{\mathrm{L}}_{i}\\ d'^{\mathrm{L}}_{i}\end{pmatrix}, \qquad l'^{\mathrm{R}}_{i} = \omega_{\mathrm{R}}l'_{i},$$

Quarks				Fermions			
type	Y_{W}	I^3_{W}	Q	type	Y_{W}	I^3_{W}	Q
u_i^L	$+1/3$	$+1/2$	$+2/3$	ν_i^L	-1	$+1/2$	0
d_i^L	$+1/3$	$-1/2$	$-1/3$	l_i^{L}	-1	$-1/2$	-1
u_i^{R}	$+4/3$	0	$+2/3$	l_i^{R}	-2	0	-1
d_i^{R}	$-2/3$	0	$-1/3$				

Table 2.1.: The EW quantum numbers carried by up-type quarks (u_i), down-type quarks (d_i), charged leptons (l_i), and neutrinos (ν_i), $i = 1, 2, 3$.

$$u_i'^{\mathrm{R}} = \omega_{\mathrm{R}} u_i', \qquad d_i'^{\mathrm{R}} = \omega_{\mathrm{R}} d_i', \tag{2.26}$$

where $\omega_{\mathrm{L/R}} = \frac{1}{2}(1 \mp \gamma_5)$ denote the chiral projection operators. Due to the maximal parity violation of the weak isospin, right-chiral neutrinos are singlets with respect to the SM gauge group. Further, neutrinos are assumed to be massless within the SM. Therefore, right-chiral neutrinos completely decouple from the rest of the theory and consequently are not present within the SM. In Tab. 2.1 we list the fermions of the SM with their respective $SU(2)_{\mathrm{W}} \times U(1)_{\mathrm{Y}}$ quantum numbers and electric charges. The kinetic terms and EW gauge interactions for the fermions read

$$\mathcal{L}^{\mathrm{SM}}_{\mathrm{Fermion}} = \sum_j \left(\mathrm{i}\bar{L}_j'^{\mathrm{L}} \not{D} L_j'^{\mathrm{L}} + \mathrm{i}\bar{Q}_j'^{\mathrm{L}} \not{D} Q_j'^{\mathrm{L}} + \mathrm{i}\bar{l}_j'^{\mathrm{R}} \not{D} l_j'^{\mathrm{R}} + \mathrm{i}\bar{u}_j'^{\mathrm{R}} \not{D} u_j'^{\mathrm{R}} + \mathrm{i}\bar{d}_j'^{\mathrm{R}} \not{D} d_j'^{\mathrm{R}} \right), \tag{2.27}$$

where we made use of the "slashed notation" $\not{D} = \gamma^\mu D_\mu$, with the gamma matrices γ_μ and the covariant derivative given by Eq. (2.6).
In the EWSM, the Higgs doublet is used to introduce mass terms for the fermion fields in a gauge-invariant way. The respective Yukawa part of the Lagrangian reads

$$\mathcal{L}^{\mathrm{SM}}_{\mathrm{Yukawa}} = -\sum_{i,j} (\bar{L}_i'^{\mathrm{L}} G^l_{ij} l_j'^{\mathrm{R}} \Phi + \bar{Q}_i'^{\mathrm{L}} G^u_{ij} u_j'^{\mathrm{R}} \tilde{\Phi} + \bar{Q}_i'^{\mathrm{L}} G^d_{ij} d_j'^{\mathrm{R}} \Phi + \mathrm{h.c.}). \tag{2.28}$$

Here i, j runs over the three fermion generations, G^l_{ij}, G^u_{ij}, and G^d_{ij} are the Yukawa coupling-constant matrices, and the charge-conjugated Higgs doublet is given by $\tilde{\Phi} \equiv ((\phi^0)^*, -\phi^-)^{\mathrm{T}}$. To obtain the mass eigenbasis, the matrices G^l_{ij}, G^u_{ij}, and G^d_{ij} have to be diagonalized. This is achieved by an appropriate bi-unitary transformation of the form

$$f_i^{\mathrm{L}} = U^{f,\mathrm{L}}_{ij} f_j'^{\mathrm{L}}, \qquad f_i^{\mathrm{R}} = U^{f,\mathrm{R}}_{ij} f_j'^{\mathrm{R}}, \qquad f = l, u, d. \tag{2.29}$$

The resulting masses for the fermions are given by

$$m_{f,i} = \frac{v}{\sqrt{2}} U^{f,\mathrm{L}}_{ij} G^f_{jk} \left(U^{f,\mathrm{R}}_{ki} \right)^\dagger. \tag{2.30}$$

While the unitary matrices $U_{ij}^{f,\mathrm{L/R}}$ systematically cancel in the fermion–neutral-gauge-boson interactions, Eq. (2.29) introduces the Cabibbo–Kobayashi–Maskawa (CKM) [55, 56] matrix

$$V_{\mathrm{CKM}} = U_{ij}^{u,\mathrm{L}} \left(U_{ij}^{d,\mathrm{L}}\right)^{\dagger}, \tag{2.31}$$

in the quark–W-boson and quark–$\phi^{\pm}$-boson interactions. This non-diagonal unitary matrix can be parameterized by three angles and a complex phase. The CKM matrix allows for flavour-changing charged currents in the quark sector and provides the only source of CP violation within the EWSM. The absence of a neutrino mass matrix in Eq. (2.28) allows to choose the fields corresponding to the physical neutrinos according to

$$\nu_i^{\mathrm{L}} = U_{ij}^{l,\mathrm{L}} \nu_j'^{\mathrm{L}}. \tag{2.32}$$

This choice results in a diagonal matrix in the lepton–W-boson and lepton–$\phi^{\pm}$-boson interactions, showcasing that no flavour-changing charged currents are present in the leptonic sector. This, however, is only true if the SM-like neutrinos are assumed to be massless (or if all neutrinos have the same mass) whereas the so-called Pontecorvo–Maki–Nakagawa–Sakata (PMNS) [57, 58] matrix has to be taken into account otherwise.

2.2. The QCD Lagrangian

To complete our description of the SM, we briefly discuss the main features of QCD. The theory of QCD is based on the $SU(3)_{\mathrm{C}}$ part of the SM gauge group and governs the strong interactions. In the SM the $SU(3)_{\mathrm{C}}$ part of the gauge group fully factorises from the EW part described in the previous section.
The mediators of the strong force are the massless gluons. In total, there are eight gluons, associated with the eight generators T^a, $a = 1, ..., 8$, of $SU(3)_{\mathrm{C}}$. The charge associated with the $SU(3)_{\mathrm{C}}$ is called colour charge. There are three colours: red, green, and blue. In the SM only quarks and gluons carry colour charge, i.e. are affected by the strong interactions. The quarks transform as triplets[4] under $SU(3)_{\mathrm{C}}$ and, therefore, carry an additional colour index c

$$\psi_{q,c} = \begin{pmatrix} \psi_{q,\mathrm{red}} \\ \psi_{q,\mathrm{green}} \\ \psi_{q,\mathrm{blue}} \end{pmatrix}. \tag{2.33}$$

To account for the three colours in the quark parts of Eqs. (2.27) and (2.28) an implicit sum over the colours is assumed. The gluon fields themselves transform according to the adjoint (octet) representation of $SU(3)_{\mathrm{C}}$. The respective part of

[4] Antiquarks carry the respective anti-colours: anti-red, anti-green, and anti-blue.

the Lagrangian, describing the kinetic terms for the gluons as well as the strong gauge interactions of the quarks, reads

$$\mathcal{L}_{\text{QCD}}^{\text{SM}} = -\frac{1}{4} G_{\mu\nu}^{a} G^{a,\mu\nu} + \mathrm{i} g_{\text{s}} \sum_{q_i} \bar{q}_i \not{G}^{a} T^{a} q_i, \tag{2.34}$$

where $T^a = \frac{\lambda^a}{2}$, $a = 1, \ldots, 8$, with the Gell-Mann matrices λ^a, are the eight generators in the fundamental representation of $SU(3)_{\text{C}}$, G_μ^a are the gluon fields, g_{s} is the coupling constant corresponding to the strong interactions, and the sum runs over all up- and down-type quarks $q_i = u_i, d_i$, $i = 1, 2, 3$. The field-strength tensors of the gluons are given by

$$G_{\mu\nu}^{a} = \partial_\mu G_\nu^a - \partial_\nu G_\mu^a + g_{\text{s}} f^{abc} G_\mu^b G_\nu^c, \qquad a, b, c = 1, \ldots, 8, \tag{2.35}$$

with the structure constants f^{abc} of $SU(3)_{\text{C}}$.
The gauge-fixing procedure for QCD is done similarly to the one of the EW sector. Using 't Hooft–Feynman gauge, we add the respective gauge-fixing part

$$\mathcal{L}_{\text{QCD,fix}} = -\frac{1}{2} \left(F^{G_a} \right)^2, \qquad F^{G_a} = \partial^\mu G_\mu^a, \tag{2.36}$$

and the corresponding ghost part

$$\mathcal{L}_{\text{QCD,FP}}(x) = -\int \mathrm{d}^4 y \, \bar{u}^a(x) \left(\frac{\delta F^a(x)}{\delta \theta^b(y)} \right) u^b(y), \qquad a, b = G_1, \ldots, G_8, \tag{2.37}$$

with the $SU(3)_{\text{C}}$ group parameters θ^b, to $\mathcal{L}_{\text{QCD}}^{\text{SM}}$ to complete the construction of the SM Lagrangian.

2.3. Physics Beyond the SM

Countless predictions of the SM show an impressive agreement with their respective high-precision collider measurements. Moreover, all particles postulated by the SM are found and their predicted properties agree precisely with the corresponding experimental results, further highlighting the outstanding predictive power of the SM. Nevertheless, there are several open questions that cannot be addressed by the SM in its current form. Some of the most pressing ones are:

- In the SM neutrinos are assumed to be massless. This is, however, in contradiction to the observed neutrino oscillations [59, 60]. These oscillations are sensitive to the squared mass differences between the three neutrino generations, implying that at least two of the three neutrinos must be massive. There are several ongoing studies aiming to determine the masses of the neutrinos through β-decay [61] or via cosmological observations (see e.g. Refs. [24, 62] and references therein). However, to the present day, these analyses are only capable of setting upper limits on the neutrino masses or the sum of the masses of the three generations, respectively.

- There are several observations, e.g. measurements of rotation curves of galaxies [63] that hint towards the existence of so-called "dark matter" (DM). Modern experiments suggest that DM makes up 27% [62] of the energy density of the universe. Yet, observations suggest that DM cannot be made up of SM particles (as required e.g. by Big Bang nucleosynthesis, see e.g. Ref. [64] and references therein). If DM is assumed to be of particle nature its constituents have to be electrically neutral; stable on cosmological scales; "cold", i.e. non-relativistic during the epoch of structure formation (for more details see e.g. Ref. [65]); and have a small self-interaction cross section (also referred to as "collisionless" in the literature) [66].

- The SM offers no explanation for the matter–antimatter asymmetry observed in the visible universe. If we assume that the universe started in a symmetric phase (with equal amounts of matter and antimatter), the baryon asymmetry must have been generated dynamically in the early universe. Such a process is called baryogenesis. For baryogenesis to happen three necessary conditions have to be fulfilled [67]: there have to be baryon-number violating processes, there have to be C- and CP-violating processes, and finally, there has to be some non-equilibrium present in the process of baryogenesis. In the SM all of these effects are possible: there are (non-perturbative) baryon-number violating processes present at high temperatures, C- and CP-violation is present within the EW part of the SM, and the out-of-equilibrium condition is provided by the EW phase transition. With this setting a baryon asymmetry could have been generated in the SM via the so-called EW baryogenesis. Nonetheless, it has been shown that the magnitude of CP violation present in the EWSM is not sufficient to account for the observed matter–antimatter asymmetry in the visible universe and that the second-order phase transition present in the SM does not allow for the creation of a sizable baryon asymmetry within the setting of the EW baryogenesis.

- Within the SM there is no explanation for the origin of "dark energy", which drives the accelerated expansion of the present universe. Modern experiments performed, e.g. by the Planck Collaboration [62], suggest that dark energy makes up 68% of the total energy density of the universe. A possible contribution to this energy density could originate from the cosmological constant describing a respective energy density that is constant within spacetime. However, some estimates of the SM vacuum energy, i.e. its possible contributions to the cosmological constant, yield an energy density that is 120 orders of magnitude larger than the measured energy density (see Ref. [68] and references therein).

- Due to the lack of a quantum-field-theoretical description of the gravitational force, gravity is not included in the SM.

These unresolved issues clearly demonstrate that the SM cannot be the ultimate

theory describing Nature, but should rather be seen as an effective model of some more fundamental theory. In addition to the previously mentioned problems, one might include the long-standing tension between the high-precision SM prediction and the measurement of the anomalous magnetic moment of the muon:

- The SM prediction for the anomalous magnetic moment of the muon, $(g-2)_\mu$, shows a 5.1σ deviation from its measured value [3]. However, recent developments in the field of lattice QCD (see e.g. Ref. [5]) raised questions on the correct determination of the so-called hadronic vacuum polarization $\Delta\alpha^{(5)}_{\text{had}}$ which enters the theoretical prediction for $(g-2)_\mu$. Using the lattice results for $\Delta\alpha^{(5)}_{\text{had}}$ to predict $(g-2)_\mu$ leads to reasonably good agreement (1.7σ) between its SM prediction and the measured value. Thus, clarification on the correct theoretical treatment is needed. However, if the tension between prediction and measurement remains, BSM physics might yield an explanation for the observed discrepancy.

3. The Dark Abelian Sector Model

In the following, we define the Dark Abelian Sector Model (DASM) and discuss in detail all its additional features with respect to the SM. Further, in Sect. 3.6, we give a particularly intuitive set of input parameters, which is used in the renormalization of the model described in Chapter 4 and the phenomenological investigation of the DASM discussed in Chapter 5. Finally, the resulting Feynman rules for the DASM are listed in Appendix F. Note that the results presented in Chapters 3 and 4 have already been published in Ref. [38].

The DASM adds an additional $U(1)_\mathrm{d}$ gauge symmetry, with corresponding gauge field C^μ, of a possible hidden sector to the SM gauge group. Thus, its underlying gauge group is given by

$$SU(3)_\mathrm{C} \times SU(2)_\mathrm{W} \times U(1)_\mathrm{Y} \times U(1)_\mathrm{d}. \tag{3.1}$$

The SM is a singlet with respect to the new $U(1)_\mathrm{d}$. Further, a Higgs field ρ and a Dirac fermion f'_d, which are both singlets with respect to the SM, but carry charge of the $U(1)_\mathrm{d}$, are introduced in the DASM. Finally, the DASM introduces right-handed SM-like neutrino fields $\nu_j'^\mathrm{R}$, $j = e, \mu, \tau$, which are singlets with respect to the gauge group of the DASM. This leads to various additional terms that have to be added to the SM Lagrangian discussed in the previous chapter. As already stated in Chapter 2, we adopt the notation and conventions from Ref. [54] for all field-theoretical quantities.
It is convenient to split up the full Lagrangian of the DASM in a similar way as it was done for the SM case

$$\mathcal{L}_\mathrm{DASM} = \mathcal{L}_\mathrm{YM} + \mathcal{L}_\mathrm{Fermion} + \mathcal{L}_\mathrm{Higgs} + \mathcal{L}_\mathrm{QCD}. \tag{3.2}$$

Below we discuss the non-SM contributions to the individual parts of $\mathcal{L}_\mathrm{DASM}$ in detail. Note that the QCD part of the DASM $\mathcal{L}_\mathrm{QCD}$ is equivalent to its SM counterpart and, therefore, its description given in Section 2.2 accounts for the QCD part of the DASM as well.

3.1. Higgs sector

The presence of an additional complex Higgs field ρ leads to modifications of the scalar sector compared to its SM counterpart. The respective Higgs part of the DASM Lagrangian reads

$$\mathcal{L}_{\text{Higgs}} = (D_\mu \Phi)^\dagger (D^\mu \Phi) + (D_{\text{d},\mu}\rho)^\dagger (D_{\text{d}}^\mu \rho) - V(\Phi, \rho). \tag{3.3}$$

Since the SM-like Higgs doublet is not charged under the additional $U(1)_\text{d}$ gauge symmetry, its covariant derivative is equivalent to the one in the SM given in Eq. (2.6). For the Higgs field ρ the covariant derivative is given by

$$D_{\text{d}}^\mu = \partial^\mu + \mathrm{i}\tilde{q} e_\text{d} C^\mu, \qquad \tilde{q}\rho = \tilde{q}_\rho \rho, \qquad \tilde{q}_\rho = 1, \tag{3.4}$$

where we introduced the charge operator $\tilde{q}$ and the coupling constant e_d of the $U(1)_\text{d}$. Note that the choice $\tilde{q}_\rho = 1$ will, without loss of generality, only provide a normalization of the coupling constant e_d.
To obtain the most general renormalizable (mass dimension ≤ 4) and gauge-invariant scalar potential $V(\Phi, \rho)$ we have to add three additional terms to the SM Higgs potential (see Eq. (2.11)),

$$\begin{aligned} V(\Phi,\rho) =& -\mu_2^2 \Phi^\dagger\Phi - 2\mu_1^2 \rho^\dagger\rho + \frac{\lambda_2}{4}(\Phi^\dagger\Phi)^2 + 4\lambda_1(\rho^\dagger\rho)^2 + 2\lambda_{12}\Phi^\dagger\Phi\rho^\dagger\rho \\ =& V^{\text{SM}}(\Phi) - 2\mu_1^2\rho^\dagger\rho + 4\lambda_1(\rho^\dagger\rho)^2 + 2\lambda_{12}\Phi^\dagger\Phi\rho^\dagger\rho, \end{aligned} \tag{3.5}$$

which introduces the three additional real free parameters[1] μ_1^2, λ_1, and λ_{12}. The last term of Eq. (3.5) is of particular interest since it opens a portal from the SM to the hidden sector of the DASM by allowing for mixing between the SM-like Higgs doublet Φ and the Higgs field ρ. The strength of this mixing is ruled by the free parameter λ_{12}. The Higgs fields Φ and ρ can be parameterized as

$$\Phi = \begin{pmatrix} \phi^+ \\ \frac{1}{\sqrt{2}}(h_2 + v_2 + \mathrm{i}\chi_2) \end{pmatrix}, \qquad \rho = \frac{1}{\sqrt{2}}(h_1 + v_1 + \mathrm{i}\chi_1), \tag{3.6}$$

with the CP-even Higgs fields h_2, h_1, the neutral CP-odd would-be Goldstone-boson fields χ_2, χ_1, and the charged would-be Goldstone-boson field ϕ^+. The real and positive constants v_2 and v_1 quantify the non-vanishing vevs of Φ and ρ, respectively. To ensure the stability of the vacuum the parameters of the Higgs potential have to fulfill the conditions

$$\lambda_1 > 0, \quad \lambda_2 > 0, \quad \lambda_1\lambda_2 - \lambda_{12}^2 > 0. \tag{3.7}$$

Combining Eqs. (3.5) and (3.6) leads to

$$V = -t_1 h_1 - t_2 h_2$$

[1] We choose their normalization such that it matches previous studies of Higgs singlet extensions (see, e.g., Refs. [69]).

$$
\begin{aligned}
&+ \frac{1}{2}(h_2, h_1)\mathrm{M}^2_{\mathrm{Higgs}} \begin{pmatrix} h_2 \\ h_1 \end{pmatrix} + \frac{1}{2}(\chi_1, \chi_2)\mathrm{M}^2_{\chi} \begin{pmatrix} \chi_1 \\ \chi_2 \end{pmatrix} + \mathrm{M}^2_{\phi^+\phi^-}\phi^-\phi^+ \\
&+ \text{interaction terms.}
\end{aligned} \tag{3.8}
$$

The first line of Eq. (3.8) contains the tadpole terms, $t_1 h_1$ and $t_2 h_2$, with the tadpole constants given by

$$
t_1 = -v_1\left(4v_1^2\lambda_1 + v_2^2\lambda_{12} - 2\mu_1^2\right), \qquad t_2 = -v_2\left(\frac{v_2^2}{4}\lambda_2 + v_1^2\lambda_{12} - \mu_2^2\right). \tag{3.9}
$$

The mass terms of the component fields are given in the second line of Eq. (3.8), with their corresponding mass matrices

$$
\mathrm{M}^2_{\mathrm{Higgs}} = \begin{pmatrix} \frac{v_2^2}{2}\lambda_2 - \frac{t_2}{v_2} & 2v_1v_2\lambda_{12} \\ 2v_1v_2\lambda_{12} & 8v_1^2\lambda_1 - \frac{t_1}{v_1} \end{pmatrix}, \qquad \mathrm{M}^2_{\chi} = \begin{pmatrix} -\frac{t_1}{v_1} & 0 \\ 0 & -\frac{t_2}{v_2} \end{pmatrix}, \tag{3.10}
$$

and the masses of the charged would-be Goldstone-boson fields are given by

$$
\mathrm{M}^2_{\phi^+\phi^-} = -\frac{t_2}{v_2}. \tag{3.11}
$$

The last line of Eq. (3.8) summarizes all scalar self-interaction terms, i.e., all terms containing three or four scalar fields. Similar to the SM, the tadpole constants t_1 and t_2 are set to zero at leading order. This ensures at LO that the Higgs potential acquires its minimum at the vevs, i.e. for $h_i = \chi_i = \phi^+ = 0$ with $i = 1, 2$. Since they play a special role in the renormalization procedure, we keep them explicit in the following.

In order to obtain the field basis corresponding to physical particles we have to rotate the Higgs fields h_1, h_2 into the fields h, H, which correspond to the desired mass eigenstates. Therefore, we diagonalize the respective mass matrix $\mathrm{M}^2_{\mathrm{Higgs}}$ with the following rotation by an angle α,

$$
\begin{pmatrix} h \\ H \end{pmatrix} = \begin{pmatrix} \cos\alpha & -\sin\alpha \\ \sin\alpha & \cos\alpha \end{pmatrix} \begin{pmatrix} h_2 \\ h_1 \end{pmatrix}. \tag{3.12}
$$

Expressing the potential given in Eq. (3.8) in terms of h and H reads

$$
\begin{aligned}
V = &- t_h h - t_H H \\
&+ \frac{1}{2}(h, H) \begin{pmatrix} M_{\mathrm{h}}^2 & M_{\mathrm{hH}}^2 \\ M_{\mathrm{hH}}^2 & M_{\mathrm{H}}^2 \end{pmatrix} \begin{pmatrix} h \\ H \end{pmatrix} + \frac{1}{2}(\chi_1, \chi_2)\mathrm{M}^2_{\chi} \begin{pmatrix} \chi_1 \\ \chi_2 \end{pmatrix} + M^2_{\phi^+\phi^-}\phi^-\phi^+ \\
&+ \text{interaction terms,}
\end{aligned} \tag{3.13}
$$

with the rotated tadpole constants

$$
t_h = c_\alpha t_2 - s_\alpha t_1, \qquad t_H = s_\alpha t_2 + c_\alpha t_1. \tag{3.14}
$$

Here we introduced the shorthands $c_\alpha = \cos\alpha$ and $s_\alpha = \sin\alpha$, which will be used throughout this thesis to keep expressions compact. In this field basis, the coefficients of the Higgs-boson mass matrix are given by

$$M_{\mathrm{h}}^2 = c_\alpha^2 \frac{v_2^2}{2}\lambda_2 - c_\alpha^2 \frac{t_2}{v_2} + 8 s_\alpha^2 v_1^2 \lambda_1 - s_\alpha^2 \frac{t_1}{v_1} - 4 s_\alpha c_\alpha v_1 v_2 \lambda_{12}, \tag{3.15}$$

$$M_{\mathrm{H}}^2 = s_\alpha^2 \frac{v_2^2}{2}\lambda_2 - s_\alpha^2 \frac{t_2}{v_2} + 8 c_\alpha^2 v_1^2 \lambda_1 - c_\alpha^2 \frac{t_1}{v_1} + 4 s_\alpha c_\alpha v_1 v_2 \lambda_{12}, \tag{3.16}$$

$$M_{\mathrm{hH}}^2 = M_{\mathrm{Hh}}^2 = s_\alpha c_\alpha \left(\frac{v_2^2}{2}\lambda_2 - \frac{t_2}{v_2} - 8 v_1^2 \lambda_1 - \frac{t_1}{v_1} \right) + 2(c_\alpha^2 - s_\alpha^2) v_1 v_2 \lambda_{12}. \tag{3.17}$$

The diagonalization condition fixing the rotation angle α thus reads

$$M_{\mathrm{hH}}^2 = s_\alpha c_\alpha \left(\frac{v_2^2}{2}\lambda_2 - \frac{t_2}{v_2} - 8 v_1^2 \lambda_1 - \frac{t_1}{v_1} \right) + 2(c_\alpha^2 - s_\alpha^2) v_1 v_2 \lambda_{12} \stackrel{!}{=} 0, \tag{3.18}$$

and for $t_1 = t_2 = 0$ one finds

$$t_{2\alpha} = \frac{8 v_1 v_2 \lambda_{12}}{16 v_1^2 \lambda_1 - v_2^2 \lambda_2}. \tag{3.19}$$

Without loss of generality we enforce the mass hierarchy $M_{\mathrm{h}} < M_{\mathrm{H}}$ by allowing for $\alpha \in (-\frac{\pi}{2}, \frac{\pi}{2}]$ and simultaneously demanding $s_{2\alpha}\lambda_{12} \geq 0$. This fixes α to

$$s_{2\alpha} = \frac{8 v_1 v_2 \lambda_{12}}{\sqrt{(8 v_1 v_2 \lambda_{12})^2 + (16 v_1^2 \lambda_1 - v_2^2 \lambda_2)^2}}, \tag{3.20}$$

$$c_{2\alpha} = \frac{16 v_1^2 \lambda_1 - v_2^2 \lambda_2}{\sqrt{(8 v_1 v_2 \lambda_{12})^2 + (16 v_1^2 \lambda_1 - v_2^2 \lambda_2)^2}}. \tag{3.21}$$

The relation between the mass eigenvalues of the Higgs bosons h and H, and the original parameters of the Lagrangian (see Eqs. (3.5) and (3.6)) are given by

$$M_{\mathrm{h}}^2 = \frac{1}{4} v_2^2 \lambda_2 + 4 v_1^2 \lambda_1 - \frac{1}{4}\sqrt{(8 v_1 v_2 \lambda_{12})^2 + (16 v_1^2 \lambda_1 - v_2^2 \lambda_2)^2}, \tag{3.22}$$

$$M_{\mathrm{H}}^2 = \frac{1}{4} v_2^2 \lambda_2 + 4 v_1^2 \lambda_1 + \frac{1}{4}\sqrt{(8 v_1 v_2 \lambda_{12})^2 + (16 v_1^2 \lambda_1 - v_2^2 \lambda_2)^2}. \tag{3.23}$$

In total, the Higgs sector extension of the DASM introduces three additional free parameters to the theory. The tadpole constants t_1 and t_2 (or equivalently t_h and t_H) are fixed by the definition of the EW vacuum and, therefore, do not count as free input parameters. As mentioned above, we only keep them here for later convenience. Choosing the input parameters to be the most intuitive and phenomenologically easily accessible, we use M_{h}, M_{H}, the mixing angle α, and the dimensionless scalar self-coupling λ_{12} to express the original parameters of the Higgs potential,

$$\lambda_1 = \frac{1}{8 v_1^2}\left(c_\alpha^2 M_{\mathrm{H}}^2 + s_\alpha^2 M_{\mathrm{h}}^2 \right) + \frac{1}{8 v_1^3} t_1, \tag{3.24}$$

$$\lambda_2 = \frac{2}{v_2^2}\left(c_\alpha^2 M_\mathrm{h}^2 + s_\alpha^2 M_\mathrm{H}^2\right) + \frac{2}{v_2^3} t_2, \tag{3.25}$$

$$\mu_1^2 = \frac{1}{4}\left(s_\alpha^2 M_\mathrm{h}^2 + c_\alpha^2 M_\mathrm{H}^2\right) + \frac{1}{2} v_2^2 \lambda_{12} + \frac{3}{4v_1} t_1, \tag{3.26}$$

$$\mu_2^2 = v_1^2 \lambda_{12} + \frac{1}{2}\left(c_\alpha^2 M_\mathrm{h}^2 + s_\alpha^2 M_\mathrm{H}^2\right) + \frac{3}{2v_2} t_2, \tag{3.27}$$

$$v_1 = \frac{\left(M_\mathrm{H}^2 - M_\mathrm{h}^2\right) s_{2\alpha}}{4 v_2 \lambda_{12}}. \tag{3.28}$$

In the DASM, similar to the SM case, the vev v_2 is determined by the W-boson mass (see Sect. 3.2 for more details). From Eqs. (3.24)–(3.28) it is obvious that the vacuum stability constraints given in Eq. (3.7) as well as the requirement of symmetry breaking $\mu_1^2 > 0$ or $\mu_2^2 > 0$ are automatically fulfilled for physical input parameters, i.e. $M_\mathrm{h}, M_\mathrm{H} > 0$.
Expanding the interaction terms in the last line of Eq. (3.13) one finds three and four particle scalar self-interaction terms of the form

$$\begin{aligned} V_\mathrm{int} = {} & c_\mathrm{hhh} h^3 + c_\mathrm{hhH} h^2 H + c_\mathrm{hHH} h H^2 + c_\mathrm{HHH} H^3 \\ & + c_\mathrm{hhhh} h^4 + c_\mathrm{hhhH} h^3 H + c_\mathrm{hhHH} h^2 H^2 + c_\mathrm{hHHH} h H^3 + c_\mathrm{HHHH} H^4 \\ & + \frac{1}{2}(c_{\mathrm{h}\phi\phi} h + c_{\mathrm{H}\phi\phi} H + c_{\mathrm{hh}\phi\phi} h^2 + c_{\mathrm{hH}\phi\phi} h H + c_{\mathrm{HH}\phi\phi} H^2)(2\phi^+\phi^- + \chi_2^2) \\ & + \frac{1}{2}(c_{\mathrm{h}\chi\chi} h + c_{\mathrm{H}\chi\chi} H + c_{\mathrm{hh}\chi\chi} h^2 + c_{\mathrm{hH}\chi\chi} h H + c_{\mathrm{HH}\chi\chi} H^2)\chi_1^2 \\ & + \frac{\lambda_2}{16}(2\phi^+\phi^- + \chi_2^2)^2 + \frac{\lambda_{12}}{2}\chi_1^2(\chi_2^2 + 2\phi^-\phi^+) + \lambda_1 \chi_1^4, \end{aligned} \tag{3.29}$$

with the coupling constants

$$c_\mathrm{hhh} = v_2 c_\alpha \left(\lambda_{12} s_\alpha^2 + \frac{\lambda_2 c_\alpha^2}{4}\right) - v_1 s_\alpha \left(\lambda_{12} c_\alpha^2 + 4\lambda_1 s_\alpha^2\right), \tag{3.30}$$

$$c_\mathrm{hhH} = v_1 \lambda_{12} c_\alpha^3 + v_2 \lambda_{12} s_\alpha^3 + s_{2\alpha}\left(v_2 c_\alpha (\frac{3}{8}\lambda_2 - \lambda_{12}) + v_1 s_\alpha (6\lambda_1 - \lambda_{12})\right), \tag{3.31}$$

$$c_\mathrm{hHH} = v_2 \lambda_{12} c_\alpha^3 - v_1 \lambda_{12} s_\alpha^3 + s_{2\alpha}\left(s_\alpha v_2 (\frac{3}{8}\lambda_2 - \lambda_{12}) + c_\alpha v_1 (\lambda_{12} - 6\lambda_1)\right), \tag{3.32}$$

$$c_\mathrm{HHH} = v_2 s_\alpha \left(\lambda_{12} c_\alpha^2 + \frac{\lambda_2 s_\alpha^2}{4}\right) + v_1 c_\alpha (\lambda_{12} s_\alpha^2 + 4\lambda_1 c_\alpha^2), \tag{3.33}$$

$$c_\mathrm{hhhh} = s_\alpha^4 \lambda_1 + \frac{1}{2} s_\alpha^2 c_\alpha^2 \lambda_{12} + \frac{c_\alpha^4}{16}\lambda_2, \tag{3.34}$$

$$c_\mathrm{hhhH} = \frac{\lambda_2}{8} s_{2\alpha} c_\alpha^2 - 2 s_{2\alpha} s_\alpha^2 \lambda_1 - \frac{\lambda_{12}}{2} c_{2\alpha} s_{2\alpha}, \tag{3.35}$$

$$c_\mathrm{hhHH} = \frac{3\lambda_1}{2} s_{2\alpha}^2 + \frac{3\lambda_2}{32} s_{2\alpha}^2 + \frac{\lambda_{12}}{4}\left(2c_{2\alpha}^2 - s_{2\alpha}^2\right), \tag{3.36}$$

$$c_\mathrm{hHHH} = \frac{\lambda_2}{8} s_{2\alpha} s_\alpha^2 - 2\lambda_1 s_{2\alpha} c_\alpha^2 + \frac{\lambda_{12}}{2} c_{2\alpha} s_{2\alpha}, \tag{3.37}$$

$$c_{\mathrm{HHHH}} = c_\alpha^4 \lambda_1 + \frac{s_\alpha^4}{16}\lambda_2 + \frac{1}{2}s_\alpha^2 c_\alpha^2 \lambda_{12}, \tag{3.38}$$

$$c_{\mathrm{h}\phi\phi} = \frac{v_2}{2}\lambda_2 c_\alpha - 2 s_\alpha v_1 \lambda_{12}, \tag{3.39}$$

$$c_{\mathrm{H}\phi\phi} = \frac{v_2}{2}\lambda_2 s_\alpha + 2 v_1 \lambda_{12} c_\alpha, \tag{3.40}$$

$$c_{\mathrm{hh}\phi\phi} = \frac{\lambda_2}{4} c_\alpha^2 + s_\alpha^2 \lambda_{12}, \tag{3.41}$$

$$c_{\mathrm{hH}\phi\phi} = \frac{\lambda_2}{2} s_\alpha c_\alpha - 2\lambda_{12} s_\alpha c_\alpha, \tag{3.42}$$

$$c_{\mathrm{HH}\phi\phi} = \frac{\lambda_2}{4} s_\alpha^2 + \lambda_{12} c_\alpha^2, \tag{3.43}$$

$$c_{\mathrm{h}\chi\chi} = 2 v_2 \lambda_{12} c_\alpha - 8 v_1 \lambda_1 s_\alpha, \tag{3.44}$$

$$c_{\mathrm{H}\chi\chi} = 8 v_1 \lambda_1 c_\alpha + 2 v_2 \lambda_{12} s_\alpha, \tag{3.45}$$

$$c_{\mathrm{hh}\chi\chi} = \lambda_{12} c_\alpha^2 + 4\lambda_1 s_\alpha^2, \tag{3.46}$$

$$c_{\mathrm{hH}\chi\chi} = 2\lambda_{12} s_\alpha c_\alpha - 8\lambda_1 s_\alpha c_\alpha, \tag{3.47}$$

$$c_{\mathrm{HH}\chi\chi} = 4\lambda_1 c_\alpha^2 + \lambda_{12} s_\alpha^2. \tag{3.48}$$

3.2. Gauge sector

Due to the presence of the additional $U(1)_\mathrm{d}$ gauge group, the gauge sector of the DASM governs several additional terms compared to its SM counterpart. In the past, several types of $U(1)$ extensions have been discussed qualitatively in the literature (see e.g. [13, 25–28]). However, to match the precision of modern EW precision measurements at least NLO precision is needed. In this work, we give the DASM in R_ξ gauge, which is the most common and convenient framework for the calculation of the higher-order corrections performed in the following Chapters 4 and 5.

Due to the extension of the SM gauge group by an additional $U(1)_\mathrm{d}$, further terms have to be added to the SM YM part to obtain its DASM counterpart,

$$\mathcal{L}_\mathrm{YM} = \mathcal{L}_\mathrm{YM}^\mathrm{SM} + \mathcal{L}_\mathrm{YM}^\mathrm{d}, \tag{3.49}$$

where

$$\mathcal{L}_\mathrm{YM}^\mathrm{d} = -\frac{1}{4} C^{\mu\nu} C_{\mu\nu} - \frac{a}{2} B^{\mu\nu} C_{\mu\nu}. \tag{3.50}$$

The gauge-invariant field-strength tensors

$$B_{\mu\nu} = \partial_\mu B_\nu - \partial_\nu B_\mu, \qquad C_{\mu\nu} = \partial_\mu C_\nu - \partial_\nu C_\mu, \tag{3.51}$$

correspond to the gauge fields B_μ and C_μ of the $U(1)_\mathrm{Y}$ and $U(1)_\mathrm{d}$, respectively. While the first term on the right-hand side of Eq. (3.50) simply gives the kinetic

term for the gauge field C_μ, the gauge invariance of field-strength tensors of abelian gauge groups (see Sect. 2.1.1) further allows for kinetic mixing described by the second term. The strength of this mixing is ruled by the free parameter a.

3.2.1. Physical gauge bosons

In a first step towards constructing the field basis corresponding to the physical gauge bosons, we diagonalize the kinetic terms by redefining the fields [27],

$$\begin{pmatrix} C_\mu \\ B_\mu \end{pmatrix} = \begin{pmatrix} \frac{1}{\sqrt{1-a^2}} & 0 \\ -\frac{a}{\sqrt{1-a^2}} & 1 \end{pmatrix} \begin{pmatrix} C'_\mu \\ B'_\mu \end{pmatrix}. \tag{3.52}$$

With this redefinition the kinetic terms for the primed fields C'_μ and B'_μ are in the common canonically normalized form

$$\begin{aligned} \mathcal{L}_{\mathrm{YM}} &= -\frac{1}{4} C^{\mu\nu} C_{\mu\nu} - \frac{a}{2} B^{\mu\nu} C_{\mu\nu} - \frac{1}{4} B^{\mu\nu} B_{\mu\nu} - \frac{1}{4} W^{b,\mu\nu} W^b_{\mu\nu} \\ &= -\frac{1}{4} C'^{\mu\nu} C'_{\mu\nu} - \frac{1}{4} B'^{\mu\nu} B'_{\mu\nu} - \frac{1}{4} W^{b,\mu\nu} W^b_{\mu\nu}. \end{aligned} \tag{3.53}$$

Note that we have to restrict the kinetic mixing strength to $|a| \leq 1$ to maintain the self-consistency of the theory, since choosing $|a| > 1$ would lead to a wrong signature for one of the kinetic terms. Rewriting the covariant derivatives for the Higgs fields Φ and ρ given in Eqs. (2.6) and (3.4), respectively, in terms of the primed fields and expanding the kinetic part of the Higgs Lagrangian given by Eq. (3.3) leads to the mass terms of the EW gauge bosons,

$$\mathcal{L}_{\mathrm{M_V}} = \frac{1}{2} \left(B'_\mu, W^3_\mu, C'_\mu \right) \mathrm{M}^2_{\mathrm{V}} \begin{pmatrix} B'_\mu \\ W^3_\mu \\ C'_\mu \end{pmatrix} + M^2_{\mathrm{W}} W^+ W^-. \tag{3.54}$$

Similar to the SM case the mass of the W boson is given

$$M_{\mathrm{W}} = \frac{g_2 v_2}{2} \tag{3.55}$$

and the mass matrix for the neutral vector bosons by

$$\mathrm{M}^2_{\mathrm{V}} = \begin{pmatrix} \frac{s^2_{\mathrm{w}} M^2_{\mathrm{W}}}{c^2_{\mathrm{w}}} & \frac{s_{\mathrm{w}} M^2_{\mathrm{W}}}{c_{\mathrm{w}}} & -\frac{\eta s^2_{\mathrm{w}} M^2_{\mathrm{W}}}{c^2_{\mathrm{w}}} \\ \frac{s_{\mathrm{w}} M^2_{\mathrm{W}}}{c_{\mathrm{w}}} & M^2_{\mathrm{W}} & -\frac{\eta s_{\mathrm{w}} M^2_{\mathrm{W}}}{c_{\mathrm{w}}} \\ -\frac{\eta s^2_{\mathrm{w}} M^2_{\mathrm{W}}}{c^2_{\mathrm{w}}} & -\frac{\eta s_{\mathrm{w}} M^2_{\mathrm{W}}}{c_{\mathrm{w}}} & \frac{\eta^2 s^2_{\mathrm{w}} M^2_{\mathrm{W}}}{c^2_{\mathrm{w}}} + M^2_{\mathrm{C}} \end{pmatrix}, \tag{3.56}$$

where we introduced the shorthands

$$\eta = \frac{a}{\sqrt{1-a^2}}, \qquad M_{\mathrm{C}} = \tilde{e} v_1, \qquad \tilde{e} = \frac{e_{\mathrm{d}}}{\sqrt{1-a^2}},$$

$$s_{\mathrm{w}} \equiv \sin\theta_{\mathrm{w}} = \frac{g_1}{\sqrt{g_1^2 + g_2^2}}, \qquad c_{\mathrm{w}} \equiv \cos\theta_{\mathrm{w}}. \tag{3.57}$$

Note that the mass matrix $\mathrm{M}_{\mathrm{V}}^2$ is not of full rank, i.e. $\mathrm{rank}\,(\mathrm{M}_{\mathrm{V}}^2) = 2$. Thus, to obtain the fields corresponding to the physical neutral gauge bosons we can diagonalize $\mathrm{M}_{\mathrm{V}}^2$ by a combination of two appropriate rotations of the neutral gauge-boson fields,

$$\begin{pmatrix} B'_\mu \\ W^3_\mu \\ C'_\mu \end{pmatrix} = \mathrm{R}_{\mathrm{V}} \begin{pmatrix} A_\mu \\ Z_\mu \\ Z'_\mu \end{pmatrix}, \qquad \mathrm{R}_{\mathrm{V}} = \begin{pmatrix} c_{\mathrm{w}} & s_{\mathrm{w}} & 0 \\ -s_{\mathrm{w}} & c_{\mathrm{w}} & 0 \\ 0 & 0 & 1 \end{pmatrix} \begin{pmatrix} 1 & 0 & 0 \\ 0 & c_\gamma & -s_\gamma \\ 0 & s_\gamma & c_\gamma \end{pmatrix}, \tag{3.58}$$

where we introduced the shorthands $s_\gamma \equiv \sin\gamma$, $c_\gamma \equiv \cos\gamma$. It is easy to see that in the case $\gamma = 0$ the rotation R_{V} reduces to its SM counterpart (see Eq. (2.18)). To determine the mixing angle γ we use Eq. (3.58) to express Eq. (3.53) in terms of the fields corresponding to the mass eigenbasis and diagonalize the resulting mass matrix for the neutral gauge fields,

$$\mathrm{R}_{\mathrm{V}}^{\mathrm{T}} \mathrm{M}_{\mathrm{V}}^2 \mathrm{R}_{\mathrm{V}} = \begin{pmatrix} 0 & 0 & 0 \\ 0 & M_{\mathrm{Z}}^2 & M_{\mathrm{ZZ'}}^2 \\ 0 & M_{\mathrm{ZZ'}}^2 & M_{\mathrm{Z'}}^2 \end{pmatrix}, \tag{3.59}$$

where

$$\begin{aligned} M_{\mathrm{Z}}^2 &= s_\gamma^2 M_{\mathrm{C}}^2 + \frac{M_{\mathrm{W}}^2 \left(c_\gamma - s_\gamma s_{\mathrm{w}} \eta\right)^2}{c_{\mathrm{w}}^2}, \\ M_{\mathrm{Z'}}^2 &= c_\gamma^2 M_{\mathrm{C}}^2 + \frac{M_{\mathrm{W}}^2 \left(s_\gamma + c_\gamma s_{\mathrm{w}} \eta\right)^2}{c_{\mathrm{w}}^2}, \\ M_{\mathrm{ZZ'}}^2 &= s_\gamma c_\gamma M_{\mathrm{C}}^2 + \frac{M_{\mathrm{W}}^2 \left[s_{2\gamma} \left(s_{\mathrm{w}}^2 \eta^2 - 1\right) - 2 s_{\mathrm{w}} c_{2\gamma} \eta\right]}{2 c_{\mathrm{w}}^2}. \end{aligned} \tag{3.60}$$

As required by QED, the photon remains massless

$$M_{\mathrm{A}}^2 = 0, \tag{3.61}$$

and, similar to the SM case, demanding the photon–fermion coupling to reproduce its respective QED form relates the electric unit charge e directly to the gauge couplings g_1 and g_2,

$$e = \frac{g_1 g_2}{\sqrt{g_1^2 + g_2^2}}. \tag{3.62}$$

The diagonalization condition

$$M_{\mathrm{ZZ'}}^2 = s_\gamma c_\gamma M_{\mathrm{C}}^2 + \frac{M_{\mathrm{W}}^2 \left[s_{2\gamma} \left(s_{\mathrm{w}}^2 \eta^2 - 1\right) - 2 s_{\mathrm{w}} c_{2\gamma} \eta\right]}{2 c_{\mathrm{w}}^2} \stackrel{!}{=} 0 \tag{3.63}$$

yields a relation between the mixing angle γ and the original parameters of the Lagrangian of the form

$$t_{2\gamma} \equiv \tan 2\gamma = \frac{-2\eta s_{\mathrm{w}}}{1-\eta^2 s_{\mathrm{w}}^2 - c_{\mathrm{w}}^2 \frac{M_{\mathrm{C}}^2}{M_{\mathrm{W}}^2}}. \tag{3.64}$$

Further, choosing $\gamma \in (-\frac{\pi}{4}, \frac{\pi}{4}]$ we find

$$s_{2\gamma} = \frac{t_{2\gamma}}{\sqrt{1+t_{2\gamma}^2}} = -\frac{2\eta s_{\mathrm{w}} \mathrm{sgn}\left\{1-\eta^2 s_{\mathrm{w}}^2 - c_{\mathrm{w}}^2 \frac{M_{\mathrm{C}}^2}{M_{\mathrm{W}}^2}\right\}}{\sqrt{\left(1-\eta^2 s_{\mathrm{w}}^2 - c_{\mathrm{w}}^2 \frac{M_{\mathrm{C}}^2}{M_{\mathrm{W}}^2}\right)^2 + 4\eta^2 s_{\mathrm{w}}^2}}, \tag{3.65}$$

$$c_{2\gamma} = \frac{1}{\sqrt{1+t_{2\gamma}^2}} = \frac{\left|1-\eta^2 s_{\mathrm{w}}^2 - c_{\mathrm{w}}^2 \frac{M_{\mathrm{C}}^2}{M_{\mathrm{W}}^2}\right|}{\sqrt{\left(1-\eta^2 s_{\mathrm{w}}^2 - c_{\mathrm{w}}^2 \frac{M_{\mathrm{C}}^2}{M_{\mathrm{W}}^2}\right)^2 + 4\eta^2 s_{\mathrm{w}}^2}}, \tag{3.66}$$

and the mass eigenvalues of the two neutral, massive gauge bosons are given by

$$M_{\mathrm{Z}}^2 = \frac{M_{\mathrm{W}}^2}{c_{\mathrm{w}}^2}\left(1 - s_{\mathrm{w}} t_\gamma \eta\right), \qquad M_{\mathrm{Z}'}^2 = \frac{M_{\mathrm{W}}^2}{c_{\mathrm{w}}^2}\left(1 + \frac{s_{\mathrm{w}}\eta}{t_\gamma}\right). \tag{3.67}$$

Again, we choose the phenomenologically easily accessible parameters e and M_{W} as well as the masses of the two neutral gauge-bosons M_{Z} and $M_{\mathrm{Z}'}$, and the mixing angle γ as input parameters of the gauge-boson sector of the DASM. Note that, in contrast to the scalar sector where we imposed the mass hierarchy $M_{\mathrm{h}} < M_{\mathrm{H}}$, we do not enforce any mass hierarchy between the Z- and Z′- boson masses, leaving $M_{\mathrm{Z}} < M_{\mathrm{Z}'}$ as well as $M_{\mathrm{Z}} > M_{\mathrm{Z}'}$ as valid parameter choices. Using Eq. (3.60), we express the original parameters of the Lagrangian in terms of our input parameters and find

$$c_{\mathrm{w}} = \frac{M_{\mathrm{W}}}{\sqrt{c_\gamma^2 M_{\mathrm{Z}}^2 + s_\gamma^2 M_{\mathrm{Z}'}^2}}, \qquad M_{\mathrm{C}}^2 = \frac{c_{\mathrm{w}}^2 M_{\mathrm{Z}}^2 M_{\mathrm{Z}'}^2}{M_{\mathrm{W}}^2}, \qquad \eta = \frac{s_{2\gamma} c_{\mathrm{w}}^2 \left(M_{\mathrm{Z}'}^2 - M_{\mathrm{Z}}^2\right)}{2 s_{\mathrm{w}} M_{\mathrm{W}}^2}, \tag{3.68}$$

and further

$$\tilde{e} = \frac{c_{\mathrm{w}} M_{\mathrm{Z}} M_{\mathrm{Z}'}}{v_1 M_{\mathrm{W}}}, \qquad e_{\mathrm{d}} = \frac{c_{\mathrm{w}} M_{\mathrm{Z}} M_{\mathrm{Z}'}}{v_1 M_{\mathrm{W}} \sqrt{1+\eta^2}}, \qquad a = \frac{\eta}{\sqrt{1+\eta^2}}. \tag{3.69}$$

Here, we did not fully insert all analytical dependences to keep the expressions compact. However, using the relations given in Eqs. (3.24)–(3.28), and (3.57) it is straightforward to relate the Lagrangian parameters directly to our chosen input parameter set. Furthermore, without loss of generality we choose the coupling constant of the $U(1)_{\mathrm{d}}$ to be positive, i.e. $e_{\mathrm{d}} > 0$ and absorb[2] the sign into the

[2]This is possible since we do not constrain the sign of the kinetic-mixing parameter a.

definition of the gauge field C_μ. Additionally, Eq. (3.68) yields the lowest-order restriction

$$M_{\mathrm{W}}^2 < c_\gamma^2 M_{\mathrm{Z}}^2 + s_\gamma^2 M_{\mathrm{Z}'}^2 \tag{3.70}$$

for the parameters of the DASM. Thus, in the DASM the mass of the W boson M_{W} differs from $c_{\mathrm{w}} M_{\mathrm{Z}}$. Therefore, in contrast to the SM, the ρ parameter [70, 71] in the DASM is already at LO not equal to 1 and in order to obey constraints from EW precision data, the mixing angle γ needs to be fine-tuned to small values in the DASM.

3.2.2. Gauge-fixing part

Expanding the kinetic terms of the Higgs fields Φ and ρ (see Eq. (3.3)) in terms of their component fields one finds terms that lead to non-diagonal propagators in the gauge-boson–would-be-Goldstone-boson system,

$$\begin{aligned}\mathcal{L}_{V\chi} = \mathrm{i}M_{\mathrm{W}} \left[\left(\partial^\mu \phi^+\right) W_\mu^- - \left(\partial_\mu \phi^-\right) W_\mu^+\right] + \left[M_{\mathrm{C}} s_\gamma \left(\partial^\mu \chi_1\right) + \frac{c_{\mathrm{w}} c_\gamma M_{\mathrm{Z}}^2}{M_{\mathrm{W}}} \left(\partial^\mu \chi_2\right)\right] Z_\mu \\ + \left[M_{\mathrm{C}} c_\gamma \left(\partial^\mu \chi_1\right) - \frac{c_{\mathrm{w}} s_\gamma M_{\mathrm{Z}'}^2}{M_{\mathrm{W}}} \left(\partial^\mu \chi_2\right)\right] Z'_\mu.\end{aligned} \tag{3.71}$$

At LO these unpleasant mixing terms can be canceled by choosing R_ξ gauge-fixing conditions. Therefore, we introduce a gauge-fixing Lagrangian

$$\mathcal{L}_{\mathrm{fix}} = -\frac{1}{2\xi_A} \left(F^A\right)^2 - \frac{1}{2\xi_Z} \left(F^Z\right)^2 - \frac{1}{2\xi_{Z'}} \left(F^{Z'}\right)^2 - \frac{1}{\xi_W} F^+ F^-, \tag{3.72}$$

where the gauge-fixing functionals are given by

$$\begin{aligned} F^\pm &= \partial^\mu W_\mu^\pm \mp \mathrm{i}\xi_W M_{\mathrm{W}} \phi^\pm, \\ F^Z &= \partial^\mu Z_\mu - \xi_Z \left[M_{\mathrm{C}} s_\gamma \chi_1 + \frac{c_{\mathrm{w}} c_\gamma M_{\mathrm{Z}}^2}{M_{\mathrm{W}}} \chi_2\right], \\ F^{Z'} &= \partial^\mu Z'_\mu - \xi_{Z'} \left[M_{\mathrm{C}} c_\gamma \chi_1 - \frac{c_{\mathrm{w}} s_\gamma M_{\mathrm{Z}'}^2}{M_{\mathrm{W}}} \chi_2\right], \\ F^A &= \partial^\mu A_\mu. \end{aligned} \tag{3.73}$$

This choice of gauge-fixing will not only eliminate the unpleasant mixing in the massive gauge-boson propagators, but introduces masses to the would-be Goldstone bosons as well. While the masses of the charged would-be Goldstone bosons are given by $M_{\phi^\pm} = \sqrt{\xi_W} M_{\mathrm{W}}$, our choice of the gauge-fixing introduces a non-diagonal mass matrix M_χ^2 for the neutral would-be Goldstone bosons χ and χ'. To diagonalize this mass matrix, we perform a rotation of the neutral would-be Goldstone-boson fields by an angle θ_x,

$$\begin{pmatrix} \chi' \\ \chi \end{pmatrix} = \mathrm{R}_\chi^{\mathrm{T}} \begin{pmatrix} \chi_1 \\ \chi_2 \end{pmatrix}, \qquad \mathrm{R}_\chi^{\mathrm{T}} = \begin{pmatrix} c_x & -s_x \\ s_x & c_x \end{pmatrix}, \tag{3.74}$$

where we used the shorthands $s_x \equiv \sin\theta_x$, $c_x \equiv \cos\theta_x$. The resulting mass matrix of the χ, χ' system is given by

$$\mathrm{R}_\chi^{\mathrm{T}} \mathrm{M}_\chi^2 \mathrm{R}_\chi = \xi_{\mathrm{V}} \begin{pmatrix} M^2_{\chi'\chi'} & M^2_{\chi\chi'} \\ M^2_{\chi\chi'} & M^2_{\chi\chi} \end{pmatrix}, \tag{3.75}$$

with

$$\begin{aligned} M^2_{\chi'\chi'} &= M^2_{\mathrm{C}} c_x^2 + \frac{M^2_{\mathrm{W}} s_x^2 + \eta s_{\mathrm{w}} s_x M_{\mathrm{W}} \left(2 M_{\mathrm{C}} c_x c_{\mathrm{w}} + M_{\mathrm{W}} \eta s_{\mathrm{w}} s_x\right)}{c_{\mathrm{w}}^2} - \frac{s_x^2 v_1 t_2 + c_x^2 v_2 t_1}{v_1 v_2 \xi_{\mathrm{V}}}, \\ M^2_{\chi\chi} &= M^2_{\mathrm{C}} s_x^2 + \frac{M^2_{\mathrm{W}} c_x^2 + \eta s_{\mathrm{w}} c_x M_{\mathrm{W}} \left(M_{\mathrm{W}} \eta s_{\mathrm{w}} c_x - 2 M_{\mathrm{C}} c_{\mathrm{w}} s_x\right)}{c_{\mathrm{w}}^2} - \frac{c_x^2 v_1 t_2 + s_x^2 v_2 t_1}{v_1 v_2 \xi_{\mathrm{V}}}, \\ M^2_{\chi\chi'} &= \frac{s_{2x}}{2}\left(M^2_{\mathrm{C}} - \frac{M^2_{\mathrm{W}}}{c_{\mathrm{w}}^2}\right) - \frac{M_{\mathrm{W}} \eta s_{\mathrm{w}} \left(2 M_{\mathrm{C}} c_{\mathrm{w}} c_{2x} + M_{\mathrm{W}} \eta s_{\mathrm{w}} s_{2x}\right)}{2 c_{\mathrm{w}}^2} + \frac{s_x c_x \left(v_1 t_2 - v_2 t_1\right)}{v_1 v_2 \xi_{\mathrm{V}}}. \end{aligned} \tag{3.76}$$

Here we chose a common gauge parameter $\xi_{\mathrm{V}} = \xi_Z = \xi_{Z'}$ for the two neutral gauge bosons for convenience. Setting the tadpole terms to zero the diagonalization condition reads

$$M^2_{\chi\chi'} = \frac{s_{2x}}{2}\left(M^2_{\mathrm{C}} - \frac{M^2_{\mathrm{W}}}{c_{\mathrm{w}}^2}\right) - \frac{M_{\mathrm{W}} \eta s_{\mathrm{w}} \left(2 M_{\mathrm{C}} c_{\mathrm{w}} c_{2x} + M_{\mathrm{W}} \eta s_{\mathrm{w}} s_{2x}\right)}{2 c_{\mathrm{w}}^2} \stackrel{!}{=} 0, \tag{3.77}$$

and we find

$$t_{2x} \equiv \tan(2\theta_x) = \frac{-2\eta M_{\mathrm{C}} s_{\mathrm{w}} c_{\mathrm{w}}}{M_{\mathrm{W}}\left(1 + \eta^2 s_{\mathrm{w}}^2 - c_{\mathrm{w}}^2 \frac{M^2_{\mathrm{C}}}{M^2_{\mathrm{W}}}\right)} = \frac{c_{\mathrm{w}} M_{\mathrm{C}} t_{2\gamma}}{M_{\mathrm{W}}\left(1 - \eta s_{\mathrm{w}} t_{2\gamma}\right)} \tag{3.78}$$

for the mixing angle θ_x. Further, choosing

$$s_{2x} = \frac{c_{\mathrm{w}} s_{2\gamma} M_{\mathrm{C}}}{M_{\mathrm{W}}}, \qquad c_{2x} = c_{2\gamma} - s_{\mathrm{w}} \eta s_{2\gamma} \tag{3.79}$$

connects the masses of the χ and χ' to the masses of the neutral massive gauge bosons Z and Z′, respectively, via

$$M_\chi = \sqrt{\xi_{\mathrm{V}}} M_{\mathrm{Z}}, \qquad M_{\chi'} = \sqrt{\xi_{\mathrm{V}}} M_{\mathrm{Z}'}. \tag{3.80}$$

With this choice, we find the useful relations

$$s_x = \frac{c_{\mathrm{w}} s_\gamma M_{\mathrm{Z}'}}{M_{\mathrm{W}}}, \qquad c_x = \frac{c_{\mathrm{w}} c_\gamma M_{\mathrm{Z}}}{M_{\mathrm{W}}}, \qquad t_x = \frac{M_{\mathrm{Z}'}}{M_{\mathrm{Z}}} t_\gamma, \tag{3.81}$$

and, similar to the SM case, the gauge-fixing functionals reduce to their simple form

$$F^\pm = \partial^\mu W^\pm_\mu \mp \mathrm{i}\xi_{\mathrm{W}} M_{\mathrm{W}} \phi^\pm \xrightarrow[\xi_{\mathrm{W}} \to 1]{} \partial^\mu W^\pm_\mu \mp \mathrm{i} M_{\mathrm{W}} \phi^\pm,$$

$$
\begin{aligned}
F^Z &= \partial^\mu Z_\mu - \xi_{\mathrm{V}} M_{\mathrm{Z}} \chi \xrightarrow[\xi_{\mathrm{V}}\to 1]{} \partial^\mu Z_\mu - M_{\mathrm{Z}}\chi, \\
F^{Z'} &= \partial^\mu Z'_\mu - \xi_{\mathrm{V}} M_{\mathrm{Z}'} \chi' \xrightarrow[\xi_{\mathrm{V}}\to 1]{} \partial^\mu Z'_\mu - M_{\mathrm{Z}'}\chi', \\
F^A &= \partial^\mu A_\mu,
\end{aligned} \tag{3.82}
$$

where in the last expression of each line we employed the 't Hooft–Feynman gauge, i.e. $\xi_A = \xi_W = \xi_V = 1$, which is used in the calculations presented in Chapter 5.

3.2.3. Ghost part

A corresponding Faddeev–Popov ghost part

$$
\mathcal{L}_{\mathrm{FP}}(x) = -\int \mathrm{d}^4 y\, \bar{u}^a(x) \left(\frac{\delta F^a(x)}{\delta \theta^b(y)}\right) u^b(y), \tag{3.83}
$$

where $a, b = \pm, Z, Z', A$, has to be added to the Lagrangian for the consistency of the gauge-fixing procedure in the functional integral. Here the $\bar{u}^a$ and u^a denote unphysical, anti-commuting ghost fields. The corresponding ghosts will never represent external states, but only appear as inner lines of Feynman diagrams. We give the infinitesimal gauge transformations of the scalar and EW gauge-boson fields in Appendix B. Using these transformations it is straightforward to evaluate the infinitesimal gauge variations $\frac{\delta F^a(x)}{\delta\theta^b(y)}$ of the gauge-fixing functionals F^a by the gauge-group parameters $\theta^b(y)$ needed to evaluate Eq. (3.83). Finally, the ghost Lagrangian in the DASM explicitly reads

$$
\begin{aligned}
\mathcal{L}_{\mathrm{FP}} = &- \bar{u}^A \partial^\mu \partial_\mu u^A + \mathrm{i}e(\partial^\mu \bar{u}^A)\left(W^+_\mu u^- - W^-_\mu u^+\right) \\
&- \bar{u}^Z\left(\partial_\mu\partial^\mu + \xi_{\mathrm{V}} M^2_{\mathrm{Z}}\right) u^Z - \frac{\mathrm{i}e c_\gamma c_{\mathrm{w}}}{s_{\mathrm{w}}}\left(\partial^\mu \bar{u}^Z\right)\left(W^+_\mu u^- - W^-_\mu u^+\right) \\
&+ \frac{c_x e}{2 s_{\mathrm{w}}} \xi_{\mathrm{V}} M_{\mathrm{Z}} \bar{u}^Z \left(\phi^+ u^- + \phi^- u^+\right) \\
&- \bar{u}^Z \xi_{\mathrm{V}} M_{\mathrm{Z}} \left\{\left[\frac{e c_\alpha c_x c_\gamma c_{\mathrm{w}} M^2_{\mathrm{Z}}}{2 s_{\mathrm{w}} M^2_{\mathrm{W}}} - \tilde{e} s_\gamma s_x s_\alpha\right] h + \left[\tilde{e} s_\gamma s_x c_\alpha + \frac{e s_\alpha c_x c_\gamma c_{\mathrm{w}} M^2_{\mathrm{Z}}}{2 s_{\mathrm{w}} M^2_{\mathrm{W}}}\right] H\right\} u^Z \\
&+ \bar{u}^Z \xi_{\mathrm{V}} M_{\mathrm{Z}} \left\{\left[\tilde{e} c_\gamma s_x s_\alpha + \frac{e c_x c_\alpha s_\gamma c_{\mathrm{w}} M^2_{\mathrm{Z}'}}{2 s_{\mathrm{w}} M^2_{\mathrm{W}}}\right] h - \left[\tilde{e} c_\gamma s_x c_\alpha - \frac{e c_x s_\alpha s_\gamma c_{\mathrm{w}} M^2_{\mathrm{Z}'}}{2 s_{\mathrm{w}} M^2_{\mathrm{W}}}\right] H\right\} u^{Z'} \\
&- \bar{u}^{Z'}\left(\partial_\mu\partial^\mu + \xi_{\mathrm{V}} M^2_{\mathrm{Z}'}\right) u^{Z'} + \frac{\mathrm{i}e s_\gamma c_{\mathrm{w}}}{s_{\mathrm{w}}}\left(\partial^\mu \bar{u}^{Z'}\right)\left(W^+_\mu u^- - W^-_\mu u^+\right) \\
&- \bar{u}^{Z'} \frac{s_x e}{2 s_{\mathrm{w}}} \xi_{\mathrm{V}} M_{\mathrm{Z}'} \left(\phi^+ u^- + \phi^- u^+\right) \\
&- \bar{u}^{Z'} \xi_{\mathrm{V}} M_{\mathrm{Z}'} \left\{\left[\frac{e c_\alpha s_x s_\gamma c_{\mathrm{w}} M^2_{\mathrm{Z}'}}{2 s_{\mathrm{w}} M^2_{\mathrm{W}}} - \tilde{e} c_\gamma c_x s_\alpha\right] h + \left[\frac{e s_\alpha s_x s_\gamma c_{\mathrm{w}} M^2_{\mathrm{Z}'}}{2 s_{\mathrm{w}} M^2_{\mathrm{W}}} + \tilde{e} c_\gamma c_x c_\alpha\right] H\right\} u^{Z'} \\
&+ \bar{u}^{Z'} \xi_{\mathrm{V}} M_{\mathrm{Z}'} \left\{\left[\frac{e c_\alpha s_x c_\gamma c_{\mathrm{w}} M^2_{\mathrm{Z}}}{2 s_{\mathrm{w}} M^2_{\mathrm{W}}} + \tilde{e} s_\gamma s_\alpha c_x\right] h + \left[\frac{e s_\alpha s_x c_\gamma c_{\mathrm{w}} M^2_{\mathrm{Z}}}{2 s_{\mathrm{w}} M^2_{\mathrm{W}}} - \tilde{e} s_\gamma c_x c_\alpha\right] H\right\} u^Z
\end{aligned}
$$

$$
\begin{aligned}
&+\Bigg\{ -\bar{u}^{+}(\partial_\mu\partial^\mu + \xi_{\mathrm{W}} M_{\mathrm{W}}^2)u^{+} + \mathrm{i}e(\partial^\mu\bar{u}^{+})\left[A_\mu - \frac{c_{\mathrm{w}}}{s_{\mathrm{w}}}(c_\gamma Z_\mu - s_\gamma Z'_\mu)\right] u^{+} \\
&\quad -\bar{u}^{+}\frac{e}{2s_{\mathrm{w}}}\xi_{\mathrm{W}} M_{\mathrm{W}}\left[c_\alpha h + s_\alpha H + \mathrm{i}(c_x\chi - s_x\chi')\right] u^{+} - \mathrm{i}e\left(\partial^\mu\bar{u}^{+}\right) W_\mu^{+} u^{A} \\
&\quad +\bar{u}^{+}\xi_{\mathrm{W}} M_{\mathrm{W}} e\phi^{+} u^{A} + \frac{\mathrm{i}ec_{\mathrm{w}}}{s_{\mathrm{w}}}\left(\partial^\mu\bar{u}^{+}\right) W_\mu^{+}\left(c_\gamma u^{Z} - s_\gamma u^{Z'}\right) \\
&\quad + \bar{u}^{+}\xi_{\mathrm{W}} M_{\mathrm{W}} e\phi^{+}\left[\left(\frac{c_\gamma\left(s_{\mathrm{w}}^2 - c_{\mathrm{w}}^2\right)}{2c_{\mathrm{w}}s_{\mathrm{w}}} - \frac{s_\gamma\eta}{2c_{\mathrm{w}}}\right)u^{Z} - \left(\frac{s_\gamma\left(s_{\mathrm{w}}^2 - c_{\mathrm{w}}^2\right)}{2s_{\mathrm{w}}c_{\mathrm{w}}} + \frac{c_\gamma\eta}{2c_{\mathrm{w}}}\right)u^{Z'}\right] \\
&\quad +(u^{+}\to u^{-}, \bar{u}^{+}\to\bar{u}^{-}, W^{+}\to W^{-}, \phi^{+}\to\phi^{-}, \mathrm{i}\to -\mathrm{i})\Bigg\}. \qquad (3.84)
\end{aligned}
$$

Similar to the SM case, in the chosen R_ξ gauge the masses of the ghost fields match the masses of the respective would-be Goldstone bosons (and therefore, in the 't Hooft–Feynman gauge, used in the calculations in Chapter 5, they match the masses of the corresponding gauge bosons as well).

3.3. Fermion and Yukawa sectors

The presence of the right-handed counterparts $\nu_j'^{\mathrm{R}}$, $j = e, \mu, \tau$, to the left-handed SM-like neutrino fields $\nu_j'^{\mathrm{L}}$ as well as the additional non-chiral Dirac fermion f_{d}' of the hidden sector of the DASM leads to several modifications to the SM fermion sector. Note that the non-chiral nature of the additional fermion f_{d}' ensures that no anomalies are introduced in the DASM. Similar to the discussion of the SM fermion sector, throughout this section, we use primed fields to denote the gauge-interaction eigenbasis, whereas non-primed fields indicate the mass eigenbasis.
The right-handed neutrino fields $\nu_j'^{\mathrm{R}}$ are assumed to be singlets under the gauge group of the DASM. The fermion field f_{d}' is a singlet with respect to the SM part of the DASM gauge group, i.e. carries no weak hypercharge, nor weak isospin nor colour. However, it carries the charge $\tilde{q}_{\mathrm{f}} e_{\mathrm{d}}$ of the $U(1)_{\mathrm{d}}$ gauge group. We choose

$$\tilde{q}_{\mathrm{f}} = \tilde{q}_\rho = 1, \qquad (3.85)$$

where $\tilde{q}_\rho e_{\mathrm{d}}$ is the charge of the Higgs field ρ introduced in Eq. (3.4). This allows for an additional portal term from the SM to the hidden sector in the fermion part of the DASM Lagrangian. Therefore, the relation (3.85) between the two charges is, in contrast to the mere normalization of the $U(1)_{\mathrm{d}}$ coupling constant provided by choosing $\tilde{q}_\rho = 1$ (see Sect. 3.1), a choice that leads to the most interesting BSM structures in the fermion sector of the DASM. In detail, it allows for an additional Yukawa term connecting the Higgs field ρ with the right-handed neutrinos $\nu_j'^{\mathrm{R}}$ and the fermion f_{d}' resulting in

$$\mathcal{L}_{\mathrm{Fermion}} = \mathcal{L}_{\mathrm{Fermion}}^{\mathrm{SM}} + \mathcal{L}_{\mathrm{Yukawa}}^{\mathrm{SM}} + \bar{f}_{\mathrm{d}}'\left(\mathrm{i}\not{D}_{\mathrm{d}} - m_{\mathrm{f_d}}\right) f_{\mathrm{d}}' - \sum_{k,l=\mathrm{e},\mu,\tau}\left(\bar{L}_k'^{\mathrm{L}} G'^{\nu}_{kl}\nu_l'^{\mathrm{R}}\Phi^{\mathrm{C}} + \mathrm{h.c.}\right)$$

$$+\sum_{j=e,\mu,\tau}\left[\bar{\nu}_j'^{\mathrm{R}}\mathrm{i}\partial\!\!\!/\nu_j'^{\mathrm{R}}-\left(y_{\rho,j}\rho\bar{f}_{\mathrm{d}}'^{\mathrm{L}}\nu_j'^{\mathrm{R}}+\mathrm{h.c.}\right)\right], \tag{3.86}$$

for the fermion part of the Lagrangian. The covariant derivative D_{d}^{μ}, governing the gauge interactions of the hidden sector fermion, is given in Eq. (3.4). Further, without loss of generality, we choose the Dirac mass $m_{\mathrm{f_d}}$ of f_{d}' to be real and positive. This can always be achieved by adjusting a chiral phase of f_{d}' appropriately. The sum in the first line of Eq. (3.86) governs the Yukawa terms for the three SM-like neutrino generations with their respective Yukawa coupling constants $G_{kl}'^{\nu}$. In general, they lead to mass terms and a PMNS-like matrix structure in the SM-like neutrino sector, which are of particular interest in flavour and neutrino physics (see, e.g., Ref. [24] and references therein). However, as we shall see in the following discussion, they do not affect our phenomenological analysis of collider observables and will therefore play no further role in this work. The second line of Eq. (3.86) governs the kinetic terms of the right-handed neutrinos as well as the Yukawa interactions connecting them to the hidden sector, i.e. to ρ and f_{d}', with respective Yukawa couplings $y_{\rho,j}$. Finally, there is the possibility for Majorana mass terms for the right-handed neutrinos, which we do not further consider in this work.

Plugging the decomposition of the Higgs fields (see Eq. (3.6)) into Eq. (3.86) and decomposing $f_{\mathrm{d}}' = f_{\mathrm{d}}'^{\mathrm{L}} + f_{\mathrm{d}}'^{\mathrm{R}}$, with $f_{\mathrm{d}}'^{\mathrm{L/R}} = \omega_{\mathrm{L/R}} f_{\mathrm{d}}'$, the mass terms for the neutral fermions become

$$\mathcal{L}_{f_{\mathrm{d}}'\nu}^{\mathrm{m}} = -\begin{pmatrix}\bar{\nu}_{\mathrm{e}}'^{\mathrm{L}}, \bar{\nu}_{\mu}'^{\mathrm{L}}, \bar{\nu}_{\tau}'^{\mathrm{L}}, \bar{f}_{\mathrm{d}}'^{\mathrm{L}}\end{pmatrix}\mathrm{M}_{\mathrm{f_d}}'\begin{pmatrix}\nu_{\mathrm{e}}'^{\mathrm{R}}\\ \nu_{\mu}'^{\mathrm{R}}\\ \nu_{\tau}'^{\mathrm{R}}\\ f_{\mathrm{d}}'^{\mathrm{R}}\end{pmatrix} + \mathrm{h.c.}\,, \tag{3.87}$$

with the non-diagonal, non-symmetric, complex mass matrix

$$\mathrm{M}_{\mathrm{f_d}}' = \begin{pmatrix} m_{11} & m_{12} & m_{13} & 0\\ m_{21} & m_{22} & m_{23} & 0\\ m_{31} & m_{32} & m_{33} & 0\\ \tilde{y}_{\mathrm{e}} & \tilde{y}_{\mu} & \tilde{y}_{\tau} & m_{\mathrm{f_d}}\end{pmatrix}, \quad \tilde{y}_i = \frac{v_1 y_{\rho,i}}{\sqrt{2}}, \quad m_{ij} = \frac{v_2 G_{ij}^{\nu}}{\sqrt{2}}. \tag{3.88}$$

In general $\mathrm{M}_{\mathrm{f_d}}'$ can be diagonalized by a bi-unitary transformation of the form

$$\mathrm{U}_{\mathrm{L}}^{\dagger}\mathrm{M}_{\mathrm{f_d}}'\mathrm{U}_{\mathrm{R}} = \mathrm{M}_{\nu}, \qquad \mathrm{M}_{\nu,\alpha\beta} = m_{\nu,\alpha}\delta_{\alpha\beta}, \qquad m_{\nu,\alpha} \geq 0, \qquad \alpha,\beta = 1,2,3,4, \tag{3.89}$$

with the unitary matrices $\mathrm{U_L}$ and $\mathrm{U_R}$. This can, in general, be achieved by transforming the fields of the interaction eigenbasis (primed fields) into the mass eigenbasis (non-primed fields) via

$$\begin{pmatrix}\nu_{\mathrm{e}}'^{\mathrm{R}}\\ \nu_{\mu}'^{\mathrm{R}}\\ \nu_{\tau}'^{\mathrm{R}}\\ f_{\mathrm{d}}'^{\mathrm{R}}\end{pmatrix} = \mathrm{U_R}\begin{pmatrix}\nu_1^{\mathrm{R}}\\ \nu_2^{\mathrm{R}}\\ \nu_3^{\mathrm{R}}\\ \nu_4^{\mathrm{R}}\end{pmatrix}, \qquad \begin{pmatrix}\nu_{\mathrm{e}}'^{\mathrm{L}}\\ \nu_{\mu}'^{\mathrm{L}}\\ \nu_{\tau}'^{\mathrm{L}}\\ f_{\mathrm{d}}'^{\mathrm{L}}\end{pmatrix} = \mathrm{U_L}\begin{pmatrix}\nu_1^{\mathrm{L}}\\ \nu_2^{\mathrm{L}}\\ \nu_3^{\mathrm{L}}\\ \nu_4^{\mathrm{L}}\end{pmatrix}. \tag{3.90}$$

3.3.1. Neutrino mixing for small SM-like neutrino masses

In this section, we investigate the interesting features of the diagonalization of the neutral fermion mass matrix under the assumption of small SM-like neutrino masses. These are highly favoured by experimental studies, like attempts to measure the masses of the neutrinos by analyzing β-decay (see e.g. [61]).
In more detail, we assume all entries of the SM-like mass matrix (m_{kl}, $k,l = 1,2,3$) in Eq. (3.88) to be of some small scale m_ν, representing the SM-like neutrino mass scale. However, we assume not all entries of the mass matrix $\mathrm{M}'_{\mathrm{f_d}}$ to be of this small scale,

$$m_{kl} = \mathcal{O}(m_\nu), \quad m_\nu \ll \widetilde{m} \equiv \max\{\tilde{y}, m_{\mathrm{f_d}}\}, \quad \tilde{y}^2 \equiv |\tilde{y}_\mathrm{e}|^2 + |\tilde{y}_\mu|^2 + |\tilde{y}_\tau|^2, \quad \tilde{y} \geq 0. \tag{3.91}$$

With this hierarchy, the fermion mass matrix Eq. (3.88) has the structure

$$\mathrm{M}'_{\mathrm{f_d}} = \begin{pmatrix} \mathcal{O}(m_\nu) & \begin{matrix} 0 \\ 0 \\ 0 \end{matrix} \\ \begin{matrix} \tilde{y}_\mathrm{e} & \tilde{y}_\mu & \tilde{y}_\tau \end{matrix} & m_{\mathrm{f_d}} \end{pmatrix}. \tag{3.92}$$

To determine the resulting neutrino masses one simply calculates the square roots of the eigenvalues of the matrices $\mathrm{M}'_{\mathrm{f_d}}\mathrm{M}'^{\dagger}_{\mathrm{f_d}}$ or $\mathrm{M}'_{\mathrm{f_d}}\mathrm{M}'^{\dagger}_{\mathrm{f_d}}$. In our parameter hierarchy, the former one has the form

$$\mathrm{M}'_{\mathrm{f_d}}\mathrm{M}'^{\dagger}_{\mathrm{f_d}} = \begin{pmatrix} \mathcal{O}(m_\nu^2) & \begin{matrix} \mathcal{O}(m_\nu\widetilde{m}) \\ \mathcal{O}(m_\nu\widetilde{m}) \\ \mathcal{O}(m_\nu\widetilde{m}) \end{matrix} \\ \begin{matrix} \mathcal{O}(m_\nu\widetilde{m}) & \mathcal{O}(m_\nu\widetilde{m}) & \mathcal{O}(m_\nu\widetilde{m}) \end{matrix} & m_{\mathrm{f_d}}^2 + \tilde{y}^2 \end{pmatrix}, \tag{3.93}$$

where the $\mathcal{O}(m_\nu^2)$ represents a 3×3 matrix with each element being of order $\mathcal{O}(m_\nu^2)$. We find the following mass hierarchy

$$m_{\nu_k} = \mathcal{O}(m_\nu), \quad k = 1,2,3, \qquad m_{\nu_4} = \sqrt{m_{\mathrm{f_d}}^2 + \tilde{y}^2} + \mathcal{O}(m_\nu), \tag{3.94}$$

for the resulting neutrino masses. Further, the mixing matrix for the left-handed fields, responsible for the diagonalization of $\mathrm{M}'_{\mathrm{f_d}}\mathrm{M}'^{\dagger}_{\mathrm{f_d}}$ via

$$\underbrace{\mathrm{U}_\mathrm{L}^\dagger \mathrm{M}'_{\mathrm{f_d}} \mathrm{U}_\mathrm{R}}_{=\mathrm{M}_\nu} \underbrace{\mathrm{U}_\mathrm{R}^\dagger \mathrm{M}'^{\dagger}_{\mathrm{f_d}} \mathrm{U}_\mathrm{L}}_{=\mathrm{M}_\nu^\dagger} = \mathrm{U}_\mathrm{L}^\dagger \mathrm{M}'_{\mathrm{f_d}} \mathrm{M}'^{\dagger}_{\mathrm{f_d}} \mathrm{U}_\mathrm{L} = \mathrm{diag}(m_{\nu_1}^2, m_{\nu_2}^2, m_{\nu_3}^2, m_{\nu_4}^2), \tag{3.95}$$

has the structure

$$\mathrm{U}_\mathrm{L} = \begin{pmatrix} \hat{\mathrm{U}}_\mathrm{L} & \begin{matrix} 0 \\ 0 \\ 0 \end{matrix} \\ \begin{matrix} 0 & 0 & 0 \end{matrix} & 1 \end{pmatrix} + \mathcal{O}\left(\frac{m_\nu}{\widetilde{m}}\right), \qquad \hat{\mathrm{U}}_\mathrm{L} = \mathcal{O}(1), \tag{3.96}$$

with the 3×3 unitary matrix $\hat{\mathrm{U}}_{\mathrm{L}}$ with elements of $\mathcal{O}(1)$ introducing mixing of the left-handed SM-like neutrinos, i.e. resembling effects of a PMNS-like matrix for the SM-like part of the fermion sector. The more interesting feature of Eq. (3.96) is the large suppression of the mixing between the left-handed SM-like neutrino fields and $f_{\mathrm{d}}'^{\mathrm{L}}$, practically decoupling the SM and hidden parts in the left-handed fermion sector[3]. By contrast, the structure of the right-handed unitary mixing matrix is more complicated and, in general, no entries of U_{R} are suppressed in our mass hierarchy. In a similar way to the determination of U_{L} it can, e.g., be determined via

$$\mathrm{U}_{\mathrm{R}}^{\dagger}\mathrm{M}_{\mathrm{f_d}}'^{\dagger}\mathrm{M}_{\mathrm{f_d}}'\mathrm{U}_{\mathrm{R}} = \mathrm{diag}(m_{\nu_1}^2, m_{\nu_2}^2, m_{\nu_3}^2, m_{\nu_4}^2). \tag{3.97}$$

Having Eq. (3.92) in mind we write U_{R} as product of two successive unitary field transformations $\mathrm{U}_{\mathrm{R}} = \mathrm{U}_{\mathrm{R},1}\mathrm{U}_{\mathrm{R},2}$. We choose $\mathrm{U}_{\mathrm{R},1}$

$$\mathrm{U}_{\mathrm{R},1} = \begin{pmatrix} & & & 0 \\ \mathbf{e}' & \mathbf{e}'' & \mathbf{e} & 0 \\ & & & 0 \\ 0 & 0 & 0 & 1 \end{pmatrix}, \quad (\tilde{y}_{\mathrm{e}}, \tilde{y}_{\mu}, \tilde{y}_{\tau}) = \tilde{y}\,\mathbf{e}^{\dagger}, \quad \tilde{y} \geq 0, \tag{3.98}$$

with the orthogonal unit vectors $\{\mathbf{e}, \mathbf{e}', \mathbf{e}''\}$, $|\mathbf{e}| = |\mathbf{e}'| = |\mathbf{e}''| = 1$, $\mathbf{e}^{\dagger}\mathbf{e}' = 0$, such that it aligns the first three components of the last row of Eq. (3.92), $(\tilde{y}_{\mathrm{e}}, \tilde{y}_{\mu}, \tilde{y}_{\tau})$, along the unit vector $(0, 0, 1)$. Starting from this point

$$\mathrm{M}_{\mathrm{f_d}}'\mathrm{U}_{\mathrm{R},1} = \begin{pmatrix} & & 0 \\ \mathcal{O}(m_{\nu}) & & 0 \\ & & 0 \\ 0 & 0 & \tilde{y} \quad m_{\mathrm{f_d}} \end{pmatrix}, \tag{3.99}$$

the second rotation $\mathrm{U}_{\mathrm{R},2}$ is used to rotate the remaining two non-zero entries in the last row of Eq. (3.99), $(\tilde{y}, m_{\mathrm{f_d}})$, into $(0, m_{\nu_4})$ resulting in

$$\mathrm{M}_{\mathrm{f_d}}'\mathrm{U}_{\mathrm{R},1}\mathrm{U}_{\mathrm{R},2} = \begin{pmatrix} & & 0 \\ \mathcal{O}(m_{\nu}) & & 0 \\ & & \mathcal{O}(m_{\nu}) \\ 0 & 0 & 0 \quad m_{\nu_4} \end{pmatrix}. \tag{3.100}$$

Therefore, while the alignment of the SM-like right-handed neutrinos done with $\mathrm{U}_{\mathrm{R},1}$ does not affect the right-handed field from the hidden sector, the rotation $\mathrm{U}_{\mathrm{R},2}$ is responsible for the mixing of the right-handed SM-like neutrinos with $f_{\mathrm{d}}'^{\mathrm{R}}$. With all the insights gained in this section we can now define the simplified fermion sector of the DASM in Sect. 3.4.

[3]Note that $f_{\mathrm{d}}'^{\mathrm{L}}$ still appears in several NLO calculations due to its gauge interactions.

3.4. The simplified fermion sector of the DASM

In this work, we are not interested in any observables that are sensitive to SM-like neutrino masses or mixings. Having the previous section in mind, we thus restrict the fermion sector of the DASM to the case $m_{ij} = 0$, $i, j = 1, 2, 3$. Applying the alignment transformation for the right-handed neutrino fields given in Eq. (3.98) the Lagrangian given in Eq. (3.86) becomes

$$\begin{aligned}\mathcal{L}_{\text{Fermion}} = \mathcal{L}^{\text{SM}}_{\text{Fermion}} + \mathcal{L}^{\text{SM}}_{\text{Yukawa}} + \bar{f}'_{\text{d}} \left(\mathrm{i}\not{D}_{\text{d}} - m_{\text{f}_\text{d}}\right) f'_{\text{d}} - \left(y_\rho \rho \bar{f}'^{\text{L}}_{\text{d}} \nu'^{\text{R}}_3 + \text{h.c.}\right) \\ + \sum_{j=1,2,3} \left[\bar{\nu}'^{\text{R}}_j \mathrm{i}\not{\partial} \nu'^{\text{R}}_j\right], \end{aligned} \tag{3.101}$$

with $y_\rho = \sqrt{2}\tilde{y}/v_1$. In this simplified scenario the mass matrix for the neutrinos and the fermion from the hidden sector has the simple form

$$\mathrm{M}'_{\text{f}_\text{d}} = \begin{pmatrix} 0 & 0 & 0 & 0 \\ 0 & 0 & 0 & 0 \\ 0 & 0 & 0 & 0 \\ 0 & 0 & \tilde{y} & m_{\text{f}_\text{d}} \end{pmatrix}, \tag{3.102}$$

where we can always adjust (chiral) phases of the fields such that $\tilde{y}, m_{\text{f}_\text{d}} \geq 0$. For the unitary matrices U_{L} and $\mathrm{U}_{\text{R},2}$ needed for the diagonalization of Eq. (3.102) we make the ansatz

$$\mathrm{U}_{\text{L}} = \begin{pmatrix} 1 & 0 & 0 & 0 \\ 0 & 1 & 0 & 0 \\ 0 & 0 & \cos\theta_{\text{l}} & \sin\theta_{\text{l}} \\ 0 & 0 & -\sin\theta_{\text{l}} & \cos\theta_{\text{l}} \end{pmatrix}, \qquad \mathrm{U}_{\text{R},2} = \begin{pmatrix} 1 & 0 & 0 & 0 \\ 0 & 1 & 0 & 0 \\ 0 & 0 & \cos\theta_{\text{r}} & \sin\theta_{\text{r}} \\ 0 & 0 & -\sin\theta_{\text{r}} & \cos\theta_{\text{r}} \end{pmatrix}. \tag{3.103}$$

This leads to the two diagonalization conditions

$$0 = \sin\theta_{\text{l}} \left(\tilde{y} \sin\theta_{\text{r}} + m_{\text{f}_\text{d}} \cos\theta_{\text{r}}\right), \qquad 0 = \cos\theta_{\text{l}} \left(\tilde{y} \cos\theta_{\text{r}} - m_{\text{f}_\text{d}} \sin\theta_{\text{r}}\right), \tag{3.104}$$

which determine the rotation angles θ_{l} and θ_{r} of the left- and right-handed field rotations, respectively, to

$$\sin\theta_{\text{l}} = 0, \qquad \tan\theta_{\text{r}} = \frac{\tilde{y}}{m_{\text{f}_\text{d}}}. \tag{3.105}$$

We choose

$$\theta_{\text{l}} = 0, \qquad s_{\theta_{\text{r}}} \equiv \sin\theta_{\text{r}} = \frac{\tilde{y}}{\sqrt{\tilde{y}^2 + m^2_{\text{f}_\text{d}}}}, \qquad c_{\theta_{\text{r}}} \equiv \cos\theta_{\text{r}} = \frac{m_{\text{f}_\text{d}}}{\sqrt{\tilde{y}^2 + m^2_{\text{f}_\text{d}}}}, \tag{3.106}$$

with $\theta_{\text{r}} \in [0, \frac{\pi}{2}]$, to fix the rotations into the fields corresponding to the mass eigenstates. The resulting neutrino masses are given by

$$m_{\nu_1} = m_{\nu_2} = m_{\nu_3} = 0, \qquad m_{\nu_4} = \sqrt{\tilde{y}^2 + m^2_{\text{f}_\text{d}}}. \tag{3.107}$$

Therefore, in this simplified fermion sector of the DASM we have no mixing between the left-handed fields $\mathrm{U_L} = \mathbb{1}_4$, and, thus, the flavour and mass eigenstate coincide in the case of vanishing neutrino masses m_{ν_1,ν_2,ν_3}. In particular, this leaves the freedom of any unitary transformation $\mathrm{U_L}$ of the left-handed SM-like neutrino fields (see Eq. (3.96) for $m_\nu = 0$). Thus, the simplified version of the DASM neutrino sector will not account for any PMNS-like mixing matrix, i.e. there are no lepton-flavour-changing charged-current interactions present at LO.
In total, the extension of the fermion sector introduces two free parameters to the theory. Again, choosing the most intuitive and phenomenologically easily accessible input parameters we take the mixing angle for the right-handed neutrino fields θ_r as well as the mass m_{ν_4} of the heavy neutrino field ν_4. Using Eqs. (3.106) and (3.107) we can easily connect the original parameters of the Lagrangian with the chosen input parameters resulting in

$$\tilde{y} = s_{\theta_\mathrm{r}} m_{\nu_4}, \qquad m_{\mathrm{f_d}} = c_{\theta_\mathrm{r}} m_{\nu_4}. \tag{3.108}$$

Finally, expressing the Lagrangian (3.101) in terms of the new input parameters and the fermion mass eigenstates ν_i, $i = 1,2,3,4$, with the help of Eq. (3.6) we find

$$\begin{aligned}
\mathcal{L}_\mathrm{Fermion} = \mathcal{L}^\mathrm{SM}_\mathrm{Fermion} + \mathcal{L}^\mathrm{SM}_\mathrm{Yukawa} + \bar{\nu}_4 \left(\mathrm{i}\partial\!\!\!/ - m_{\nu_4}\right) \nu_4 + \sum_{j=1,2,3} \bar{\nu}_j^\mathrm{R} \mathrm{i}\partial\!\!\!/ \nu_j^\mathrm{R} \\
+ \frac{s_{\theta_\mathrm{r}} m_{\nu_4}}{v_1} \left(s_{\theta_\mathrm{r}} s_\alpha h \bar{\nu}_4^\mathrm{L} \nu_4^\mathrm{R} + c_{\theta_\mathrm{r}} s_\alpha h \bar{\nu}_4^\mathrm{L} \nu_3^\mathrm{R} - s_{\theta_\mathrm{r}} c_\alpha H \bar{\nu}_4^\mathrm{L} \nu_4^\mathrm{R} - c_{\theta_\mathrm{r}} c_\alpha H \bar{\nu}_4^\mathrm{L} \nu_3^\mathrm{R} + \mathrm{h.c.} \right) \\
- \Big[\mathrm{i} \frac{s_{\theta_\mathrm{r}} m_{\nu_4}}{v_1} \left(s_{\theta_\mathrm{r}} s_x \chi \bar{\nu}_4^\mathrm{L} \nu_4^\mathrm{R} + c_{\theta_\mathrm{r}} s_x \chi \bar{\nu}_4^\mathrm{L} \nu_3^\mathrm{R} + s_{\theta_\mathrm{r}} c_x \chi' \bar{\nu}_4^\mathrm{L} \nu_4^\mathrm{R} + c_{\theta_\mathrm{r}} c_x \chi' \bar{\nu}_4^\mathrm{L} \nu_3^\mathrm{R} \right) \\
+ \mathrm{h.c.} \Big] - \tilde{e} \left(s_\gamma Z_\mu + c_\gamma Z'_\mu \right) \left(\bar{\nu}_4^\mathrm{L} \gamma^\mu \nu_4^\mathrm{L} + c_{\theta_\mathrm{r}}^2 \bar{\nu}_4^\mathrm{R} \gamma^\mu \nu_4^\mathrm{R} + s_{\theta_\mathrm{r}}^2 \bar{\nu}_3^\mathrm{R} \gamma^\mu \nu_3^\mathrm{R} \right. \\
\left. - \left[s_{\theta_\mathrm{r}} c_{\theta_\mathrm{r}} \bar{\nu}_4^\mathrm{R} \gamma^\mu \nu_3^\mathrm{R} + \mathrm{h.c.} \right] \right)
\end{aligned} \tag{3.109}$$

for the fermion sector Lagrangian of the DASM.

3.5. Non-linear representation of the DASM Higgs sector

In the previous sections the DASM was introduced for the well-known linear representation (see Eq. (3.6)) of the Higgs fields Φ and ρ. In the following, we briefly introduce a non-linear representation for the two Higgs fields, which is used in the tadpole renormalization procedure described in Sect. 4.2.1. For the discussion in this section we closely follow the strategies outlined in Refs. [72–75] and apply them to the DASM.
To introduce the non-linear representation we first define the 2×2 matrix notation

for the linear representation of the Higgs doublet,

$$\mathbf{\Phi} \equiv \left(\Phi^{\mathrm{C}}, \Phi\right) = \frac{1}{\sqrt{2}}\left[(v_2 + h_2)\,\mathbb{1} + 2\mathrm{i}\boldsymbol{\phi}\right], \qquad \boldsymbol{\phi} \equiv \frac{\phi_j \boldsymbol{\sigma}_j}{2}. \tag{3.110}$$

Note that, throughout this section, we use bold symbols to indicate the matrix structure of the respective objects. In Eq. (3.110) the ϕ_i, $i = 1, 2, 3$, represent the real would-be Goldstone-boson fields. They are connected to the ones defined in Eq. (3.6) via

$$\phi^{\pm} = \frac{1}{\sqrt{2}}\left(\phi_2 \pm \mathrm{i}\phi_1\right), \qquad \chi_2 = -\phi_3, \tag{3.111}$$

and the $\boldsymbol{\sigma}_i$ denote the Pauli matrices. The kinetic terms for the Higgs doublet as well as its gauge-invariant mass operator needed for the Higgs part of the Lagrangian (see Eq. (3.3)) are obtained by applying the trace in the matrix formulation, resulting in

$$\mathcal{L}_{\Phi,\mathrm{kin}} = \frac{1}{2}\mathrm{tr}\left[\left(D_\mu \mathbf{\Phi}\right)^\dagger \left(D^\mu \mathbf{\Phi}\right)\right], \qquad \Phi^\dagger \Phi = \frac{1}{2}\mathrm{tr}\left[\mathbf{\Phi}^\dagger \mathbf{\Phi}\right]. \tag{3.112}$$

Moreover, since ρ only carries $U(1)_{\mathrm{d}}$ charge, we do not have to introduce a matrix representation for it. With this, we can now switch to a non-linear representation of the Higgs fields by introducing

$$\mathbf{\Phi} = \frac{1}{\sqrt{2}}\left(h_2^{\mathrm{nl}} + v_2\right)\exp\left(\frac{\mathrm{i}\zeta_j \boldsymbol{\sigma}_j}{v_2}\right), \qquad \rho = \frac{1}{\sqrt{2}}\left(h_1^{\mathrm{nl}} + v_1\right)\exp\left(\frac{\mathrm{i}\chi_1^{\mathrm{nl}}}{v_1}\right). \tag{3.113}$$

Here the fields h_1^{nl} and h_2^{nl} are the gauge-invariant Higgs fields which will, after a rotation similar to the one given in Eq. (3.12), lead to the two Higgs fields corresponding to the physical Higgs bosons. The real would-be Goldstone-boson fields of the non-linear representation are denoted by χ_1^{nl} and ζ_i, $i = 1, 2, 3$. Note that these fields in general differ from their corresponding counterparts in the linear representation. For our choice (3.113) we find the relations

$$h_1 = \left(h_1^{\mathrm{nl}} + v_1\right)\cos\left(\frac{\chi_1^{\mathrm{nl}}}{v_1}\right) - v_1, \qquad h_2 = \left(h_2^{\mathrm{nl}} + v_2\right)\cos\left(\frac{|\vec{\zeta}|}{v_2}\right) - v_2, \tag{3.114}$$

$$\chi_1 = \left(h_1^{\mathrm{nl}} + v_1\right)\sin\left(\frac{\chi_1^{\mathrm{nl}}}{v_1}\right), \qquad \phi_i = \left(h_2^{\mathrm{nl}} + v_2\right)\sin\left(\frac{|\vec{\zeta}|}{v_2}\right)\frac{\zeta_i}{|\vec{\zeta}|}, \tag{3.115}$$

with $\vec{\zeta} = (\zeta_1, \zeta_2, \zeta_3)^{\mathrm{T}}$, between the fields in the two representations. Therefore, the respective Higgs fields of the linear and non-linear representations agree up to linear order in the would-be Goldstone-boson fields.

The scalar potential in the non-linear representation, spelled out explicitly in terms of the component fields, is given by

$$V^{\mathrm{nl}}(\Phi, \rho) = -\frac{\mu_2^2}{2}\left(h_2^{\mathrm{nl}} + v_2\right)^2 - \mu_1^2\left(h_1^{\mathrm{nl}} + v_1\right)^2$$

$$+\frac{\lambda_2}{16}\left(h_2^{\mathrm{nl}}+v_2\right)^4+\lambda_1\left(h_1^{\mathrm{nl}}+v_1\right)^4+\frac{\lambda_{12}}{2}\left(h_2^{\mathrm{nl}}+v_2\right)^2\left(h_1^{\mathrm{nl}}+v_1\right)^2. \tag{3.116}$$

From Eq. (3.116) it is obvious that the Feynman rules for the Higgs self-interactions coincide in the linear and non-linear representations. In contrast to the linear representation, no would-be Goldstone-boson fields appear in the scalar potential of the non-linear representation. In the non-linear representation the Higgs–would-be-Goldstone-boson interactions as well as the 4-point would-be Goldstone-boson interactions are contained in the kinetic parts of the Higgs Lagrangian. Further, the Higgs fields in the linear and non-linear representations coincide to LO in the would-be Goldstone-boson fields and, therefore, the Feynman rules for the Higgs–gauge-boson interactions coincide in the two representations. The same is true for the Higgs–fermion interactions. The explicit expressions for the respective Feynman rules can be taken from Appendix F. Finally, we want to emphasize that, due to the gauge invariance of the Higgs fields h_1^{nl} and h_2^{nl}, there are no interactions between the Higgs bosons and ghost particles in the non-linear representation.

3.6. Input parameters

Setting up the theoretical framework for any BSM model, it is of uttermost importance to choose input parameters that are intuitive and phenomenologically easily accessible. In the previously described DASM extensions of the SM Higgs, gauge, and fermion sectors in total seven additional free parameters have been introduced. To this end, we choose

- the mass $M_{h'}$ of the additional Higgs boson, where h' represents the non-SM-like Higgs boson of h and H, the scalar mixing angle α, which is most directly connected to the measured signal strength of the SM-like Higgs boson, and the scalar self-coupling constant λ_{12} in place of the three additional free parameters λ_1, λ_{12}, and μ_1^2 (see Eqs. (3.24)-(3.28)) in the extended Higgs sector of the DASM.

- the mass $M_{\mathrm{Z}'}$ of the additional neutral gauge boson as well as the additional rotation angle γ in the neutral gauge-boson system, which most directly influences all couplings of the SM-like Z boson and especially rules its coupling strength to particles from the hidden sector, instead of two new parameters a and e_{d} (see Eq. (3.69)) in the extended gauge sector of the DASM.

- the mass m_{ν_4} of the heavy neutrino and the mixing angle θ_{r} in the right-handed neutrino system for the two additional parameters $m_{\mathrm{f_d}}$ and $\tilde{y}$ (see Eq. (3.108)) in the extended fermion sector of the DASM.

With these additional parameters our complete set of phenomenologically easily accessible and intuitive input parameters for the DASM is given by[4]

$$\{M_{\mathrm{W}}, M_{\mathrm{Z}}, M_{\mathrm{Z}'}, M_{\mathrm{H}}, M_{\mathrm{h}}, \alpha_{\mathrm{em}}, \gamma, \alpha, \theta_{\mathrm{r}}, \lambda_{12}, m_{f,i}, m_{\nu_4}, V_{ij}, \alpha_{\mathrm{s}}\}. \tag{3.117}$$

In this parameter basis, the DASM incorporates the following SM limits

$$\begin{array}{llll}
1) & \gamma \to 0, & M_{h'} \to M_{\mathrm{h}}^{\mathrm{SM}}, & \lambda_{12} \to 0, \\
2) & M_{\mathrm{Z}'} \to M_{\mathrm{Z}}, & M_{h'} \to M_{\mathrm{h}}^{\mathrm{SM}}, & \lambda_{12} \to 0, \\
3) & \gamma \to 0, & \alpha \to \begin{cases} 0 & \text{for} \quad M_{\mathrm{h}} = M_{\mathrm{h}}^{\mathrm{SM}} \\ \pm\frac{\pi}{2} & \text{for} \quad M_{\mathrm{H}} = M_{\mathrm{h}}^{\mathrm{SM}} \end{cases}, & \lambda_{12} \to 0, \\
4) & M_{\mathrm{Z}'} \to M_{\mathrm{Z}}, & \alpha \to \begin{cases} 0 & \text{for} \quad M_{\mathrm{h}} = M_{\mathrm{h}}^{\mathrm{SM}} \\ \pm\frac{\pi}{2} & \text{for} \quad M_{\mathrm{H}} = M_{\mathrm{h}}^{\mathrm{SM}} \end{cases}, & \lambda_{12} \to 0,
\end{array} \tag{3.118}$$

where, again, h' denotes the non-SM-like Higgs boson of h and H, fully decoupling the hidden sector from the SM parts of the theory. Note that the decoupling of the extension in the gauge and scalar sectors described in Eq. (3.118) will automatically lead to a decoupling of the fermion sector. However, the limit $\theta_{\mathrm{r}} \to 0$ will not, as one might naively expect, decouple the fermion sector extension from the rest of the theory, due to the remaining non-zero gauge couplings of ν_4 to the Z and Z′ bosons.

[4]Note that we do not give a detailed description of the QCD part of the DASM since it is equivalent to its SM counterpart described in Sect. 2.2. Nevertheless, we included the strong coupling constant α_{s} in the input parameter set for completeness.

4. Renormalization of the DASM

In the following phenomenological analysis of the DASM, we are interested in 1-loop precision for the BSM contributions to the investigated POs. In any analyses of EW POs, at least this level of accuracy of predictions is crucial to match the precision of modern collider measurements, like analyses performed with LHC data, or of other high-precision observables like the $(g-2)_\mu$ results. In order to perform the necessary higher-order calculations, a proper regularization scheme is needed to regularize appearing ultraviolet (UV) divergences. We use dimensional regularization [76,77] (see Appendix C for a brief summary) throughout this work. Further, a suitable renormalization scheme is needed to obtain phenomenologically sound predictions. In Sect. 4.1, we introduce the renormalization transformation for the parameters and fields used in the renormalization procedure. The full renormalization of the DASM is discussed in Sect. 4.2. There, we define on-shell (OS) renormalization conditions for the chosen set of input parameters[1] given in Eq. (3.117). Additionally, we set up $\overline{\text{MS}}$ renormalization for the BSM mixing angles. For both cases, we give explicit expressions for the resulting renormalization constants as well as interesting intermediate results.

4.1. Renormalization transformation

For the following renormalization procedure of the DASM we split the bare parameters and fields into their renormalized counterparts and corresponding renormalization constants. At NLO the renormalization transformations for the SM and BSM input parameters read

$$
\begin{aligned}
M^2_{\text{h},0} &= M^2_{\text{h}} + \delta M^2_{\text{h}}, & M^2_{\text{H},0} &= M^2_{\text{H}} + \delta M^2_{\text{H}},\\
M^2_{\text{Z},0} &= M^2_{\text{Z}} + \delta M^2_{\text{Z}}, & M^2_{\text{Z}',0} &= M^2_{\text{Z}'} + \delta M^2_{\text{Z}'},\\
M^2_{\text{W},0} &= M^2_{\text{W}} + \delta M^2_{\text{W}}, & e_0 &= (1+\delta Z_e)\, e = e + \delta e,\\
\gamma_0 &= \gamma + \delta\gamma, & \alpha_0 &= \alpha + \delta\alpha,
\end{aligned}
$$

[1] Note that for λ_{12} an OS renormalization condition is phenomenologically not appropriate as long as the non-SM Higgs boson is not found. Therefore, we use an $\overline{\text{MS}}$ renormalization condition for the renormalization of λ_{12}.

$$\begin{aligned} \lambda_{12,0} &= \lambda_{12} + \delta\lambda_{12}, & m_{f,i,0} &= m_{f,i} + \delta m_{f,i}, \\ V_{ij,0} &= V_{ij} + \delta V_{ij}, & \theta_{\mathrm{r},0} &= \theta_{\mathrm{r}} + \delta\theta_{\mathrm{r}}. \end{aligned} \tag{4.1}$$

It is common to label bare parameters and fields with a subscript "0", and we adopt this notation throughout this chapter. A bare parameter p_0 is connected to its renormalized counterpart p (without subscript) via the renormalization constant δp. Thus, the choice of the respective renormalization constant determines the interpretation of the renormalized parameter and gives it its (physical) meaning. The definition of suitable renormalization conditions for the input parameters of the DASM is the subject of Sect. 4.2. The renormalization transformation of the fields that correspond to mass and charge eigenstates read

$$\begin{aligned} \begin{pmatrix} h_0 \\ H_0 \end{pmatrix} &= \left(\mathbb{1}_2 + \frac{1}{2}\delta\mathrm{Z_S}\right)\begin{pmatrix} h \\ H \end{pmatrix}, & \delta\mathrm{Z_S} &= \begin{pmatrix} \delta Z_{hh} & \delta Z_{hH} \\ \delta Z_{Hh} & \delta Z_{HH} \end{pmatrix}, \\ \begin{pmatrix} A_0 \\ Z_0 \\ Z'_0 \end{pmatrix} &= \left(\mathbb{1}_3 + \frac{1}{2}\delta\mathrm{Z_V}\right)\begin{pmatrix} A \\ Z \\ Z' \end{pmatrix}, & \delta\mathrm{Z_V} &= \begin{pmatrix} \delta Z_{AA} & \delta Z_{AZ} & \delta Z_{AZ'} \\ \delta Z_{ZA} & \delta Z_{ZZ} & \delta Z_{ZZ'} \\ \delta Z_{Z'A} & \delta Z_{Z'Z} & \delta Z_{Z'Z'} \end{pmatrix}, \\ W_0^{\pm} &= \left(1 + \frac{1}{2}\delta Z_W\right) W^{\pm}, \\ f_{i,0}^{\mathrm{L}} &= \left(1 + \frac{1}{2}\delta Z_i^{f,\mathrm{L}}\right) f_i^{\mathrm{L}}, & f_{i,0}^{\mathrm{R}} &= \left(\delta_{ij} + \frac{1}{2}\delta Z_{ij}^{f,\mathrm{R}}\right) f_j^{\mathrm{R}}, \end{aligned} \tag{4.2}$$

where, to account for the possibility of mixing between the respective fields, we introduce a matrix structure for the Higgs fields h, H, the gauge-boson fields A, Z, Z', and the right-handed fermion fields f_i^{R}. For charged leptons, up-, and down-type quarks the indices i, j run over the three fermion generations. In the DASM the BSM fermion field f'_{d} mixes with the neutrino fields. To account for this additional mixing in the DASM, for $f = \nu$ the indices i, j run over the three SM-like generations as well as ν_4. In the following phenomenological analysis we do not consider any flavour-sensitive observables. Thus, we set the CKM matrix to the unit matrix and do not introduce a matrix structure in renormalization transformations of the quark sector. The renormalization for a non-diagonal CKM matrix in the DASM would, however, exactly follow the respective SM procedure (see, e.g., Refs [51, 54] and references therein).
Finally, we introduce the renormalization transformation

$$t_{h,0} = t_h + \delta t_h, \qquad t_{H,0} = t_H + \delta t_H, \tag{4.3}$$

for the tadpole parameters defined in Eq. (3.14). While Eq. (3.14) holds for the bare and renormalized tadpole parameters, $\{t_{1,0}, t_{2,0}, t_{\mathrm{h},0}, t_{\mathrm{H},0}\}$ and $\{t_1, t_2, t_{\mathrm{h}}, t_{\mathrm{H}}\}$, respectively, the parameter relations given in Eq. (3.9) depend on the chosen renormalization scheme and, thus, are in general only valid for the bare parameters, but do not hold for the renormalized ones.

The remaining freedom of the choice of the renormalization of the unphysical sector, i.e. the gauge parameters, ghost fields, and would-be Goldstone-boson fields, does not affect S-matrix elements, and the counterterms introduced above are sufficient to render S-matrix elements finite. Thus, we choose the renormalization of the unphysical sector such that the gauge-fixing functionals will not introduce any counterterms, i.e. the gauge-fixing Lagrangian has the form Eq. (3.72) with Eq. (3.73) for renormalized parameters and fields.
Employing the renormalization transformations Eqs. (4.1) and (4.2), the Lagrangian of the DASM $\mathcal{L}_0$ written in terms of the bare parameters and fields can, at NLO, be split up in the following way

$$\mathcal{L}_0 = \mathcal{L} + \mathcal{L}_{\text{ct}}, \tag{4.4}$$

where $\mathcal{L}$ has the same form as $\mathcal{L}_0$, but with the bare quantities replaced by their respective renormalized ones, and $\mathcal{L}_{\text{ct}}$ yields the counterterm contributions. In particular, this means that the respective LO Feynman rules are recovered at NLO, but with renormalized parameters instead of the bare ones. Furthermore, we find additional Feynman rules originating from $\mathcal{L}_{\text{ct}}$ that introduce the respective renormalization constants in calculations.

4.2. Renormalization conditions

As already mentioned above, the precise choice of the renormalization constants defines the physical meaning of the renormalized quantities. The renormalization constants are obtained by imposing renormalization conditions on the corresponding fields and parameters. In the following, we set up a renormalization scheme that employs OS renormalization conditions for the fields and input parameters. OS renormalization conditions tie the input parameters directly to some physical quantities, making them more directly accessible in suitable experiments and giving them a rather intuitive meaning. Furthermore, this direct connection to physical objects results in several desirable features of OS schemes (see discussions below). As the only exception within this OS scheme, we renormalize the input parameter λ_{12} with an $\overline{\text{MS}}$ renormalization condition, since a sensible OS renormalization condition will only be applicable if the non-SM Higgs boson is found. The $\overline{\text{MS}}$ renormalization of λ_{12} will, however, not jeopardize any of the nice benefits of our OS scheme, like the independence of predictions on the tadpole treatment (see Sect. 4.2.1), since the dimensionless scalar self-coupling λ_{12} is not connected to the mass generation of any of the particles. Having the OS scheme set up, we alternatively set up $\overline{\text{MS}}$ renormalization for the BSM mixing angles introduced by the DASM. In $\overline{\text{MS}}$ renormalization schemes, the respective renormalization constants only absorb the standard UV divergence of dimensional regularization (see Eq. (C.2)), i.e. their finite parts are zero. Since the structure of the UV divergences is unique within a given theory, the UV-divergent parts of the

renormalization constants coincide in all renormalization schemes. Thus, having the OS renormalization scheme established, we can simply switch to $\overline{\text{MS}}$ renormalization by setting the finite parts of the respective renormalization constants to zero.

4.2.1. Tadpole treatment

Before we define the OS and $\overline{\text{MS}}$ renormalization of the DASM, we briefly discuss the treatment of the tadpoles, i.e. of the EW vacuum, following the discussion of the authors of Refs. [54, 72, 73], where a more detailed and comprehensive discussion of tadpole schemes can be found. While predictions of observables in full OS renormalization schemes are independent of the tadpole treatment[2], tadpoles are particularly important whenever any parameters related to masses are renormalized via $\overline{\text{MS}}$ conditions. In the latter case, predictions of observables are sensitive to the choice of the tadpole scheme. In this section, we discuss three important tadpole schemes. The historically most relevant schemes are the *Parameter Renormalized Tadpole Scheme* (PRTS) [78, 79] and the *Fleischer-Jegerlehner Tadpole Scheme* (FJTS) [80]. As an alternative to these schemes, more recently, the *Gauge-Invariant Vacuum expectation value Scheme* (GIVS) was proposed by the authors of Refs. [72, 73].

Due to the spontaneous symmetry breaking introduced by the non-vanishing vevs of the Higgs fields ρ and Φ, explicit tadpole contributions have to be taken into account in calculations within the DASM, whenever the minimum of the effective Higgs potential is not at the renormalized vevs v_1, v_2. From a technical point of view one wants to avoid the appearance of these tadpole contributions as far as possible. This can be achieved by suitable parameter and field definitions. Furthermore, a bad choice of the tadpole scheme and, thus, of the expansion point of the Higgs fields around the respective vevs can lead to large missing higher-order corrections, i.e. large uncertainties of predictions.
Forcing the bare tadpole terms to be zero, i.e. $t_{h,0} = t_{H,0} = 0$, eliminates the tadpole contributions at LO. At NLO, tadpole contributions of the form

$$\mathrm{i}\Gamma^h = \mathrm{i}T^h = \quad \overset{h}{-\!-\!-} \bigcirc, \qquad \mathrm{i}\Gamma^H = \mathrm{i}T^H = \quad \overset{H}{-\!-\!-} \bigcirc, \tag{4.5}$$

where the blobs represent any 1-loop subdiagrams, enter calculations. To eliminate the appearance of these explicit tadpole contributions, one generates tadpole counterterms of the form $\delta t_h h$ and $\delta t_H H$ in the NLO Lagrangian and fixes them such that they cancel against the unrenormalized NLO contributions to the renor-

[2] Note that, even in full OS schemes, intermediate results, like renormalization constants, in general do depend on the tadpole treatment. However, this dependence cancels out systematically in the calculation of observables.

malized 1-point functions $\Gamma^h_{\rm R}$ and $\Gamma^H_{\rm R}$ of the physical Higgs fields h and H,

$$\begin{aligned} \Gamma^h_{\rm R} &= T^h + \delta t_h = 0 \qquad \Rightarrow \qquad \delta t_h = -T^h, \\ \Gamma^H_{\rm R} &= T^H + \delta t_H = 0 \qquad \Rightarrow \qquad \delta t_H = -T^H. \end{aligned} \tag{4.6}$$

While all three tadpole schemes discussed in this section enforce Eq. (4.6), they introduce these tadpole terms in different ways. Therefore, the respective tadpole counterterms will enter the Lagrangian at different places.
The *Fleischer-Jegerlehner Tadpole Scheme* introduces the tadpole counterterms via field shifts of the physical Higgs fields

$$\begin{aligned} h &\to h + \Delta v_h^{\rm FJTS}, \qquad \Delta v_h^{\rm FJTS} = -\frac{\delta t_h^{\rm FJTS}}{M_{\rm h}^2}, \\ H &\to H + \Delta v_H^{\rm FJTS}, \qquad \Delta v_H^{\rm FJTS} = -\frac{\delta t_H^{\rm FJTS}}{M_{\rm H}^2}, \end{aligned} \tag{4.7}$$

while setting the explicit bare tadpole terms $t_{h,0}$ and $t_{H,0}$ to zero. Due to the gauge dependence of the unrenormalized contributions T^h and T^H to the Higgs 1-point functions, $\Delta v_h^{\rm FJTS}$ and $\Delta v_H^{\rm FJTS}$ turn out to be gauge dependent as well. However, the field redefinitions Eq. (4.7) are mere shifts in the integration variables of the functional integral. Thus, it cannot introduce any gauge dependence to the predictions for observables in either OS or $\overline{\rm MS}$ renormalization schemes. However, the FJTS tends to introduce large tadpole contributions to mass parameter renormalization constants, that can jeopardize the perturbative stability of predictions in $\overline{\rm MS}$ schemes[3] (see e.g. Refs. [69, 72, 73, 81, 82]).
In the *Parameter Renormalized Tadpole Scheme* the tadpoles are treated similarly to input parameters, and, consequently, the tadpole counterterms are introduced via the parameter renormalization transformations given by Eq. (4.3). In the PRTS the minimum of the renormalized effective Higgs potential is at the renormalized vevs v_1 and v_2. To achieve this, the renormalized tadpoles are set to zero $t_h = t_H = 0$, leading to $\delta t_h = t_{h,0}$ and $\delta t_H = t_{H,0}$. Combining

$$\begin{aligned} \delta t_1 &= -v_{1,0}\left(4v_{1,0}^2\lambda_{1,0} + v_{2,0}^2\lambda_{12,0} - 2\mu_{1,0}^2\right), \\ \delta t_2 &= -v_{2,0}\left(\frac{v_{2,0}^2}{4}\lambda_{2,0} + v_{1,0}^2\lambda_{12,0} - \mu_{2,0}^2\right), \\ \lambda_{1,0} &= \frac{v_{1,0}\left(c_{\alpha,0}^2 M_{\rm H,0}^2 + s_{\alpha,0}^2 M_{\rm h,0}^2\right) + c_{\alpha,0}\delta t_H - s_{\alpha,0}\delta t_h}{8v_{1,0}^3}, \\ \lambda_{2,0} &= \frac{2\left[v_{2,0}\left(c_{\alpha,0}^2 M_{\rm h,0}^2 + s_{\alpha,0}^2 M_{\rm H,0}^2\right) + c_{\alpha,0}\delta t_h + s_{\alpha,0}\delta t_H\right]}{v_{2,0}^3}, \end{aligned} \tag{4.8}$$

with Eq. (3.28) for the bare and renormalized vev $v_{1,0}$ and v_1, respectively, the tadpole counterterms in the PRTS can be restored to the Lagrangian, where the bare tadpole terms are set to zero, by the simple replacements

[3] Recall that the tadpole scheme dependence of predictions for observables cancels in OS schemes.

$$\mu_{1,0}^2 \to \mu_{1,0}^2 + \frac{3\left(c_\alpha \delta t_H^{\text{PRTS}} - s_\alpha \delta t_h^{\text{PRTS}}\right)}{4v_1}, \quad \mu_{2,0}^2 \to \mu_{2,0}^2 + \frac{3\left(c_\alpha \delta t_h^{\text{PRTS}} + s_\alpha \delta t_H^{\text{PRTS}}\right)}{2v_2},$$
$$\lambda_{1,0} \to \lambda_{1,0} + \frac{c_\alpha \delta t_H^{\text{PRTS}} - s_\alpha \delta t_h^{\text{PRTS}}}{8v_1^3}, \qquad \lambda_{2,0} \to \lambda_{2,0} + \frac{2\left(c_\alpha \delta t_h^{\text{PRTS}} + s_\alpha \delta t_H^{\text{PRTS}}\right)}{v_2^3},$$
$$\lambda_{12,0} \to \lambda_{12,0}. \tag{4.9}$$

In the PRTS, in contrast to the FJTS, the renormalized vev parameters denote the minimum of the renormalized Higgs potential. Therefore, the PRTS leads to small corrections to renormalized mass parameters. However, the gauge-dependent tadpole counterterms enter the relations between the bare original parameters of the Lagrangian and the chosen bare input parameters. This leads to a gauge dependence in the parameterization of predictions in terms of renormalized parameters for observables in $\overline{\text{MS}}$ renormalization schemes. Therefore, using $\overline{\text{MS}}$ renormalization, one has to fix a gauge once and for all, or the values of the input parameters have to be converted between different gauge choices, to obtain consistent results within the PRTS. Recall that full OS schemes are independent of the tadpole scheme and, thus, there is no such gauge dependence introduced.
As a third option, the *Gauge-Invariant Vacuum expectation value Scheme* was developed to combine the gauge independence of the FJTS and the perturbative stability of the PRTS in a single tadpole scheme. Therefore, it introduces two parts $\delta t_{S,1}^{\text{GIVS}}$ and $\delta t_{S,2}^{\text{GIVS}}$, $S = h, H$, of the respective tadpole renormalization constants δt_S. The former ones are introduced via a parameter renormalization transformation (similar to the PRTS) and the latter ones via a field redefinition (similar to the FJTS). To determine $\delta t_{S,1}^{\text{GIVS}}$, one switches to the non-linear representation (see Sect. 3.5), where the Higgs fields that correspond to the physical Higgs bosons are gauge invariant. Consequently, the resulting tadpole functions are gauge independent as well. These are used to determine the first parts of the tadpole constants via

$$\delta t_{h,1}^{\text{GIVS}} = -T_{\text{nl}}^h, \qquad \delta t_{H,1}^{\text{GIVS}} = -T_{\text{nl}}^H, \tag{4.10}$$

where the subscript "nl" marks the non-linear representation. At NLO they explicitly read

$$T_{\text{nl}}^S = \sum_{V=Z,Z',W} \lambda_{SV}\left[3A_0(M_{\text{V}}^2) - 2M_{\text{V}}^2\right] + \sum_{S'=h,H}\left[\lambda_{SS'}A_0(M_{S'}^2)\right]$$
$$+ \lambda_{SF}\sum_{f=l,u,d}\left[N_{C,f}m_f^2 A_0(m_f^2)\right] + \lambda_{S\nu_4}m_{\nu_4}^2 A_0(m_{\nu_4}^2), \qquad S = h, H, \tag{4.11}$$

where $N_{C,f}$ is the respective colour factor of a fermion f. The various coupling constants in the non-linear representation are given by

$$\lambda_{hZ} = \frac{c_{\text{w}}^2 M_{\text{Z}}^2\left(v_1 c_\alpha c_\gamma^2 M_{\text{Z}}^2 - v_2 s_\alpha s_\gamma^2 M_{\text{Z}'}^2\right)}{16\pi^2 v_1 v_2 M_{\text{W}}^2}, \quad \lambda_{HZ} = \frac{c_{\text{w}}^2 M_{\text{Z}}^2\left(v_1 s_\alpha c_\gamma^2 M_{\text{Z}}^2 + v_2 c_\alpha s_\gamma^2 M_{\text{Z}'}^2\right)}{16\pi^2 v_1 v_2 M_{\text{W}}^2},$$

$$\lambda_{hZ'} = \frac{c_{\mathrm{w}}^2 M_{\mathrm{Z}'}^2 \left(v_1 c_\alpha s_\gamma^2 M_{\mathrm{Z}'}^2 - v_2 s_\alpha c_\gamma^2 M_{\mathrm{Z}}^2\right)}{16\pi^2 v_1 v_2 M_{\mathrm{W}}^2}, \quad \lambda_{HZ'} = \frac{c_{\mathrm{w}}^2 M_{\mathrm{Z}'}^2 \left(v_1 s_\alpha s_\gamma^2 M_{\mathrm{Z}'}^2 + v_2 c_\alpha c_\gamma^2 M_{\mathrm{Z}}^2\right)}{16\pi^2 v_1 v_2 M_{\mathrm{W}}^2},$$

$$\lambda_{hW} = \frac{c_\alpha M_{\mathrm{W}}^2}{8\pi^2 v_2}, \qquad \lambda_{HW} = \frac{s_\alpha M_{\mathrm{W}}^2}{8\pi^2 v_2},$$

$$\lambda_{hh} = \frac{3 c_{\mathrm{hhh}}}{16\pi^2}, \qquad \lambda_{Hh} = \frac{c_{\mathrm{hhH}}}{16\pi^2},$$

$$\lambda_{hH} = \frac{c_{\mathrm{hHH}}}{16\pi^2}, \qquad \lambda_{HH} = \frac{3 c_{\mathrm{HHH}}}{16\pi^2},$$

$$\lambda_{hF} = -\frac{c_\alpha}{4\pi^2 v_2}, \qquad \lambda_{HF} = -\frac{s_\alpha}{4\pi^2 v_2},$$

$$\lambda_{h\nu_4} = \frac{s_\alpha s_{\theta_{\mathrm{r}}}^2}{4\pi^2 v_1}, \qquad \lambda_{H\nu_4} = -\frac{c_\alpha s_{\theta_{\mathrm{r}}}^2}{4\pi^2 v_1}, \tag{4.12}$$

where we made use of the shorthands for the Higgs self-couplings introduced in Sect. 3.1, and $A_0(m^2)$ denotes the standard 1-loop 1-point integral in dimensional regularization in the conventions of Ref. [54]. Similar to the PRTS, the resulting (gauge-independent) tadpole counterterms $\delta t_{h,1}^{\mathrm{GIVS}}$ and $\delta t_{H,1}^{\mathrm{GIVS}}$ can be restored in the Lagrangian, where $t_{h,0}$ and $t_{H,0}$ are set to zero, via the replacements

$$\mu_{1,0}^2 \to \mu_{1,0}^2 + \frac{3\left(c_\alpha \delta t_{H,1}^{\mathrm{GIVS}} - s_\alpha \delta t_{h,1}^{\mathrm{GIVS}}\right)}{4 v_1}, \qquad \mu_{2,0}^2 \to \mu_{2,0}^2 + \frac{3\left(c_\alpha \delta t_{h,1}^{\mathrm{GIVS}} + s_\alpha \delta t_{H,1}^{\mathrm{GIVS}}\right)}{2 v_2},$$

$$\lambda_{1,0} \to \lambda_{1,0} + \frac{c_\alpha \delta t_{H,1}^{\mathrm{GIVS}} - s_\alpha \delta t_{h,1}^{\mathrm{GIVS}}}{8 v_1^3}, \qquad \lambda_{2,0} \to \lambda_{2,0} + \frac{2\left(c_\alpha \delta t_{h,1}^{\mathrm{GIVS}} + s_\alpha \delta t_{H,1}^{\mathrm{GIVS}}\right)}{v_2^3},$$

$$\lambda_{12,0} \to \lambda_{12,0}. \tag{4.13}$$

Since we want to employ the linear Higgs representation in practical calculations, we need to introduce further tadpole renormalization constants—in addition to $\delta t_{h,1}^{\mathrm{GIVS}}$ and $\delta t_{H,1}^{\mathrm{GIVS}}$—to the Lagrangian to ensure the full cancelation of the explicit tadpole loop contributions in NLO calculations. These additional tadpole renormalization constants $\delta t_{h,2}^{\mathrm{GIVS}}$ and $\delta t_{H,2}^{\mathrm{GIVS}}$ are gauge dependent, but can, nevertheless, be introduced such that predictions of observables stay gauge independent (even in $\overline{\mathrm{MS}}$ schemes) via field shifts similarly to the ones performed in the FJTS,

$$h \to h + \Delta v_h^{\mathrm{GIVS}}, \qquad \Delta v_h^{\mathrm{GIVS}} = -\frac{\delta t_{h,2}^{\mathrm{GIVS}}}{M_{\mathrm{h}}^2},$$

$$H \to H + \Delta v_H^{\mathrm{GIVS}}, \qquad \Delta v_H^{\mathrm{GIVS}} = -\frac{\delta t_{H,2}^{\mathrm{GIVS}}}{M_{\mathrm{H}}^2}. \tag{4.14}$$

The explicit field shifts read

$$\Delta v_S^{\mathrm{GIVS}} = \frac{T^S - T_{\mathrm{nl}}^S}{M_S^2} = \lambda_{S\chi} A_0(\xi_{\mathrm{V}} M_{\mathrm{Z}}) + \lambda_{S\chi'} A_0(\xi_{\mathrm{V}} M_{\mathrm{Z}'}) + \lambda_{S\phi} A_0(\xi_{\mathrm{W}} M_{\mathrm{W}}), \tag{4.15}$$

with $S = h, H$ and the respective constants are given by

$$\lambda_{h\chi} = \frac{v_1 c_\alpha c_x^2 - v_2 s_\alpha s_x^2}{32\pi^2 v_1 v_2}, \qquad \lambda_{H\chi} = \frac{v_1 s_\alpha c_x^2 + v_2 c_\alpha s_x^2}{32\pi^2 v_1 v_2},$$

$$\lambda_{h\chi'} = \frac{v_1 c_\alpha s_x^2 - v_2 s_\alpha c_x^2}{32\pi^2 v_1 v_2}, \qquad \lambda_{H\chi'} = \frac{v_1 s_\alpha s_x^2 + v_2 c_\alpha c_x^2}{32\pi^2 v_1 v_2},$$
$$\lambda_{h\phi} = \frac{c_\alpha}{16\pi^2 v_2}, \qquad \lambda_{H\phi} = \frac{s_\alpha}{16\pi^2 v_2}. \tag{4.16}$$

Introducing the two parts of the tadpole renormalization constants in this way will tie the renormalized vevs v_1 and v_2 to the minimum of the renormalized effective Higgs potential without introducing any gauge dependence to the parameterization of observables. Thus, the GIVS combines the benefits of the PRTS and FJTS, making it a perturbatively stable, gauge-independent tadpole scheme.
As previously mentioned, for $\overline{\text{MS}}$ renormalization the choice of the tadpole treatment has an impact on the predictions for observables. Whenever we use $\overline{\text{MS}}$ renormalization in this work, we make use of the PRTS, which is the most commonly used tadpole scheme. Similar to the SM, the THDM, and the SESM cases, it is expected that the results in the DASM obtained within the PRTS deviate only marginally from the corresponding results obtained within the GIVS [72,73]. However, for the $\overline{\text{MS}}$ renormalization of the mixing angles we explicitly give all expressions needed to translate the respective results from the PRTS to the GIVS and FJTS.

4.2.2. Mass and field renormalization

We renormalize fields and masses using well-known OS conditions. To introduce these OS renormalization conditions we follow the procedure described in Refs. [54,79]. The resulting OS-renormalized fields are canonically normalized and do not mix with each other. Furthermore, the renormalized mass parameters corresponding to physical particles mark the positions of the poles of the real parts of the propagators. The renormalization conditions for the renormalized two-point vertex functions Γ^{ab}_{R} of the fields a, b, for OS external particles read

$$\text{Re}\,\Gamma^{V^\dagger V'}_{\text{R},\mu\nu}(-k,k)\varepsilon^\nu(k)|_{k^2=M_V^2} = 0, \qquad V, V' = A, Z, Z', W^\pm, \tag{4.17}$$

$$\lim_{k^2\to M_V^2} \frac{1}{k^2 - M_V^2}\,\text{Re}\,\Gamma^{V^\dagger V}_{\text{R},\mu\nu}(-k,k)\varepsilon^\nu(k) = -\varepsilon_\mu(k), \tag{4.18}$$

$$\text{Re}\,\Gamma^{SS'}_{\text{R}}(-k,k)|_{k^2=M_S^2} = 0, \qquad S, S' = h, H, \tag{4.19}$$

$$\lim_{k^2\to M_S^2} \frac{1}{k^2 - M_S^2}\,\text{Re}\,\Gamma^{SS}_{\text{R}}(-k,k) = 1, \tag{4.20}$$

$$\text{Re}\,\Gamma^{\bar f f}_{\text{R},ij}(-p,p)u_j(p)\Big|_{p^2=m_{f,j}^2} = 0, \tag{4.21}$$

$$\lim_{p^2\to m_{f,i}^2} \frac{\not p + m_{f,i}}{p^2 - m_{f,i}^2}\,\text{Re}\,\Gamma^{\bar f f}_{\text{R},ii}(-p,p)u_i(p) = u_i(p). \tag{4.22}$$

Here, we introduced the polarization vectors $\varepsilon^\mu(k)$ and the spinors $u_i(p)$ for the OS external vector bosons and fermions with momenta k and p, respectively. The

renormalized two-point vertex functions can further be decomposed using their respective covariant decompositions. In 't Hooft–Feynman gauge they are given by

$$\Gamma^{V^\dagger V'}_{\mathrm{R},\mu\nu}(-k,k) = -g_{\mu\nu}(k^2 - M_V^2)\delta_{VV'} - \left(g_{\mu\nu} - \frac{k_\mu k_\nu}{k^2}\right)\Sigma^{V^\dagger V'}_{\mathrm{R,T}}(k^2) - \frac{k_\mu k_\nu}{k^2}\Sigma^{V^\dagger V'}_{\mathrm{R,L}}(k^2),$$
$$\Gamma^{SS'}_{\mathrm{R}}(-k,k) = \left(k^2 - M_S^2\right)\delta_{SS'} + \Sigma^{SS'}_{\mathrm{R}}(k^2), \tag{4.23}$$

with the renormalized transversal and longitudinal self-energies, $\Sigma^{V^\dagger V'}_{\mathrm{R,T}}(k^2)$ and $\Sigma^{V^\dagger V'}_{\mathrm{R,L}}(k^2)$, for the renormalized vector boson two-point functions. Further, in our conventions all self-energies can be split up into

$$\Sigma\left(k^2\right) = \Sigma_{\mathrm{1PI}}\left(k^2\right) + \Sigma_{\delta t} + \Sigma_{\mathrm{tad}}, \tag{4.24}$$

with the one-particle irreducible (1PI) contributions Σ_{1PI}, the reducible tadpole contributions Σ_{tad}, and the 1- and 2-point tadpole counterterms $\Sigma_{\delta t}$ (see Ref. [54] for further details). Similarly to the case of the neutral gauge bosons, the possibility of mixing fields in the scalar sector of the DASM leads to a non-diagonal structure in the renormalized Higgs self-energies given by

$$\Sigma^{SS'}_{\mathrm{R}}(k^2) = \Sigma^{SS'}(k^2) + \frac{1}{2}(k^2 - M_S^2)\delta Z_{SS'} + \frac{1}{2}(k^2 - M_{S'}^2)\delta Z_{S'S} - \delta_{SS'}\delta M_S^2, \tag{4.25}$$

with $S, S' = h, H$. Combining Eqs. (4.17)–(4.20) with Eqs. (4.23)–(4.25) finally leads to the well-known results

$$\delta M_V^2 = \mathrm{Re}\,\Sigma^{V^\dagger V}_{\mathrm{T}}(M_V^2), \quad \delta Z_{V^\dagger V} = -\mathrm{Re}\,\frac{\partial\Sigma^{V^\dagger V}_{\mathrm{T}}(k^2)}{\partial k^2}\bigg|_{k^2=M_{\mathrm{V}}^2}, \quad V = A, Z, Z', W^\pm,$$
$$\delta Z_{VV'} = -2\mathrm{Re}\,\frac{\Sigma^{V^\dagger V'}_{\mathrm{T}}(M_{V'}^2)}{M_{V'}^2 - M_V^2}, \qquad VV' = AZ, ZA, AZ', Z'A, ZZ', Z'Z, \tag{4.26}$$

for the renormalization constants in the vector-boson sector and

$$\delta M_S^2 = \mathrm{Re}\,\Sigma^{SS}(M_S^2), \qquad \delta Z_{SS} = -\,\mathrm{Re}\,\frac{\partial\Sigma^{SS}(k^2)}{\partial k^2}\bigg|_{k^2=M_S^2},$$
$$\delta Z_{SS'} = -2\mathrm{Re}\,\frac{\Sigma^{S'S}(M_{S'}^2)}{M_{S'}^2 - M_S^2}, \qquad S{\neq}S', \qquad S, S' = h, H, \tag{4.27}$$

for the renormalization constants of the scalar sector. The covariant decomposition of the renormalized fermion two-point vertex function is given by

$$\Gamma^{f\bar{f}}_{\mathrm{R},ij}(-p,p) = \not{p}\omega_{\mathrm{L}}\Gamma^{f,\mathrm{L}}_{\mathrm{R},ij}(p^2) + \not{p}\omega_{\mathrm{R}}\Gamma^{f,\mathrm{R}}_{\mathrm{R},ij}(p^2) + \omega_{\mathrm{L}}\Gamma^{f,\mathrm{l}}_{\mathrm{R},ij}(p^2) + \omega_{\mathrm{R}}\Gamma^{f,\mathrm{r}}_{\mathrm{R},ij}(p^2), \tag{4.28}$$

with the chiral projectors $\omega_{\mathrm{L/R}} = \frac{1}{2}\left(1 \mp \gamma_5\right)$ and the renormalized left- and right-handed vector and scalar parts of the fermion two-point vertex function are denoted

by $\Gamma^{f,\mathrm{L}}_{\mathrm{R},ij}(p^2)$, $\Gamma^{f,\mathrm{R}}_{\mathrm{R},ij}(p^2)$, $\Gamma^{f,\mathrm{l}}_{\mathrm{R},ij}(p^2)$, and $\Gamma^{f,\mathrm{r}}_{\mathrm{R},ij}(p^2)$, respectively. Adopting this notation for the covariants of the self-energies, the different contributions to the two-point function can be further decomposed in terms of unrenormalized self-energy contributions and renormalization constants leading to

$$\Gamma^{f,\mathrm{L}}_{\mathrm{R},ij}(p^2) = \delta_{ij} + \Sigma^{f,\mathrm{L}}_{ij}\left(p^2\right) + \frac{1}{2}\left(\delta Z^{f,\mathrm{L}}_{ij} + \delta Z^{f,\mathrm{L}\dagger}_{ij}\right), \tag{4.29}$$

$$\Gamma^{f,\mathrm{R}}_{\mathrm{R},ij}(p^2) = \delta_{ij} + \Sigma^{f,\mathrm{R}}_{ij}\left(p^2\right) + \frac{1}{2}\left(\delta Z^{f,\mathrm{R}}_{ij} + \delta Z^{f,\mathrm{R}\dagger}_{ij}\right), \tag{4.30}$$

$$\Gamma^{f,\mathrm{l}}_{\mathrm{R},ij}(p^2) = -m_{f,i}\delta_{ij} + \Sigma^{f,l}_{ij}\left(p^2\right) - \frac{1}{2}\left(m_{f,i}\delta Z^{f,\mathrm{L}}_{ij} + m_{f,j}\delta Z^{f,\mathrm{R}\dagger}_{ij}\right) - \delta_{ij}\delta m_{f,i}, \tag{4.31}$$

$$\Gamma^{f,\mathrm{r}}_{\mathrm{R},ij}(p^2) = -m_{f,i}\delta_{ij} + \Sigma^{f,r}_{ij}\left(p^2\right) - \frac{1}{2}\left(m_{f,i}\delta Z^{f,\mathrm{R}}_{ij} + m_{f,j}\delta Z^{f,\mathrm{L}\dagger}_{ij}\right) - \delta_{ij}\delta m_{f,i}, \tag{4.32}$$

where $\delta Z^{\dagger}_{ij} = \delta Z^{*}_{ji}$ follows from the hermiticity of $\mathcal{L}$. Combining Eqs. (4.21) and (4.22) with Eqs. (4.28)–(4.32), we find, similarly to the SM case [51, 54, 79],

$$\begin{aligned}
\delta m_{f,i} &= \frac{1}{2}\mathrm{Re}\left[m_{f,i}\Big(\Sigma^{f,\mathrm{L}}_{ii}(m^2_{f,i}) + \Sigma^{f,\mathrm{R}}_{ii}(m^2_{f,i})\Big) + \Sigma^{f,\mathrm{l}}_{ii}(m^2_{f,i}) + \Sigma^{f,\mathrm{r}}_{ii}(m^2_{f,i})\right],\\
\delta Z^{f,\mathrm{L}}_{ii} &= -\mathrm{Re}\,\Sigma^{f,\mathrm{L}}_{ii}(m^2_{f,i}) - m_{f,i}\frac{\partial}{\partial p^2}\mathrm{Re}\left[m_{f,i}\Big(\Sigma^{f,\mathrm{L}}_{ii}(p^2) + \Sigma^{f,\mathrm{R}}_{ii}(p^2)\Big)\right.\\
&\quad \left. + \Sigma^{f,\mathrm{l}}_{ii}(p^2) + \Sigma^{f,\mathrm{r}}_{ii}(p^2)\right]\Big|_{p^2=m^2_{f,i}},\\
\delta Z^{f,\mathrm{R}}_{ii} &= -\mathrm{Re}\,\Sigma^{f,\mathrm{R}}_{ii}(m^2_{f,i}) - m_{f,i}\frac{\partial}{\partial p^2}\mathrm{Re}\left[m_{f,i}\Big(\Sigma^{f,\mathrm{L}}_{ii}(p^2) + \Sigma^{f,\mathrm{R}}_{ii}(p^2)\Big)\right.\\
&\quad \left. + \Sigma^{f,\mathrm{l}}_{ii}(p^2) + \Sigma^{f,\mathrm{r}}_{ii}(p^2)\right]\Big|_{p^2=m^2_{f,i}},\\
\delta Z^{f,\mathrm{R}}_{ij} &= \frac{2}{m^2_{f,i} - m^2_{f,j}}\mathrm{Re}\Big[m^2_{f,j}\Sigma^{f,\mathrm{R}}_{ij}(m^2_{f,j}) + m_{f,i}m_{f,j}\Sigma^{f,\mathrm{L}}_{ij}(m^2_{f,j}) + m_{f,j}\Sigma^{f,\mathrm{l}}_{ij}(m^2_{f,j})\\
&\quad + m_{f,i}\Sigma^{f,\mathrm{r}}_{ij}(m^2_{f,j})\Big], \qquad i \neq j,
\end{aligned} \tag{4.33}$$

for the field and mass renormalization constants of the fermion sector.

4.2.3. Mixing-angle renormalization

In many BSM models, where some sort of mixing of fields appears, mixing angles, like γ, α, or θ_{r} in the DASM, are introduced to parameterize the BSM modifications of certain couplings of SM-like particles. This intuitive interpretation and direct experimental accessibility make them a natural choice as input parameters. However, they are often introduced to diagonalize mass matrices of mixing fields and, thus, are related to the masses of the corresponding particles. Therefore, $\overline{\mathrm{MS}}$ renormalization of these mixing angles will, in general, lead to a dependence of predictions for observables on the choice of the tadpole renormalization scheme

(see Sect. 4.2.1). Hence, a proper OS renormalization for mixing angles is desirable. In the past, several OS renormalization schemes for mixing angles were developed. A comprehensive overview of such schemes and a detailed discussion of their benefits and downsides is given in Ref. [81]. Following this discussion, a good OS renormalization scheme for mixing angles should have several desirable properties:

- Resulting OS renormalization constants should be gauge independent. This guarantees that predictions for observables are gauge-independent functions of the renormalized mixing angles.
- Resulting higher-order corrections to observables should be of moderate size, i.e., the renormalization scheme should not spoil the stability of the perturbative approach in calculations. In detail, there should be no region in the (otherwise perturbative region of the) parameter space, where the corrections to S-matrix elements become unreasonably large or even develop a singularity. Accordingly, the OS renormalization constants should not introduce any "dead corners" to the parameter space for extreme values of the respective mixing angle or in the case of degeneracy of the masses of the mixing particles that are not already present in the LO coupling structure of the model.
- The renormalization of the mixing angle should not distinguish between the mixing fields. Thus, it should be symmetric with respect to the mixing degrees of freedom. Furthermore, it should be as process independent as possible.
- The renormalization scheme should respect the LO decoupling properties of heavy particles [83].

Having this in mind, we now define OS renormalization conditions for the mixing angles present in the DASM.

4.2.3.1. Renormalization of the gauge-boson mixing angle γ

Following the approach for OS renormalization of scalar-sector mixing angles discussed in Ref. [81], we introduce a "fake fermion" ω_d that carries an infinitesimal charge of the new $U(1)_\mathrm{d}$ gauge group. Besides that, it is a singlet under the remaining gauge symmetry of the DASM. Introducing ω_d to the theory, we have to add the most general gauge-invariant, renormalizable Lagrangian that includes the fake fermion,

$$\mathcal{L}_{\omega_\mathrm{d}} = \bar{\omega}_\mathrm{d} \left(\mathrm{i}\not{D}_\mathrm{d} - m_{\omega_\mathrm{d}}\right) \omega_\mathrm{d} = \bar{\omega}_\mathrm{d} \left[\mathrm{i}\not{\partial} - \tilde{e}\tilde{q}_\omega \left(s_\gamma \not{Z} + c_\gamma \not{Z}'\right) - m_{\omega_\mathrm{d}}\right] \omega_\mathrm{d}, \tag{4.34}$$

to the Lagrangian of the DASM. Here $\tilde{q}$ represents the $U(1)_\mathrm{d}$ charge and m_{ω_d} is the Dirac mass parameter of ω_d, which is present since ω_d is non-chiral[4]. Equation

[4]Note that this also ensures that no anomalies are introduced to the theory by introducing the fake fermion.

(4.34) introduced two additional vertices with the respective Feynman rules[5]

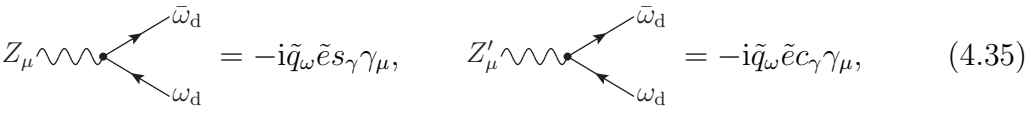

(4.35)

to the theory, which vanish in the limit $\tilde{q} \to 0$, where the DASM is recovered. However, we can use these additional interaction terms, or rather the possible[6] $\mathrm{Z}/\mathrm{Z}' \to \bar{\omega}_\mathrm{d}\omega_\mathrm{d}$ decays to define the OS renormalization condition for γ. To this end, we parameterize the matrix elements of the two decays by the OS formfactors $\mathcal{F}^{V\bar{\omega}_\mathrm{d}\omega_\mathrm{d}}$, $(V = Z, Z')$, via

$$\mathcal{M}^{\mathrm{Z}\to\bar{\omega}_\mathrm{d}\omega_\mathrm{d}} = [\bar{u}_{\omega_\mathrm{d}} \not{\varepsilon} v_{\omega_\mathrm{d}}]_Z \mathcal{F}^{Z\bar{\omega}_\mathrm{d}\omega_\mathrm{d}}, \qquad \mathcal{M}^{\mathrm{Z}'\to\bar{\omega}_\mathrm{d}\omega_\mathrm{d}} = [\bar{u}_{\omega_\mathrm{d}} \not{\varepsilon} v_{\omega_\mathrm{d}}]_{Z'} \mathcal{F}^{Z'\bar{\omega}_\mathrm{d}\omega_\mathrm{d}}, \tag{4.36}$$

with the spinors of the final-state fermions $\bar{u}_{\omega_\mathrm{d}}$ and v_{ω_d}, and the polarization vector of the respective gauge boson ε_μ. Further, the subscripts of the spinor chains $[\dots]_{Z/Z'}$ indicate the respective decay kinematics. These OS formfactors can now be used to determine the gauge-boson mixing angle renormalization constant $\delta\gamma$ at NLO. To this end, we use the ratio of the two formfactors and demand that the NLO corrections to this ratio in the limit $\tilde{q} \to 0$ vanish

$$\lim_{\tilde{q}_\omega \to 0} \frac{\mathcal{F}^{Z\bar{\omega}_\mathrm{d}\omega_\mathrm{d}}_\mathrm{NLO}}{\mathcal{F}^{Z'\bar{\omega}_\mathrm{d}\omega_\mathrm{d}}_\mathrm{NLO}} \stackrel{!}{=} \frac{\mathcal{F}^{Z\bar{\omega}_\mathrm{d}\omega_\mathrm{d}}_\mathrm{LO}}{\mathcal{F}^{Z'\bar{\omega}_\mathrm{d}\omega_\mathrm{d}}_\mathrm{LO}} = \frac{s_\gamma}{c_\gamma}. \tag{4.37}$$

We specifically choose this ratio since it only depends on γ, but no other parameter at LO. In this way, we can ensure that we do not absorb any corrections that are related to other parameters of the model into the definition of $\delta\gamma$. Otherwise, this misalignment can potentially lead to unnaturally large corrections (see e.g. Ref. [81] and references therein). Using OS renormalization for the fields, the renormalized formfactors are given by

$$\begin{aligned}
\mathcal{F}^{Z\bar{\omega}_\mathrm{d}\omega_\mathrm{d}}_\mathrm{NLO} &= \mathcal{F}^{Z\bar{\omega}_\mathrm{d}\omega_\mathrm{d}}_\mathrm{LO} \left(1 + \frac{\delta\tilde{e}}{\tilde{e}} + \frac{\delta s_\gamma}{s_\gamma} + \delta Z_{\omega_\mathrm{d}} + \frac{1}{2}\delta Z_{ZZ} + \frac{c_\gamma}{2s_\gamma}\delta Z_{Z'Z} + \delta^{Z\bar{\omega}_\mathrm{d}\omega_\mathrm{d}}_\mathrm{loop}\right), \\
\mathcal{F}^{Z'\bar{\omega}_\mathrm{d}\omega_\mathrm{d}}_\mathrm{NLO} &= \mathcal{F}^{Z'\bar{\omega}_\mathrm{d}\omega_\mathrm{d}}_\mathrm{LO} \left(1 + \frac{\delta\tilde{e}}{\tilde{e}} + \frac{\delta c_\gamma}{c_\gamma} + \delta Z_{\omega_\mathrm{d}} + \frac{1}{2}\delta Z_{Z'Z'} + \frac{s_\gamma}{2c_\gamma}\delta Z_{ZZ'} + \delta^{Z'\bar{\omega}_\mathrm{d}\omega_\mathrm{d}}_\mathrm{loop}\right).
\end{aligned} \tag{4.38}$$

Here we introduced the unrenormalized relative 1-loop corrections to the two vertices $\delta^{Z/Z'\bar{\omega}_\mathrm{d}\omega_\mathrm{d}}_\mathrm{loop}$, respectively, as well as the field renormalization constant for $\delta Z_{\omega_\mathrm{d}}$ of ω_d. In combination with Eq. (4.37) we find

[5] In our convention for Feynman rules all fields are considered incoming.

[6] The mass of the fake fermion can always be chosen such that these decays are possible.

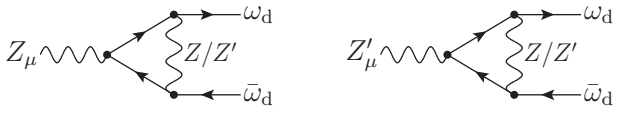

Figure 4.1.: Feynman diagrams contribution to $\delta_{\mathrm{loop}}^{Z/Z'\bar{\omega}_\mathrm{d}\omega_\mathrm{d}}$.

$$\frac{\mathcal{F}_{\mathrm{NLO}}^{Z\bar{\omega}_\mathrm{d}\omega_\mathrm{d}}}{\mathcal{F}_{\mathrm{NLO}}^{Z'\bar{\omega}_\mathrm{d}\omega_\mathrm{d}}} = \frac{\mathcal{F}_{\mathrm{LO}}^{Z\bar{\omega}_\mathrm{d}\omega_\mathrm{d}}}{\mathcal{F}_{\mathrm{LO}}^{Z'\bar{\omega}_\mathrm{d}\omega_\mathrm{d}}}\Bigg[1 + \frac{\delta s_\gamma}{s_\gamma} - \frac{\delta c_\gamma}{c_\gamma} + \frac{1}{2}\left(\delta Z_{ZZ} - \delta Z_{Z'Z'} + \frac{c_\gamma}{s_\gamma}\delta Z_{Z'Z} - \frac{s_\gamma}{c_\gamma}\delta Z_{ZZ'}\right) + \delta_{\mathrm{loop}}^{Z\bar{\omega}_\mathrm{d}\omega_\mathrm{d}} - \delta_{\mathrm{loop}}^{Z'\bar{\omega}_\mathrm{d}\omega_\mathrm{d}}\Bigg]. \tag{4.39}$$

The only NLO contributions to the vertex corrections are introduced by the respective Feynman diagrams shown in Fig. 4.1. Thus, we find $\delta_{\mathrm{loop}}^{Z/Z'\bar{\omega}_\mathrm{d}\omega_\mathrm{d}} = \mathcal{O}(\tilde{q}_\mathrm{d}^2)$ for $\tilde{q}_\mathrm{d} \to 0$. Similarly, the Feynman diagrams contributing to $\delta Z_{\omega_\mathrm{d}}$ include at least two couplings of the Z or Z′ boson to ω_d and, thus, $\delta Z_{\omega_\mathrm{d}} = \mathcal{O}(\tilde{q}_\mathrm{d}^2)$ as well. Therefore, combining the renormalization condition Eq. (4.37) with Eq. (4.39) and taking the decoupling limit $\tilde{q}_\mathrm{d} \to 0$ for the fake fermion leads to

$$\delta\gamma_{\mathrm{OS}} = \frac{1}{2}s_\gamma c_\gamma\left(\delta Z_{Z'Z'} - \delta Z_{ZZ}\right) + \frac{1}{2}\left(s_\gamma^2\delta Z_{ZZ'} - c_\gamma^2\delta Z_{Z'Z}\right), \tag{4.40}$$

where we made use of $\delta s_\gamma = c_\gamma\delta\gamma$.
This OS renormalization combines several of the desirable properties mentioned above:

- By defining the OS condition in terms of OS formfactors, the resulting renormalization constant is based on S-matrix elements resulting in a gauge-independent combination of field renormalization constants.
- It is symmetric in the neutral gauge-boson fields Z and Z'.
- $\delta\gamma_{\mathrm{OS}}$ has smooth limits for $s_\gamma \to 0$ and $c_\gamma \to 0$.
- The renormalization constant $\delta\gamma_{\mathrm{OS}}$ does not depend on a specific physical process.
- Predictions using this OS renormalization are stable in the degeneracy limit $M_{\mathrm{Z}'} \to M_{\mathrm{Z}}$. To see this, we first note that all appearance of γ originating from parameter replacements of the original parameters of the Lagrangian in terms of our chosen input parameter set (see e.g. Eqs. (3.68) and (3.69) for e_d and a) include a prefactor $M_{\mathrm{Z}}^2 - M_{\mathrm{Z}'}^2$. This prefactor cancels the respective poles introduced to $\delta\gamma_{\mathrm{OS}}$ via the off-diagonal gauge-boson field renormalization constants in Eq. (4.40). Additionally, $\delta\gamma_{\mathrm{OS}}$ is explicitly introduced to the theory by the field rotation matrix Eq. (3.58). In combination with the introduced OS field renormalization Eq. (4.2) we find at NLO

$$\mathrm{R_V}(\gamma_0; c_{\mathrm{w},0}) = \mathrm{R_V}(\gamma, c_\mathrm{w}) + \delta\mathrm{R_V}(\gamma, c_\mathrm{w}, \delta\gamma, \delta c_\mathrm{w}), \tag{4.41}$$

and finally

$$\begin{pmatrix} B'_\mu \\ W^3_\mu \\ C'_\mu \end{pmatrix} = \mathrm{R_V}(\gamma, c_\mathrm{w}) \left(1 + \mathrm{R_V^T}(\gamma, c_\mathrm{w}) \delta \mathrm{R_V}(\gamma, c_\mathrm{w}, \delta\gamma, \delta c_\mathrm{w}) + \frac{1}{2}\delta \mathrm{Z_V}\right) \begin{pmatrix} A_\mu \\ Z_\mu \\ Z'_\mu \end{pmatrix}. \tag{4.42}$$

The explicit $\delta\gamma$ terms originating from $\delta\mathrm{R_V}$ are always introduced in either one of the combinations

$$-\delta\gamma + \frac{1}{2}\delta Z_{ZZ'}, \qquad \delta\gamma + \frac{1}{2}\delta Z_{Z'Z}, \tag{4.43}$$

which in either case only introduces the off-diagonal field renormalization constants $\delta Z_{Z'Z}$ and $\delta Z_{ZZ'}$ in the combination

$$\delta Z_{Z'Z} + \delta Z_{ZZ'} = 2\mathrm{Re}\frac{\Sigma_\mathrm{T}^{ZZ'}(M_\mathrm{Z}^2) - \Sigma_\mathrm{T}^{Z'Z}(M_{\mathrm{Z}'}^2)}{M_{\mathrm{Z}'}^2 - M_\mathrm{Z}^2}. \tag{4.44}$$

This combination is stable for $M_{\mathrm{Z}'} \to M_\mathrm{Z}$ making the OS scheme perturbatively stable in this limit.

- As discussed in Sect. 4.2.1, having full OS renormalization for all parameters related to masses leads to a cancelation of all tadpole contributions in predictions for observables.

Having this OS renormalization set up, it is straightforward to derive the respective $\overline{\mathrm{MS}}$ result by simply setting the finite parts of $\delta\gamma_\mathrm{OS}$ to zero and only keeping the terms proportional to the standard 1-loop UV divergence of dimensional regularization Δ_UV,

$$\delta\gamma_{\overline{\mathrm{MS}}} = \delta\gamma_\mathrm{OS}\big|_\mathrm{UV}. \tag{4.45}$$

The explicit result for $\delta\gamma_{\overline{\mathrm{MS}}}$ in the PRTS is given in Appendix D. Note that even though the dependence on the tadpole treatment cancels exactly in predictions of observables using OS renormalization, $\delta\gamma_\mathrm{OS}$ itself depends on the chosen tadpole scheme. So does $\delta\gamma_{\overline{\mathrm{MS}}}$ (see Eq. (4.45)). Its tadpole contributions in the three tadpole schemes described in Sect. 4.2.1 explicitly read

$$\delta\gamma^\mathrm{PRTS}_{\overline{\mathrm{MS}},\mathrm{tad}} = 0, \tag{4.46}$$

$$\delta\gamma^\mathrm{FJTS}_{\overline{\mathrm{MS}},\mathrm{tad}} = -\frac{\left(c_{\mathrm{ZZ'h}}\Delta v_\mathrm{h}^\mathrm{FJTS} + c_{\mathrm{ZZ'H}}\Delta v_\mathrm{H}^\mathrm{FJTS}\right)}{M_\mathrm{Z}^2 - M_{\mathrm{Z}'}^2}\bigg|_\mathrm{UV}, \tag{4.47}$$

$$\delta\gamma^\mathrm{GIVS}_{\overline{\mathrm{MS}},\mathrm{tad}} = -\frac{\left(c_{\mathrm{ZZ'h}}\Delta v_\mathrm{h}^\mathrm{GIVS} + c_{\mathrm{ZZ'H}}\Delta v_\mathrm{H}^\mathrm{GIVS}\right)}{M_\mathrm{Z}^2 - M_{\mathrm{Z}'}^2}\bigg|_\mathrm{UV}, \tag{4.48}$$

where we introduced

$$c_{\mathrm{ZZ'h}} = -s_{2\gamma}\left(c_\alpha v_1 + s_\alpha v_2\right)\frac{M_{\mathrm{C}}^2}{v_1 v_2}, \qquad c_{\mathrm{ZZ'H}} = s_{2\gamma}\left(c_\alpha v_2 - s_\alpha v_1\right)\frac{M_{\mathrm{C}}^2}{v_1 v_2}, \tag{4.49}$$

representing the couplings $c_{\mathrm{ZZ'h}} h Z'_\mu Z^\mu + c_{\mathrm{ZZ'H}} H Z'_\mu Z^\mu$ in the Lagrangian. In the PRTS, and, thus, in the GIVS, tadpole terms are explicitly introduced in the relations between the bare parameters of the Higgs potential $\lambda_{1,0}, \lambda_{2,0}, \lambda_{12,0}, \mu_{1,0}^2, \mu_{2,0}^2$ and the bare vevs, masses, and mixing angles, introducing a tadpole scheme dependence to the latter. The relation between the bare gauge-boson mixing angles in the PRTS and FJTS is given by

$$\gamma_0^{\mathrm{PRTS}} = \gamma_0^{\mathrm{FJTS}} - \frac{1}{M_{\mathrm{Z}}^2 - M_{\mathrm{Z'}}^2}\left(c_{\mathrm{ZZ'h}}\frac{\delta t_{\mathrm{h}}^{\mathrm{FJTS}}}{M_{\mathrm{h}}^2} + c_{\mathrm{ZZ'H}}\frac{\delta t_{\mathrm{H}}^{\mathrm{FJTS}}}{M_{\mathrm{H}}^2}\right), \tag{4.50}$$

leading, in combination with Eqs. (4.46) and (4.47), to the (gauge-dependent) shift

$$\begin{aligned}\gamma_{\overline{\mathrm{MS}}}^{\mathrm{PRTS}} - \gamma_{\overline{\mathrm{MS}}}^{\mathrm{FJTS}} &= \gamma_0^{\mathrm{PRTS}} - \gamma_0^{\mathrm{FJTS}} - \left(\delta\gamma_{\overline{\mathrm{MS}}}^{\mathrm{PRTS}} - \delta\gamma_{\overline{\mathrm{MS}}}^{\mathrm{FJTS}}\right) \\ &= \frac{1}{M_{\mathrm{Z}}^2 - M_{\mathrm{Z'}}^2}\left(c_{\mathrm{ZZ'h}}\frac{T^h}{M_{\mathrm{h}}^2} + c_{\mathrm{ZZ'H}}\frac{T^H}{M_{\mathrm{H}}^2}\right)\Bigg|_{\mathrm{finite}},\end{aligned} \tag{4.51}$$

for the $\overline{\mathrm{MS}}$-renormalized mixing angle. Here the subscript "finite" indicates that only the finite parts are kept. Similarly one finds the (gauge-independent) shift

$$\gamma_{\overline{\mathrm{MS}}}^{\mathrm{GIVS}} - \gamma_{\overline{\mathrm{MS}}}^{\mathrm{FJTS}} = \frac{1}{M_{\mathrm{Z}}^2 - M_{\mathrm{Z'}}^2}\left(c_{\mathrm{ZZ'h}}\frac{T_{\mathrm{nl}}^h}{M_{\mathrm{h}}^2} + c_{\mathrm{ZZ'H}}\frac{T_{\mathrm{nl}}^H}{M_{\mathrm{H}}^2}\right)\Bigg|_{\mathrm{finite}}, \tag{4.52}$$

for the connection between the GIVS and FJTS values of the $\overline{\mathrm{MS}}$ renormalized mixing angle. Finally, we want to emphasize that predictions using an $\overline{\mathrm{MS}}$ renormalized γ are in general not stable in the limit $M_{\mathrm{Z'}} \to M_{\mathrm{Z}}$.

4.2.3.2. Renormalization of the Higgs mixing angle α

Since the Higgs field ρ is charged under the $U(1)_{\mathrm{d}}$ gauge group, no gauge-invariant interaction with a "fake fermion" (that allows us to recover the original theory by taking an "easy" decoupling limit), as proposed in Ref. [81], is possible in the DASM. Consequently, no fully process-independent OS definition is suitable for the Higgs mixing angle α. In this section, we define two different, process-dependent OS renormalization conditions for α and additionally give the result for its $\overline{\mathrm{MS}}$ renormalization. Note that a comparison of predictions obtained with these different schemes can provide an estimate of the theoretical uncertainties of the predictions. In order to define the first OS scheme, we make use of the decays $\mathrm{h/H} \to \bar{\nu}_4\nu_4$. Naturally, this is only applicable in the case $M_{\mathrm{h}} > 2m_{\nu_4}$. We use the ratio of the respective on-shell formfactors $\mathcal{F}^{h/H\bar{\nu}_4\nu_4}$ of the two decays, defined by

$$\mathcal{M}^{\mathrm{h}\to\bar{\nu}_4\nu_4} = [\bar{u}_{\nu_4} v_{\nu_4}]_h \mathcal{F}^{h\bar{\nu}_4\nu_4}, \qquad \mathcal{M}^{\mathrm{H}\to\bar{\nu}_4\nu_4} = [\bar{u}_{\nu_4} v_{\nu_4}]_H \mathcal{F}^{H\bar{\nu}_4\nu_4}, \tag{4.53}$$

to define our OS renormalization condition. Recall that in our notation $[\dots]_{h/H}$ represent the kinematics of the respective decays, and $\bar{u}_{\nu_4}$ and v_{ν_4} denote the spinors of the final-state fermions. For our NLO renormalization of α, we demand all NLO corrections to the ratio of the real parts of these formfactors to vanish

$$\frac{\mathrm{Re}\,\mathcal{F}^{h\bar{\nu}_4\nu_4}_{\mathrm{NLO}}}{\mathrm{Re}\,\mathcal{F}^{H\bar{\nu}_4\nu_4}_{\mathrm{NLO}}} \stackrel{!}{=} \frac{\mathcal{F}^{h\bar{\nu}_4\nu_4}_{\mathrm{LO}}}{\mathcal{F}^{H\bar{\nu}_4\nu_4}_{\mathrm{LO}}} = -\frac{s_\alpha}{c_\alpha}. \tag{4.54}$$

In the presented OS scheme we treat α as a real parameter, and, thus, the real parts on the left-hand side of Eq. (4.54) are needed to ensure that absorptive parts are not taken into account in the renormalization condition. At LO the ratio Eq. (4.54) only depends on the parameter α and, thus, it is particularly well suited for the Higgs mixing angle renormalization (see discussion below Eq. (4.37)). Decomposing the two formfactors at NLO leads to

$$\begin{aligned}
\mathcal{F}^{h\bar{\nu}_4\nu_4}_{\mathrm{NLO}} &= \mathcal{F}^{h\bar{\nu}_4\nu_4}_{\mathrm{LO}}\Bigg[1 + \frac{\delta s_\alpha}{s_\alpha} + \frac{\delta s_{\theta_\mathrm{r}}}{s_{\theta_\mathrm{r}}} + \frac{\delta\tilde{y}}{\tilde{y}} - \frac{\delta v_1}{v_1} \\
&\qquad + \frac{1}{2}\left(2\delta Z^{\nu}_{44} + \delta Z_{hh} - \frac{c_\alpha}{s_\alpha}\delta Z_{Hh} + \frac{c_{\theta_\mathrm{r}}}{s_{\theta_\mathrm{r}}}\delta Z^{\nu,\mathrm{R}}_{34}\right) + \delta^{h\bar{\nu}_4\nu_4}_{\mathrm{loop}}\Bigg], \\
\mathcal{F}^{H\bar{\nu}_4\nu_4}_{\mathrm{NLO}} &= \mathcal{F}^{H\bar{\nu}_4\nu_4}_{\mathrm{LO}}\Bigg[1 + \frac{\delta c_\alpha}{c_\alpha} + \frac{\delta s_{\theta_\mathrm{r}}}{s_{\theta_\mathrm{r}}} + \frac{\delta\tilde{y}}{\tilde{y}} - \frac{\delta v_1}{v_1} \\
&\qquad + \frac{1}{2}\left(2\delta Z^{\nu}_{44} + \delta Z_{HH} - \frac{s_\alpha}{c_\alpha}\delta Z_{hH} + \frac{c_{\theta_\mathrm{r}}}{s_{\theta_\mathrm{r}}}\delta Z^{\nu,\mathrm{R}}_{34}\right) + \delta^{H\bar{\nu}_4\nu_4}_{\mathrm{loop}}\Bigg],
\end{aligned} \tag{4.55}$$

where we introduced the shorthands $\delta^{h\bar{\nu}_4\nu_4}_{\mathrm{loop}}$ and $\delta^{H\bar{\nu}_4\nu_4}_{\mathrm{loop}}$ for the unrenormalized relative 1-loop corrections to the two decays, respectively. Note that these process-dependent parts will not cancel and enter the final result for the renormalization constant obtained via the presented OS renormalization procedure. The introduced field renormalization constant for the fermion ν_4 is given by

$$\delta Z^{\nu}_{44} = \frac{1}{2}\left(\delta Z^{\nu,\mathrm{L}}_{44} + \delta Z^{\nu,\mathrm{R}}_{44}\right). \tag{4.56}$$

Combining Eq. (4.54) with Eq. (4.55) leads to

$$\begin{aligned}
\frac{\mathrm{Re}\,\mathcal{F}^{h\bar{\nu}_4\nu_4}_{\mathrm{NLO}}}{\mathrm{Re}\,\mathcal{F}^{H\bar{\nu}_4\nu_4}_{\mathrm{NLO}}} = &-\frac{s_\alpha}{c_\alpha}\Bigg\{1 + \frac{\delta s_\alpha}{s_\alpha} - \frac{\delta c_\alpha}{c_\alpha} + \frac{1}{2}\left[\delta Z_{hh} - \delta Z_{HH} + \frac{s_\alpha}{c_\alpha}\delta Z_{hH} - \frac{c_\alpha}{s_\alpha}\delta Z_{Hh}\right] \\
&+ \mathrm{Re}\left[\delta^{h\bar{\nu}_4\nu_4}_{\mathrm{loop}} - \delta^{H\bar{\nu}_4\nu_4}_{\mathrm{loop}}\right]\Bigg\},
\end{aligned} \tag{4.57}$$

which, with the help of $\delta s_\alpha = c_\alpha \delta\alpha$, yields

$$\begin{aligned}
\delta\alpha_{\mathrm{OS1}} = &\frac{1}{2}c_\alpha s_\alpha\left(\delta Z_{HH} - \delta Z_{hh}\right) + \frac{1}{2}\left(c^2_\alpha\delta Z_{Hh} - s^2_\alpha\delta Z_{hH}\right) \\
&+ c_\alpha s_\alpha \mathrm{Re}\left[\delta^{H\bar{\nu}_4\nu_4}_{\mathrm{loop}} - \delta^{h\bar{\nu}_4\nu_4}_{\mathrm{loop}}\right],
\end{aligned} \tag{4.58}$$

for the OS renormalization constant $\delta\alpha_{\text{OS1}}$ for the Higgs mixing angle based on the renormalization condition Eq. (4.54).
As an alternative OS renormalization condition, we employ the decays $\text{h/H} \to \bar{\nu}_3\nu_4$ or $\bar{\nu}_4 \to \text{h/H}\bar{\nu}_3$ allowing for a wider range of applications[7]. In this case, the above assumed mass hierarchy $M_\text{h} > 2m_{\nu_4}$, is relaxed to $m_{\nu_3} \ll M_\text{h}, M_\text{H}, m_{\nu_4}$. For $M_\text{h} > m_{\nu_4}$, the respective on-shell formfactors are defined by

$$\mathcal{M}^{\text{h}\to\bar{\nu}_3\nu_4} = [\bar{u}_{\nu_4}\omega_\text{R} v_{\nu_3}]_h \mathcal{F}^{h\bar{\nu}_4\nu_3}, \qquad \mathcal{M}^{\text{H}\to\bar{\nu}_3\nu_4} = [\bar{u}_{\nu_4}\omega_\text{R} v_{\nu_3}]_H \mathcal{F}^{H\bar{\nu}_4\nu_3}, \tag{4.59}$$

while for $M_\text{H} < m_{\nu_4}$ we define

$$\mathcal{M}^{\bar{\nu}_4\to\text{h}\bar{\nu}_3} = [\bar{v}_{\nu_4}\omega_\text{R} v_{\nu_3}]_h \mathcal{F}^{h\bar{\nu}_4\nu_3}, \qquad \mathcal{M}^{\bar{\nu}_4\to\text{H}\bar{\nu}_3} = [\bar{v}_{\nu_4}\omega_\text{R} v_{\nu_3}]_H \mathcal{F}^{H\bar{\nu}_4\nu_3}, \tag{4.60}$$

where the respective formfactors are formally identical in the two cases. Note that in our notation the labels of the formfactors denote incoming fields. Here we made us of the right-handed chiral projection operator $\omega_\text{R} = \frac{1}{2}(1+\gamma_5)$, $\bar{u}_{\nu_4}, v_{\nu_3}$ and $\bar{v}_{\nu_4}, v_{\nu_3}$ denote the spinors of the respective fermions, and $[\dots]_{h/H}$ indicate the respective decay kinematics. Similarly to the previous case, the ratio of the two formfactors at LO only depends on the parameter α, and as renormalization condition, we demand the higher-order corrections to the ratio of their real parts to vanish

$$\frac{\text{Re}\,\mathcal{F}^{h\bar{\nu}_4\nu_3}_\text{NLO}}{\text{Re}\,\mathcal{F}^{H\bar{\nu}_4\nu_3}_\text{NLO}} \stackrel{!}{=} \frac{\mathcal{F}^{h\bar{\nu}_4\nu_3}_\text{LO}}{\mathcal{F}^{H\bar{\nu}_4\nu_3}_\text{LO}} = -\frac{s_\alpha}{c_\alpha}. \tag{4.61}$$

At NLO the formfactors are given by

$$\begin{aligned}
\mathcal{F}^{h\bar{\nu}_4\nu_3}_\text{NLO} &= \mathcal{F}^{h\bar{\nu}_4\nu_3}_\text{LO}\Bigg[1 + \frac{\delta s_\alpha}{s_\alpha} + \frac{\delta c_{\theta_\text{r}}}{c_{\theta_\text{r}}} + \frac{\delta\tilde{y}}{\tilde{y}} - \frac{\delta v_1}{v_1} \\
&\qquad + \frac{1}{2}\left(\delta Z^{\nu,\text{R}}_{33} + \delta Z^{\nu,\text{L}}_{44} + \delta Z_{hh} - \frac{c_\alpha}{s_\alpha}\delta Z_{Hh} + \frac{s_{\theta_\text{r}}}{c_{\theta_\text{r}}}\delta Z^{\nu,\text{R}}_{43}\right) + \delta^{h\bar{\nu}_4\nu_3}_\text{loop}\Bigg], \\
\mathcal{F}^{H\bar{\nu}_4\nu_3}_\text{NLO} &= \mathcal{F}^{H\bar{\nu}_4\nu_3}_\text{LO}\Bigg[1 + \frac{\delta c_\alpha}{c_\alpha} + \frac{\delta c_{\theta_\text{r}}}{c_{\theta_\text{r}}} + \frac{\delta\tilde{y}}{\tilde{y}} - \frac{\delta v_1}{v_1} \\
&\qquad + \frac{1}{2}\left(\delta Z^{\nu,\text{L}}_{44} + \delta Z^{\nu,\text{R}}_{33} + \delta Z_{HH} - \frac{s_\alpha}{c_\alpha}\delta Z_{hH} + \frac{s_{\theta_\text{r}}}{c_{\theta_\text{r}}}\delta Z^{\nu,\text{R}}_{43}\right) + \delta^{H\bar{\nu}_4\nu_3}_\text{loop}\Bigg],
\end{aligned} \tag{4.62}$$

with the unrenormalized relative 1-loop corrections to the decays $\delta^{h/H\bar{\nu}_4\nu_3}_\text{loop}$, respectively. Evaluating the renormalization condition Eq. (4.61) with the help of Eq. (4.62), and making use of $\delta s_\alpha = c_\alpha \delta\alpha$ yields

[7] Recall that in the here considered "collider approximation", we find $m_{\nu_3} = 0$. Further note that for non-vanishing neutrino masses m_{ν_i}, $i = 1,2,3$, the full renormalization of the neutrino sector is way more involved. However, this is neither needed nor of further interest in this work.

$$\delta\alpha_{\mathrm{OS2}} = \frac{1}{2}c_\alpha s_\alpha \left(\delta Z_{HH} - \delta Z_{hh}\right) + \frac{1}{2}\left(c_\alpha^2 \delta Z_{Hh} - s_\alpha^2 \delta Z_{hH}\right) + c_\alpha s_\alpha \mathrm{Re}\left[\delta_{\mathrm{loop}}^{H\bar{\nu}_4\nu_3} - \delta_{\mathrm{loop}}^{h\bar{\nu}_4\nu_3}\right], \tag{4.63}$$

for the Higgs mixing-angle renormalization constant $\delta\alpha_{\mathrm{OS2}}$ obtained via the OS renormalization condition Eq. (4.61).
While both proposed OS renormalizations are process dependent, as can be seen by the non-vanishing higher-order contributions $\delta_{\mathrm{loop}}^{h\bar{\nu}_4\nu_j}$ and $\delta_{\mathrm{loop}}^{H\bar{\nu}_4\nu_j}$, $j = 3, 4$, in Eqs. (4.58) and (4.63), respectively, they have various other desirable features:

- Both are based on S-matrix elements and, thus, the resulting renormalization constants are gauge independent.
- They are symmetric in the fields h and H.
- Both OS renormalization constants $\delta\alpha_{\mathrm{OS}i}$, $i = 1, 2$, have smooth limits for extreme values of α, i.e. $s_\alpha \to 0$, $c_\alpha \to 0$.
- The renormalization constants $\delta\alpha_{\mathrm{OS}i}$ are designed in such a way that predictions in the degeneracy limit $M_{\mathrm{H}} \to M_{\mathrm{h}}$ are numerically stable. This can be seen by a similar argument as given above for the renormalization process of γ and is explicitly shown[8] in Ref. [81].

As a process-independent alternative $\overline{\mathrm{MS}}$ renormalization can be employed for α. The respective $\overline{\mathrm{MS}}$ renormalization constant can, e.g., be obtained by keeping only the terms of Eq. (4.58) or Eq. (4.63) that are proportional to the standard 1-loop UV divergence of dimensional regularization, i.e.

$$\delta\alpha_{\overline{\mathrm{MS}}} = \delta\alpha_{\mathrm{OS1}}\Big|_{\mathrm{UV}} = \delta\alpha_{\mathrm{OS2}}\Big|_{\mathrm{UV}}. \tag{4.64}$$

We give the explicit expression for $\delta\alpha_{\overline{\mathrm{MS}}}$ in the PRTS in Appendix D. Note that the process-independent $\delta\alpha_{\overline{\mathrm{MS}}}$ is independent of any mass hierarchy of the particles. While the tadpole contributions in full OS schemes cancel in predictions of observables this is not true if parameters related to masses are renormalized via $\overline{\mathrm{MS}}$ renormalization conditions. In general, $\delta\alpha$ depends on the tadpole treatment and the explicit tadpole contributions to $\delta\alpha_{\overline{\mathrm{MS}}}$ in the three tadpole schemes introduced in Sect. 4.2.1 read

$$\delta\alpha_{\overline{\mathrm{MS}},\mathrm{tad}}^{\mathrm{PRTS}} = 0, \tag{4.65}$$

$$\delta\alpha_{\overline{\mathrm{MS}},\mathrm{tad}}^{\mathrm{FJTS}} = -2\frac{c_{\mathrm{hhH}}\Delta v_h^{\mathrm{FJTS}} + c_{\mathrm{hHH}}\Delta v_H^{\mathrm{FJTS}}}{M_{\mathrm{H}}^2 - M_{\mathrm{h}}^2}\Bigg|_{\mathrm{UV}}, \tag{4.66}$$

[8] Note that they investigate pure Higgs extensions, like the Singlet Extension of the SM, where it is even possible to construct process-independent renormalization constants. The presence of the higher-order contributions is, however, irrelevant for the numerical stability in the degeneracy limit.

$$\delta\alpha^{\text{GIVS}}_{\overline{\text{MS}},\text{tad}} = -2\frac{c_{\text{hhH}}\Delta v_h^{\text{GIVS}} + c_{\text{hHH}}\Delta v_H^{\text{GIVS}}}{M_{\text{H}}^2 - M_{\text{h}}^2}\bigg|_{\text{UV}}, \tag{4.67}$$

with the scalar self-coupling constants c_{hhH} and c_{hHH} given in Eqs. (3.31) and (3.32). As discussed in Sect. 4.2.1, the tadpole counterterms enter in the relations between the original bare parameters of the Higgs sector and the chosen set of (bare) input parameters. Thus, the latter depend on the tadpole treatment. Explicitly, the bare mixing angles in the PRTS, α_0^{PRTS}, and FJTS, α_0^{FJTS}, are connected via

$$\alpha_0^{\text{PRTS}} = \alpha_0^{\text{FJTS}} - \frac{2}{M_{\text{H}}^2 - M_{\text{h}}^2}\left(c_{\text{hhH}}\frac{\delta t_h^{\text{FJTS}}}{M_{\text{h}}^2} + c_{\text{hHH}}\frac{\delta t_H^{\text{FJTS}}}{M_{\text{H}}^2}\right). \tag{4.68}$$

Combining this with Eqs. (4.65) and (4.66) leads to

$$\begin{aligned}\alpha^{\text{PRTS}}_{\overline{\text{MS}}} - \alpha^{\text{FJTS}}_{\overline{\text{MS}}} &= \alpha_0^{\text{PRTS}} - \alpha_0^{\text{FJTS}} - \left(\delta\alpha^{\text{PRTS}}_{\overline{\text{MS}}} - \delta\alpha^{\text{FJTS}}_{\overline{\text{MS}}}\right) \\ &= \frac{2}{M_{\text{H}}^2 - M_{\text{h}}^2}\left(c_{\text{hhH}}\frac{T^h}{M_{\text{h}}^2} + c_{\text{hHH}}\frac{T^H}{M_{\text{H}}^2}\right)\bigg|_{\text{finite}},\end{aligned} \tag{4.69}$$

representing a gauge-dependent shift between the values of the $\overline{\text{MS}}$-renormalized mixing angle in the two schemes. Similarly, one finds for the relation between the values of the $\overline{\text{MS}}$-renormalized Higgs mixing angle in the FJTS and the GIVS the gauge-independent shift

$$\alpha^{\text{GIVS}}_{\overline{\text{MS}}} - \alpha^{\text{FJTS}}_{\overline{\text{MS}}} = \frac{2}{M_{\text{H}}^2 - M_{\text{h}}^2}\left(c_{\text{hhH}}\frac{T^h_{\text{nl}}}{M_{\text{h}}^2} + c_{\text{hHH}}\frac{T^H_{\text{nl}}}{M_{\text{H}}^2}\right)\bigg|_{\text{finite}}. \tag{4.70}$$

Note that predictions based on an $\overline{\text{MS}}$ renormalized α are in general not stable in the limit $M_{\text{H}} \to M_{\text{h}}$.

4.2.3.3. Renormalization of the fermion mixing angle θ_{r}

The OS renormalization of the mixing angle in the fermion sector closely follows the renormalization procedure for the gauge and Higgs mixing angles presented in the previous two sections. Similarly to the case of the Higgs mixing angle α no fully process-independent OS renormalization for θ_{r} is possible. In the following, we give two possible OS renormalization conditions for the mixing angle θ_{r} as well as the result for its $\overline{\text{MS}}$ renormalization.
For the first OS renormalization condition we assume the mass hierarchy $M_{\text{H}} > 2m_{\nu_4}$ and make use of the OS formfactors of the decays $\text{H} \to \bar{\nu}_4\nu_4$ and $\text{H} \to \bar{\nu}_3\nu_4$ defined by

$$\mathcal{M}^{\text{H}\to\bar{\nu}_4\nu_4} = [\bar{u}_{\nu_4} v_{\nu_4}]_H \mathcal{F}^{H\bar{\nu}_4\nu_4}, \quad \mathcal{M}^{\text{H}\to\bar{\nu}_3\nu_4} = [\bar{u}_{\nu_4}\omega_{\text{R}} v_{\nu_3}]_H \mathcal{F}^{H\bar{\nu}_4\nu_3}, \tag{4.71}$$

where the spinors of the final-state fermions are given by $\bar{u}_{\nu_4}$ and v_j, $j = \nu_3, \nu_4$, $\omega_{\text{R}} = \frac{1}{2}(1+\gamma_5)$ is the right-handed chiral projection operator, and $[\dots]_H$ denotes

the kinematics of the decay. The respective OS renormalization condition is defined by demanding the NLO corrections to the ratio of the real parts of the NLO formfactors to vanish

$$\frac{\mathrm{Re}\,\mathcal{F}^{H\bar{\nu}_4\nu_4}_{\mathrm{NLO}}}{\mathrm{Re}\,\mathcal{F}^{H\bar{\nu}_4\nu_3}_{\mathrm{NLO}}} \stackrel{!}{=} \frac{\mathcal{F}^{H\bar{\nu}_4\nu_4}_{\mathrm{LO}}}{\mathcal{F}^{H\bar{\nu}_4\nu_3}_{\mathrm{LO}}} = \frac{s_{\theta_\mathrm{r}}}{c_{\theta_\mathrm{r}}}. \tag{4.72}$$

Note that this ratio is especially well suited for the renormalization of the fermion mixing angle, since it does not depend on any other parameter but θ_r. The explicit decompositions of $\mathcal{F}^{H\bar{\nu}_4\nu_4}_{\mathrm{NLO}}$ and $\mathcal{F}^{H\bar{\nu}_4\nu_3}_{\mathrm{NLO}}$ are given by Eqs. (4.55) and (4.62), respectively, and yield

$$\begin{aligned}\frac{\mathrm{Re}\,\mathcal{F}^{H\bar{\nu}_4\nu_4}_{\mathrm{NLO}}}{\mathrm{Re}\,\mathcal{F}^{H\bar{\nu}_4\nu_3}_{\mathrm{NLO}}} = \frac{s_{\theta_\mathrm{r}}}{c_{\theta_\mathrm{r}}}\Bigg\{1 + \frac{\delta s_{\theta_\mathrm{r}}}{s_{\theta_\mathrm{r}}} - \frac{\delta c_{\theta_\mathrm{r}}}{c_{\theta_\mathrm{r}}} + \frac{1}{2}\left[\delta Z^{\nu,\mathrm{R}}_{44} - \delta Z^{\nu,\mathrm{R}}_{33} + \frac{c_{\theta_\mathrm{r}}}{s_{\theta_\mathrm{r}}}\delta Z^{\nu,\mathrm{R}}_{34} - \frac{s_{\theta_\mathrm{r}}}{c_{\theta_\mathrm{r}}}\delta Z^{\nu,\mathrm{R}}_{43}\right] \\ + \mathrm{Re}\left[\delta^{H\bar{\nu}_4\nu_4}_{\mathrm{loop}} - \delta^{H\bar{\nu}_4\nu_3}_{\mathrm{loop}}\right]\Bigg\}.\end{aligned} \tag{4.73}$$

Combining this with the OS renormalization condition Eq. (4.72) one finds

$$\begin{aligned}\delta\theta^{\mathrm{H}}_{\mathrm{r,OS}} = \frac{1}{2}c_{\theta_\mathrm{r}}s_{\theta_\mathrm{r}}\left(\delta Z^{\nu,\mathrm{R}}_{33} - \delta Z^{\nu,\mathrm{R}}_{44}\right) + \frac{1}{2}\left(s^2_{\theta_\mathrm{r}}\delta Z^{\nu,\mathrm{R}}_{43} - c^2_{\theta_\mathrm{r}}\delta Z^{\nu,\mathrm{R}}_{34}\right) \\ + c_{\theta_\mathrm{r}}s_{\theta_\mathrm{r}}\mathrm{Re}\left[\delta^{H\bar{\nu}_4\nu_3}_{\mathrm{loop}} - \delta^{H\bar{\nu}_4\nu_4}_{\mathrm{loop}}\right],\end{aligned} \tag{4.74}$$

where we used $\delta s_{\theta_\mathrm{r}} = c_{\theta_\mathrm{r}}\delta\theta_\mathrm{r}$.
As an alternative to Eq. (4.74), we briefly sketch a second OS renormalization for θ_r making use of the OS formfactors $\mathcal{F}^{Z'\bar{\nu}^{\mathrm{R}}_3\nu^{\mathrm{R}}_3}$ and $\mathcal{F}^{Z'\bar{\nu}_4\nu_3}_1$ defined by the decays $\mathrm{Z}' \to \bar{\nu}^{\mathrm{R}}_3\nu^{\mathrm{R}}_3$ and $\mathrm{Z}' \to \bar{\nu}_3\nu_4$ via

$$\mathcal{M}^{\mathrm{Z}'\to\bar{\nu}^{\mathrm{R}}_3\nu^{\mathrm{R}}_3} = [\bar{u}_{\nu_3}\not{\varepsilon}\omega_\mathrm{R}v_{\nu_3}]_{Z'}\,\mathcal{F}^{Z'\bar{\nu}^{\mathrm{R}}_3\nu^{\mathrm{R}}_3}, \tag{4.75}$$

$$\mathcal{M}^{\mathrm{Z}'\to\bar{\nu}_3\nu_4} = [\bar{u}_{\nu_4}\not{\varepsilon}\omega_\mathrm{R}v_{\nu_3}]_{Z'}\,\mathcal{F}^{Z'\bar{\nu}_4\nu_3}_1 + [\bar{u}_{\nu_4}\omega_\mathrm{R}v_{\nu_3}]_{Z'}\left(\varepsilon_\mu p^\mu_{\nu_3}\right)\mathcal{F}^{Z'\bar{\nu}_4\nu_3}_2, \tag{4.76}$$

where the spinors of the final-state fermions are represented by $\bar{u}_{\nu_j}$ and v_{ν_3}, $j = 3, 4$, ε_μ is the polarization vector of the Z′ boson, and $\omega_\mathrm{R} = \frac{1}{2}(1+\gamma_5)$ is the right-handed chirality projector. Further, p_{ν_3} is the momentum of the neutrino ν_3 and the decay kinematics are denoted by $[\ldots]_{Z'}$. Here we want to stress that in the $\mathrm{Z}' \to \bar{\nu}_3\nu_4$ decay an additional, loop-induced, formfactor $\mathcal{F}^{Z'\bar{\nu}_4\nu_3}_2$ appears at NLO. However, due to the unique decomposition of the matrix element into different covariants spanning the underlying Z′-truncated Green function, we can formulate the OS renormalization conditions by only using $\mathcal{F}^{Z'\bar{\nu}_4\nu_3}_1$.
With these formfactors we can now define a second, alternative OS renormalization condition for θ_r. To this end, we demand, similarly to Eq. (4.72), that the higher-order corrections to the ratio of the real parts of the respective NLO formfactors

$$\frac{\mathrm{Re}\,\mathcal{F}^{Z'\bar{\nu}^{\mathrm{R}}_3\nu^{\mathrm{R}}_3}_{\mathrm{NLO}}}{\mathrm{Re}\,\mathcal{F}^{Z'\bar{\nu}_4\nu_3}_{1,\mathrm{NLO}}} \stackrel{!}{=} \frac{\mathcal{F}^{Z'\bar{\nu}^{\mathrm{R}}_3\nu^{\mathrm{R}}_3}_{\mathrm{LO}}}{\mathcal{F}^{Z'\bar{\nu}_4\nu_3}_{1,\mathrm{LO}}} = -\frac{s_{\theta_\mathrm{r}}}{c_{\theta_\mathrm{r}}}, \tag{4.77}$$

vanish. Even though the $\mathrm{Z}' \to \bar{\nu}_3 \nu_4$ decay requires the mass hierarchy $M_{\mathrm{Z}'} > m_{\nu_4}$, for $M_{\mathrm{Z}'} < m_{\nu_4}$, we can simply switch from the $\mathrm{Z}' \to \bar{\nu}_3 \nu_4$ decay to the $\nu_4 \to \mathrm{Z}' \nu_3$ decay in Eq. (4.77) to cover the whole parameter space (within our collider approximation where $m_{\nu_3} = 0$), without changing the formal result of the renormalization constant $\delta\theta^{\mathrm{Z}'}_{\mathrm{r,OS}}$. Following the same recipe as given above for the derivation of $\delta\theta^{\mathrm{H}}_{\mathrm{r,OS}}$, leads to

$$\begin{aligned}\delta\theta^{\mathrm{Z}'}_{\mathrm{r,OS}} = \frac{1}{2} s_{\theta_\mathrm{r}} c_{\theta_\mathrm{r}} \left(\delta Z^{\nu,\mathrm{R}}_{44} - \delta Z^{\nu,\mathrm{R}}_{33}\right) + \frac{1}{2}\left(c^2_{\theta_\mathrm{r}} \delta Z^{\nu,\mathrm{R}}_{43} - s^2_{\theta_\mathrm{r}} \delta Z^{\nu,\mathrm{R}}_{34}\right) \\ + s_{\theta_\mathrm{r}} c_{\theta_\mathrm{r}} \mathrm{Re}\left[\delta^{Z'\nu_4\nu_3}_{\mathrm{loop}} - \delta^{Z'\nu_3\nu_3}_{\mathrm{loop}}\right], \end{aligned} \tag{4.78}$$

for the renormalization constant $\delta\theta^{\mathrm{Z}'}_{\mathrm{r,OS}}$ defined by Eq. (4.77). Here, $\delta^{Z'\nu_i\nu_3}_{\mathrm{loop}}$, $i = 3, 4$, denote the unrenormalized relative NLO contributions to the decays, respectively. While both presented OS renormalization schemes for θ_r are process dependent, they both incorporate several desirable features. Not only will predictions of observables in full OS renormalization schemes be independent of the tadpole treatment, but also both $\delta\theta^{\mathrm{H}}_{\mathrm{r,OS}}$ and $\delta\theta^{\mathrm{Z}'}_{\mathrm{r,OS}}$ are directly connected to S-matrix elements and, therefore, are gauge-independent combinations of quantum-field-theoretical quantities. Furthermore, they are well-behaved for exceptional values of θ_r, i.e. $s_{\theta_\mathrm{r}} \to 0$, $c_{\theta_\mathrm{r}} \to 0$.
As a process-independent alternative, $\overline{\mathrm{MS}}$ renormalization can be employed. The respective renormalization constant $\delta\theta_{\mathrm{r},\overline{\mathrm{MS}}}$ can be obtained by dropping all finite parts in either $\delta\theta^{\mathrm{H}}_{\mathrm{r,OS}}$ or $\delta\theta^{\mathrm{Z}'}_{\mathrm{r,OS}}$

$$\delta\theta_{\mathrm{r},\overline{\mathrm{MS}}} = \delta\theta^{\mathrm{H}}_{\mathrm{r,OS}}\Big|_{\mathrm{UV}} = \delta\theta^{\mathrm{Z}'}_{\mathrm{r,OS}}\Big|_{\mathrm{UV}}. \tag{4.79}$$

While this is true in any tadpole scheme, the renormalization of θ_r in general depends on the tadpole treatment. We give the explicit result for $\delta\theta_{\mathrm{r},\overline{\mathrm{MS}}}$ in the PRTS in Appendix D. Predictions of observables based on $\theta_{\mathrm{r},\overline{\mathrm{MS}}}$ in general depend on the tadpole treatment. The tadpole contributions to $\delta\theta_{\mathrm{r},\overline{\mathrm{MS}}}$ in the different schemes introduced in Sect. 4.2.1 are given by

$$\delta\theta^{\mathrm{PRTS}}_{\mathrm{r},\overline{\mathrm{MS}},\mathrm{tad}} = 0, \tag{4.80}$$

$$\delta\theta^{\mathrm{FJTS}}_{\mathrm{r},\overline{\mathrm{MS}},\mathrm{tad}} = \frac{1}{m_{\nu_4}} \left(c_{\mathrm{h}\bar{\nu}_4\nu_3} \Delta v^{\mathrm{FJTS}}_h + c_{\mathrm{H}\bar{\nu}_4\nu_3} \Delta v^{\mathrm{FJTS}}_H\right)\Big|_{\mathrm{UV}}, \tag{4.81}$$

$$\delta\theta^{\mathrm{GIVS}}_{\mathrm{r},\overline{\mathrm{MS}},\mathrm{tad}} = \frac{1}{m_{\nu_4}} \left(c_{\mathrm{h}\bar{\nu}_4\nu_3} \Delta v^{\mathrm{GIVS}}_h + c_{\mathrm{H}\bar{\nu}_4\nu_3} \Delta v^{\mathrm{GIVS}}_H\right)\Big|_{\mathrm{UV}}, \tag{4.82}$$

with the coupling constants

$$c_{\mathrm{h}\bar{\nu}_4\nu_3} = \frac{1}{v_1} s_\alpha s_{\theta_\mathrm{r}} c_{\theta_\mathrm{r}} m_{\nu_4}, \qquad c_{\mathrm{H}\bar{\nu}_4\nu_3} = -\frac{1}{v_1} c_\alpha s_{\theta_\mathrm{r}} c_{\theta_\mathrm{r}} m_{\nu_4}, \tag{4.83}$$

of the respective $c_{\mathrm{h}\bar{\nu}_4\nu_3} h\bar{\nu}_4\nu_3 + c_{\mathrm{H}\bar{\nu}_4\nu_3} H\bar{\nu}_4\nu_3$ terms in the Lagrangian. Similarly to the case for γ_0 and α_0 the definition of $\theta_{\mathrm{r},0}$ depends on the tadpole scheme. The relation between the bare mixing angles in the PRTS and the FJTS is given by

$$\theta_{\mathrm{r},0}^{\mathrm{PRTS}} = \theta_{\mathrm{r},0}^{\mathrm{FJTS}} + \frac{1}{m_{\nu_4}} \left(c_{\mathrm{h}\bar{\nu}_4\nu_3} \frac{\delta t_h^{\mathrm{FJTS}}}{M_{\mathrm{h}}^2} + c_{\mathrm{H}\bar{\nu}_4\nu_3} \frac{\delta t_H^{\mathrm{FJTS}}}{M_{\mathrm{H}}^2} \right), \tag{4.84}$$

leading, in combination with Eqs. (4.80) and (4.81), to the gauge-dependent shift

$$\begin{aligned} \theta_{\mathrm{r},\overline{\mathrm{MS}}}^{\mathrm{PRTS}} - \theta_{\mathrm{r},\overline{\mathrm{MS}}}^{\mathrm{FJTS}} &= \theta_{\mathrm{r},0}^{\mathrm{PRTS}} - \theta_{\mathrm{r},0}^{\mathrm{FJTS}} - \left(\delta\theta_{\mathrm{r},\overline{\mathrm{MS}}}^{\mathrm{PRTS}} - \delta\theta_{\mathrm{r},\overline{\mathrm{MS}}}^{\mathrm{FJTS}} \right) \\ &= -\frac{1}{m_{\nu_4}} \left(c_{\mathrm{h}\bar{\nu}_4\nu_3} \frac{T^h}{M_{\mathrm{h}}^2} + c_{\mathrm{H}\bar{\nu}_4\nu_3} \frac{T^H}{M_{\mathrm{H}}^2} \right) \Bigg|_{\mathrm{finite}}, \end{aligned} \tag{4.85}$$

between the values of the $\overline{\mathrm{MS}}$-renormalized mixing angles in the PRTS and FJTS. Similarly, a gauge-independent shift

$$\theta_{\mathrm{r},\overline{\mathrm{MS}}}^{\mathrm{GIVS}} - \theta_{\mathrm{r},\overline{\mathrm{MS}}}^{\mathrm{FJTS}} = -\frac{1}{m_{\nu_4}} \left(c_{\mathrm{h}\bar{\nu}_4\nu_3} \frac{T_{\mathrm{nl}}^h}{M_{\mathrm{h}}^2} + c_{\mathrm{H}\bar{\nu}_4\nu_3} \frac{T_{\mathrm{nl}}^H}{M_{\mathrm{H}}^2} \right) \Bigg|_{\mathrm{finite}}, \tag{4.86}$$

connects the renormalized mixing angles in the GIVS and FJTS.

4.2.4. Charge renormalization in the DASM

To complete the renormalization of the DASM, we need to define the renormalization of the electric unit charge. The electric unit charge is commonly defined via the low-energy photon–fermion interaction, i.e. via the $A\bar{f}f$-vertex for on-shell fermions f in the Thomson limit, i.e. in the limit of vanishing photon momentum. To derive the resulting charge renormalization constant, we follow the procedure presented in Ref. [84], which generalizes the OS charge renormalization in the SM to a wide range of BSM theories that include at least one $U(1)$ gauge symmetry[9], like the broken $U(1)_{\mathrm{Y}}$ representing the weak hypercharge in the SM and the DASM. In the following we make use of the all-order recipe given in Ref. [84] and briefly sketch the derivation of δZ_e in the DASM at NLO using our notation and conventions.

To start, we emphasize that higher-order corrections to the coupling strength of the photon to any charged particle—typically chosen to be fermions—in the Thomson limit do not depend on the specific properties (besides the charge) of the charged particle. This fact is commonly known as charge universality. This can, e.g., be proven via the background field method [51, 84–86], where the complexity of the electric-charge renormalization of the SM is greatly reduced. Taking charge universality as a starting point for our derivation of the NLO OS charge renormalization

[9] The proof relies on the freedom to choose the $U(1)$ gauge-group charge of any particle at will, since their charges turn out to be not quantized.

constant in the DASM, we introduce a second "fake fermion" field[10] κ to the theory. This fake fermion field carries an infinitesimal weak hypercharge $Y_{\mathrm{W},\kappa}$, but transforms as a singlet under the remaining gauge group of the DASM. This infinitesimal weak hypercharge leads to an infinitesimal electric charge $Q_\kappa = Y_{\mathrm{W},\kappa}/2$ (see Eq. (2.14)). To account for the presence of this fermion field, we have to add the most general renormalizable gauge-invariant Lagrangian that includes the fake fermion field

$$\begin{aligned}\mathcal{L}_\kappa &= \bar{\kappa}\left(\mathrm{i}\partial\!\!\!/ - \frac{Y_{\mathrm{w},\kappa}}{2} g_1 B\!\!\!/ - m_\kappa\right)\kappa \\ &= \bar{\kappa}\left\{\mathrm{i}\partial\!\!\!/ - eQ_\kappa\left[A\!\!\!/ + \frac{1}{c_\mathrm{w}}\left(\left(s_\mathrm{w}c_\gamma - \eta s_\gamma\right) Z\!\!\!/ - \left(s_\mathrm{w}s_\gamma + \eta c_\gamma\right) Z\!\!\!/'\right)\right] - m_\kappa\right\}\kappa, \quad (4.87)\end{aligned}$$

to the Lagrangian of the DASM. The first term in the upper line represents the kinetic term of the fermion field, the second term represents its gauge interaction with the neutral gauge fields (see also second line), and the last term represents a possible Dirac mass term (present since κ is non-chiral). Note that the infinitesimal hypercharge does not allow for any Yukawa-type interactions between κ and the scalar bosons of the DASM.
From Eq. (4.87) it is obvious that the resulting Feynman rules for the $V\bar{\kappa}\kappa$, $V = A, Z, Z'$, vertices are proportional to the charge Q_κ of the fake fermion κ. Thus, taking the limit $Q_\kappa \to 0$ (or equivalently $Y_{\mathrm{W},\kappa} \to 0$) will decouple κ completely from the theory and the DASM is recovered. As discussed above, charge universality implies that any charged particle can be used to derive the renormalization constant of the electric unit charge and restore its low-energy interpretation. Thus, we define the charge renormalization constant in the DASM by demanding that all higher-order corrections to the $A\bar{\kappa}\kappa$ vertex vanish in the Thomson limit. This means that the respective NLO renormalized vertex function recovers its LO result, i.e.

$$\bar{u}(p)\Gamma^{A\bar{\kappa}\kappa}_{\mathrm{R},\mu}(0,-p,p)u(p)\bigg|_{p^2=m_\kappa^2} = -Q_\kappa e\,\bar{u}(p)\gamma_\mu u(p), \quad (4.88)$$

with the renormalized on-shell mass of the fake fermion m_κ. Further decomposing this NLO renormalized vertex function in terms of unrenormalized quantities as well as renormalization constants leads to

$$\begin{aligned}\Gamma^{A\bar{\kappa}\kappa}_{\mathrm{R},\mu}(k,\bar{p},p) = &\left(1 + \frac{1}{2}\delta Z_{AA} + \delta Z_\kappa + \delta Z_e\right)\Gamma^{A\bar{\kappa}\kappa}_{\mathrm{LO},\mu}(k,\bar{p},p) + Q_\kappa \Lambda^{A\bar{\kappa}\kappa}_\mu(k,\bar{p},p) \\ &+ \frac{1}{2}\delta Z_{ZA}\Gamma^{Z\bar{\kappa}\kappa}_{\mathrm{LO},\mu}(k,\bar{p},p) + \frac{1}{2}\delta Z_{Z'A}\Gamma^{Z'\bar{\kappa}\kappa}_{\mathrm{LO},\mu}(k,\bar{p},p), \quad (4.89)\end{aligned}$$

[10] Note that we only change the name of the fake fermion from η, used in the respective discussion in Ref. [84], to κ here, to avoid confusion with the parameter η introduced in Eq. (3.56).

where the LO vertex functions in the DASM are given by

$$\Gamma^{A\bar{\kappa}\kappa}_{\mathrm{LO},\mu}(k,\bar{p},p) = -Q_\kappa e\gamma_\mu, \tag{4.90}$$

$$\Gamma^{Z\bar{\kappa}\kappa}_{\mathrm{LO},\mu}(k,\bar{p},p) = -Q_\kappa \frac{e}{c_\mathrm{w}}\left(s_\mathrm{w}c_\gamma - \eta s_\gamma\right), \tag{4.91}$$

$$\Gamma^{Z'\bar{\kappa}\kappa}_{\mathrm{LO},\mu}(k,\bar{p},p) = Q_\kappa \frac{e}{c_\mathrm{w}}\left(s_\mathrm{w}s_\gamma + \eta c_\gamma\right). \tag{4.92}$$

Here, $\Lambda^{A\bar{\kappa}\kappa}_\mu(k,\bar{p},p)$ represents the unrenormalized vertex corrections and δZ_κ is the OS field renormalization constant for κ. Since all couplings of the fake fermion to any particles of the DASM scale with Q_κ it is obvious that

$$\delta Z_\kappa = \mathcal{O}\left(Q_\kappa^2\right), \qquad \Lambda^{A\bar{\kappa}\kappa}_\mu(k,\bar{p},p) = \mathcal{O}\left(Q_\kappa^2\right). \tag{4.93}$$

Thus, taking the limit $Q_\kappa \to 0$ and keeping only terms linear in Q_κ in Eq. (4.89), the renormalization condition Eq. (4.88) leads to

$$0 = \left[\delta Z_e + \frac{1}{2}\delta Z_{AA} + \frac{1}{2c_\mathrm{w}}\Big\{\left(s_\mathrm{w}c_\gamma - \eta s_\gamma\right)\delta Z_{ZA} - \left(s_\mathrm{w}s_\gamma + \eta c_\gamma\right)\delta Z_{Z'A}\Big\}\right]\bar{u}(p)\gamma_\mu u(p). \tag{4.94}$$

This further yields

$$\delta Z_e = -\frac{1}{2}\left[\delta Z_{AA} + \frac{s_\mathrm{w}c_\gamma - \eta s_\gamma}{c_\mathrm{w}}\delta Z_{ZA} - \frac{s_\mathrm{w}s_\gamma + \eta c_\gamma}{c_\mathrm{w}}\delta Z_{Z'A}\right], \tag{4.95}$$

for the OS charge renormalization constant in the DASM. Note that, as expected by charge universality, δZ_e is independent of any specific properties of κ, but only depends on gauge-boson self-energies. Furthermore, the well-known SM result (see e.g. Refs. [51, 54]) is recovered by taking the respective SM limit $\gamma \to 0$ (which implies $\eta \to 0$).

5. Confrontation of the DASM with precision data

After setting up the DASM as well as corresponding OS and $\overline{\text{MS}}$ renormalization schemes in the previous two chapters, we are now ready to test its predictive power. Therefore, we perform a first phenomenological study of the DASM in this chapter. After introducing the input-parameter scheme used in the following calculations in Sect. 5.1 and the computational setup implemented for the numerical evaluations in Sect. 5.2, we define two different renormalization schemes in Sect. 5.3 that are used for the following calculations. In Sect. 5.4, we derive 1-loop BSM effects and combine them with their respective state-of-the-art SM predictions to obtain even more precise predictions for several precision observables (POs) within the DASM.
Higgs singlet extensions, introducing scalar sector extensions to the SM that are similar to the extended Higgs sector within the DASM, are already discussed in the literature in quite some detail, and several analyses (see e.g. Refs [16,87] and references therein) on their phenomenological implications have been performed. Thus, we mainly focus on the gauge-sector extension of the DASM in the phenomenological analysis presented in this work. We investigate four EW POs, namely the W-boson mass, derived from muon decay, the anomalous magnetic moment of the muon $(g-2)_\mu$, the leptonic partial decay width of the Z boson, and the leptonic effective weak mixing angle. In Sect. 5.4, we give the theoretical setup of these POs in the DASM as well as explicit results for interesting intermediate steps in their derivations. Further, this section includes a detailed discussion of the dependences of each of the predictions for these POs on the BSM parameters introduced by the DASM. This is done for both renormalization schemes defined in Sect. 5.3, and interesting differences between the results of the two respective renormalization schemes are discussed in detail.
In the last part of this chapter (see Sect. 5.5), we perform a global fit to find the BSM parameter values that minimize the tension between all investigated PO predictions in the DASM and measurements. Trying to be as general as possible, we include the possibilities for the Z' boson and the BSM Higgs boson to be heavier or lighter than their respective SM counterparts. To account for parametric un-

certainties of our predictions, we also take some SM-like parameters as free input parameters in the fit. Treating them similar to the POs described above, they are constrained by their respective measured values via additional contributions to the investigated χ^2 function (see Sect. 5.5.1.1 for more details).

5.1. Input-parameter scheme

In order to perform precision calculations in any QFT, a consistent set of input parameters is of uttermost importance to ensure the consistency of the results. A careless change of the set of input parameters or their respective values within a calculation could not only break gauge invariance (if it is done in gauge-dependent subparts of the calculation), but also destroy the cancellation of UV or infrared divergences, rendering the result meaningless. In contrast, a good choice of the set of input parameters will incorporate well-defined and precisely measured parameters which minimize the parametric uncertainties in theory predictions. For the DASM, we chose Eq. (3.117) as intuitive input-parameter set and formulated renormalization schemes based on these input parameters in the previous chapter. It is common to define the electromagnetic coupling constant

$$\alpha_{\text{em}} = \frac{e^2}{4\pi} \tag{5.1}$$

from the electric unit charge. In the following discussion, we closely follow the arguments of Ref. [54]. Depending on the quantities investigated in EW calculations, one of three different input-parameter schemes is commonly used for the electromagnetic coupling constant, to further improve the precision of predictions: the first scheme employs the fine-structure constant $\alpha_{\text{em}}(0)$, representing the electric unit charge in the Thomson limit (see Sect. 4.2.4); the second scheme uses $\alpha(M_{\text{Z}}^2)$, where the renormalization group equation is used to evolve the running electromagnetic coupling constant from $\alpha_{\text{em}}(Q^2 = 0)$ to $\alpha_{\text{em}}(Q^2 = M_{\text{Z}}^2)$, where Q denotes the energy scale where the running electromagnetic coupling constant $\alpha_{\text{em}}(Q^2)$ is evaluated; and as a third option, one can use the so-called G_μ-scheme, where the very precisely known Fermi constant G_μ is used to derive an effective value α_{G_μ} for the electromagnetic coupling α_{em} using muon decay. While the fine-structure constant $\alpha_{\text{em}}(0)$ can be used straightforwardly with our choice of charge renormalization, the two latter schemes need some further explanations. At $Q^2 = M_{\text{Z}}^2$, the running electromagnetic coupling constant is given by

$$\alpha_{\text{em}}(M_{\text{Z}}^2) = \frac{\alpha_{\text{em}}(0)}{1 - \Delta\alpha_{\text{em}}}. \tag{5.2}$$

It allows us to resum the large logarithms of light-fermion masses appearing in the charge renormalization constant δZ_e, via the so-called vacuum polarization $\Delta\alpha_{\text{em}}$ (see Eq. (5.22) for the explicit definition). These logarithms of the light-fermion

masses can lead to numerical instabilities as well as large higher-order corrections. Additionally, it can be used to drastically reduce uncertainties of predictions, originating from the appearance of light-quark masses. From a practical point of view, one can introduce the $\alpha(M_{\mathrm{Z}}^2)$-scheme by substituting

$$\alpha_{\mathrm{em}}(0) \to \alpha_{\mathrm{em}}(M_{\mathrm{Z}}^2), \qquad \delta Z_e \to \delta Z_e|_{\alpha_{\mathrm{em}}(M_{\mathrm{Z}}^2)} = \delta Z_e - \frac{1}{2}\Delta\alpha_{\mathrm{em}}, \tag{5.3}$$

where δZ_e is the charge renormalization constant defined in the Thomson limit (see Eq. (4.95)). The last term in Eq. (5.3) has to be introduced to avoid double counting of any corrections introduced by the first replacement of Eq. (5.3). For further details on the $\alpha(M_{\mathrm{Z}}^2)$-scheme we refer the reader to Sect. 5.4.1 (and references therein), where we use muon decay to eliminate the W-boson mass from our input-parameter scheme in favour of G_μ. In the G_μ-scheme the electromagnetic coupling constant is connected to the Fermi constant via muon decay, yielding at NLO

$$\alpha_{G_\mu} = \frac{\sqrt{2}G_\mu s_{\mathrm{w}}^2 M_{\mathrm{W}}^2}{\pi} = \alpha_{\mathrm{em}}(0)(1 + \Delta r_{\mathrm{NLO}}), \tag{5.4}$$

where Δr_{NLO} represents the NLO EW corrections to muon decay. The exact definition of Δr_{NLO} is given in Sect. 5.4.1 (see Eq. (5.16)), where we investigate the prediction for muon decay in the DASM at NLO in full detail. In general, the G_μ-scheme allows to largely absorb universal corrections originating from the renormalization of the weak mixing angle by introducing the precisely measured quantity G_μ. Thus, it can be used to greatly reduce the size of radiative corrections, especially for processes with W-boson couplings at LO. At NLO it can, e.g., be introduced in calculations via the replacements

$$\alpha_{\mathrm{em}}(0) \to \alpha_{G_\mu}, \qquad \delta Z_e \to \delta Z_e|_{\alpha_{G_\mu}} = \delta Z_e - \frac{1}{2}\Delta r_{\mathrm{NLO}}. \tag{5.5}$$

Equations (5.3) and (5.5) show that the choice of the input scheme for the electromagnetic coupling is merely a choice of the renormalization of the electric unit charge, differing only by the finite parts $\frac{1}{2}\Delta\alpha_{\mathrm{em}}$ and $\frac{1}{2}\Delta r_{\mathrm{NLO}}$, respectively. We want to emphasize that, in some calculations, it is possible to define gauge-invariant subsets of contributions that ultimately add up to the desired prediction. While one has to stick to one input-parameter scheme within these subsets, it is possible (and sometimes even desirable) to use different input schemes for different gauge-invariant subsets.

5.1.1. Input-parameter values and benchmark scenarios

With the discussion of the previous section in mind, we now define the explicit values for the SM-like input parameters used in the discussion of the dependence of the POs on the BSM parameters given below (see Sect. 5.4). We choose

$$(\alpha_{\mathrm{em}}(0))^{-1} = 137.035999180, \qquad G_\mu = 1.1663788 \cdot 10^{-5}\,\mathrm{GeV}^{-2},$$

$$\begin{aligned}
\Delta\alpha^{(5)}_{\text{had}} &= 0.02768, & \alpha_{\text{s}}(M_{\text{Z}}^2) &= 0.1179,\\
M_{\text{Z}} &= 91.1876\,\text{GeV}, & M_S &= 125.25\,\text{GeV},\\
m_{\text{e}} &= 0.51099895\cdot 10^{-3}\,\text{GeV}, & m_\mu &= 0.1056583755\,\text{GeV},\\
m_\tau &= 1.77686\,\text{GeV}, & m_{\text{u}} &= 0.1\,\text{GeV},\\
m_{\text{d}} &= 0.1\,\text{GeV}, & m_{\text{s}} &= 0.1\,\text{GeV},\\
m_{\text{c}} &= 1.27\,\text{GeV}, & m_{\text{b}} &= 4.18\,\text{GeV},\\
m_{\text{t}} &= 172.5\,\text{GeV}, & & \qquad (5.6)
\end{aligned}$$

closely following the recommendations of Ref. [16]. Here, S denotes the SM-like Higgs boson, which can either be h or H, depending on the investigated DASM scenario. Even though the W-boson mass M_{W} is part of our input-parameter set for the DASM defined in Eq. (3.117), we use the predicted value from muon decay derived in Sect. 5.4.1, as its input value in the calculation of all other POs, effectively trading it for the Fermi constant G_μ in our numerical input-parameter set. For our discussion of the parameter dependences of the investigated POs in Sect. 5.4, we further define the two benchmark scenarios

$$\begin{aligned}
\text{(i)}\quad & \gamma = 0.01,\ M_{\text{Z}'} = 50\,\text{GeV},\quad \alpha = 0.2,\ \lambda_{12}= 0.01,\ M_{\text{H}} = 500\,\text{GeV},\\
& \theta_{\text{r}} = 0.5,\quad m_{\nu_4} = 200\,\text{GeV}, \qquad (5.7)\\
\text{(ii)}\quad & \gamma = 0.01,\ M_{\text{Z}'} = 50\,\text{GeV},\quad \alpha' = 0.2,\ \lambda_{12}= 0.01,\ M_{\text{h}} = 30\,\text{GeV},\\
& \theta_{\text{r}} = 0.5,\quad m_{\nu_4} = 200\,\text{GeV}, \qquad (5.8)
\end{aligned}$$

for the BSM parameters of the DASM, which are, of course, only used for the parameters that are not varied in the respective plots. Here we defined $\alpha' = \frac{\pi}{2} - \alpha$ representing the "distance" to the SM limit in the case $M_{\text{H}} = M_{\text{h}}^{\text{SM}}$ (benchmark scenario (ii)), and the values given for $M_{h'}$, $h' = \text{h}, \text{H}$, is the mass of the non-SM-like Higgs boson, respectively. Note that the two benchmark points (5.7) and (5.8) are chosen such that they showcase the influence of the BSM parameters on the predictions of the investigated POs in the case of the new Higgs boson being heavier (scenario (i)) or lighter (scenario (ii)) than the observed SM-like Higgs boson.

5.1.2. Perturbativity constraints

All predictions for observables investigated in this work are based on a perturbation theory[1]. The respective expansion parameters[2] are the coupling constants g_2, g_1, and e_{d} of the gauge groups $SU(2)_{\text{W}}$, $U(1)_{\text{Y}}$, and $U(1)_{\text{d}}$, respectively, the coupling constants λ_1, λ_2, and λ_{12} introduced by the Higgs potential, and the Yukawa coupling constant y_ρ introduced in the fermion sector of the DASM. If the absolute

[1] For details see Appendix A and references therein.

[2] Note that we only explicitly list the respective expansion parameters that are critical for our analysis here.

value of any of these parameters becomes too large, the higher-order contributions to the perturbative series are no longer sufficiently suppressed, leading to a bad convergence behaviour of predictions, ultimately invalidating the perturbative approach. To ensure perturbativity of the theory, we constrain these parameters in our phenomenological analysis to some upper limit. For the new parameters introduced in the Higgs potential we demand that the absolute values of the coupling constants appearing in the respective Feynman rules of $h_i^2 h_j^2$, $i,j = 1,2$, interactions, resulting from the Higgs potential

$$V_{4S} = \lambda_1 h_1^4 + \frac{\lambda_2}{16} h_2^4 + \frac{\lambda_{12}}{2} h_1^2 h_2^2, \tag{5.9}$$

are in the interval $[0, 2\pi]$, i.e.

$$\frac{4!\,\lambda_1}{4\pi} \leq \frac{1}{2}, \qquad \frac{4!\,\lambda_2}{64\pi} \leq \frac{1}{2}, \qquad \frac{2!\,2!\,\lambda_{12}}{8\pi} \leq \frac{1}{2}. \tag{5.10}$$

Similarly, we demand the absolute value of the coupling constant y_ρ appearing in the respective Feynman rule for the $h_1 \bar{f}_{\mathrm{d}}^{\prime \mathrm{L}} \nu_3^{\mathrm{R}}$ vertex to be in the interval $\left[0, \sqrt{2\pi}\right]$, i.e. $\frac{y_\rho^2}{8\pi} \leq \frac{1}{2}$. Inspired by the typical parameter combinations Eq. (5.1) and $\alpha_{\mathrm{s}} = \frac{g_{\mathrm{s}}^2}{4\pi}$ used for the power counting of higher-order corrections, we demand $\alpha_i = \frac{g_i^2}{4\pi} \leq \frac{1}{2}$, $g_i = g_1, g_2, e_{\mathrm{d}}$, for the respective gauge-coupling strengths. In total, this leads to the additional constraints

$$g_2^2, g_1^2, e_{\mathrm{d}}^2 \leq 2\pi, \quad |\lambda_1| \leq \frac{\pi}{12}, \quad |\lambda_2| \leq \frac{4}{3}\pi, \quad |\lambda_{12}| \leq \pi, \quad y_\rho^2 \leq 4\pi, \tag{5.11}$$

for the respective coupling parameters of the DASM.

5.2. Computational setup

In high-energy physics, most calculations for quantum-field-theoretical quantities involve the evaluation of many Feynman diagrams. While for most 2-loop (and beyond) calculations, many needed results for loop integrals are still unknown, for 1-loop calculations a complete basis of standard integrals exists (see e.g. [79]), covering all integrals possibly appearing in the evaluation of 1-loop diagrams. However, simply due to the large amount of Feynman diagrams that need to be calculated already at 1-loop, especially in BSM theories, an automation of these calculations is inevitable for any precision calculation. To this end, we produced a FeynArts [88] model file for the DASM using the Mathematica [89] package FeynRules [90]. With the help of this model file, we use the Mathematica packages FeynArts and FormCalc to construct all needed Feynman diagrams and compute them in terms of standard integrals, respectively. The results of the POs presented in Sects. 5.4.1, 5.4.2, and 5.4.4–5.4.5 are checked against a second implementation (using FeynArts and FormCalc as well) using a second

model file created by Heidi Rzehak. To achieve the time efficiency of the numerical evaluation of these analytic expressions needed for the global fit (see Sect. 5.5), we export them in the form of C++ libraries. For the numerical evaluation of the appearing loop integrals, the results are linked to the Fortran library Collier [91–94], using the private code Linc [95]. Collier is particularly well suited for the computations occurring in BSM global fits since it is designed to be numerically stable even for extreme input parameter regions of the loop integrals. This C++ implementation was tested against results obtained using the Mathematica package LoopTools [96] for both FeynArts model files. Finally, the numerical results are used in our global fit routine, which makes use of the python interface *iminuit* [97] for the C++ library *Minuit2* [98] (see Sect. 5.5.2 for more details on the technical setup of the fit).

5.3. Definition of renormalization schemes

In Chapter 4, we have discussed the full renormalization of the DASM including OS as well as $\overline{\text{MS}}$ renormalization conditions for the renormalization constants of the entire DASM input-parameter set. Here, we define two complete renormalization schemes, an OS schemes and a hybrid scheme, which are then used in the following study of the phenomenology of the DASM.

5.3.1. OS scheme

For the OS scheme, we take OS renormalization conditions for the parameters and fields[3]. The OS mass and field renormalization constants are defined in Sect. 4.2.2 and the OS renormalization constant of the gauge-boson mixing angle γ is given in Eq. (4.40). All DASM predictions for the observables discussed in the following are independent of the renormalization conditions for the Higgs mixing angle α and the mixing angle θ_r of the fermion sector. Therefore, we either take Eq. (4.58) or Eq. (4.63), and Eq. (4.74) or Eq. (4.78) for $\delta\alpha_\text{OS}$ and $\delta\theta_\text{r,OS}$, respectively, to complete the definition of the OS scheme. This OS renormalization scheme incorporates all benefits of pure OS renormalization, like the independence of predictions on the tadpole treatment, the numerical stability in the case of degenerate masses of particles corresponding to mixing fields, etc., as already discussed in detail in Chapter 4.
However, it turns out that our definitions of the OS mixing angles can introduce so-called threshold effects to predictions in specific parameter regions[4]. These effects

[3] This excludes the renormalization of λ_{12}, where we only define an $\overline{\text{MS}}$ renormalization condition. However, all observables considered here are independent of the renormalization constant for λ_{12} at 1-loop level.

[4] For similar OS renormalization conditions for mixing angles of scalar BSM sectors, similar results were found by the authors of Ref. [99].

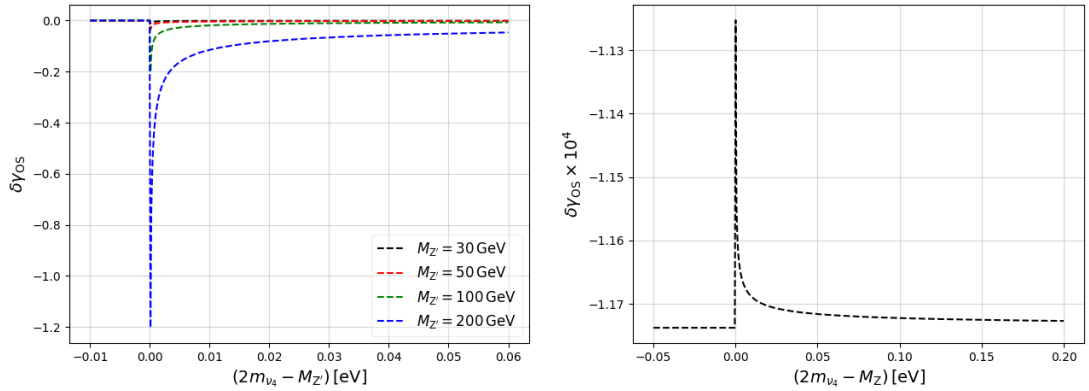

Figure 5.1.: The renormalization constant $\delta\gamma_{\mathrm{OS}}$ is shown, illustrating the appearance of threshold effects introduced, e.g., via the self-energy contributions of the Z′ and Z with a virtual ν_4 loop, in the vicinity of $M_{\mathrm{Z}'/\mathrm{Z}} = 2m_{\nu_4}$.

are non-physical artifacts of the OS scheme originating from neglecting the unstable nature of decaying particles. Including the respective width effects via, e.g., the so-called complex-mass scheme (see Refs. [54, 100–102]) can cure these non-physical threshold effects. The threshold effects enter, e.g., $\delta\gamma_{\mathrm{OS}}$, via self-energy diagrams (and their derivatives) introduced by the renormalization constants $\delta Z_{VV'}$, $V, V' = Z, Z'$. At the 1-loop level, they can appear whenever the invariant mass of the momentum is close to the sum of the two masses in the 1-loop bubble Feynman diagram. For illustration, we show the dependence of $\delta\gamma_{\mathrm{OS}}$ on m_{ν_4} in the vicinity of $M_{\mathrm{Z}'/\mathrm{Z}} = 2m_{\nu_4}$ in Fig. 5.1 using Eq. (5.6) for the SM-like input parameters and for the remaining BSM input parameters we use the values defined by benchmark scenario (5.7) as well as $\Delta_{\mathrm{UV}} = 0$, $\mu^2 = M_{\mathrm{Z}}^2$ for the standard 1-loop UV divergence and the reference scale μ of dimensional regularization (see Sect. C), respectively. Fig. 5.1 shows that $\delta\gamma_{\mathrm{OS}}$ develops a divergence at $M_{\mathrm{Z}'/\mathrm{Z}} = 2m_{\nu_4}$. However, the affected regions turn out to be very small compared to the overall magnitude of the respective masses[5]. Nevertheless, their size, in general, depends on the exact input parameter configuration. Therefore, we exclude these regions in our global fit performed in Sect. 5.5 to ensure that we obtain trustworthy results.

5.3.2. Hybrid scheme

In a second renormalization scheme, we take over the OS conditions for masses and fields, but use an $\overline{\mathrm{MS}}$ renormalization condition for the mixing angle γ. For the tadpole renormalization scheme, we choose the PRTS, which tends to lead

[5] In the discussion of the parameter dependence of the various investigated POs given below (see Sect. 5.4) the affected regions are often so small, that they are below the sample precision and, thus, cannot be seen in some plots at all.

to reasonably small higher-order corrections. In the following, this scheme is denoted as the hybrid scheme. In the hybrid scheme, the $\overline{\text{MS}}$ renormalization of γ introduces a dependence on the reference scale of dimensional regularization. We choose $\mu^2 = M_{\text{Z}}^2$ in all predictions shown in the following. While the hybrid scheme is not affected by any of the unphysical threshold effects introduced by $\delta\gamma_{\text{OS}}$ (see above), it has severe other downsides, like the large dependence on the treatment of the tadpoles or numerical instabilities for degenerate masses of the mixing particles (e.g. for $M_{\text{Z}'} \to M_{\text{Z}}$), etc., (see Sect. 4.2.3 for details).
We use the OS scheme, with all its desired features, as default renormalization scheme in the following discussions. However, the analyses presented in Sect. 5.4 and the minimization performed in Sect. 5.5 are done in both the OS and hybrid schemes, since a comparison of their respective results yields a good estimate for the theoretical uncertainty of the predictions. To account for the different definitions of the renormalized mixing angle in the two schemes, a proper parameter scheme conversion of γ is performed in these comparisons. To this end, we make use of their connection via the bare mixing angle γ_0,

$$\gamma_0 = \gamma_{\text{OS}} + \delta\gamma_{\text{OS}} = \gamma_{\overline{\text{MS}}} + \delta\gamma_{\overline{\text{MS}}}, \tag{5.12}$$

and find

$$\gamma_{\overline{\text{MS}}} = \gamma_{\text{OS}} + \Delta\delta\gamma, \qquad \Delta\delta\gamma = \delta\gamma_{\text{OS}} - \delta\gamma_{\overline{\text{MS}}}. \tag{5.13}$$

5.4. Selected precision observables in the DASM

In this section, we describe the theoretical definitions of the investigated POs and their derivation in the DASM at NLO. Assuming BSM effects to be small, for each PO we add SM corrections beyond NLO to the respective NLO DASM predictions to obtain the best possible DASM predictions. Further, we give a detailed discussion of the dependences on the new parameters introduced by the DASM extensions for each of the POs separately and discuss any interesting differences between the predictions in the OS and hybrid scheme (after proper scheme conversion of γ). The predictions derived in this section form the basis for the χ^2 function used in the global fit in Sect. 5.5 to find the input parameter values that lead to the least tension between DASM predictions and measurements.

5.4.1. M_{W} prediction from muon decay

As a first PO, we derive the prediction for the mass of the W boson from muon decay in the DASM. The high-precision measurement [103] of the lifetime of the muon τ_μ makes it a perfect observable to test the predictive power of the DASM. Further, considering the significant deviation of 7σ between the SM prediction and the most recent measurement of the CDF collaboration [7], it is certainly interesting—for any BSM model—to investigate whether a potential new physics

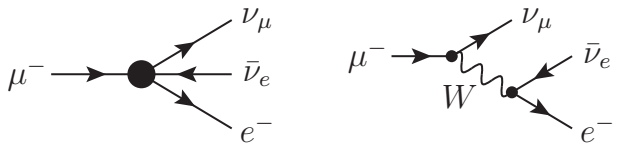

Figure 5.2.: The LO Feynman diagrams representing muon decay in the Fermi theory (left) and in the SM/DASM (right).

effect could explain such measured values, or at least loosen this tension. Note, however, that the CDF result is also at variance with the previous experimental world average, which is in reasonable agreement with its SM prediction [8]. Therefore, we investigate two scenarios in this section, using either the experimental world average or the CDF result, as measured values in our analysis.
Experimentally, τ_μ is used to determine the Fermi constant G_μ of the Fermi theory. Thus, we effectively compare the prediction for τ_μ in the Fermi theory, τ_μ^{F}, to the respective prediction in the DASM, τ_μ^{DASM}, to obtain our prediction for the W-boson mass. The Fermi theory is an effective field theory in which charged-current interactions are described by 4-fermion contact interactions. Figure 5.2 shows the LO diagrams describing muon decay in the Fermi theory (left) and in the DASM (right). At LO, neglecting relative contributions of $\mathcal{O}\left(\frac{m_\mu^2}{M_{\mathrm{W}}^2}\right)$ in the DASM, one finds the well-known results

$$\frac{1}{\tau_{\mu,\mathrm{LO}}^{\mathrm{F}}} = \frac{G_\mu^2 m_\mu^5}{192\pi^3}\left(1-\frac{8m_e^2}{m_\mu^2}\right), \quad \frac{1}{\tau_{\mu,\mathrm{LO}}^{\mathrm{DASM}}} = \frac{\alpha_{\mathrm{em}}^2}{384\pi}\frac{m_\mu^5}{M_{\mathrm{W}}^4 s_{\mathrm{w}}^4}\left(1-\frac{8m_e^2}{m_\mu^2}+\mathcal{O}\left(\frac{m_\mu^2}{M_{\mathrm{W}}^2}\right)\right), \tag{5.14}$$

for the prediction of the muon lifetime in the two models. A comparison of the two LO predictions yields

$$G_\mu = \frac{\alpha_{\mathrm{em}}\pi}{\sqrt{2}s_{\mathrm{w}}^2 M_{\mathrm{W}}^2} + \ldots, \tag{5.15}$$

where the "..." represent contributions of $\mathcal{O}\left(\frac{m_\mu^2}{M_{\mathrm{W}}^2}\right)$, connecting the W-boson mass M_{W} of the DASM with the precisely measured Fermi constant G_μ of the Fermi theory. Note that even though Eq. (5.15) has the same form as the respective equation for the SM, the appearance of s_{w} introduces a dependence on the BSM parameters γ and $M_{\mathrm{Z}'}$ of the DASM (see Eq. (3.57)) already at LO. To match the experimental precision, higher-order predictions for $\tau_\mu^{\mathrm{F/DASM}}$ are needed. At NLO, neglecting electron and muon masses throughout the calculation, Eq. (5.15) generalizes to

$$\begin{aligned} G_\mu &= \frac{\alpha_{\mathrm{em}}\pi}{\sqrt{2}s_{\mathrm{w}}^2 M_{\mathrm{W}}^2}\left(1+\Delta r\right) \\ &= \frac{\alpha_{\mathrm{em}}\pi}{\sqrt{2}s_{\mathrm{w}}^2 M_{\mathrm{W}}^2}\left(1+2\delta Z_e - \frac{\delta s_{\mathrm{w}}^2}{s_{\mathrm{w}}^2} - \frac{\delta M_{\mathrm{W}}^2}{M_{\mathrm{W}}^2} + \frac{\Sigma_{\mathrm{T}}^{WW}(0)}{M_{\mathrm{W}}^2} + \delta_{\mathrm{vert+box}}\right), \end{aligned} \tag{5.16}$$

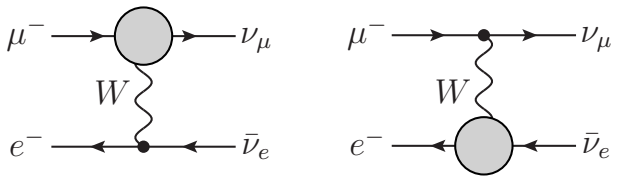

Figure 5.3.: Feynman diagrams contributing to the vertex corrections δ_{vertex} to muon decay. The grey blobs represent the renormalized vertex corrections at NLO.

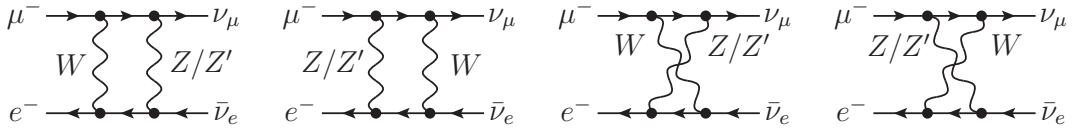

Figure 5.4.: Exchange of the massive Z, Z′, and W bosons between initial- and final-state particles in the DASM at NLO, leading to the box diagram contributions $\delta_{\text{box}}^{\text{massive}}$.

where Δr [104] denotes the relative NLO corrections to Eq. (5.15) originating from the NLO contributions to muon decay in the Fermi theory and the DASM. Further, we introduced

$$\delta_{\text{vert+box}} = \delta_{\text{vertex}} + \delta_{\text{box}}^{\text{massive}} + \delta_{\text{box}}^{\gamma\text{W}}, \tag{5.17}$$

denoting the relative NLO vertex corrections to the $W\mu\bar{\nu}_\mu$ and $W\nu_e e^+$ vertices in the DASM in δ_{vertex} (see Fig. 5.3), the relative corrections coming from massive box diagrams in $\delta_{\text{box}}^{\text{massive}}$ (see Fig. 5.4), and the QED corrections to both, the Fermi theory and the DASM predictions in $\delta_{\text{box}}^{\gamma\text{W}}$ (see Figs. 5.5 and 5.6).
Neglecting initial- and final-state masses, their contribution to Δr is given by

$$\begin{aligned}\delta_{\text{box}}^{\text{massive}} = \frac{\alpha_{\text{em}} M_{\text{W}}^2}{8\pi c_{\text{w}}^2 s_{\text{w}}^2} \Bigg[& \frac{\log \frac{M_{\text{Z}}^2}{M_{\text{W}}^2}}{M_{\text{Z}}^2 - M_{\text{W}}^2} \left(c_\gamma^2 \left(5 - 10 s_{\text{w}}^2 + 2 s_{\text{w}}^4 \right) + 6 s_{\text{w}}^3 \eta c_\gamma s_\gamma - 3 s_{\text{w}}^2 \eta^2 s_\gamma^2 \right) \\ & + \frac{\log \frac{M_{\text{Z}'}^2}{M_{\text{W}}^2}}{M_{\text{Z}'}^2 - M_{\text{W}}^2} \left(s_\gamma^2 \left(5 - 10 s_{\text{w}}^2 + 2 s_{\text{w}}^4 \right) - 6 s_{\text{w}}^3 \eta c_\gamma s_\gamma - 3 s_{\text{w}}^2 \eta^2 c_\gamma^2 \right) \Bigg]. \end{aligned} \tag{5.18}$$

The Feynman diagrams representing the NLO QED corrections to muon decay in the Fermi theory are shown in Fig. 5.5. The respective QED contributions to Δr in the DASM and the SM originating from bremsstrahlung effects as well as the box diagram including photon exchange between the initial-state muon and the final-state electron (see Fig. 5.6) are identical. Note that the right diagram in Fig. 5.6 is, due to the presence of a second W-boson propagator, suppressed by an additional factor $\frac{1}{M_{\text{W}}^2}$, and, therefore, only contributes at $\mathcal{O}\left(\frac{m_\mu^2}{M_{\text{W}}^2}\right)$, which is neglected in the derivation. Thus, combining these contributions from the DASM

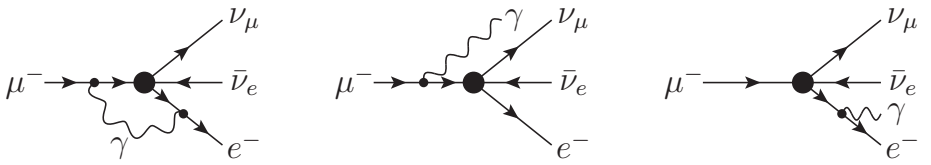

Figure 5.5.: Feynman diagrams representing the virtual (left) and bremsstrahlung (middle and right) corrections to muon decay in the Fermi theory at NLO.

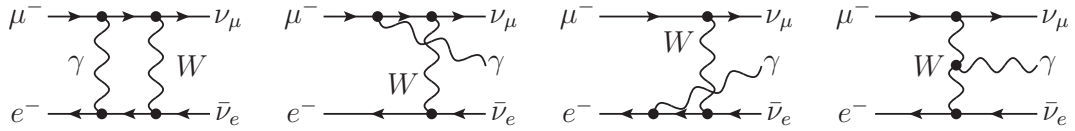

Figure 5.6.: Feynman diagrams representing the QED virtual (first diagram on the left) and bremsstrahlung (three diagrams on the right) corrections to muon decay in the DASM at NLO.

and the Fermi theory leads, as for the SM case, to [105]

$$\delta_{\text{box}}^{\gamma\text{W}} = \frac{\alpha_{\text{em}}}{4\pi}\left(\log\frac{M_{\text{W}}}{m_e} + \log\frac{M_{\text{W}}}{m_\mu} - 2\log\frac{m_e}{\lambda} - 2\log\frac{m_\mu}{\lambda} + \frac{9}{2}\right), \tag{5.19}$$

where we introduced an infinitesimal photon mass λ for infrared regularization. Finally, combining $\delta_{\text{box}}^{\text{massive}}$ and $\delta_{\text{box}}^{\gamma\text{W}}$ with the weak vertex corrections (see Fig. 5.3) one finds

$$\begin{aligned}\delta_{\text{vert+box}} = \frac{\alpha_{\text{em}}}{16\pi s_{\text{w}}^2}\Bigg\{16\left(\Delta_{\text{UV}} - \log\frac{M_{\text{W}}^2}{\mu^2}\right) + 24 - \frac{1}{c_{\text{w}}^2}\sum_{V=\text{Z,Z}'}\Bigg[\frac{\sigma_V \log\frac{M_V^2}{M_{\text{W}}^2}}{(M_V^2 - M_{\text{W}}^2)} \\ \times\left(\sigma_V[3M_{\text{W}}^2[s_{\text{w}}^2(2+\eta^2)-1] + 10c_{\text{w}}^4 M_V^2] + c_{2\gamma}(3M_{\text{W}}^2\right. \\ \left.\times[1+s_{\text{w}}^2(\eta^2-2)] - 10c_{\text{w}}^4 M_V^2) + 6\eta s_{2\gamma}s_{\text{w}}^3 M_{\text{W}}^2\right)\Bigg]\Bigg\},\end{aligned} \tag{5.20}$$

with $\sigma_{\text{Z/Z}'} = \mp 1$, the standard 1-loop UV divergence Δ_{UV}, and the reference scale μ of dimensional regularization (see Sect. C).

To further reduce theoretical uncertainties in the DASM prediction for the W-boson mass, we use the running electromagnetic coupling $\alpha_{\text{em}}(M_{\text{Z}}^2)$ instead of the fine-structure constant $\alpha_{\text{em}}(0)$ in our calculation. This allows us to absorb the strong dependence of Δr on the light-quark masses, introduced via non-perturbative effects of the photonic vacuum polarization at low energies by the charge renormalization constant δZ_e, into (measured) input parameters. In addition, we resum the leading SM terms of the top-quark mass dependence $\Delta\rho$ at least up to order $\mathcal{O}(\alpha_{\text{em}}^2)$ to further reduce the uncertainties of our prediction. In detail,

the replacements described above can be summarized by [70, 71, 104, 106, 107]

$$\alpha_{\rm em} \to \alpha_{\rm em}(M_{\rm Z}^2) = \frac{\alpha_{\rm em}(0)}{1-\Delta\alpha_{\rm em}}, \quad s_{\rm w}^2 \to \bar{s}_{\rm w}^2 = s_{\rm w}^2 + c_{\rm w}^2\Delta\rho, \quad \Delta r \to \Delta r_{\rm rem}, \tag{5.21}$$

where

$$\Delta\alpha_{\rm em} = \Delta\alpha_{\rm had}^{(5)} + \Delta\alpha_{\rm lep} = \left.\frac{\partial\Sigma_{f\neq t}^{AA}(k^2)}{\partial k^2}\right|_{k^2=0} - \left.\frac{\Sigma_{f\neq t}^{AA}(k^2)}{k^2}\right|_{k^2=M_{\rm Z}^2}, \tag{5.22}$$

$$\begin{aligned}\frac{c_{\rm w}^2}{s_{\rm w}^2}\Delta\rho = {} & \frac{3\alpha_{\rm em}m_{\rm t}^2M_{\rm Z}^2}{16\pi\left(M_{\rm W,1}^2-M_{\rm Z}^2\right)^2} \\ & + \frac{3\alpha_{\rm em}s_\gamma^2m_{\rm t}^2\left[M_{\rm Z'}^2\left(M_{\rm W,1}^2+M_{\rm Z}^2\right)-M_{\rm Z}^2\left(M_{\rm W,1}^2+2M_{\rm W,2}^2+M_{\rm Z}^2\right)\right]}{16\pi\left(M_{\rm W,1}^2-M_{\rm Z}^2\right)^3} + \mathcal{O}\left(s_\gamma^3\right),\end{aligned} \tag{5.23}$$

$$\Delta r = \Delta\alpha_{\rm em} - \frac{c_{\rm w}^2}{s_{\rm w}^2}\Delta\rho + \Delta r_{\rm rem}. \tag{5.24}$$

Note that, in addition to the leading SM contributions, we resum the leading (for small values of γ) top-quark mass contributions to Δr originating from the BSM part of the DASM, given in the second line of Eq. (5.23), as well. Here, we introduced the expansion

$$M_{\rm W}^2 = M_{\rm W,1}^2 + M_{\rm W,2}^2s_\gamma^2 + \mathcal{O}\left(s_\gamma^4\right), \tag{5.25}$$

to keep the results compact. Explicit expressions for $M_{\rm W,1}^2$ and $M_{\rm W,2}^2$ can easily be obtained by solving Eq. (5.15) for $M_{\rm W}^2$ and then expanding in s_γ. The quantities $\Delta\alpha_{\rm lep}$ and $\Delta\alpha_{\rm had}^{(5)}$, the so-called leptonic and hadronic vacuum polarizations, respectively, summarize the aforementioned contributions of lepton- and light-quark (excluding only the top-quark) mass logarithms introduced via δZ_e. Taking all of the above into account, Eq. (5.16) is modified to

$$G_\mu = \frac{\alpha_{\rm em}(M_{\rm Z}^2)\pi}{\sqrt{2}\bar{s}_{\rm w}^2M_{\rm W}^2}\left(1+\Delta r_{\rm rem}\right). \tag{5.26}$$

In the following, we solve Eq. (5.26) for $M_{\rm W}$ to obtain the desired NLO prediction for the W-boson mass in the DASM. In detail, we eliminate $M_{\rm W}$ in the NLO parts of Eq. (5.26) in favor of the Fermi constant by using their LO relation[6] (given in Eq. (5.15)) and then solve Eq. (5.26) for $M_{\rm W}$. As mentioned above, we complement our NLO prediction in the DASM with SM corrections to muon decay beyond NLO. Assuming higher-order BSM effects to be small compared to their respective SM counterparts—which clearly is a well-founded assumption when considering the

[6]Note that one has to first plug in the full dependence on $M_{\rm W}$ coming from $s_{\rm w}$ before solving for the W-boson mass.

astonishing predictive power of the SM for all collider experiments—this yields an even better prediction for M_{W} in the DASM. Therefore, we add the difference between the NLO DASM and NLO SM predictions to the best W-boson mass prediction taken from Ref. [6],

$$M_{\mathrm{W}}^{\mathrm{DASM}} = M_{\mathrm{W}}^{\mathrm{SM}} + \Delta M_{\mathrm{W}}, \qquad \Delta M_{\mathrm{W}} = M_{\mathrm{W,NLO}}^{\mathrm{DASM}} - M_{\mathrm{W,NLO}}^{\mathrm{SM}}. \tag{5.27}$$

The authors of Ref. [6] give an approximation for the parametric dependence of their result, which is used for all predictions for $M_{\mathrm{W}}^{\mathrm{SM}}$. With the input-parameter values given in Eq. (5.6), we find $M_{\mathrm{W}}^{\mathrm{SM}} = 80.3536\,\mathrm{GeV}$. Note that, in contrast to the NLO case, we use $\Delta\alpha_{\mathrm{lep,SM}} = 0.0314977$ given in Ref. [6] in the computation of $M_{\mathrm{W}}^{\mathrm{SM}}$ for consistency. For the experimental counterpart we use [16]

$$M_{\mathrm{W}}^{\mathrm{exp}} = (80.377 \pm 0.012)\,\mathrm{GeV}. \tag{5.28}$$

Additionally, due to the large variance between the world average (5.28) and the CDF measurement [7]

$$M_{\mathrm{W,CDF}}^{\mathrm{exp}} = (80.4335 \pm 0.094)\,\mathrm{GeV}, \tag{5.29}$$

we include the $M_{\mathrm{W,CDF}}^{\mathrm{exp}}$ in the comparison.
In the following, we discuss the dependence of $M_{\mathrm{W}}^{\mathrm{DASM}}$ on the various BSM parameters in the OS and the hybrid schemes. We use the input values (5.6) for the SM-like input parameters as well as the benchmark points of Eqs. (5.7) and (5.8) for the remaining BSM parameters and show the dependence of $M_{\mathrm{W}}^{\mathrm{DASM}}$ on the BSM parameters in the OS scheme. To account for the approximations $M_B \gg m_\mu$, $B = \mathrm{h}, \mathrm{Z}'$, used in the derivation of $M_{\mathrm{W}}^{\mathrm{DASM}}$, we restrict our discussion to $M_{\mathrm{h}}, M_{\mathrm{Z}'} > 1\,\mathrm{GeV}$. In certain regions of the parameter space differences in the parameter dependence of the $M_{\mathrm{W}}^{\mathrm{DASM}}$ predictions in the OS and hybrid scheme can be observed, indicating potentially large theoretical uncertainties of the prediction in these regions. Thus, whenever any interesting feature, which distinguishes the OS and hybrid scheme predictions, can be observed, we will show the respective hybrid scheme predictions, after proper scheme conversion of the mixing angle γ, in addition to the OS predictions. Furthermore, whenever any curve (representing a certain benchmark scenario) is shown only for an interval smaller than the respective x-axis, this means that the remaining parameter points violate our perturbativity limits given in Eq. (5.11).

5.4.1.1. Benchmark Scenario (i): $M_{\mathrm{h}} = M_{\mathrm{h}}^{\mathrm{SM}}$

In benchmark scenario (i) (see Eq. (5.7)), we identify the Higgs boson h with the discovered SM-like Higgs boson, i.e. $M_{\mathrm{h}} = M_{\mathrm{h}}^{\mathrm{SM}} = 125.25\,\mathrm{GeV}$. In the upper-left plot of Fig. 5.7, we show the dependence of $M_{\mathrm{W}}^{\mathrm{DASM}}$ on the mixing angle γ_{OS} for several values of $M_{\mathrm{Z}'}$. Note that the predictions are symmetric in the parameter γ_{OS} ($\gamma_{\mathrm{OS}} \to -\gamma_{\mathrm{OS}}$). At $\gamma_{\mathrm{OS}} = 0$, the predictions for all shown values of $M_{\mathrm{Z}'}$ coincide, reflecting the decoupling of the gauge sector at this parameter point. At

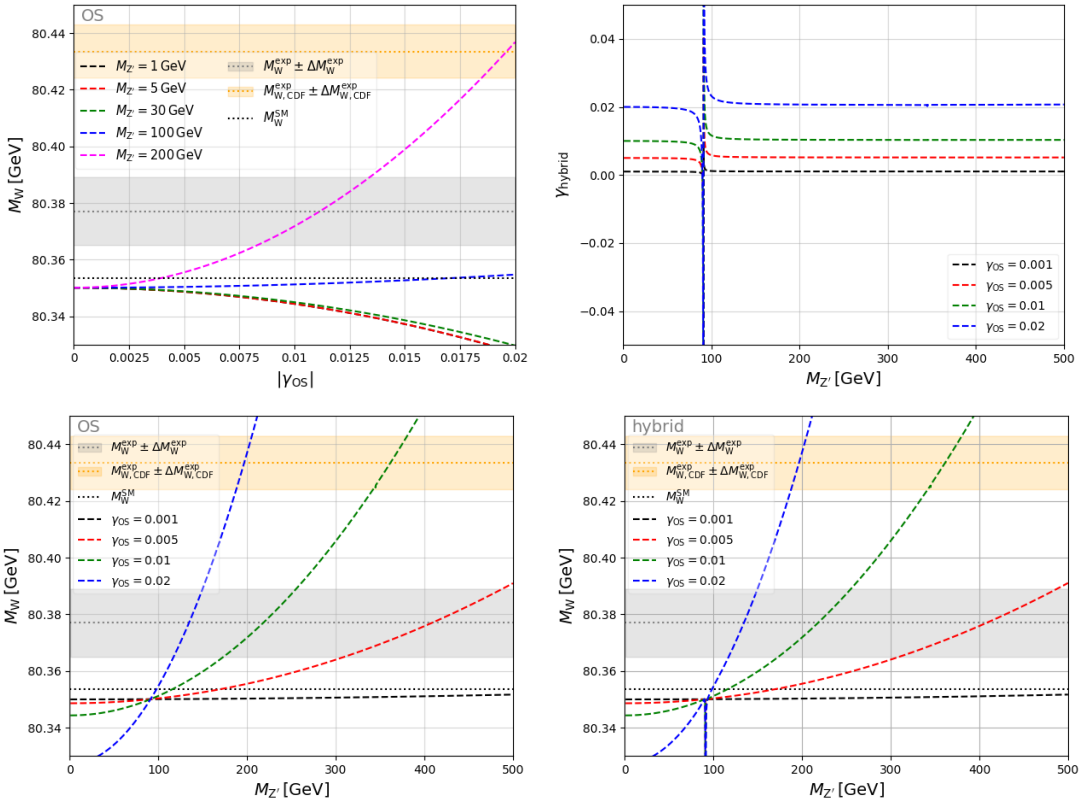

Figure 5.7.: Dependence of M_W^{DASM} in the OS scheme on $|\gamma_{OS}|$ (upper left) as well as its dependence on $M_{Z'}$ in the OS scheme (lower left), and hybrid scheme (lower right) after proper scheme conversion of γ for benchmark scenario (i). The scheme conversion of γ depending on $M_{Z'}$ is shown in the upper-right plot.

this point the remaining downward shift (with respect to the SM prediction) of the DASM prediction reflects the influence of the Higgs- and fermion-sector extensions of the DASM for the chosen values of the input parameters. For $M_{Z'} > M_Z$ the predictions for M_W^{DASM} increase with increasing $|\gamma_{OS}|$ and can describe the experimental world average M_W^{exp} and even the CDF measurement M_W^{CDF}, as well as the full interval between the two experimental results for a wide range of $|\gamma_{OS}|$–$M_{Z'}$ combinations. Further, for larger values of $M_{Z'}$, the increase of the prediction with increasing $|\gamma_{OS}|$ becomes steeper. For $M_{Z'} < M_Z$ the prediction decreases with increasing $|\gamma_{OS}|$, driving the DASM prediction further away from the experimental measurements.

We complement this discussion by showing the dependence of M_W^{DASM} on $M_{Z'}$ for different values of γ_{OS} in more detail in the plots shown in the lower line of Fig. 5.7. In addition to the prediction in the OS scheme (lower left), we show the respective prediction in the hybrid scheme (lower right) after proper scheme conversion of γ, and the relation between the shown γ_{OS} values and their respective counter-

parts γ_{hybrid} after scheme conversion (upper right). As expected, the OS prediction shows an increase of $M_{\text{W}}^{\text{DASM}}$ for increasing values of $M_{\text{Z}'}$ that becomes steeper for larger values of $|\gamma_{\text{OS}}|$. Further, the predictions for all shown values of $|\gamma_{\text{OS}}|$ coincide at $M_{\text{Z}'} = M_{\text{Z}}$, reflecting the decoupling of the gauge sector at this point. The $M_{\text{W}}^{\text{DASM}}$ prediction in the hybrid scheme widely follows its respective prediction in the OS scheme. However, for $M_{\text{Z}'} \approx M_{\text{Z}}$, we see a divergent behaviour of the prediction of the hybrid scheme. As mentioned above, $\overline{\text{MS}}$ renormalization of mixing angles, as done for γ in the hybrid scheme, can lead to divergences in the case of degenerate masses of the particles corresponding to the respective mixing fields (see also Ref. [81]), introduced by the respective off-diagonal field renormalization constants. However, the respective field renormalization constants do not appear in $M_{\text{W}}^{\text{DASM}}$ and the observed divergences are simply introduced via the scheme conversion of γ as can be seen by the upper-right plot[7]. Note that this is a general feature of the parameter conversion of γ between the OS and hybrid scheme, which will often show up in respective plots.
In Fig. 5.8, we show the dependence of the W-boson mass prediction on M_{H} in the OS scheme in the upper-left plot and the hybrid scheme in the upper-right plot. For increasing M_{H}, the predictions in both, the OS and hybrid schemes, decrease. However, this decrease is small compared to the experimental uncertainty. For $M_{\text{H}} \to M_{\text{h}}$ the parameters λ_1 as well as e_{d} (for $M_{\text{Z}'} > M_{\text{Z}}$), become large and eventually reach their perturbativity limits. While the predictions in the two schemes agree well for almost all given input values, they start to develop significant deviations from one another in this region for $M_{\text{Z}'} = 200\,\text{GeV}$, showcasing the potential for large theory uncertainties in certain regions of the parameter space. The dependence of $M_{\text{W}}^{\text{DASM}}$ on the Higgs mixing angle α is shown in the lower plot of Fig. 5.8. For increasing values of α, the M_{W} predictions decrease. Again, this is only a small effect with respect to the experimental uncertainty. In the limit $\alpha \to 0$ the parameter λ_1 becomes large and eventually enters the non-perturbative region. Further, the predictions are symmetric in the parameter α ($\alpha \to -\alpha$) and we find the effect of a sign flip of λ_{12} ($\lambda_{12} \to -\lambda_{12}$) to be negligible for the investigated values in both benchmark scenarios (i) and (ii). Note that, due to our convention $s_{2\alpha}\lambda_{12} > 0$, we adjust the respective signs of the values of the input parameters λ_{12} or α in the following accordingly, if needed.
The influence of the remaining BSM parameters λ_{12}, m_{ν_4}, and θ_{r} on the W-boson mass prediction is negligible (not shown) in benchmark scenario (i).

5.4.1.2. Benchmark Scenario (ii): $M_{\text{H}} = M_{\text{h}}^{\text{SM}}$

For the benchmark scenario Eq. (5.8), we chose the heavy Higgs boson H to be the SM-like Higgs boson, i.e. $M_{\text{H}} = M_{\text{h}}^{\text{SM}} = 125.25\,\text{GeV}$. In Fig. 5.9, we show

[7] This is expected, since our definition of $\delta\gamma_{\text{OS}}$ is designed to exactly cancel the aforementioned divergences systematically, so that the resulting predictions are well-behaved in the degeneracy limit for the masses (see Sect. 4.2.3).

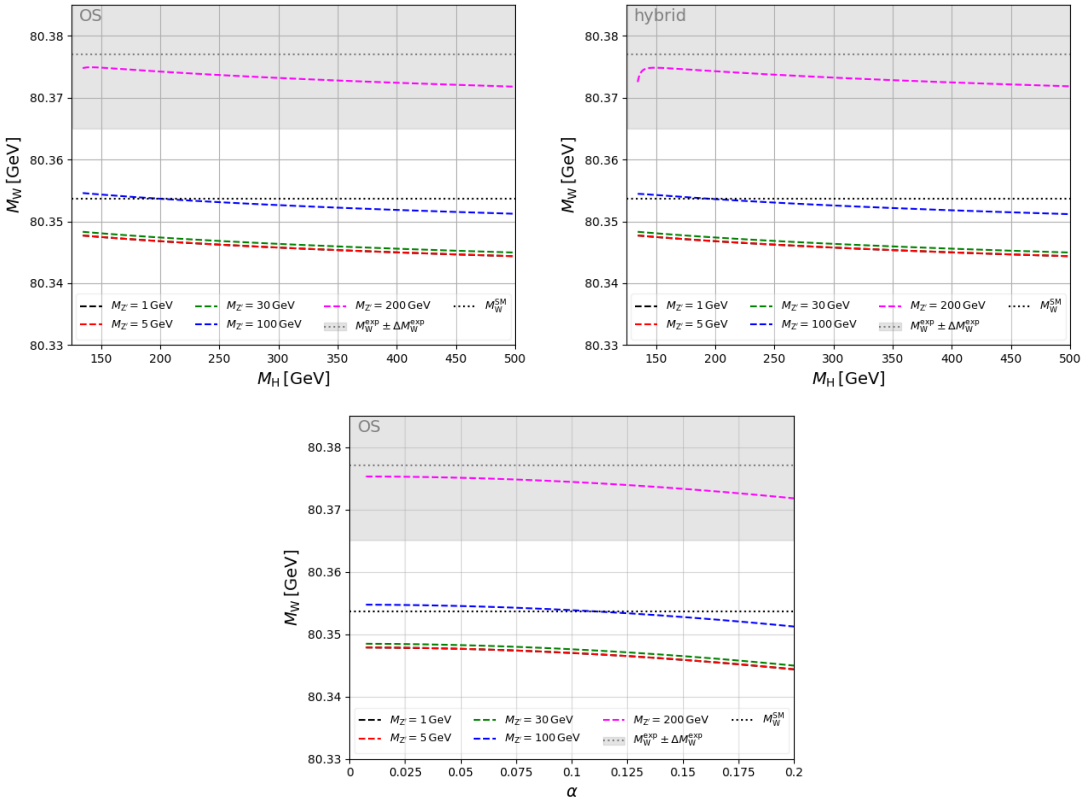

Figure 5.8.: Dependence of M_W^{DASM} on M_H in the OS scheme (upper left) and hybrid scheme (after proper scheme conversion of γ) (upper right), as well as its dependence on the Higgs mixing angle α in the OS scheme (lower plot) for benchmark scenario (i).

the dependence of the OS prediction of M_W^{DASM} on $|\gamma_{OS}|$ (left) and $M_{Z'}$ (right). While the γ_{OS} dependence shows a similar behaviour as for benchmark scenario (i), for $\gamma_{OS} \to 0$ one finds, that, in contrast to the corresponding parameter point in benchmark scenario (i), the extensions in the Higgs and fermion sectors lead to an upward shift of the DASM predictions with respect to the SM prediction (leading to a better description of the experimental data by the prediction already for $\gamma_{OS} \to 0$). The plot on the right-hand side of Fig. 5.9 shows, similar to its counterpart for the benchmark point (i), an increase of the prediction with increasing mass of the Z′ boson, which is steeper for larger values of $|\gamma_{OS}|$. Furthermore, threshold effects at $M_{Z'} \approx 2m_{\nu_4} = 400\,\text{GeV}$ (see Sect. 5.3) become visible.
In Fig. 5.10, we show the dependence of the W-boson mass prediction on the additional parameters of the Higgs sector M_h, $\alpha' = \frac{\pi}{2} - \alpha$, and λ_{12}. The predictions are shown in the OS scheme and the hybrid scheme after scheme conversion of γ. In contrast to the case $M_h = M_h^{SM}$ (see benchmark scenario (i)), the W-boson mass prediction in the OS renormalization scheme increases the more M_h and α' differ from their respective values in the SM limit, i.e. M_W^{DASM} grows for decreas-

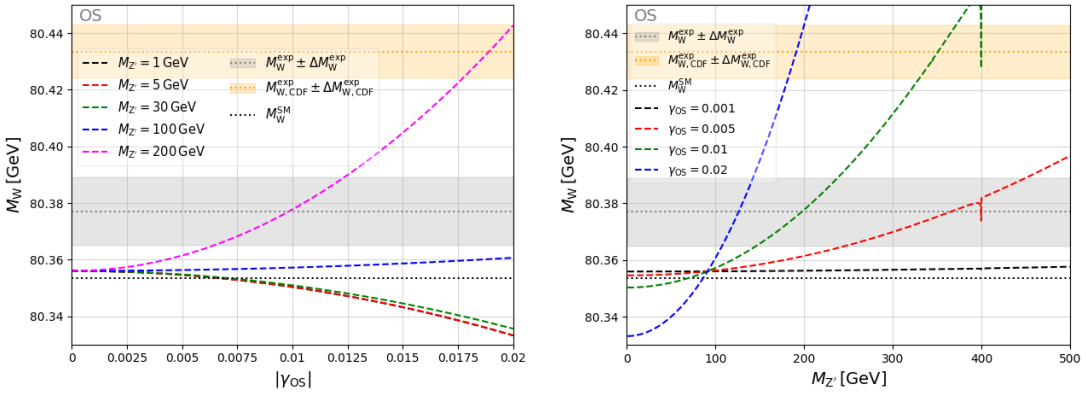

Figure 5.9.: Dependence of $M_{\text{W}}^{\text{DASM}}$ on $|\gamma_{\text{OS}}|$ (left) and $M_{\text{Z}'}$ (right) in the OS renormalization scheme in benchmark scenario (ii).

ing M_{h} and increasing α'. For small values of $M_{\text{Z}'} \leq 100\,\text{GeV}$ the dependence of the prediction on λ_{12} is negligible. For $M_{\text{Z}'} = 200\,\text{GeV}$ a decrease of the prediction is visible for increasing values of λ_{12}. However, all influences of the Higgs sector parameters are small with respect to the experimental uncertainty. For $M_{\text{h}} \to M_{\text{H}}$, $\alpha' \to 0$, and large enough values of λ_{12} the parameters λ_1 and e_{d} (for $M_{\text{Z}'} > M_{\text{Z}}$) enter the non-perturbative region. Comparing the respective OS and hybrid scheme predictions one observes an increasing scheme dependence for $M_{\text{Z}'} > M_{\text{Z}}$ in these regions.
Finally, we show the dependence of $M_{\text{W}}^{\text{DASM}}$ on m_{ν_4} in the benchmark scenario (ii) in Fig. 5.11. While the OS scheme predictions are widely independent[8] of m_{ν_4}, for $M_{\text{Z}'} > M_{\text{Z}}$ one finds large differences between the OS and hybrid schemes in the region $m_{\nu_4} \geq 1\,\text{TeV}$. Note that in this region of the parameter space, the Yukawa coupling y_ρ is close to its non-perturbativity limit.
As for benchmark scenario (i) the dependence of $M_{\text{W}}^{\text{DASM}}$ on the fermionic mixing angle θ_{r} is negligible in benchmark scenario (ii).

In summary, we find for both benchmark scenarios a large dependence of $M_{\text{W}}^{\text{DASM}}$ on the new parameters γ and $M_{\text{Z}'}$ of the gauge sector. In both cases, we find for $M_{\text{Z}'} > M_{\text{Z}}$ a wide range of $|\gamma|$–$M_{\text{Z}'}$ combinations that can lead to agreement between the W-boson mass prediction and the experimental world average $M_{\text{W}}^{\text{exp}}$ or even the CDF measurement $M_{\text{W}}^{\text{CDF}}$. Further, the new parameters introduced in the Higgs sector can lead to downward or upward shifts of the predictions for $M_{\text{h}} = M_{\text{h}}^{\text{SM}}$ or $M_{\text{h}} = M_{\text{H}}^{\text{SM}}$, respectively, which are, however, small compared to the experimental uncertainty. Finally, the OS scheme prediction is widely unaffected by variations of the parameters θ_{r} and m_{ν_4} introduced by a possible dark

[8] Using a scan precision of $\approx 100\,\text{MeV}$ here, we see only one of the discussed threshold effects of the OS scheme at $m_{\nu_4} = M_{\text{Z}'}/2 = 100\,\text{GeV}$. Note that, due to the scheme conversion $\gamma_{\text{OS}} \to \gamma_{\text{hybrid}}$ it is introduced to the prediction in the hybrid scheme as well.

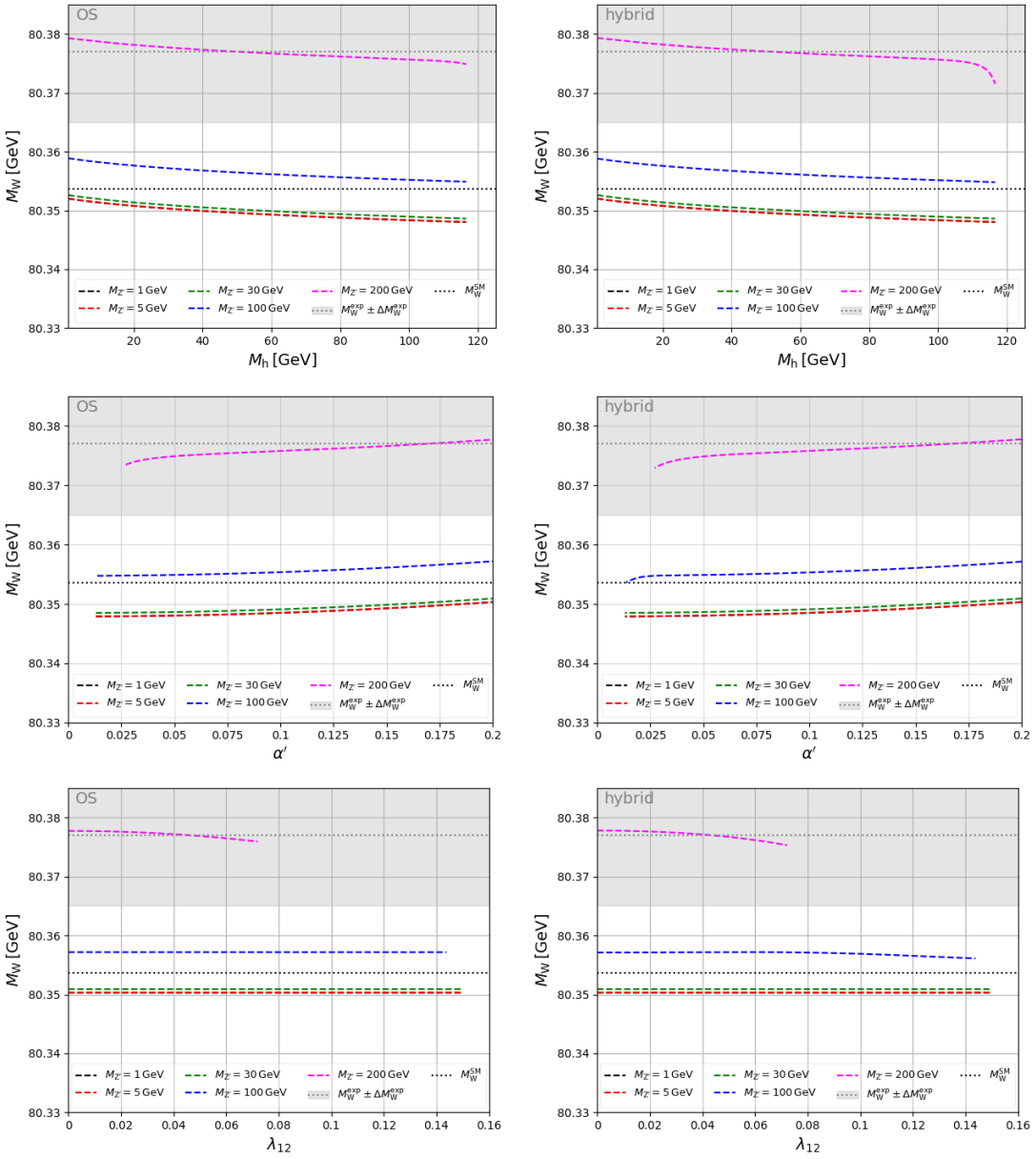

Figure 5.10.: Dependence of M_W^{DASM} on the BSM Higgs sector parameters M_h (upper row), $\alpha' = \frac{\pi}{2} - \alpha$ (middle row), and λ_{12} (lower row) in the OS scheme (left column) and the hybrid scheme (right column) after proper scheme conversion of γ for benchmark scenario (ii).

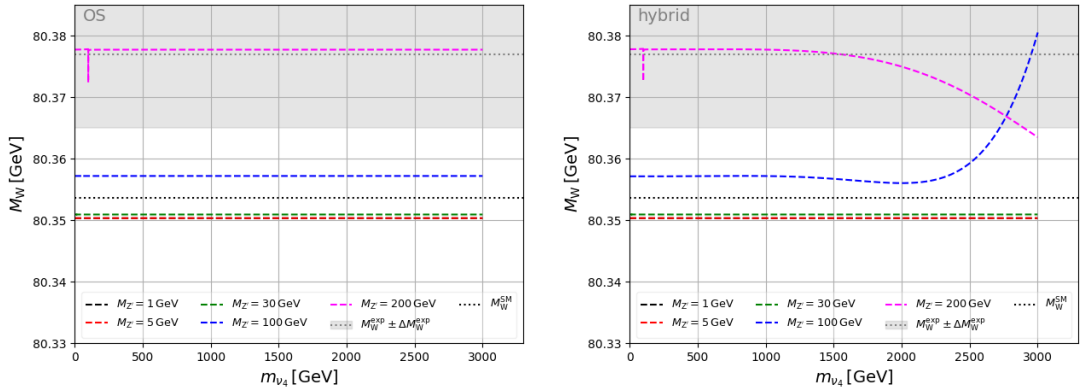

Figure 5.11.: Dependence of M_W^{DASM} on m_{ν_4} in the OS scheme (left), and in the hybrid scheme (right) after proper scheme conversion of γ for benchmark scenario (ii).

fermion. However, we observe a significant renormalization scheme dependence of M_W^{DASM} in benchmark scenario (ii) for $m_{\nu_4} \geq 1\,\text{TeV}$, signalling the onset of non-perturbative effects induced by a too large Yukawa coupling to the dark neutrino sector.

5.4.2. The anomalous magnetic moment of the muon

The measurement of the anomalous magnetic moment of the muon, a_μ, provides a second powerful test of the predictive power of the DASM. Not only is it measured with extremely high precision, but also its theoretical prediction within the SM matches this astonishing precision. There is a 5.1σ discrepancy between the experimental world average [3] and the SM prediction, making a_μ a possible candidate hinting towards BSM physics. However, according to recent developments, more reliable lattice results are available that tend to disagree with the data-driven determination of non-perturbative parts of a_μ via the e^+e^- dispersion relation and also seem to agree better with measurements. To properly define a_μ, we follow the discussion of Ref. [108], starting with the equations of motion for a muon in an external electromagnetic field A_ν^{ext},

$$\begin{aligned}(\mathrm{i}\not{\partial} - e(\not{A} + \not{A}^{\text{ext}}) - m_\mu)\psi = 0,\\ (\partial_\nu\partial^\nu g_{\kappa\rho} - (1 - \frac{1}{\xi_A})\partial_\kappa\partial^\rho)A^\kappa = e\bar{\psi}\gamma^\rho\psi,\end{aligned} \tag{5.30}$$

with the radiation field A_ν and ψ denoting the Dirac spinor of the muon field. Note that we here used the suffix μ to refer to the muon (and it should not be read as a Lorentz index). Also, in this section bold symbols are used to represent 3-vectors. Neglecting the radiative field for illustrative purposes at first, we are, thus, interested in the solution of the equations of motion of a muon in an external

field described by

$$\mathrm{i}\frac{\partial\psi}{\partial t} = \left[\gamma^0\boldsymbol{\gamma}\left(\mathbf{p} - e\mathbf{A}\right) + e\Phi + \gamma^0 m_\mu\right]\psi, \tag{5.31}$$

where we introduced $A_\nu^{\mathrm{ext}} = (\Phi, \mathbf{A})$. The non-relativistic limit of the Dirac equation (5.31) is obtained by performing the so-called Foldy–Wouthuysen transformation [109], leading to the Pauli equation

$$\mathrm{i}\frac{\partial\hat{\varphi}}{\partial t} = \left[\frac{1}{2m_\mu}\left(\mathbf{p} - e\mathbf{A}\right)^2 + e\Phi - \frac{e}{2m_\mu}\boldsymbol{\sigma}\cdot\mathbf{B}\right]\hat{\varphi}, \tag{5.32}$$

where $\mathbf{B} = \mathrm{rot}\mathbf{A}$ and $\psi = \begin{pmatrix}\hat{\varphi}\\ \hat{\chi}\end{pmatrix} e^{-\mathrm{i}m_\mu t}$. For our discussion of the anomalous magnetic moment of the muon, the last term of Eq. (5.32), present due to the intrinsic spin of the muon, is of interest. It has the form of a contribution to the potential energy of a magnetic dipole in an external field. The resulting magnetic moment induced by the spin of the muon is given by

$$\boldsymbol{\mu}_{\mathrm{s}} = -g_\mu\frac{e\boldsymbol{\sigma}}{4m_\mu} = -g_\mu\frac{e}{2m_\mu}\mathbf{s}, \tag{5.33}$$

where we introduced the gyromagnetic ratio g_μ of the muon. It is given by the ratio of a magnetic moment and the spin operator $\mathbf{s} = \frac{\sigma}{2}$ in units[9] of $\mu_0 = \frac{e}{2m_\mu}$. A comparison of Eqs. (5.32) and (5.33) yields $g_\mu = 2$. With the presence of the radiation field (see Eq. (5.30)) the Foldy–Wouthuysen transformation cannot be performed in a closed analytic way. One can, however, derive the effective Hamiltonian of Eq. (5.30) in the non-relativistic limit by expanding in $\frac{1}{\mathrm{c}}$, where c is the speed of light (for further details see Ref. [108] and references therein).
We are interested in the anomalous magnetic moment of the muon taking into account relativistic quantum corrections. These can be derived via a simultaneous expansion in the fine-structure constant $\alpha_{\mathrm{em}}(0)$ and the external field (assuming the latter to be weak). In detail, we investigate the $\gamma\mu\mu$ vertex function $\Gamma^\kappa_{\gamma\mu\mu}$, with on-shell muons. Its most general covariant decomposition (respecting electromagnetic current conservation) is given by

$$\begin{aligned}\mathrm{i}\bar{u}\left(p'\right)\Gamma^\alpha_{\gamma\mu\mu}(q,-p',p)u\left(p\right) = \mathrm{i}e\bar{u}\left(p'\right)\Bigg[&\gamma^\alpha F_{\mathrm{E}}\left(q^2\right) + \left(\gamma^\alpha - \frac{2m_\mu q^\alpha}{q^2}\right)\gamma_5 F_{\mathrm{A}}\left(q^2\right)\\ &+ \mathrm{i}\sigma^{\alpha\nu}\frac{q_\nu}{2m_\mu}F_{\mathrm{M}}\left(q^2\right) + \sigma^{\alpha\nu}\frac{q_\nu}{2m_\mu}\gamma_5 F_{\mathrm{D}}\left(q^2\right)\Bigg]u\left(p\right).\end{aligned} \tag{5.34}$$

[9] By convention the gyromagnetic ratio is normalized such that its respective value originating from orbital momentum is -1. For the electron one finds $\mu_0 = \mu_{\mathrm{B}} = \frac{e}{2m_{\mathrm{e}}}$, where μ_{B} is Bohr's magneton.

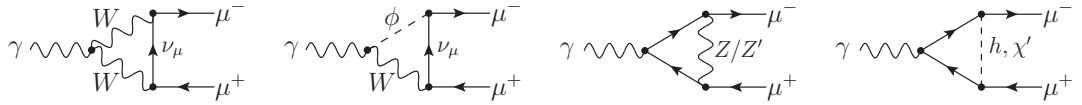

Figure 5.12.: Relevant Feynman diagrams contributing to a_μ in the DASM at the 1-loop level. Here the second diagram, describing ϕ-exchange, is, of course, meant to also represent its related diagram, where the W and ϕ bosons are interchanged.

Here we introduced the photon momentum $q = p' - p$, the electric charge form factor $F_{\mathrm{E}}(q^2)$, the parity violating anapole moment $F_{\mathrm{A}}(q^2)$, with $F_{\mathrm{A}}(0) = 0$, and $F_{\mathrm{D}}(q^2)$ is the CP-violating electric dipole moment, respectively. Finally, the $F_{\mathrm{M}}(q^2)$ is the magnetic form factor yielding, for zero photon momentum, the anomalous magnetic moment

$$a_\mu = \frac{1}{2}\left(g_\mu - 2\right) = F_{\mathrm{M}}\left(q^2 = 0\right). \tag{5.35}$$

In this work, we are interested in the prediction for a_μ in the DASM at 1-loop order up to $\mathcal{O}\left(\frac{m_\mu^4}{M_X^4}\right)$, with $X = \mathrm{H}, \mathrm{Z}, \mathrm{W}$. The pure QED radiative corrections do not change with respect to their SM counterparts, resulting in the well-known correction $a_{\mu,\mathrm{QED}}^{\mathrm{DASM}} = \frac{\alpha_{\mathrm{em}}(0)}{2\pi}$ [110]. Taking this into account, all Feynman diagrams representing the relevant 1-loop weak corrections $a_{\mu,1-\mathrm{loop}}^{\mathrm{DASM}}$ that contribute to a_μ^{DASM} in the DASM are shown in Fig. 5.12. Note that in our derivation we include the contributions originating from the h and χ' exchange diagrams (Fig. 5.12 right-hand side diagrams), to explicitly account for the possibility of low Z′- and h-boson masses in our calculation. For the explicit computations of these diagrams we use the G_μ-scheme described in Sect. 5.1. In the Thomson limit, i.e. for photon momentum transfer of $q^2 \to 0$, the contributions of the first two diagrams shown in Fig. 5.12 to a_μ^{DASM} are given by

$$a_\mu^{\mathrm{WW}} = \frac{7\alpha_{G_\mu}^{\mathrm{SM}} m_\mu^2}{48\pi\left(1 - \frac{M_{\mathrm{W}}^2}{M_{\mathrm{Z}}^2}\right) M_{\mathrm{W}}^2}, \qquad a_\mu^{\mathrm{W}\phi} = \frac{\alpha_{G_\mu}^{\mathrm{SM}} m_\mu^2}{16\pi\left(1 - \frac{M_{\mathrm{W}}^2}{M_{\mathrm{Z}}^2}\right) M_{\mathrm{W}}^2}, \tag{5.36}$$

where, after switching to the G_μ-scheme in the DASM, we introduced the standard input parameter of the G_μ-scheme in the SM via

$$\alpha_{\mathrm{em}} \to \alpha_{G_\mu} = \alpha_{G_\mu}^{\mathrm{SM}} \frac{s_{\mathrm{w}}^2}{1 - \frac{M_{\mathrm{W}}^2}{M_{\mathrm{Z}}^2}}, \qquad \alpha_{G_\mu}^{\mathrm{SM}} = \frac{\sqrt{2} G_\mu M_{\mathrm{W}}^2 \left(1 - \frac{M_{\mathrm{W}}^2}{M_{\mathrm{Z}}^2}\right)}{\pi}. \tag{5.37}$$

In this form it is obvious that the contributions (5.36) coincide with their respective SM counterparts (see e.g. [111, 112]) and, therefore, do not contribute any BSM effects to a_μ^{DASM}. However, the Z-, Z′-, h-, and χ'-exchange diagrams present in

the DASM differ from their respective SM counterparts. Their contributions to the anomalous magnetic moment of the muon are given by

$$a_\mu^{\mathrm{Z}} = \frac{\alpha_{G_\mu}^{\mathrm{SM}} m_\mu^2 \left(4M_{\mathrm{W}}^4 - 6M_{\mathrm{W}}^2 M_{\mathrm{Z}}^2 + M_{\mathrm{Z}}^4\right) c_\gamma^2}{12\pi M_{\mathrm{W}}^2 \left(M_{\mathrm{Z}}^2 - M_{\mathrm{W}}^2\right)\left(c_\gamma^2 M_{\mathrm{Z}}^2 + s_\gamma^2 M_{\mathrm{Z}'}^2\right)} + \ldots, \tag{5.38}$$

$$a_\mu^{\mathrm{Z}'} = \frac{\alpha_{G_\mu}^{\mathrm{SM}} m_\mu^2 M_{\mathrm{Z}}^2 \left(4M_{\mathrm{W}}^4 - 6M_{\mathrm{W}}^2 M_{\mathrm{Z}'}^2 + M_{\mathrm{Z}'}^4\right) s_\gamma^2}{12\pi M_{\mathrm{W}}^2 M_{\mathrm{Z}'}^2 \left(M_{\mathrm{Z}}^2 - M_{\mathrm{W}}^2\right)\left(c_\gamma^2 M_{\mathrm{Z}}^2 + s_\gamma^2 M_{\mathrm{Z}'}^2\right)} + \ldots, \tag{5.39}$$

$$a_\mu^{\chi'} = \frac{\alpha_{G_\mu}^{\mathrm{SM}} m_\mu^4 M_{\mathrm{Z}}^2 \left(11 + 6\ln\frac{m_\mu^2}{M_{\mathrm{Z}'}^2}\right) s_\gamma^2}{48\pi M_{\mathrm{W}}^2 (M_{\mathrm{Z}}^2 - M_{\mathrm{W}}^2)(c_\gamma^2 M_{\mathrm{Z}}^2 + s_\gamma^2 M_{\mathrm{Z}'}^2)} + \ldots, \tag{5.40}$$

$$a_\mu^{\mathrm{h}} = \frac{\alpha_{G_\mu}^{\mathrm{SM}} m_\mu^4 M_{\mathrm{Z}}^2 \left(7 + 6\ln\frac{m_\mu^2}{M_{\mathrm{h}}^2}\right) c_\alpha^2}{48\pi M_{\mathrm{h}}^2 M_{\mathrm{W}}^2 (M_{\mathrm{W}}^2 - M_{\mathrm{Z}}^2)} + \ldots. \tag{5.41}$$

Here, we only spell out the respective leading terms for $M_B \gg m_\mu$, $B = \mathrm{Z}, \mathrm{Z}', \chi', \mathrm{h}$, explicitly to keep the expressions compact, but use the full mass dependence of the results in our numerical evaluations if necessary, such that the results remain valid in the region of small Z' and h masses. Assuming BSM effects to be small compared to the SM contributions, we take the difference between the DASM and the SM at 1-loop, and add it to the best SM prediction [4],

$$a_\mu^{\mathrm{DASM}} = a_\mu^{\mathrm{SM}} + \Delta a_{\mu,1-\mathrm{loop}}^{\mathrm{DASM}}, \qquad \Delta a_{\mu,1-\mathrm{loop}}^{\mathrm{DASM}} = a_{\mu,1-\mathrm{loop}}^{\mathrm{DASM}} - a_{\mu,1-\mathrm{loop}}^{\mathrm{SM}}, \tag{5.42}$$

to obtain the best DASM prediction.
As mentioned above, there are two different results for the LO hadronic vacuum polarization contributions $\Delta\alpha_{\mathrm{had},a_\mu}^{\mathrm{LO}}$ entering a_μ^{SM}: one obtained via a data-driven approach (see Ref. [4] and references therein for more details) and a second one calculated via lattice computations (see, e.g., Refs. [4, 5] and references therein). The prediction for a_μ^{SM} significantly depends on the value of this non-perturbative contribution. However, the two approaches are at variance with one another. In this work, we consider the two results separately, taking the value

$$a_{\mu,e^+e^-}^{\mathrm{SM}} = (116591810 \pm 44) \times 10^{-11} \tag{5.43}$$

from [4] for the discussion of the prediction using the data-driven determination of $\Delta\alpha_{\mathrm{had},a_\mu}^{\mathrm{LO}}$. For the lattice result, we use the value $\Delta\alpha_{\mathrm{had},a_\mu}^{\mathrm{LO,lattice}} = (7075 \pm 55) \times 10^{-11}$ given in Ref. [5] and combine it with the remaining contributions given in Ref. [4] to obtain

$$a_{\mu,\mathrm{lattice}}^{\mathrm{SM}} = (116591954 \pm 58) \times 10^{-11}. \tag{5.44}$$

For the experimental counterpart we use the world average

$$a_\mu^{\mathrm{exp}} = (116592059 \pm 22) \times 10^{-11}, \tag{5.45}$$

from Ref. [3].
In the following, we discuss the explicit parameter dependence of a_μ on the additional parameters introduced by the DASM. As standard input, we choose Eq. (5.6) for the SM-like input parameters and Eqs. (5.7) and (5.8) for the BSM parameters of the DASM, which is, of course, only used for the parameters that are not varied in the respective plot. As in the discussion of the W-boson mass prediction, whenever any curve is shown only for an interval smaller than the full range of the x-axis, we find that the remaining parameter points violate the perturbativity limits given by Eq. (5.11).
Since a_μ is a loop-induced quantity, no renormalization constants appear in its derivation at the 1-loop level. However, we use the prediction for M_W as input for a_μ, which introduces an additional dependence of the predictions on the new parameters of the Higgs and fermion sectors. Further, this can lead to differences between the predictions in the OS and hybrid schemes. While this is the only dependence on the BSM fermion-sector parameters introduced to $(g-2)_\mu$, the BSM parameters of the Higgs sector additionally enter the calculation via the Higgs-boson exchange diagram (see Fig. 5.12 right diagram with h exchange). Even though the result for $(g-2)_\mu$ is valid for very low masses of the BSM Higgs boson, like e.g., $M_\mathrm{h}, M_{\mathrm{Z}'} \ll m_\mu$, this is not true for the prediction of the W-boson mass (as discussed in the previous section). Thus, we restrict the analysis here to $M_\mathrm{h}, M_{\mathrm{Z}'} \geq 1\,\mathrm{GeV}$.
In this region, we find a_μ^DASM to be widely independent of the additional Higgs sector parameters α, λ_{12}, and $M_{h'}$, where h' denotes the BSM Higgs boson of h and H. The dependence of a_μ^DASM on θ_r and m_{ν_4} is also negligible in both benchmark scenarios and for both the OS and hybrid renormalization scheme. However, there is a strong dependence of a_μ^DASM on the new parameters of the gauge sector γ and $M_{\mathrm{Z}'}$, which is shown in Fig. 5.13 using the input values of benchmark scenario[10] (i) for the two scenarios using either $a_{\mu,e^+e^-}^\mathrm{SM}$ or $a_{\mu,\mathrm{lattice}}^\mathrm{SM}$ to derive the SM prediction[11]. The a_μ^DASM prediction is symmetric with respect to $\gamma_\mathrm{OS} \to -\gamma_\mathrm{OS}$. An increase of the prediction for increasing values of $|\gamma_\mathrm{OS}|$ can be observed for all shown values of $M_{\mathrm{Z}'}$. The magnitude of this increase strongly depends on the Z′-boson mass and is greatly enhanced for small Z′ masses. This can be seen even clearer in the plot on the right-hand side, where we show the dependence of a_μ^DASM on $M_{\mathrm{Z}'}$. For the given values of $|\gamma_\mathrm{OS}|$ one observes a steep increase of a_μ^DASM for $M_{\mathrm{Z}'} \to 1\,\mathrm{GeV}$, but no visible effect for larger Z′-boson masses ($M_{\mathrm{Z}'} > 25\,\mathrm{GeV}$). For small values of $M_{\mathrm{Z}'}$ we find a wide range of $|\gamma_\mathrm{OS}|$–$M_{\mathrm{Z}'}$ combinations that can explain the measured value a_μ^exp using either of the SM predictions $a_{\mu,e^+e^-}^\mathrm{SM}$ or $a_\mathrm{lattice}^\mathrm{SM}$.

[10] The negligible influence of the remaining BSM parameters on a_μ^DASM leads to a negligibly small difference between the respective results in the two benchmark scenarios.
[11] Note that switching between the best SM predictions leads effectively only to an overall shift of the measured value in the plots shown in Fig. 5.13.

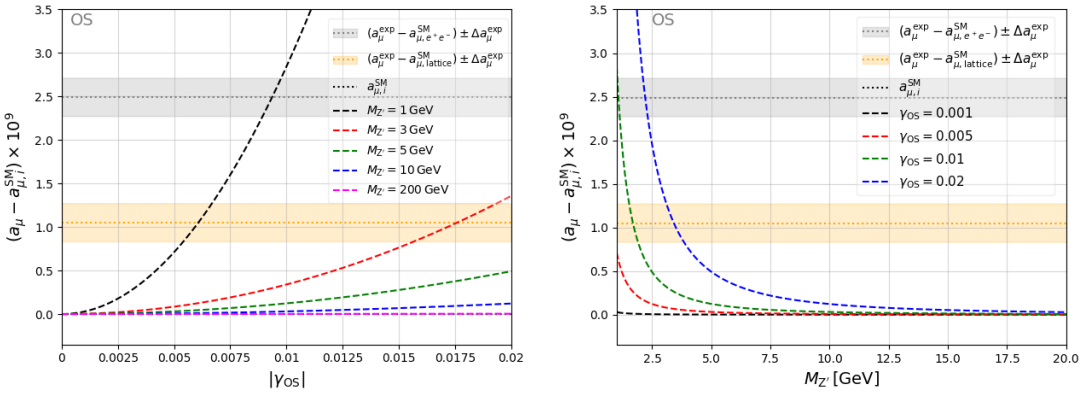

Figure 5.13.: Dependence of a_μ^{DASM} on $|\gamma_{\text{OS}}|$ (left) and $M_{Z'}$ (right) within benchmark scenario (i). The predictions are given as difference to the SM value $a_{\mu,i}^{\text{SM}}$, which is either chosen to be $a_{\mu,e^+e^-}^{\text{SM}}$ or $a_{\mu,\text{lattice}}^{\text{SM}}$.

For an observable $\mathcal{O}_i$ the pull is defined via

$$\text{pull} = \frac{\mathcal{O}_i^{\text{theo}} - \mathcal{O}_i^{\text{exp}}}{\Delta\mathcal{O}_i}, \tag{5.46}$$

where $\Delta\mathcal{O}_i$ denotes the uncertainty of the observable and $\mathcal{O}_i^{\text{theo}}$ and $\mathcal{O}_i^{\text{exp}}$ are the theory prediction and the measured value of the observable, respectively. In Fig 5.14 the pull for a_μ in the $|\gamma_{\text{OS}}|$–$M_{Z'}$ plane in benchmark scenario (i) is shown. In order to derive the predictions within the DASM, either $a_{\mu,e^+e^-}^{\text{SM}}$ (left plot) or $a_{\mu,\text{lattice}}^{\text{SM}}$ (right plot) is used. For both cases, we give the parameter points where the respective DASM predictions are within the 1σ uncertainty band of the measurement (black dotted lines). The black dashed line denotes the points where predictions and measurement agree exactly. In the shown parameter regions the points of exact agreement yield a distinct direction in the $|\gamma_{\text{OS}}|$–$M_{Z'}$ plane for both cases. Using $a_{\mu,e^+e^-}^{\text{SM}}$ (left) the preferred $|\gamma_{\text{OS}}|$–$M_{Z'}$ combinations roughly fulfill $\gamma_{\text{OS}} \approx (0.0089 M_{Z'} + 0.0004)\,\text{GeV}^{-1}$ and using $a_{\mu,\text{lattice}}^{\text{SM}}$ (right) in the predictions leads to $\gamma_{\text{OS}} \approx (0.00583 M_{Z'} + 0.00002)\,\text{GeV}^{-1}$. In both scenarios, we find a stronger increase of the pull below these lines than above (with respect to the y-axis). Finally, in either scenario, for increasing values of $|\gamma_{\text{OS}}|$ the regions of the predictions that lie within the 1σ uncertainty band of the measurement widen up.

5.4.3. The forward–backward asymmetry in the DASM

In the era of the Large Electron–Positron Collider (LEP) [113] various precision measurements of a large set of observables were performed by the experiments ALEPH, DELPHI, L3, and OPAL (see Refs. [114–117]). Colliding electrons and positrons with a centre-of-mass energy close to the Z-boson resonance, high-precision measurements of cross sections ("Z lineshape"), and forward–backward

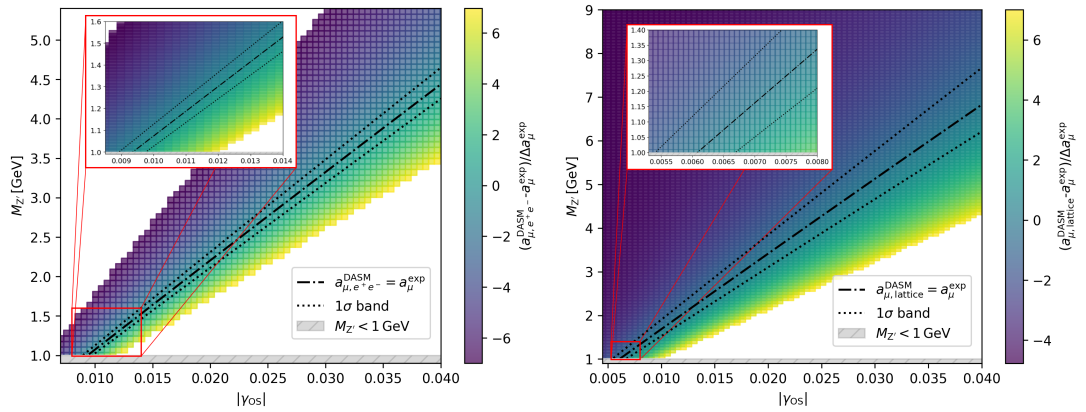

Figure 5.14.: The pull for a_μ in the $|\gamma_{OS}|$–$M_{Z'}$ plane within benchmark scenario (i). We use either $a_{\mu,e^+e^-}^{SM}$ (left) or $a_{\mu,\text{lattice}}^{SM}$ (right) for the derivation of a_μ^{DASM}. The black dashed line marks the $|\gamma_{OS}|$–$M_{Z'}$ combinations that lead to exact agreement between predictions and measurement, and the black dotted lines mark the 1σ uncertainty band of the measurement.

asymmetries A_{FB} were performed. The four experiments decided to combine their results for the POs in a widely model-independent way [118]. Therefore, they parameterize the measured POs by a common set of pseudo-observables[12]. Finally, the results for these pseudo-observables for each experiment were combined resulting in even more accurate results. In this section, we briefly discuss the influence of BSM effects introduced by the DASM on the leptonic forward–backward asymmetry A_{FB}^l, which is one of the (true) observables measured by each of the experiments. This is done to ensure that the BSM contributions do not spoil the effective parameterization of their measurements by the pseudo-observables used in the combination of the results from the four experiments[13]. In the Sects. 5.4.4 and 5.4.5, we present the prediction for two of the above mentioned pseudo-observables, the leptonic effective weak mixing angle $s^2_{w,\text{eff},l}$ and the leptonic partial decay width of the Z boson, $\Gamma_{Z\to ll}$, in the DASM. Both yield excellent tests of the Zll-coupling structure, and, thus, excellent tests of any SM extension that modifies lepton–Z-boson interactions.

[12]Note that we will explicitly differentiate between the terminologies of pseudo-observables (inherently model dependent) and "real" observables, i.e. counting rates, in the discussions given in Sects. 5.4.3-5.4.5, but use the term observable throughout the rest of this work for either of the two.

[13]Even though the parameterization of the results in terms of the pseudo-observables is widely model independent, it still assumes a certain SM-like particle content. The analysis given in Sect. 5.4.3 will confirm that the presence of the Z′ boson will not spoil this assumption in the interesting regions of the parameter space, which would otherwise add additional uncertainties to results obtained from investigating the respective pseudo-observables.

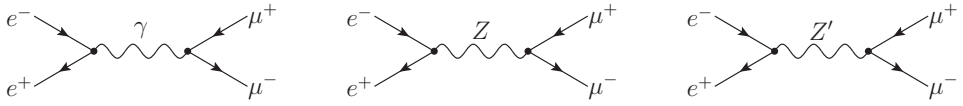

Figure 5.15.: Feynman diagrams contributing to A_{FB} at LO in the DASM.

One of the POs measured by the LEP experiments is the leptonic forward–backward asymmetry A^l_{FB}. Here, we investigate the influence of the BSM structures, introduced in A^l_{FB} by the DASM already at LO by additional contributions due to Z′-boson exchange. If we find their influence to be negligible, we can safely assume that the definitions of the pseudo-observables $s^2_{\mathrm{w,eff},l}$ and $\Gamma_{\mathrm{Z}\to ll}$, as given in Ref. [118], reflect the parameter dependences of the PO predictions within the DASM with sufficient precision. The leptonic forward–backward asymmetry is defined by

$$A^l_{\mathrm{FB}} = \frac{\sigma^l_{\mathrm{F}} - \sigma^l_{\mathrm{B}}}{\sigma^l_{\mathrm{F}} + \sigma^l_{\mathrm{B}}}, \tag{5.47}$$

with

$$\sigma^l_{\mathrm{F}} = 2\pi \int_0^1 \mathrm{d}\cos\theta \, \frac{\mathrm{d}\sigma^l}{\mathrm{d}\Omega}, \qquad \sigma^l_{\mathrm{B}} = 2\pi \int_{-1}^0 \mathrm{d}\cos\theta \, \frac{\mathrm{d}\sigma^l}{\mathrm{d}\Omega}, \tag{5.48}$$

where $\frac{\mathrm{d}\sigma^l}{\mathrm{d}\Omega}$ is the differential cross section of the process $e^+e^- \to l\bar{l}$, $l = e, \mu, \tau$, and θ is defined as the scattering angle between the incoming electron and the outgoing lepton. For simplicity, we focus on the muonic final state[14] in the following discussion. Neglecting electron-mass effects, in the DASM the three Feynman diagrams shown in Fig. 5.15 contribute to A^μ_{FB} at LO. Considering unpolarized electrons in the initial state, the LO differential cross section can be parameterized by

$$\frac{\mathrm{d}\sigma^\mu}{\mathrm{d}\Omega} = \frac{\alpha_{\mathrm{em}}(0)^2}{4s} \left[G^\mu_1(s)(1 + \cos^2\theta) + 2G^\mu_3(s)\cos\theta \right], \tag{5.49}$$

where $\sqrt{s}$ is the centre-of-mass energy. In the DASM, the factors $G_1(s)$ and $G_3(s)$ can further be split up into contributions originating from the pure Z, Z′, and γ exchange, and contributions coming from the interference of the respective diagrams

$$G_1^{\mu,\mathrm{DASM}}(s) = G_1^{\mathrm{ZZ}}(s) + G_1^{\gamma\mathrm{Z}}(s) + G_1^{\gamma\gamma}(s) + G_1^{\mathrm{Z'Z'}}(s) + G_1^{\gamma\mathrm{Z'}}(s) + G_1^{\mathrm{ZZ'}}(s), \tag{5.50}$$

$$G_3^{\mu,\mathrm{DASM}}(s) = G_3^{\mathrm{ZZ}}(s) + G_3^{\gamma\mathrm{Z}}(s) + G_3^{\mathrm{Z'Z'}}(s) + G_3^{\gamma\mathrm{Z'}}(s) + G_3^{\mathrm{ZZ'}}(s). \tag{5.51}$$

Using Eq. (5.48), the muonic forward–backward asymmetry at LO is given by

$$A^{\mu,\mathrm{DASM}}_{\mathrm{FB}}(s) = \frac{3}{4} \frac{G_3^{\mu,\mathrm{DASM}}(s)}{G_1^{\mu,\mathrm{DASM}}(s)}. \tag{5.52}$$

[14]Note that Bhabha scattering ($e^+e^- \to e^+e^-$) gets additional contributions from t-channel diagrams.

In the following, we are only interested in the kinematic region $s \approx M_{\mathrm{Z}}^2$. In this region the Z-boson exchange is resonance enhanced, and width effects, reflecting the unstable nature of the Z boson, have to be taken into account properly. To introduce the total decay width Γ_{Z} of the Z boson properly, we resum the self-energy corrections [119, 120] to the Z-boson propagator, using Dyson resummation, leading to a correction to the Z-boson propagator in the DASM with a similar structure to its SM counterpart,

$$\begin{aligned} G_{\mathrm{R}}^{\mathrm{ZZ}}(s) &\underset{s\to M_{\mathrm{Z}}^2}{\sim} \frac{\mathrm{i}}{s - M_{\mathrm{Z}}^2 + \Sigma_{\mathrm{R,T}}^{\mathrm{ZZ}}(s) + \kappa(s)}, \\ \kappa(s) &= \frac{\Sigma_{\mathrm{R,T}}^{\mathrm{AZ}}(s)(\Sigma_{\mathrm{R,T}}^{\mathrm{AZ}}(s)[s - M_{\mathrm{Z}'}^2 + \Sigma_{\mathrm{R,T}}^{\mathrm{Z'Z'}}(s)] - 2\Sigma_{\mathrm{R,T}}^{\mathrm{AZ'}}(s)\Sigma_{\mathrm{R,T}}^{\mathrm{ZZ'}}(s))}{(\Sigma_{\mathrm{R,T}}^{\mathrm{AZ'}}(s))^2 - (s + \Sigma_{\mathrm{R,T}}^{\mathrm{AA}}(s))(s - M_{\mathrm{Z}'}^2 + \Sigma_{\mathrm{R,T}}^{\mathrm{Z'Z'}}(s))} \\ &\quad + \frac{[s + \Sigma_{\mathrm{R,T}}^{\mathrm{AA}}(s)]\Sigma_{\mathrm{R,T}}^{\mathrm{ZZ'}}(s)}{(\Sigma_{\mathrm{R,T}}^{\mathrm{AZ'}}(s))^2 - (s + \Sigma_{\mathrm{R,T}}^{\mathrm{AA}}(s))(s - M_{\mathrm{Z}'}^2 + \Sigma_{\mathrm{R,T}}^{\mathrm{Z'Z'}}(s))}. \end{aligned} \tag{5.53}$$

Note, that the SM expression, i.e. $\kappa = -(\Sigma_{\mathrm{R,T}}^{\mathrm{AZ}}(s))^2/(s + \Sigma_{\mathrm{R,T}}^{\mathrm{AA}}(s))$, is directly recovered in the decoupling limit, i.e. by setting all off-diagonal self-energies with a Z′ boson to zero. For $s \approx M_{\mathrm{Z}}^2$ the quantity $\kappa(s)$ resembles at least NLO effects to the Z-boson propagator as long as $|M_{\mathrm{Z}} - M_{\mathrm{Z}'}| \gg \Sigma_{\mathrm{R,T}}^{\mathrm{VV'}}(s)$, $V, V' = \mathrm{A}, \mathrm{Z}, \mathrm{Z}'$, which is a well-motivated assumption, having the discussions of the previous chapters in mind[15]. In the quantitative discussion here, we are only interested in LO accuracy, and, thus, we can safely neglect the contributions originating from $\kappa(s)$ in the following. In on-shell renormalization, we further have

$$\mathrm{Re}\big\{\Sigma_{\mathrm{R,T}}^{\mathrm{ZV}}(M_{\mathrm{Z}}^2)\big\} = 0, \qquad V = \mathrm{A,Z,Z'}. \tag{5.54}$$

Using the optical theorem,

$$M_{\mathrm{Z}}\Gamma_{\mathrm{Z}} = \mathrm{Im}\{\Sigma_{\mathrm{R,T}}^{\mathrm{ZZ}}(M_{\mathrm{Z}}^2)\}, \tag{5.55}$$

to connect the imaginary part of the self-energy with Γ_{Z}, and the approximation

$$\mathrm{Im}\{\Sigma_{\mathrm{R,T}}^{\mathrm{ZZ}}(s)\} \approx \frac{s}{M_{\mathrm{Z}}^2}\mathrm{Im}\{\Sigma_{\mathrm{R,T}}^{\mathrm{ZZ}}(M_{\mathrm{Z}}^2)\}, \tag{5.56}$$

one finds for the Z-boson propagator in the vicinity of its pole

$$G_{\mathrm{R}}^{\mathrm{ZZ}}(s) \underset{s\to M_{\mathrm{Z}}^2}{\sim} \frac{\mathrm{i}}{s - M_{\mathrm{Z}}^2 + \mathrm{i}s\frac{\Gamma_{\mathrm{Z}}}{M_{\mathrm{Z}}}}. \tag{5.57}$$

In this approximation the various contributions to the leptonic forward–backward asymmetry at $s \sim M_{\mathrm{Z}}^2$ are given by

$$G_1^{\gamma\mathrm{Z}}(s) \underset{s\to M_{\mathrm{Z}}^2}{\sim} \frac{s v_l^2 (s - M_{\mathrm{Z}}^2)}{2c_{\mathrm{w}}^2 s_{\mathrm{w}}^2((M_{\mathrm{Z}}^2 - s)^2 + M_{\mathrm{Z}}^2\Gamma_{\mathrm{Z}}^2)} \to 0, \tag{5.58}$$

[15] Furthermore, since $M_{\mathrm{Z}'} \to M_{\mathrm{Z}}$ leads to decoupling of the gauge-sector extension introduced by the DASM, $\kappa(s)$ will, similar to the respective SM case, even in this limit only contribute at NLO to the Z-boson propagator.

$$G_1^{\mathrm{ZZ}'}(s) \underset{s\to M_\mathrm{Z}^2}{\sim} \frac{s^2(s-M_\mathrm{Z}^2)(a_l a_l' + v_l v_l')^2}{8c_\mathrm{w}^4 s_\mathrm{w}^4 (s-M_{\mathrm{Z}'}^2)((s-M_\mathrm{Z}^2)^2 + M_\mathrm{Z}^2\Gamma_\mathrm{Z}^2)} \to 0, \tag{5.59}$$

$$G_1^{\gamma\gamma}(s) \underset{s\to M_\mathrm{Z}^2}{\sim} 1, \tag{5.60}$$

$$G_1^{\mathrm{ZZ}}(s) \underset{s\to M_\mathrm{Z}^2}{\sim} \frac{s^2\left(v_l^2+a_l^2\right)^2}{16 s_\mathrm{w}^4 c_\mathrm{w}^4((s-M_\mathrm{Z}^2)^2 + M_\mathrm{Z}^2\Gamma_\mathrm{Z}^2)} \to \frac{\left(v_l^2+a_l^2\right)^2 M_\mathrm{Z}^2}{16 s_\mathrm{w}^4 c_\mathrm{w}^4 \Gamma_\mathrm{Z}^2}, \tag{5.61}$$

$$G_1^{\mathrm{Z}'\mathrm{Z}'}(s) \underset{s\to M_\mathrm{Z}^2}{\sim} \frac{s^2\left(v_l'^2+a_l'^2\right)^2}{16 c_\mathrm{w}^4 s_\mathrm{w}^4 (s-M_{\mathrm{Z}'}^2)^2} \to \frac{\left(v_l'^2+a_l'^2\right)^2 M_\mathrm{Z}^4}{16 c_\mathrm{w}^4 s_\mathrm{w}^4 (M_\mathrm{Z}^2-M_{\mathrm{Z}'}^2)^2}, \tag{5.62}$$

$$G_1^{\gamma\mathrm{Z}'}(s) \underset{s\to M_\mathrm{Z}^2}{\sim} \frac{s v_l'^2}{2c_\mathrm{w}^2 s_\mathrm{w}^2 (s-M_{\mathrm{Z}'}^2)} \to \frac{v_l'^2 M_\mathrm{Z}^2}{2c_\mathrm{w}^2 s_\mathrm{w}^2 (M_\mathrm{Z}^2-M_{\mathrm{Z}'}^2)}, \tag{5.63}$$

$$G_3^{\gamma\mathrm{Z}}(s) \underset{s\to M_\mathrm{Z}^2}{\sim} \frac{s a_l^2 (s-M_\mathrm{Z}^2)}{2c_\mathrm{w}^2 s_\mathrm{w}^2 ((s-M_\mathrm{Z}^2)^2 + M_\mathrm{Z}^2\Gamma_\mathrm{Z}^2)} \to 0, \tag{5.64}$$

$$G_3^{\mathrm{ZZ}'}(s) \underset{s\to M_\mathrm{Z}^2}{\sim} \frac{s^2(s-M_\mathrm{Z}^2)(v_l a_l' + a_l v_l')^2}{8c_\mathrm{w}^4 s_\mathrm{w}^4 (s-M_{\mathrm{Z}'}^2)((s-M_\mathrm{Z}^2)^2 + M_\mathrm{Z}^2\Gamma_\mathrm{Z}^2))} \to 0, \tag{5.65}$$

$$G_3^{\mathrm{ZZ}}(s) \underset{s\to M_\mathrm{Z}^2}{\sim} \frac{s^2 v_l^2 a_l^2}{4 s_\mathrm{w}^4 c_\mathrm{w}^4 ((s-M_\mathrm{Z}^2)^2 + M_\mathrm{Z}^2\Gamma_\mathrm{Z}^2)} \to \frac{v_l^2 a_l^2 M_\mathrm{Z}^2}{4 s_\mathrm{w}^4 c_\mathrm{w}^4 \Gamma_\mathrm{Z}^2}, \tag{5.66}$$

$$G_3^{\mathrm{Z}'\mathrm{Z}'}(s) \underset{s\to M_\mathrm{Z}^2}{\sim} \frac{s^2 v_l'^2 a_l'^2}{4 c_\mathrm{w}^4 s_\mathrm{w}^4 (s-M_{\mathrm{Z}'}^2)^2} \to \frac{v_l'^2 a_l'^2 M_\mathrm{Z}^4}{4 c_\mathrm{w}^4 s_\mathrm{w}^4 (M_\mathrm{Z}^2-M_{\mathrm{Z}'}^2)^2}, \tag{5.67}$$

$$G_3^{\gamma\mathrm{Z}'}(s) \underset{s\to M_\mathrm{Z}^2}{\sim} \frac{s a_l'^2}{2c_\mathrm{w}^2 s_\mathrm{w}^2 (s-M_{\mathrm{Z}'}^2)} \to \frac{a_l'^2 M_\mathrm{Z}^2}{2c_\mathrm{w}^2 s_\mathrm{w}^2 (M_\mathrm{Z}^2-M_{\mathrm{Z}'}^2)}, \tag{5.68}$$

where we made use of lepton universality and the limit in each row holds for $s = M_\mathrm{Z}^2$. The LO vector and axial-vector couplings of the Zll and $Z'll$ interactions are given by

$$v_l = \frac{c_\gamma c_\mathrm{w}^2 (3M_\mathrm{Z}^2 - 4M_\mathrm{W}^2)}{2M_\mathrm{W}^2}, \qquad a_l = -\frac{c_\gamma c_\mathrm{w}^2 M_\mathrm{Z}^2}{2M_\mathrm{W}^2}, \tag{5.69}$$

$$v_l' = \frac{(c_\mathrm{w}^2 - 3s_\mathrm{w}^2)\, s_\gamma - 3\eta s_\mathrm{w} c_\gamma}{2}, \qquad a_l' = \frac{\eta s_\mathrm{w} c_\gamma + s_\gamma}{2}, \tag{5.70}$$

respectively. While there is never a contribution $G_3^{\gamma\gamma}$ to A_FB, the interference terms resulting from the interference of the γ- and Z′-boson exchange diagrams with the Z-boson exchange diagram (see Eqs. (5.58),(5.59),(5.64), and (5.65)) contribute to the forward–backward asymmetry at higher loop orders even for a centre-of-mass energy $s = M_\mathrm{Z}^2$. As already mentioned above, we are here interested in the influence of the contributions originating from the presence of the right diagram in Fig. 5.15, i.e. the parts $G_i^{V\mathrm{Z}'}$, with $i = 1, 3$ and $V = \gamma, \mathrm{Z}, \mathrm{Z}'$ at $s = M_\mathrm{Z}^2$. Thus, we compare A_FB^l using the full LO result given by Eqs. (5.58)–(5.68) with $A_\mathrm{FB}^{l,\text{SM-like}}$, where we only include contributions from the γ- and Z-boson exchange diagrams, but set all $G_i^{V\mathrm{Z}'}$ to zero. To account for the results of the previous sections, we constrain the $|\gamma|$ region to small values and use the experimental world average,

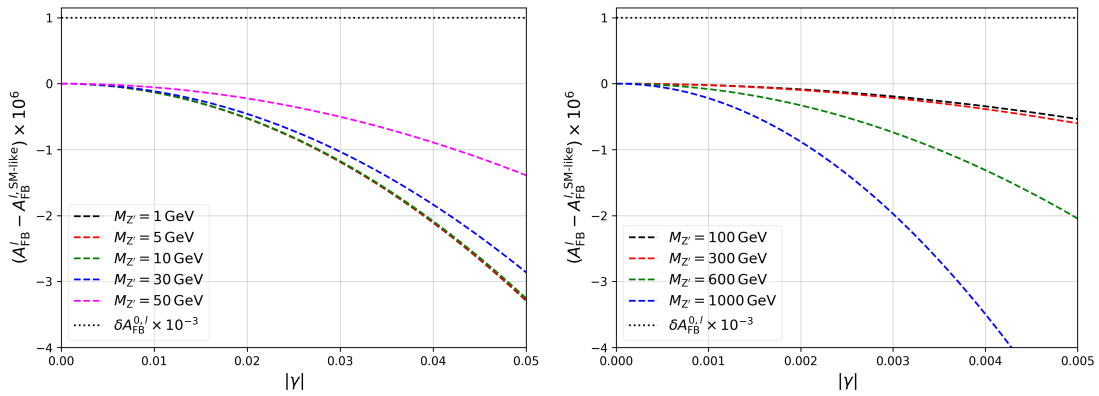

Figure 5.16.: Influence of the Z′-boson exchange diagram present in the DASM on A_{FB}^{l} at LO for different values of $|\gamma|$ and $M_{\mathrm{Z}'}$. Here, $A_{\mathrm{FB}}^{l,\mathrm{SM\text{-}like}}$ denotes the forward–backward asymmetry, where all contributions introduced by the Z′-boson exchange diagram are neglected. For comparison, the black dotted line shows the experimental uncertainty $\Delta A_{\mathrm{FB}}^{0,l} = 0.0010$ of the leptonic peak asymmetry.

$M_{\mathrm{W}} = 80.377\,\mathrm{GeV}$, for the mass of the W boson[16], as well as $\Gamma_{\mathrm{Z}} = 2.499\,\mathrm{GeV}$ [16] for the total Z-boson decay width. The remaining input parameters are taken from Eq. (5.6). Further, we note that all results in this section are symmetric with respect to $\gamma_{\mathrm{OS}} \to -\gamma_{\mathrm{OS}}$. In Fig. 5.16 the difference between A_{FB}^{l} and $A_{\mathrm{FB}}^{l,\mathrm{SM\text{-}like}}$ is given for some exemplary values for $M_{\mathrm{Z}'}$ for the cases $M_{\mathrm{Z}'} < M_{\mathrm{Z}}$ (left) and $M_{\mathrm{Z}'} > M_{\mathrm{Z}}$ (right). As a reference value for the experimental accuracy we plot the experimental uncertainty $\Delta A_{\mathrm{FB}}^{0,l} = 0.0010$ (taken from Tab. 2.13 of Ref. [118]) of the so-called leptonic peak asymmetry[17] $A_{\mathrm{FB}}^{0,l}$. The leptonic peak asymmetry is one of the aforementioned pseudo-observables, used in the combination of the results of the four LEP experiments, that resembles the weak corrections to A_{FB}^{l} at $\sqrt{s} = M_{\mathrm{Z}}$ (for the exact definition of $A_{\mathrm{FB}}^{0,l}$ see Eq. (5.75)). In general, the presence of the Z′-boson exchange diagram leads to a decrease of A_{FB}^{l} at LO, making the differences shown in Fig. 5.16 negative for all $|\gamma|$–$M_{\mathrm{Z}'}$ combinations. While the BSM effects seem to influence A_{FB}^{l} stronger in the case $M_{\mathrm{Z}'} > M_{\mathrm{Z}}$ (note the different scales of $|\gamma|$ in the two plots), their influence in the interesting regions of the parameter space is only of generic order $\sim 10^{-6}$ and thus negligible compared to the size of the experimental uncertainty $\Delta A_{\mathrm{FB}}^{0,l} = 10^{-3}$. In Fig. 5.17 the absolute magnitude of the different $G_i^{VV'}$, $i = 1, 3$, $VV' = \mathrm{gg}, \mathrm{ZZ}, \mathrm{Z}'\mathrm{Z}', g\mathrm{Z}'$, contributing to A_{FB}^{l} at LO is shown for $M_{\mathrm{Z}'} = 5\,\mathrm{GeV}$ (upper line) and $M_{\mathrm{Z}'} = 600\,\mathrm{GeV}$ (lower line). Again, one clearly finds the contributions induced by the presence of the

[16] This is only done here in the quantitative discussion of A_{FB}^{l} in this section. All other results make use of the prediction $M_{\mathrm{W}}^{\mathrm{DASM}}$ if not explicitly stated otherwise.

[17] This is the best we can do, since the combination of the results was only performed for the pseudo-observables.

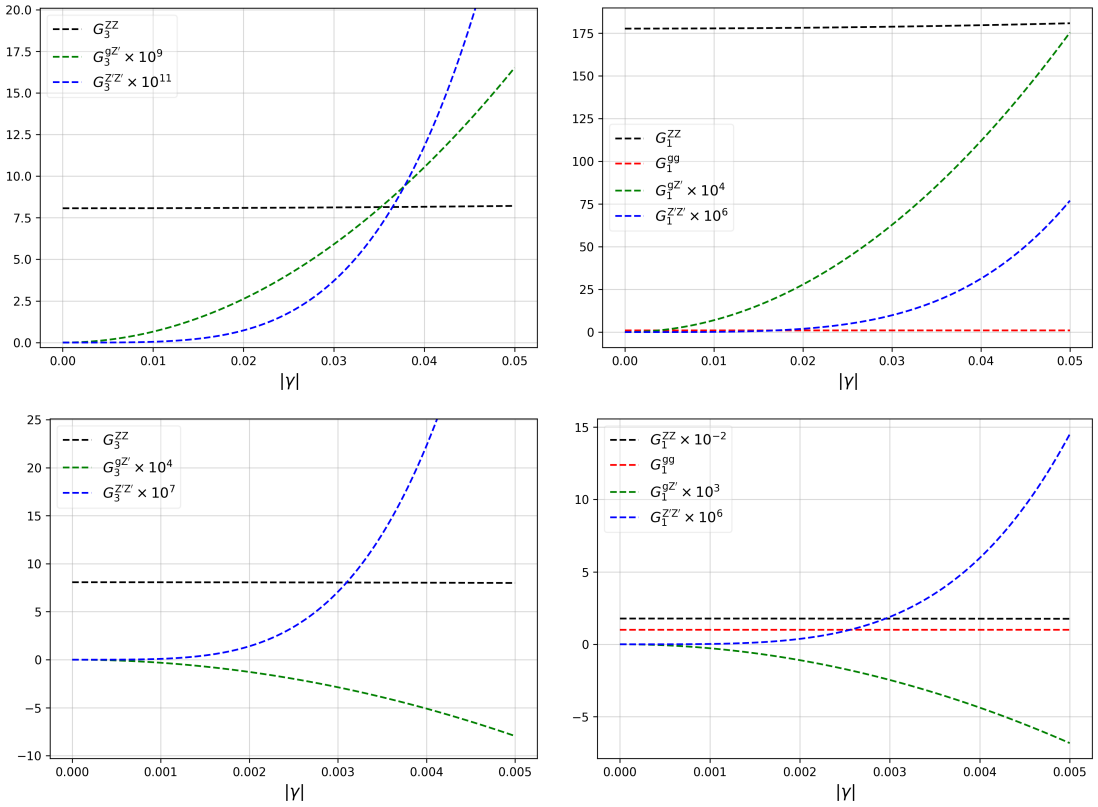

Figure 5.17.: The various LO contributions to A_{FB}^{l} for $M_{\mathrm{Z}'} = 5\,\mathrm{GeV}$ (upper row) and $M_{\mathrm{Z}'} = 600\,\mathrm{GeV}$ (lower row).

Z′-boson exchange diagram to be largely suppressed with respect to the SM-like contributions. Thus, we can safely neglect the influence of the right Feynman diagram given in Fig. 5.15 in the following.
Note that the BSM effects affecting the Z-boson exchange diagram are, of course, taken into account by the BSM effects contained in the Z-pole POs in all considerations in this and the following sections.

5.4.4. The effective leptonic weak mixing angle

Having the results of the previous section in mind, we now derive the predictions for the effective leptonic weak mixing angle in the DASM. Due to its precisely measured value it yields a high-precision test of the vector and axial-vector couplings of the Z boson to leptons.
The LO vector and axial-vector couplings (v_l and a_l, respectively) can be promoted to the effective NLO vector and axial-vector couplings (V_l and A_l, respectively). Neglecting the masses of the external leptons in the calculation, they capture the "weak" NLO corrections of the Zll interaction, i.e. the NLO EW corrections minus their pure photonic QED contributions. In detail, they are defined via promoting

the LO vector and axial-vector couplings to effective NLO couplings in the $Z \to ll$ decay matrix element

$$\mathcal{M}(Z \to ll) = \frac{e}{s_w c_w} \left[\bar{u}_l \not{\epsilon}_Z \left(V_l - A_l \gamma_5\right) v_l\right] + \ldots, \tag{5.71}$$

where the dots represent the aforementioned small corrections proportional to the mass of the final state lepton, which are neglected in this work. Using these effective NLO couplings, the effective leptonic weak mixing angle is defined by (see e.g. Ref. [118])

$$s^2_{w,\text{eff},l} = \frac{1}{4}\left(1 - \text{Re}\left\{\frac{V_l}{A_l}\right\}\right). \tag{5.72}$$

Note that at LO Eq. (5.72) does not depend on any BSM parameters and simply yields to the respective SM result

$$s^{2,\text{LO}}_{w,\text{eff},l} = 1 - \frac{M_W^2}{M_Z^2} = \left(s^{\text{SM}}_w\right)^2. \tag{5.73}$$

To obtain the best prediction in the DASM we take the difference between the NLO predictions of the DASM and the SM, and add it to the best SM prediction $s^{2,\text{SM}}_{w,\text{eff},l}$ taken from Ref. [121],

$$s^{2,\text{DASM}}_{w,\text{eff},l} = s^{2,\text{SM}}_{w,\text{eff},l} + \Delta s^{2,\text{NLO}}_{w,\text{eff},l}\,, \qquad \Delta s^{2,\text{NLO}}_{w,\text{eff},l} = s^{2,\text{DASM}}_{w,\text{eff},l,\text{NLO}} - s^{2,\text{SM}}_{w,\text{eff},l,\text{NLO}}. \tag{5.74}$$

The authors of Ref. [121] give an approximation for the parametric dependence of their result, which is used for all predictions of $s^{2,\text{SM}}_{w,\text{eff},l}$ in the following. In the discussion of the explicit parameter dependence of $s^{2,\text{DASM}}_{w,\text{eff},l}$ on the additional parameters introduced by the DASM we make use of the G_μ-scheme. As standard input we choose Eq. (5.6) for the SM-like input parameters and Eqs. (5.7) and (5.8) for the BSM parameters of the DASM, which is, of course, only used for the parameters that are not varied in the respective plot. For these values we find $s^{2,\text{SM}}_{w,\text{eff},l} = 0.23157$. Note that, at LO $s^{2,\text{DASM}}_{w,\text{eff},l}$ seems to be independent of γ (see Eq. (5.73)). However, we use the DASM prediction for the W-boson mass as input for the prediction (see Sect. 5.4.1), which introduces a dependence of the prediction on γ already at LO (and, thus, on $\delta\gamma$ at NLO). Similar to the previous discussions, we restrict the analysis here to $M_h, M_{Z'} > 1\,\text{GeV}$ to account for the approximations performed in the derivation of the W-boson mass predictions. For the experimental result we use the value from Tab. 2.13 of Ref. [118] and their definition of the leptonic peak asymmetry

$$A^{0,l}_{\text{FB}} = \frac{3\left[\text{Re}\left\{V_l/A_l\right\}\right]^2}{\left(1 + \left[\text{Re}\left\{V_l/A_l\right\}\right]^2\right)^2} = \frac{3(1 - 4s^2_{w,\text{eff},l})^2}{(1 + [1 - 4s^2_{w,\text{eff},l}]^2)^2}, \tag{5.75}$$

and find

$$s^{2,\mathrm{exp}}_{\mathrm{w,eff},l} = 0.23102 \pm 0.00056, \tag{5.76}$$

for the measured value used in our studies. Note that, Eq. (5.76) is in agreement with the official result of $s^{2,\mathrm{LEP}}_{\mathrm{w,eff},l} = 0.23153 \pm 0.00016$ given in Ref. [118]. However, their stated central value is shifted upwards by $\approx 1\sigma$ and their uncertainty is significantly smaller than the one we find (see Eq. (5.76)). To determine $s^{2,\mathrm{LEP}}_{\mathrm{w,eff},l}$, the authors of Ref. [118] do not only use the forward–backward asymmetry measurements for leptons (summarized in Tab. 2.13 of Ref. [118], which is used in this work), but further asymmetry measurements for quark pairs in the final state[18], as well as the so-called left–right asymmetries measured at SLC (for more details see Ref. [118] and references therein). To this end, a model-dependent correction has to be applied to the data in order to account for the differences between leptons and up-, and down-type quarks. These corrections are taken from the SM, which differ from the respective corrections within the DASM. Furthermore, Tab. 2.13 of Ref. [118] provides the only stated correlation coefficients connecting the measurements of the pseudo-observables, $s^{2,\mathrm{exp}}_{\mathrm{w,eff},l}$ and $\Gamma^{\mathrm{exp}}_{\mathrm{Z}\to ll}$, investigated in this work. These correlations should be taken into account in any quantitative analysis. Therefore, Eq. (5.76) is the preferred choice for the experimental result of the effective weak mixing angle used in this work. Further, we remark that in the found best fit scenarios (see Sect. 5.5.1 for details) the predictions for $s^{2,\mathrm{DASM}}_{\mathrm{w,eff},l}$ vary only loosely in the vicinity of the minimum of the minimized function and are close to the SM value. Thus, we find that $s^{2,\mathrm{DASM}}_{\mathrm{w,eff},l}$ does not lead to dominant contributions in the minimization process performed in Sect. 5.5.4.

5.4.4.1. Benchmark Scenario (i): $M_{\mathsf{h}} = M^{\mathsf{SM}}_{\mathsf{h}}$

We find $s^{2,\mathrm{DASM}}_{\mathrm{w,eff},l}$ to be symmetric with respect to $\gamma_{\mathrm{OS}} \to -\gamma_{\mathrm{OS}}$. Furthermore, in benchmark scenario (i), we see only a small (with respect to the experimental uncertainty) dependence of $s^{2,\mathrm{DASM}}_{\mathrm{w,eff},l}$ on the mixing angle γ_{OS} within the investigated interval, as can be seen in the upper-left plot in Fig. 5.18. For increasing values of $|\gamma_{\mathrm{OS}}|$, the prediction increases for $M_{\mathrm{Z}'} > M_{\mathrm{Z}}$ and decreases for $M_{\mathrm{Z}'} < M_{\mathrm{Z}}$. At $\gamma_{\mathrm{OS}} = 0$ the prediction is shifted downwards compared to the SM prediction (black dashed line), showcasing the influence of the Higgs- and fermion-sector extensions of the DASM on the prediction at this parameter point in benchmark scenario (i). In the upper-right plot of Fig. 5.18, we show the dependence of $s^{2,\mathrm{DASM}}_{\mathrm{w,eff},l}$ on $M_{\mathrm{Z}'}$. The dependence of the prediction for $s^{2,\mathrm{DASM}}_{\mathrm{w,eff},l}$ for values of $M_{\mathrm{Z}'} < 250\,\mathrm{GeV}$ is small compared to the measurement uncertainty. For $M_{\mathrm{Z}'} > 250\,\mathrm{GeV}$ the prediction decreases for an increasing mass of the Z′ boson, bringing the prediction closer to the measured value. For very small values of $|\gamma_{\mathrm{OS}}| = 10^{-3}$ the dependence on the Z′-boson mass is negligible in the entire shown interval.

[18] Here, especially the b-quark final state leads to a very precise results.

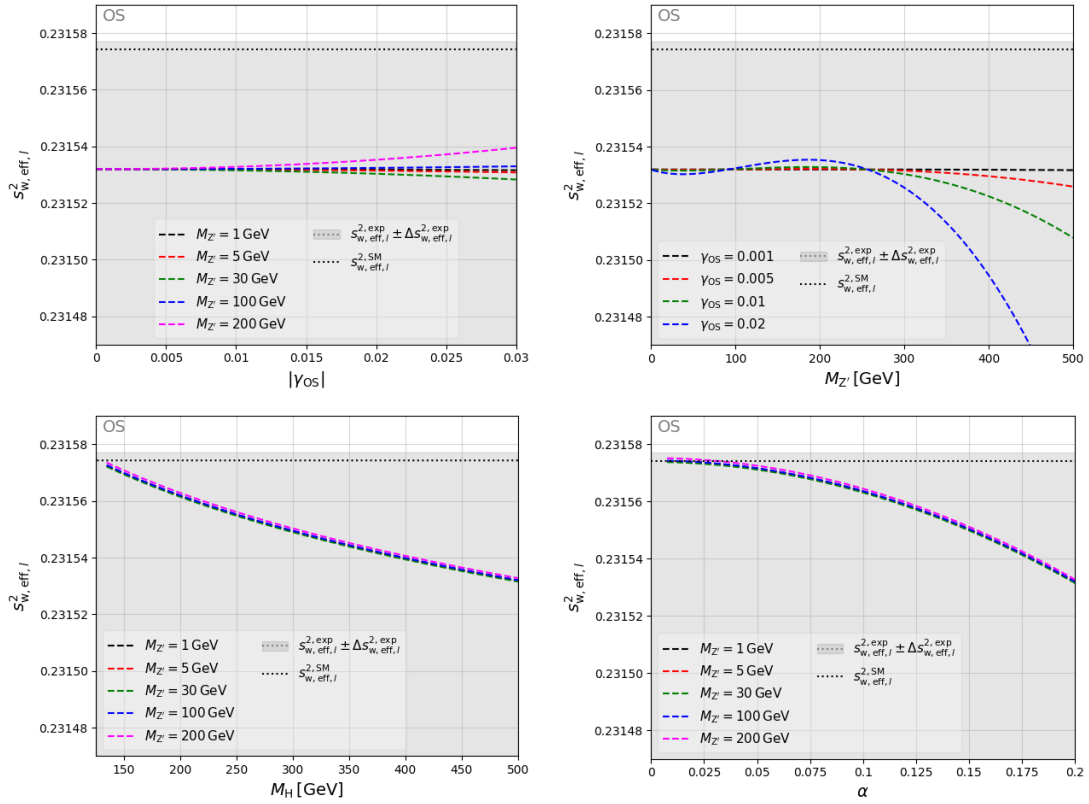

Figure 5.18.: Dependence of $s^{2,\text{DASM}}_{\text{w,eff},l}$ on $|\gamma_{\text{OS}}|$ (upper left), $M_{\text{Z}'}$ (upper right), M_{H} (lower left), and α (lower right) is shown within benchmark scenario (i).

The dependence on the mass of the additional Higgs boson M_{H} (lower left) and the Higgs mixing angle α (lower right) is shown in Fig. 5.18. We find the prediction for $s^{2,\text{DASM}}_{\text{w,eff},l}$ to be symmetric in the parameter α ($\alpha \to -\alpha$) and the influence of a sign flip of the parameter[19] λ_{12} ($\lambda_{12} \to -\lambda_{12}$) to be negligible in both benchmark scenarios (i) and (ii). For increasing values of M_{H} and α, $s^{2,\text{DASM}}_{\text{w,eff},l}$ decreases. This effect is, however, small compared to the experimental uncertainty. The influence of the remaining BSM parameters λ_{12}, θ_{r}, and m_{ν_4} on $s^{2,\text{DASM}}_{\text{w,eff},l}$ turn out to be negligible in benchmark scenario (i).

5.4.4.2. Benchmark Scenario (ii): $M_{\text{H}} = M^{\text{SM}}_{\text{h}}$

For both, the variations of $|\gamma_{\text{OS}}|$ or $M_{\text{Z}'}$, shown in the upper-left and upper-right plots of Fig. 5.19, respectively, the predictions show a very similar dependence as in benchmark scenario (i). However, investigating the influence of the Higgs- and fermion-sector extensions at $\gamma_{\text{OS}} = 0$, we find an upward shift (in contrast to the downward shift in benchmark scenario (i)) with respect to the SM prediction.

[19]Here, we always adjust the signs of λ_{12} and α such that the convention $s_{2\alpha}\lambda_{12} > 0$ is fulfilled.

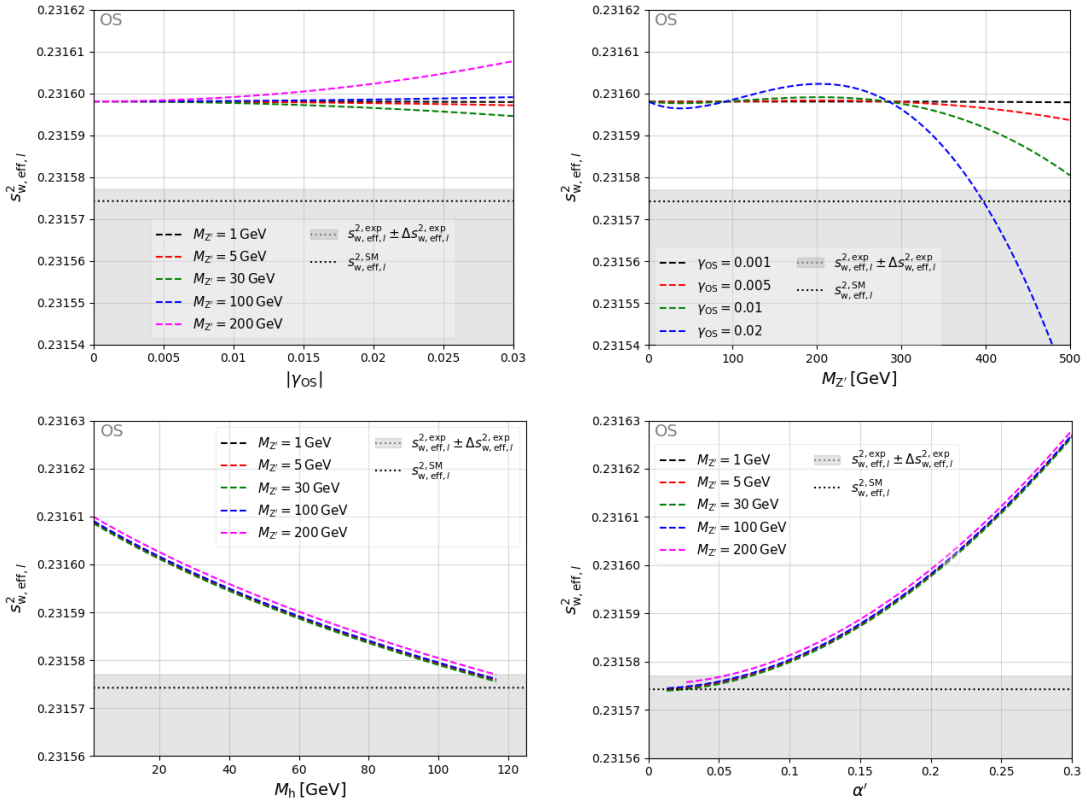

Figure 5.19.: Dependence of $s^{2,\mathrm{DASM}}_{\mathrm{w,eff},l}$ on $|\gamma_{\mathrm{OS}}|$ (upper left), $M_{\mathrm{Z}'}$ (upper right), M_{h} (lower left), and α' (lower right) in benchmark scenario (ii).

The influence of the Higgs-sector parameters M_{h} (lower left) and $\alpha' = \frac{\pi}{2} - \alpha$ (lower right) is shown in Fig. 5.19 in further detail. In contrast to the observation in benchmark scenario (i), we find an increase of the prediction the further the two Higgs-boson masses are apart and for increasing α'. Again, the influence on the remaining BSM parameters λ_{12}, θ_{r}, and m_{ν_4} is negligible in benchmark scenario (ii).

In summary, in both investigated scenarios, the dependence of $s^{2,\mathrm{DASM}}_{\mathrm{w,eff},l}$ on $|\gamma_{\mathrm{OS}}|$, $M_{\mathrm{Z}'}$, α, and $M_{h'}$, where h' denotes the non-SM Higgs boson of h and H, is small compared to the experimental uncertainty of $s^{2,\mathrm{exp}}_{\mathrm{w,eff},l}$. Further, the dependence of $s^{2,\mathrm{DASM}}_{\mathrm{w,eff},l}$ on λ_{12}, θ_{r}, and m_{ν_4} is negligible.

5.4.5. The leptonic partial decay width of the Z boson

The second considered pseudo-observable, used in the combination of the results of the LEP experiments (see above), is the leptonic partial decay width. Similarly to the effective leptonic weak mixing angle, it is defined via (see [118]) the vector

and axial-vector couplings of the Zll interaction. At NLO, it is given by

$$\Gamma_{\mathrm{Z}\to ll} = \frac{(s_{\mathrm{w}}^{\mathrm{SM}} c_{\mathrm{w}}^{\mathrm{SM}})^2}{s_{\mathrm{w}}^2 c_{\mathrm{w}}^2} \frac{G_\mu M_{\mathrm{Z}}^3}{6\sqrt{2}\pi} (1+\delta_{\mathrm{QED}}) \left(|V_l|^2+|A_l|^2\right) + \Delta_{\mathrm{ew/QCD}}, \quad \delta_{\mathrm{QED}} = \frac{3\alpha_{\mathrm{em}}(M_{\mathrm{Z}}^2)}{4\pi}, \tag{5.77}$$

where δ_{QED} accounts for NLO final-state QED corrections. Here, we introduced the SM relations for the sine and cosine of the weak mixing angle

$$\left(s_{\mathrm{w}}^{\mathrm{SM}}\right)^2 = 1 - \left(c_{\mathrm{w}}^{\mathrm{SM}}\right)^2, \qquad \left(c_{\mathrm{w}}^{\mathrm{SM}}\right)^2 = \frac{M_{\mathrm{W}}^2}{M_{\mathrm{Z}}^2}, \tag{5.78}$$

to keep the expression compact. Note that, in contrast to the case for δ_{QED}, we use the G_μ-scheme in the derivation of V_l and A_l. The term $\Delta_{\mathrm{ew/QCD}}$ in Eq. (5.77) accommodates for non-factorizable NNLO effects and, thus, can be neglected in our NLO calculation of DASM corrections. Again, assuming BSM effects to be small, we take the best SM prediction $\Gamma_{\mathrm{Z}\to ll}^{\mathrm{SM}}$ from Ref. [122], and add the difference between the DASM and the SM at NLO to get the most accurate prediction for the leptonic partial decay width of the Z boson in the DASM,

$$\Gamma_{\mathrm{Z}\to ll}^{\mathrm{DASM}} = \Gamma_{\mathrm{Z}\to ll}^{\mathrm{SM}} + \Delta\Gamma_{\mathrm{Z}\to ll}^{\mathrm{NLO}}, \qquad \Delta\Gamma_{\mathrm{Z}\to ll}^{\mathrm{NLO}} = \Gamma_{\mathrm{Z}\to ll}^{\mathrm{DASM,NLO}} - \Gamma_{\mathrm{Z}\to ll}^{\mathrm{SM,NLO}}. \tag{5.79}$$

The authors of Ref. [122] give an approximation for the parametric dependence of their result, which is used for all predictions of $\Gamma_{\mathrm{Z}\to ll}^{\mathrm{SM}}$ in the following. Using the values of Eq. (5.6) we find $\Gamma_{\mathrm{Z}\to ll}^{\mathrm{SM}} = 0.083974\,\mathrm{GeV}$. From Tab. 2.13 of Ref. [118], we take the measured values as well as the definitions

$$R_l^0 = \frac{\Gamma_{\mathrm{had}}}{\Gamma_{\mathrm{Z}\to ll}}, \qquad \sigma_{\mathrm{had}}^0 = \frac{12\pi}{M_{\mathrm{Z}}^2} \frac{\Gamma_{\mathrm{Z}\to ll}\Gamma_{\mathrm{had}}}{\Gamma_{\mathrm{Z}}^2}, \tag{5.80}$$

for the so-called hadronic decay width Γ_{had} and the hadronic pole cross section σ_{had}^0 of the Z boson, to obtain

$$\Gamma_{\mathrm{Z}\to ll}^{\mathrm{exp}} = (0.08399 \pm 0.00009)\,\mathrm{GeV}, \tag{5.81}$$

which is in good agreement with their officially stated result $\Gamma_{\mathrm{Z}\to ll}^{\mathrm{LEP}} = (0.083985 \pm 0.000086)\,\mathrm{GeV}$ [118], for the measured value of the leptonic partial decay width of the Z boson. In the following, we discuss the explicit parameter dependence of $\Gamma_{\mathrm{Z}\to ll}^{\mathrm{DASM}}$ on the BSM parameters of the DASM. As standard input we use Eq. (5.6) for the SM-like input parameters. For these input values we find $\Gamma_{\mathrm{Z}\to ll}^{\mathrm{SM}} = 0.08397\,\mathrm{GeV}$. Due to a negligible dependence of $\Gamma_{\mathrm{Z}\to ll}^{\mathrm{DASM}}$ on the BSM Higgs sector parameters, the predictions turn out to be very similar in the two benchmark scenarios. Thus, we focus on benchmark scenario (i) (see Eq. (5.7)) for the BSM parameters of the DASM in the following, if not explicitly stated otherwise. Finally, we make use of the prediction for the W-boson mass as input for $\Gamma_{\mathrm{Z}\to ll}^{\mathrm{DASM}}$ and, thus, again restrict our discussion to the case $M_{\mathrm{h}}, M_{\mathrm{Z}'} > 1\,\mathrm{GeV}$.

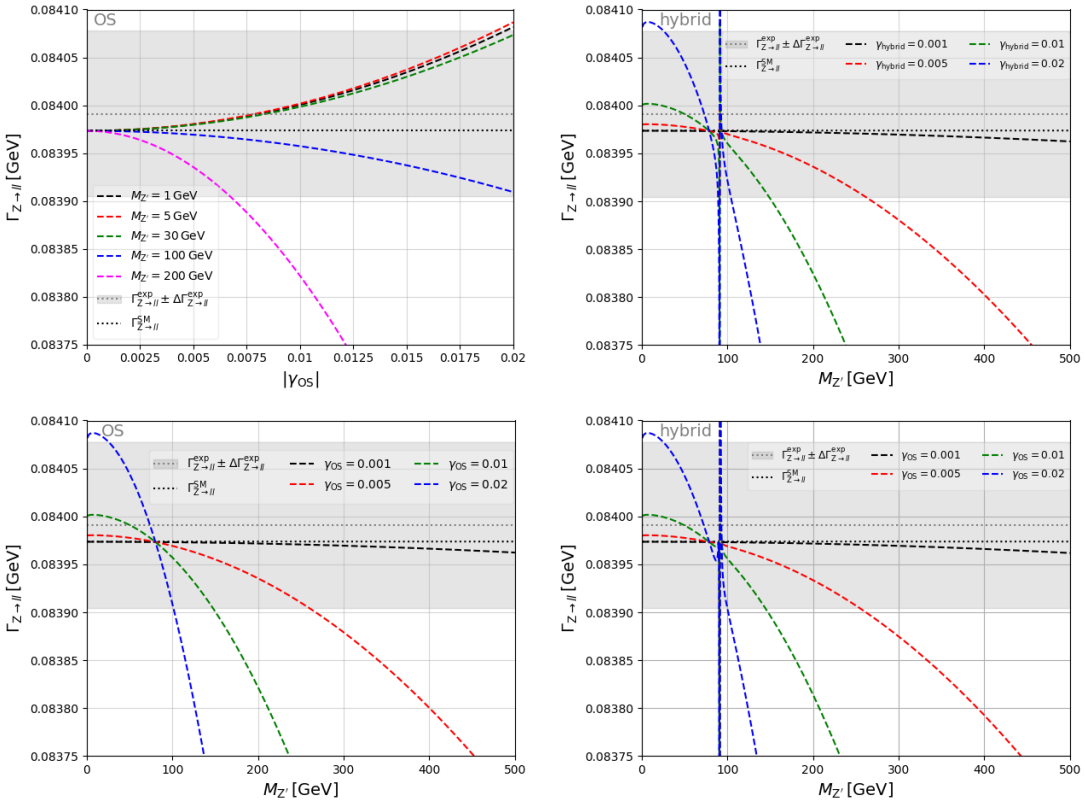

Figure 5.20.: Dependence of $\Gamma^{\mathrm{DASM}}_{\mathrm{Z}\to ll}$ on $|\gamma_{\mathrm{OS}}|$ in the OS scheme (upper left), and on $M_{\mathrm{Z}'}$ in the hybrid scheme (upper right) without scheme conversion of γ. In the lower line the dependence of $\Gamma^{\mathrm{DASM}}_{\mathrm{Z}\to ll}$ on $M_{\mathrm{Z}'}$ is shown in the OS scheme (lower left) and the hybrid scheme (lower right), after proper scheme conversion of γ.

Similarly to the other investigated observables, the prediction is symmetric with respect to $\gamma_{\mathrm{OS}} \to -\gamma_{\mathrm{OS}}$. The plot in the upper left-hand side of Figure 5.20 shows the dependence of $\Gamma^{\mathrm{DASM}}_{\mathrm{Z}\to ll}$ on $|\gamma_{\mathrm{OS}}|$. We find an increase (decrease) of the prediction for increasing values of $|\gamma_{\mathrm{OS}}|$ and $M_{\mathrm{Z}'} < M_{\mathrm{Z}}$ ($M_{\mathrm{Z}'} > M_{\mathrm{Z}}$). For $\gamma_{\mathrm{OS}} = 0$ there is no visible shift of $\Gamma^{\mathrm{DASM}}_{\mathrm{Z}\to ll}$ with respect to its SM prediction.
The dependence of the prediction on $M_{\mathrm{Z}'}$ is shown in the remaining three plots of Fig. 5.20. We give the OS prediction in the bottom-left plot. As expected in the OS scheme, we find a smooth behaviour for $M_{\mathrm{Z}'} \to M_{\mathrm{Z}}$. Further, the prediction decreases for increasing $M_{\mathrm{Z}'}$. In the bottom-right plot of Fig. 5.20 the corresponding prediction using the hybrid scheme, after proper scheme conversion of γ, is shown. One finds similar features to the ones found in the OS predictions for all points except in the vicinity of $M_{\mathrm{Z}'} \approx M_{\mathrm{Z}}$, where the prediction diverges. This divergence has two origins. For one, the scheme conversion of γ will, as previously discussed (see Sect. 5.4.1), introduce this behaviour to the hybrid scheme predictions. Additionally, $\Gamma^{\mathrm{DASM}}_{\mathrm{Z}\to ll}$ is sensitive to the field renormalization constants of

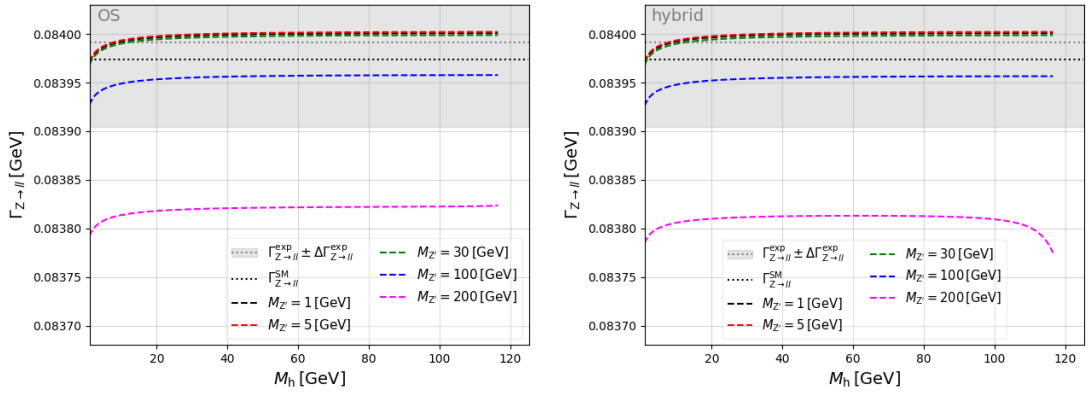

Figure 5.21.: Dependence of the prediction for $\Gamma^{\mathrm{DASM}}_{\mathrm{Z}\to ll}$ on M_{h} in benchmark scenario (ii) in the OS scheme (left) and the hybrid scheme (right) after proper scheme conversion of γ.

the massive neutral gauge-boson sector. Therefore, the observed divergence showcases the ill-defined limit $M_{\mathrm{Z}'} \to M_{\mathrm{Z}}$ for $\overline{\mathrm{MS}}$ renormalization of mixing angles (see discussion in Sect. 4.2.3 for more details). This can be seen in the top-right plot of Fig. 5.20, where we show the prediction in the hybrid scheme plotted against $M_{\mathrm{Z}'}$ without any scheme conversion of γ, i.e. using fixed values for γ_{hybrid}, clearly showing the divergence in the prediction in the case of degenerate masses of the Z and Z′ boson in the hybrid scheme.
Similarly to the case of the W-boson mass prediction, we find small differences in the dependence of the prediction on the BSM Higgs sector parameters α, M_{h}, and θ_{r} close to the non-perturbative region for the free parameters of the original Lagrangian. Additionally, for benchmark scenario (ii)—in both renormalization schemes—a significant decrease of the predictions is found for $M_{\mathrm{h}} \to 1\,\mathrm{GeV}$, (see Fig. 5.21). Besides this decrease and the small differences observed between the two renormalization schemes, we find $\Gamma^{\mathrm{DASM}}_{\mathrm{Z}\to ll}$ to be widely independent of the new parameters from the Higgs sector as well as θ_{r} and m_{ν_4} from the fermion sector.

5.5. Global fit

With the evaluation of the POs performed in the previous section, we are now perfectly equipped to perform a global fit of the parameter space of the DASM. Our fit aims towards finding regions of the parameter space that lead to significantly better agreement between the measured values of the investigated POs and their respective predictions within the DASM (described above) than the SM can provide. In the first part of this section (see Sects. 5.5.1 and 5.5.2), we give a detailed description of the fit setup and the definition of the fit function. After defining several interesting fit scenarios in Sect. 5.5.3, we dedicate the last part of this section (see Sect. 5.5.4) to a detailed discussion of the fit results.

5.5.1. Construction of the fit function

The function $\mathcal{F}$ minimized in the global fit can be split into two parts,

$$\mathcal{F}(p) = \chi^2_{\mathcal{O}}(p) + \mathcal{P}(p), \tag{5.82}$$

where $\chi^2_{\mathcal{O}}(p)$ is a measure describing the level of agreement between predictions and measured values and, therefore, in principle encodes the relevant phenomenological information. The precise definition of $\chi^2_{\mathcal{O}}(p)$ is given below. The additional cost function $\mathcal{P}(p)$ is introduced in Eq. (5.82) to account for additional limits on certain input-parameter combinations, such as perturbativity constraints for coupling constants. The explicit definition of $\mathcal{P}(p)$ used in our analysis is given in the last part of this section. Note that the presence of the cost function $\mathcal{P}(p)$ destroys the straightforward translation of $\mathcal{F}(p)$ (with its χ^2-like nature) into its probabilistic interpretation, whenever $\mathcal{P}(p)$ is non-zero. Nevertheless, $\mathcal{P}(p)$ is needed to ensure that the fit remains in regions of the parameter space that lead to meaningful predictions. Thus, we perform a detailed analysis, probing the dependence of our results on the precise choice of $\mathcal{P}(p)$ for each investigated fit scenario (see Sect. 5.5.4). The arguments of the fit function are given by

$$p = \{\gamma, \alpha, \theta_{\mathrm{r}}, \lambda_{12}, m_{\nu_4}, M_{\mathrm{h}}, M_{\mathrm{H}}, M_{\mathrm{Z}'}, M_{\mathrm{Z}}, m_{\mathrm{t}}, \Delta\alpha^5_{\mathrm{had}}, \alpha_{\mathrm{s}}\}. \tag{5.83}$$

They represent the parameters that are treated as free input parameters of the fit. Thus, besides the BSM parameters, we allow for a variation of (the potentially most influential) SM-like parameters to include effects originating from parametric uncertainties in the input. Note that for the predictions $M_{\mathrm{W}}^{\mathrm{DASM}}$, $s^{2,\mathrm{DASM}}_{\mathrm{w,eff},l}$, and $\Gamma^{\mathrm{DASM}}_{\mathrm{Z}\to ll}$, this treatment of the parametric uncertainties includes the respective variations of the best SM predictions (see Sects. 5.4.1, 5.4.4, and 5.4.5). The precise treatment of these free SM-like input parameters is discussed in the following in more detail. The values of the remaining input parameters[20] used in the numerical evaluation of $\mathcal{F}(p)$ are given in Eq. (5.6).

5.5.1.1. The χ^2 function

Assuming the probability density functions of the measurements for the investigated observables to be of Gaussian form, we choose a χ^2-distributed cost function

$$\chi^2_{\mathcal{O}}(p) = \sum_{i,j} (\mathcal{O}_i^{\mathrm{exp}} - \mathcal{O}_i^{\mathrm{pre}}(p))(V^{-1})_{ij}(\mathcal{O}_j^{\mathrm{exp}} - \mathcal{O}_j^{\mathrm{pre}}(p)), \tag{5.84}$$

encoding all relevant information on the observables in our fit. Here V denotes the covariance matrix and we introduced the vectors

[20] As mentioned in the previous sections, we use the predicted value for M_{W} from muon decay as an input value in $\mathcal{F}(p)$ for a given set of input values.

$$\mathcal{O}^{\text{pre}}(p) = (M_{\text{W}}^{\text{DASM}}, a_\mu^{\text{DASM}}, \Gamma_{\text{Z}\to ll}^{\text{DASM}}, s_{\text{w,eff},l}^{2,\text{DASM}}, M_{\text{Z}}, M_S, m_{\text{t}}, \Delta\alpha_{\text{had}}^5, \alpha_{\text{s}}), \tag{5.85}$$

$$\mathcal{O}^{\text{exp}}(p) = (M_{\text{W}}^{\text{exp}}, a_\mu^{\text{exp}}, \Gamma_{\text{Z}\to ll}^{\text{exp}}, s_{\text{w,eff},l}^{2,\text{exp}}, M_{\text{Z}}^{\text{exp}}, M_S^{\text{exp}}, m_{\text{t}}^{\text{exp}}, \Delta\alpha_{\text{had}}^{5,\text{exp}}, \alpha_{\text{s}}^{\text{exp}}), \tag{5.86}$$

where S denotes the SM-like Higgs boson of h and H. Note that, similarly to the other POs, we constrain the SM-like parameters included in the global fit with the help of their respective measurements. The inverse V^{-1} of the covariance matrix V is used to introduce the experimental uncertainties in $\chi^2_{\mathcal{O}}(p)$ and accounts for possible correlations between the different PO measurements. For the investigated POs, the only non-vanishing correlations connect the results of $\Gamma_{\text{Z}\to ll}^{\text{exp}}$, $s_{\text{w,eff},l}^{2,\text{exp}}$, and $M_{\text{Z}}^{\text{exp}}$, all being measured at LEP.
Taking this into account, we find the following form for the inverse of the covariance matrix

$$V^{-1} = \begin{pmatrix} \frac{1}{(\Delta M_{\text{W}})^2} & & & & & \\ & \frac{1}{(\Delta a_\mu)^2} & & & & \\ & & (V^{-1})_{33} & (V^{-1})_{34} & (V^{-1})_{35} & \\ & & (V^{-1})_{34} & (V^{-1})_{44} & (V^{-1})_{45} & \\ & & (V^{-1})_{35} & (V^{-1})_{45} & (V^{-1})_{55} & \\ & & & & & \hat{V}^{-1}_{p_{\text{SM}}} \end{pmatrix}, \tag{5.87}$$

where $\Delta\mathcal{O}_i$, $\mathcal{O}_i \in \{M_{\text{W}}, a_\mu\}$, are the uncertainties of the respective POs and the entries $(V^{-1})_{kl}$, $k,l = 3,4,5$, encode the information on the uncertainties and correlations of the $\Gamma_{\text{Z}\to ll}^{\text{exp}}$–$s_{\text{w,eff},l}^{2,\text{exp}}$–$M_{\text{Z}}$ system. Further, $\hat{V}^{-1}_{p_{\text{SM}}}$ denotes a 4×4 diagonal matrix with the diagonal elements $\frac{1}{(\Delta\mathcal{O}_j)^2}$, $\mathcal{O}_j = M_S, m_{\text{t}}, \Delta\alpha_{\text{had}}^5, \alpha_{\text{s}}$, given by the respective experimental uncertainties $\Delta\mathcal{O}_j$ of the measurements of the SM-like parameters [16]. All entries of V^{-1} that are not explicitly shown in Eq. (5.87) are zero. The derivation of V^{-1} and the explicit values of its entries are given in Appendix E.
In addition, we notice that the size of the theoretical uncertainty of a_μ^{SM} is comparable to its experimental counterpart. Approximating this uncertainty to be of Gaussian nature[21], we add it in quadrature to the uncertainty of the measurement to obtain the full uncertainty used in V^{-1}.
In summary, Eq. (5.84) yields a measure of the level of agreement between predictions $\mathcal{O}^{\text{pre}}$ and experimental results $\mathcal{O}^{\text{exp}}$ based on the uncertainties of the respective quantities as well as their possible correlations. In general, smaller values of $\chi^2_{\mathcal{O}}(p)$ correspond to a better agreement between theory predictions and measurements. Note that V^{-1} is positive semi-definite, and therefore, $\chi^2_{\mathcal{O}}(p)$ is bounded from below at 0, i.e. $\chi^2_{\mathcal{O}}(p) \geq 0$. This lower bound is only reached for an exact agreement between all predictions and their experimental counterparts.

[21] Note that our treatment of the theoretical uncertainty is only approximative. For a more correct treatment, a more sophisticated analysis would be needed. However, for a first confrontation of the DASM with precision data, our treatment of the theoretical uncertainty is sufficiently precise.

5.5.1.2. Perturbativity of the coupling parameters

As discussed in Sect. 5.5.1.2, we have to ensure the validity of the perturbative approach for the calculations of the investigated POs. Thus, we need to constrain the parameter region of our fit such that the constraints given in Eq. (5.11) are fulfilled. As already discussed in Sects. 3.6 and 5.5, all of the parameters of Eq. (5.11), but λ_{12}, are neither used as input parameters of the theory, nor as direct input of the fit. Thus, we have to use Eqs. (3.24)–(3.28), (3.55), (3.57), and (3.62) for the renormalized parameters to compute the values of the remaining fit input parameters that are constrained by Eq. (5.11). To introduce their respective perturbativity bounds to the fit function, we add an additional cost function of the form

$$\begin{aligned}\mathcal{P}(g_1, g_2, e_\mathrm{d}, \lambda_1, \lambda_2, y_\rho) = \sum_{g_i} \left[c_\mathrm{g}\theta(|g_i| - \mathrm{p_g})(|g_i| - \mathrm{p_g})^3\right] + c_\mathrm{s}\theta(|\lambda_1| - \mathrm{p}_1)(|\lambda_1| - \mathrm{p}_1)^3 \\ + c_\mathrm{s}\theta(|\lambda_2| - \mathrm{p}_2)(|\lambda_2| - \mathrm{p}_2)^3 + c_\mathrm{s}\theta(|y_\rho| - \mathrm{p}_3)(|y_\rho| - \mathrm{p}_3)^3,\end{aligned} \tag{5.88}$$

where the sum runs over $g_i = g_1, g_2, e_\mathrm{d}$, and $\theta(x)$ is the usual Heaviside function. The constants p_i introducing the respective perturbativity limits are given by $\mathrm{p_g} = \sqrt{2\pi}$, $\mathrm{p}_1 = \frac{\pi}{12}$, $\mathrm{p}_2 = \frac{4}{3}\pi$, and $p_3 = 4\pi$. We do not need to add an additional cost function of the form Eq. (5.88) to ensure $|\lambda_{12}| < \pi$ since the *iminuit* interface allows to directly constrain input parameters to certain regions, if needed.
The constants c_g and c_s rule the amount of extra cost that is added to the fit function if any parameter enters the non-perturbative region. Choosing them appropriately prevents the parameter scan in the minimization procedure to access the non-perturbative region. While in principle $c_\mathrm{g}, c_\mathrm{s} \to \infty$ seems to be the best choice to achieve this, the algorithms used in the minimization procedure rely on smoothness (up to the second derivative) of the minimized function. Further, having large scale differences between certain regions in the parameter space can lead to a bad convergence behaviour of the used algorithms. In the following analyses, we vary c_g and c_s to ensure that the dependence of the minimization results on the precise choice of $\mathcal{P}$ is negligible.

5.5.2. Technical setup

With the computational setup described in Sect. 5.2 we have the numerical results, needed for the desired parameter fit, accessible in Python. As already discussed before, we want our fit to minimize (5.82) in order to find the parameter region that leads to the best agreement between predictions and measurements for the investigated POs. Therefore, we perform the multidimensional minimization using the Python interface *iminuit* v.2.24.0 [97] for the C++ library *Minuit2* [98]. Using *iminuit* allows us to not only determine the best-fit parameters as well as an error estimate for them, but also to determine confidence regions using the *minos* algorithm, which effectively scans over the respective parameter while minimizing the

investigated function in all other parameters to construct the desired confidence regions. Further, *iminuit* allows to directly set limits on the free input parameters of the fit. However, to the best of our knowledge, it is not possible in *iminuit* to directly assign limits to certain combinations of input parameters, as needed in our analysis to introduce certain perturbativity limits on the original parameters of the Lagrangian. Therefore, we have to introduce them via the function $\mathcal{P}$ as described in the previous section.
In our analysis we determine the minimum of the fit function $\mathcal{F}$. As already mentioned above, the main focus of this first phenomenological analysis lies on investigating the influence of the newly introduced parameters γ and $M_{\mathrm{Z}'}$, introduced in the extension of the gauge-sector, on the considered POs. To obtain a better understanding of the fit results, we scan over the function $\mathcal{F}(p)$ in the γ–$M_{\mathrm{Z}'}$ plane in the vicinity of the minimum. In this scan, we minimize $\mathcal{F}(p)$ for each combination of γ–$M_{\mathrm{Z}'}$ leaving all remaining parameters of the fit free (within their respective limits of the global minimization). This allows for a detailed determination of the most influential POs for the minimization. Furthermore, we also determine the set of points $\mathcal{F}_{2.3}$ with

$$\mathcal{F}_{2.3} = \mathcal{F}_{\min} + \Delta\mathcal{F}_{2.3}, \qquad \Delta\mathcal{F}_{2.3} = 2.3, \tag{5.89}$$

in the 2-dimensional γ–$M_{\mathrm{Z}'}$ plane. If one assumes the fit function to be χ^2-distributed (in the vicinity of the minimum), $\mathcal{F}_{2.3}$ would define the contour corresponding to the limits of the 68% confidence region [123]. To determine these contour points we use the *minos* algorithm implemented in *iminuit*[22].

5.5.3. Fit scenarios

Having everything for the minimization set up in the previous sections, we can now define the fit scenarios of interest. Due to the strong tension between the best SM predictions for the anomalous magnetic moment of the muon $a_{\mu,e^+e^-}^{\mathrm{SM}}$ and $a_{\mu,\mathrm{lattice}}^{\mathrm{SM}}$, we choose to perform our fit twice, using either results for $a_{\mu,e^+e^-}^{\mathrm{SM}}$ or $a_{\mu,\mathrm{lattice}}^{\mathrm{SM}}$ (see Sect. 5.4.2). In both cases, we choose the OS scheme with all its previously discussed benefits as renormalization scheme. Further, we choose the world average $M_{\mathrm{W}}^{\mathrm{exp}}$ (see Eq. (5.28)) over the respective CDF result $M_{\mathrm{W}}^{\mathrm{CDF}}$ in the minimization [8]. As in the case for the analyses of the POs performed in Sect. 5.4, we demand $M_{\mathrm{h}}, M_{\mathrm{Z}'} \geq 1\,\mathrm{GeV}$ to ensure that the approximations made in the derivations of the POs in Sect. 5.4, such as assuming $m_\mu \ll M_{\mathrm{h}}, M_{\mathrm{Z}'}$, remain valid.
As mentioned above, the investigated POs are chosen to be most sensitive to the BSM gauge sector parameters and it turns out that they only loosely depend on the additional parameters of the Higgs sector. Thus, we additionally include the constraints $|\alpha| < 0.2 (\alpha' < 0.2)$ in the case $M_{\mathrm{h}} = M_{\mathrm{h}}^{\mathrm{SM}} (M_{\mathrm{H}} = M_{\mathrm{h}}^{\mathrm{SM}})$, so that our results

[22] Note that the minos algorithm will not ensure that we find all disconnected areas that fulfill $\mathcal{F}(p) \leq \mathcal{F}_{\min} + \Delta\mathcal{F}_{2.3}$.

#	ren. scheme	a_μ^{SM}	m_{ν_4}	$M_{\mathrm{h}}, M_{\mathrm{Z}'}$	$\lvert\alpha\rvert$ or α'
1.	OS	$a_{\mu,e^+e^-}^{\mathrm{SM}}$	$\in (0.1, 10)\,\mathrm{TeV}$	$> 1\,\mathrm{GeV}$	< 0.2
2.	OS	$a_{\mu,\mathrm{lattice}}^{\mathrm{SM}}$	$\in (0.1, 10)\,\mathrm{TeV}$	$> 1\,\mathrm{GeV}$	< 0.2

Table 5.1.: Fit scenarios used in our phenomenological analysis in Sect. 5.5.4. The third column gives the value used for the best SM prediction for a_μ^{DASM}. The entries of the columns 4–6 show the additional constraints imposed on the input parameters of the fit.

(roughly) obey limits for the respective mixing angle in pure Higgs singlet extensions obtained from analyzing LEP data or by analyses performed with LHC data (see Ref. [87] for details). Further, we constrain m_{ν_4} to $100\,\mathrm{GeV} < m_{\nu_4} < 10\,\mathrm{TeV}$. While the lower limit[23] is chosen to avoid that the minimization is disturbed by the non-physical threshold effects of the OS scheme (see Sect. 5.3), the upper limit of 10 TeV is some value chosen to prevent the minimization from running into numerically unstable regions. Noticing the weak dependence of the investigated observables on m_{ν_4} discussed in Sects. 5.4, it is expected to be only loosely constrained by the investigated POs anyhow. The complete fit setups, which are used to explore the phenomenology of the DASM in the following analysis, are summarized in Tab. 5.1. Note that the results discussed in the next section are derived in the OS scheme (see Tab. 5.1). Additionally, we perform the minimization using the hybrid scheme. A comparison of the minimization results obtained in the OS and hybrid schemes is used to get uncertainty estimates for the found minima and to ensure a small renormalization scheme dependence of the results (see Sect. 5.5.4).

5.5.4. Fit results

In this section, we present the results for the fits obtained within the two fit scenarios 1 and 2 (see Tab. 5.1). In addition to the minimum, we give the $\mathcal{F}_{2.3}$ contour (see Eq. (5.89)) in the γ_{OS}–$M_{\mathrm{Z}'}$ plane for both scenarios. Further, we perform a scan of the investigated function $\mathcal{F}$ in the vicinity of the minimum, where we determine the minimum value for fixed γ_{OS}–$M_{\mathrm{Z}'}$ combinations, but leave all remaining parameters of the fit free. This allows us to further understand the fit function $\mathcal{F}$ in the vicinity of the minimum, to check the robustness of the minuit result, and to discuss the several contributions to and features of $\mathcal{F}$ leading to the respective results in detail.

As mentioned in Sect. 5.4, we find all investigated POs to be symmetric with respect to $\gamma \to -\gamma$ and $\alpha \to -\alpha$. Further, their predictions only loosely change under a sign change $\lambda_{12} \to -\lambda_{12}$. While we here discuss the results choosing all of the previously mentioned parameters to be positive, one, therefore, finds almost

[23] This specific value results as compromise between the aim to constrain m_{ν_4} as little as possible to minimize any bias and the necessity to avoid artifacts.

	DASM scenario 1	SM
$\mathcal{F}_{\text{min}}$	4.5445 ± 0.0008	30.70
$\gamma_{\text{OS}} \times 10^3$	$9.24^{+2.87}_{-0.98}$	–
$M_{\text{Z}'}\,[\,\text{GeV}]$	$1^{+0.33}_{-0}$	–
α'	$0.20^{+0}_{-0.13}$	–
λ_{12}	$0.34^{+0.04}_{-0.34}$	–
$M_{\text{h}}\,[\,\text{GeV}]$	$2.2^{+87}_{-1.2}$	–
θ_{r}	$0.17^{+1.4}_{-0.17}$	–
$m_{\nu_4}\,[\,\text{GeV}]$	263^{+9737}_{-163}	–
$M_{\text{H}}\,[\,\text{GeV}]$	125.25 ± 0.17	125.25
$M_{\text{Z}}\,[\,\text{GeV}]$	91.188 ± 0.002	91.1876
$m_{\text{t}}\,[\,\text{GeV}]$	172.95 ± 0.7	172.5
$\Delta\alpha^5_{\text{had}}$	0.02766 ± 0.00007	0.02768
α_{s}	0.1178 ± 0.001	0.1179

Table 5.2.: The minimum of $\mathcal{F}$ and the corresponding parameter values in the DASM (middle) and in the SM (right) in fit scenario 1.

identical results when changing the signs of any of them[24].
In particular, constraining $\alpha, \lambda_{12} < 0$ and repeating the minimization results in a similar position of the minimum (with flipped signs for α and λ_{12}) and a shift of the minimal value of $\mathcal{O}(10^{-6})$ for either of the presented fit scenarios. This is well below their respective uncertainties of $\mathcal{O}(10^{-4})$ estimated via a comparison of the respective results in the OS and hybrid schemes (see below).

5.5.4.1. Fit scenario 1: $a_\mu^{\text{SM}} = a_{\mu,e^+e^-}^{\text{SM}}$

In fit scenario 1, we find the minimum value $\mathcal{F}_{\text{min}} = 4.5445 \pm 0.0008$ of the fit function highlighting the significant improvement in the compatibility of the DASM predictions for the considered POs with their respective measurements, as compared to the respective SM predictions (leading to $\mathcal{F}_{\text{SM}} = 30.70$ for fit scenario 1). We give all details on the input-parameter values of the minimum in Tab. 5.2. The uncertainty on the best fit value $\mathcal{F}_{\text{min}}$ in the DASM is taken as the difference between the OS result and the result obtained in the hybrid scheme, $\mathcal{F}_{\text{min}}^{\text{hybrid,conv}} = 4.5437$, after proper scheme conversion of γ. In addition, the minimization was repeated using the hybrid renormalization scheme to test the renormalization-scheme dependence of the obtained minimum. A similar result as for

[24]Note that to obtain meaningful results, for a sign change of α, one always has to change the sign of λ_{12} as well (and vice versa), to obey $s_{2\alpha}\lambda_{12} > 0$.

the OS renormalization scheme of $\mathcal{F}_{\text{min}}^{\text{hybrid}} = 4.5434$ was found.
To determine the 1σ uncertainty limits for the input parameters, we search for the values of the respective parameter—while minimizing in all remaining parameters—where $\mathcal{F}(p) = \mathcal{F}_{\text{min}} + 1$. Whenever any upper or lower parameter uncertainty is underlined, the respective parameter value reaches the limit of the allowed parameter space before our requirement for $\mathcal{F}(p)$ is reached, i.e. the corresponding parameter is not really constrained in the respective direction within the fit scenario.
The fit prefers small values for the mass of the Z′ boson and the minimum of $\mathcal{F}$ lies at the lower limit $M_{\text{Z}'} = 1^{+0.33}_{\underline{-0}}\,\text{GeV}$ of the parameter space. For the mixing angle γ in the gauge sector the minimization prefers a small value of $\gamma_{\text{OS}} = 0.0092^{+0.003}_{-0.001}$. Furthermore, the scenario $M_{\text{H}} = M_{\text{h}}^{\text{SM}}, M_{\text{h}} < M_{\text{h}}^{\text{SM}}$ is preferred. As expected (see Sect. 5.4), the BSM Higgs sector parameters come with very large uncertainties, reflecting the fact that the investigated POs only loosely depend on them. The preferred mass of the new Higgs boson $M_{\text{h}} = 2.2^{+87}_{\underline{-1.2}}\,\text{GeV}$ is close to its lower limit and $\alpha' = 0.20^{+0}_{-0.13}$ is at its upper limit, forcing the Higgs mixing angle $\alpha = \frac{\pi}{2} - \alpha'$ as far away from its respective SM-limit value as possible. For this combination of M_{h} and α', the scalar self-coupling takes the larges possible value of $\lambda_{12} = 0.34^{+0.04}_{\underline{-0.34}}$ that is allowed by the perturbativity constraint on λ_1.
Finally, the combination of the mixing angle $\theta_{\text{r}} = 0.17^{+\underline{1.4}}_{\underline{-0.17}}$ and the mass of the new fermion $m_{\nu_4} = 263^{+\underline{9737}}_{\underline{-163}}\,\text{GeV}$ is only constrained by the perturbativity limit imposed on y_ρ, i.e. they are practically unconstrained by the fit (as expected from the discussions given in Sect. 5.4), which is also reflected by their large uncertainties. Further, we want to emphasize that the found uncertainties for the SM-like input parameters agree with the experimental uncertainties used to construct $\mathcal{F}$.
In Fig. 5.22, we show the result of our minimization of $\mathcal{F}$ with minimal value $\mathcal{F}_{\text{min}}$ (black point), the respective $\mathcal{F}_{2.3}$ contour (black dashed line), and the results obtained by our scan in the vicinity of the minimum (coloured points, see Sect. 5.5.2 for details). The white regions correspond to areas with $\mathcal{F}(p) > \mathcal{F}_{\text{min}} + 3.5$, which we do not display in colour here to have a more detailed representation of the remaining (more interesting) scan results. Note that the best fit value is located at $\lambda_1 = 0.247$ and $y_\rho = 3.537$, i.e. close to their respective perturbativity limits. A variation of c_{s} and c_{g} (which rule the precise form of $\mathcal{P}$, see Eq. (5.88)) in the range 10^2–10^4 leads to a variation of $\mathcal{F}_{\text{min}}$ of $\mathcal{O}(10^{-6})$ as well as a shift of the $\mathcal{F}_{2.3}$ contour that is below the plot precision. Thus, we choose $c_{\text{s}} = c_{\text{g}} = 10^4$ here. The additional cost, added by $\mathcal{P}$ to ensure that the results respect the perturbativity limits of the parameters, is of $\mathcal{O}(10^{-7})$ for all shown points, and, thus, negligible compared to the theoretical uncertainty of $\mathcal{F}_{\text{min}}$.
While we constrain our fit to $M_{\text{Z}'} > 1\,\text{GeV}$ leading to the lower $M_{\text{Z}'}$ bound of the $\mathcal{F}_{2.3}$ contour, it reaches up to values of $M_{\text{Z}'} \approx 1.6\,\text{GeV}$. The values of γ_{OS} that can be reached within the $\mathcal{F}_{2.3}$ contour are given by $\gamma_{\text{OS}} \in [0.0077, 0.0143]$. We recall that the limitations of our predictions for the POs do not allow us to make reliable statements in the parameter region $M_{\text{Z}'} = \mathcal{O}(m_\mu)$. However, the position of the

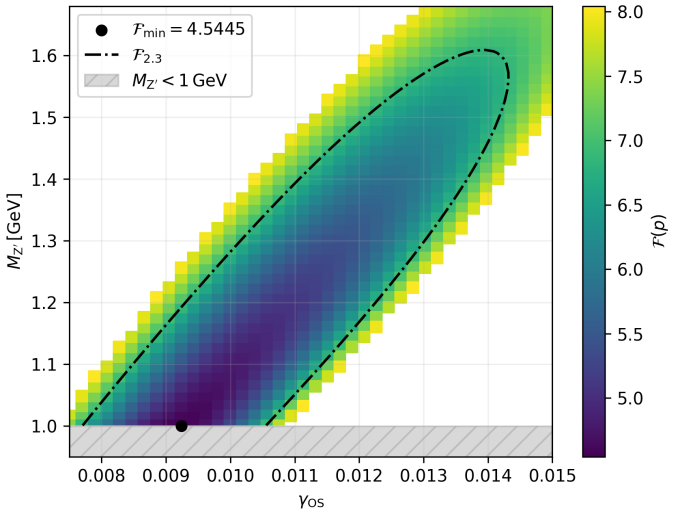

Figure 5.22.: The location of the minimum (black dot), the corresponding $\mathcal{F}_{2.3}$ contour (black dashed line), and the results for the scan of the vicinity of the minimum (coloured squares) in the γ_{OS}–$M_{\text{Z}'}$ plane for fit scenario 1.

minimum as well as the scan of $\mathcal{F}$ in the vicinity of the minimum indicate that the predictions might show even better agreement with data for even smaller values of $M_{\text{Z}'}$. Moreover, moving away from the minimum towards larger values of $M_{\text{Z}'}$, larger values for γ_{OS} are preferred. Thus, the scan reveals a valley-shaped form, highlighting a direction in the γ_{OS}–$M_{\text{Z}'}$ plane that seems, compared to all other directions, only loosely constrained by the considered POs. The direction given by this valley agrees with the one found in the left plot of Fig. 5.14 that resolves the tension between predictions and measurement of $(g-2)_\mu$. To further explore the results of the minimization in detail, we investigate the different contributions to $\mathcal{F}$ originating from each of the considered POs separately in the following.
In the left columns of Figs. 5.23 and 5.24, we give the differences of the pull values for the considered POs between the DASM and the SM, respectively. In the right columns of Figs. 5.23 and 5.24 the corresponding contributions[25] $\chi_{\mathcal{O}_i}$, $\mathcal{O}_i = a_\mu, M_{\text{W}}, s^2_{\text{w,eff},l}, \Gamma_{\text{Z}\to ll}$, to $\mathcal{F}$ originating from the diagonal elements of V^{-1} are shown. They are defined by

$$\chi_{\mathcal{O}_i} = \left[(V^{-1})_{ii}(\mathcal{O}_i^{\text{exp}} - \mathcal{O}_i^{\text{pre}})^2\right]^{\frac{1}{2}}, \tag{5.90}$$

where the $(V^{-1})_{ii}$ denote the corresponding diagonal elements of Eq. (5.87). Further, we give the values of $\chi_{\mathcal{O}_i}$ in the DASM at the location of the minimum and

[25] Note that $\chi_{\mathcal{O}_i}$ coincides with the absolute value of the pull (see Eq. (5.46)) in the case of uncorrelated observables. Whenever correlations are taken into account this relation is no longer valid.

$\mathcal{O}_i$	$\mathcal{O}_{\text{min},i}^{\text{DASM}}$	$\chi_{\mathcal{O}_i}$	$\chi_{\mathcal{O}_i,\text{SM}}$
a_μ	$1.165920528 \times 10^{-3}$	0.13	5.08
M_W	80.3567 GeV	1.69	1.95
$s^2_{\text{w,eff},l}$	0.23158	1.01	1.0
$\Gamma_{\text{Z}\to ll}$	83.9817 MeV	0.19	0.35

Table 5.3.: Values of the PO predictions $\mathcal{O}_{\text{min},i}^{\text{DASM}}$ at the location of the minimum in fit scenario 1. Further, the respective values of the $\chi_{\mathcal{O}_i}$ are given for the DASM and for the SM case.

for the SM in Tab. 5.3.
On the left side of the upper row of Fig. 5.23, the difference between the DASM and SM values of the pull for a_μ is shown. As already observed in Sect. 5.4.2, for low Z′-boson masses a large dependence of $a_{\mu,e^+e^-}^{\text{DASM}}$ on both, γ_OS and $M_{\text{Z}'}$, is found. In the upper-right plot of Fig. 5.23 the contributions χ_{a_μ} to $\mathcal{F}$ are shown. As expected from the previous discussion it shows the same valley-shaped structure that can be observed in the scan of the full function $\mathcal{F}$ (see Fig. 5.22). In agreement with the results found in Sect. 5.4.2, within this valley the DASM predictions precisely match the measured value a_μ^exp, i.e. $\chi_{a_\mu} \approx 0$. However, approaching the $\mathcal{F}_{2.3}$ contour perpendicular to this direction, one observes a strong increase of the χ_{a_μ} values. Furthermore, especially for values $\gamma_\text{OS} \leq 0.012$ this increase of χ_{a_μ} seems to dominantly determine the $\mathcal{F}_{2.3}$ contour.
In the lower row of Fig. 5.23 the differences between the DASM and SM pull values for the mass of the W boson (lower left) as well as the contributions χ_{M_W} to $\mathcal{F}$ (lower right) are shown. At the location of the minimum χ_{M_W} is lower than its SM counterpart $\chi_{M_\text{W,SM}}$ (see Tab. 5.3), i.e. there is better agreement between the measured value and the prediction within the DASM than for the SM case. Furthermore, for further decreasing values of γ_OS the agreement between theory prediction and measurement becomes even better for all given points of the scan. However, for increasing values of γ_OS, the tension between prediction and measurement increases, and χ_{M_W} surpasses its SM counterpart. For even larger values of $\gamma_\text{OS} > 0.012$, the contributions χ_{M_W} to $\mathcal{F}$ become more and more significant and play a deciding role in the determination of the $\mathcal{F}_{2.3}$ contour, especially in the aforementioned direction of the valley observed in the χ_{a_μ} scan. Note that this is in agreement with the results found in Sect. 5.4.1, where smaller values of γ_OS are preferred in the parameter regions where $M_{\text{Z}'} < M_\text{Z}$.
Throughout the entire scan region, the predictions for $s^2_{\text{w,eff},l}$ and $\Gamma_{\text{Z}\to ll}$ vary only slightly compared to the respective experimental uncertainties. The difference between their respective pulls in the DASM and SM are shown in the left column of Fig. 5.24. Furthermore, the variation as well as the absolute value of their contributions[26] $\chi_{\mathcal{O}_i}$, $\mathcal{O}_i = s^2_{\text{w,eff},l}, \Gamma_{\text{Z}\to ll}$, to $\mathcal{F}$ is small (see right column of Fig. 5.24)

[26] To keep the discussion compact, we only show the contributions $\chi_{\mathcal{O}_i}$ (see Eq. (5.90)) explicitly here, i.e. we do not explicitly show the contributions originating from the presence of

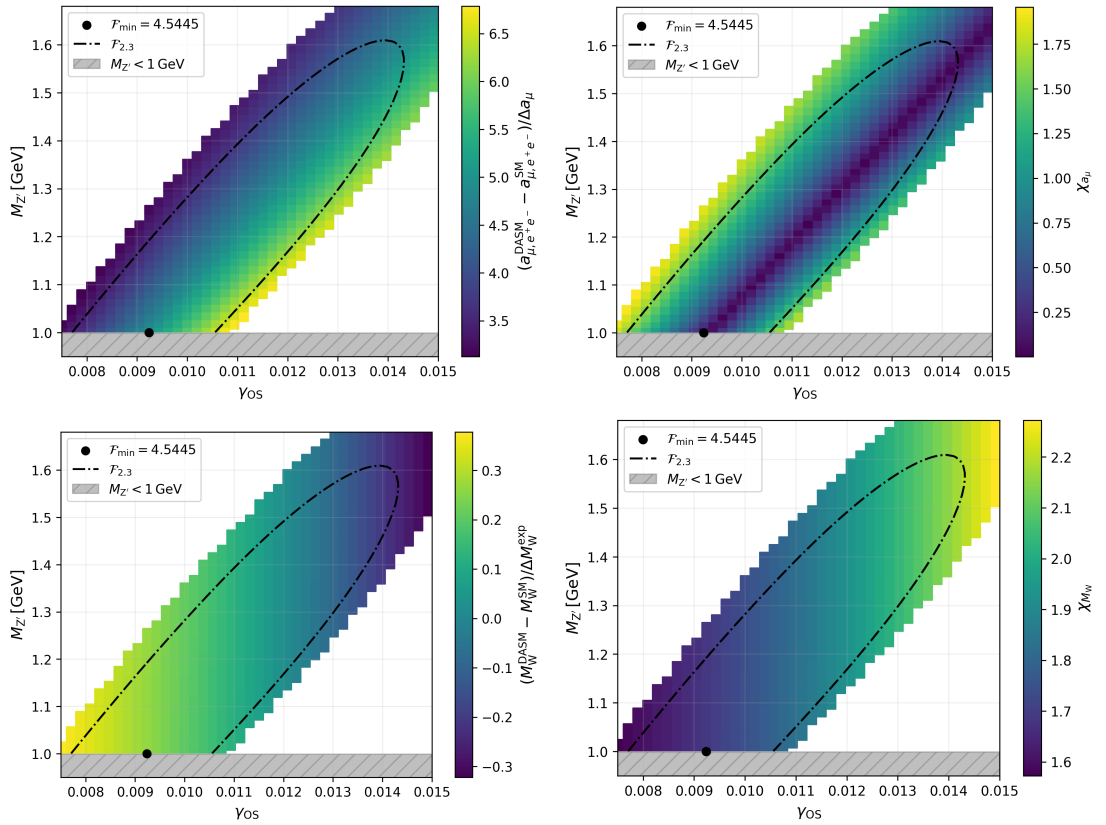

Figure 5.23.: The differences of the pull values between the DASM and the SM for $a_{\mu,e^+e^-}^{\text{DASM}}$ (upper left) and $M_{\text{W}}^{\text{DASM}}$ (lower left) and the contributions $\chi_{\mathcal{O}_i}$, $\mathcal{O}_i = a_\mu, M_{\text{W}}$, to $\mathcal{F}$ (right column) in the vicinity of the minimum for fit scenario 1.

compared to the contributions originating from M_{W} and a_μ discussed above. Starting from the location of the minimum within the $\mathcal{F}_{2.3}$ contour, the predictions for $s^2_{\text{w,eff},l}$ (upper left) decrease, while the predictions for $\Gamma_{\text{Z}\to ll}$ (lower left) increase for increasing values of γ_{OS}. Consequently, the tension between theory and measurements slightly decreases for both $s^2_{\text{w,eff},l}$ (upper right) and $\Gamma_{\text{Z}\to ll}$ (lower right). This, again, is expected having the discussion of Sect. 5.4 in mind (see Figs. 5.19 and 5.20). For values of $\gamma_{\text{OS}} \approx 0.012$ the prediction for $\Gamma_{\text{Z}\to ll}$ precisely agrees with its corresponding measured value (dark blue region in lower-right plot). For further increasing values of γ_{OS} the values of $\Gamma_{\text{Z}\to ll}^{\text{DASM}}$ further increase, leading to increasing contributions $\chi_{\Gamma_{\text{Z}\to ll}}$ to $\mathcal{F}$.
Finally, we want to emphasize that at the location of the minimum the value of the W-boson mass prediction is below its measured value. Thus, from the discussion given in Sect. 5.4.1 one would expect that all three BSM Higgs parameters adjust themselves such that they have the maximal distance to their respective values in

$(V^{-1})_{ij} \neq 0$, $i \neq j$, $i,j = 3,4,5$, since they do not show any interesting additional features.

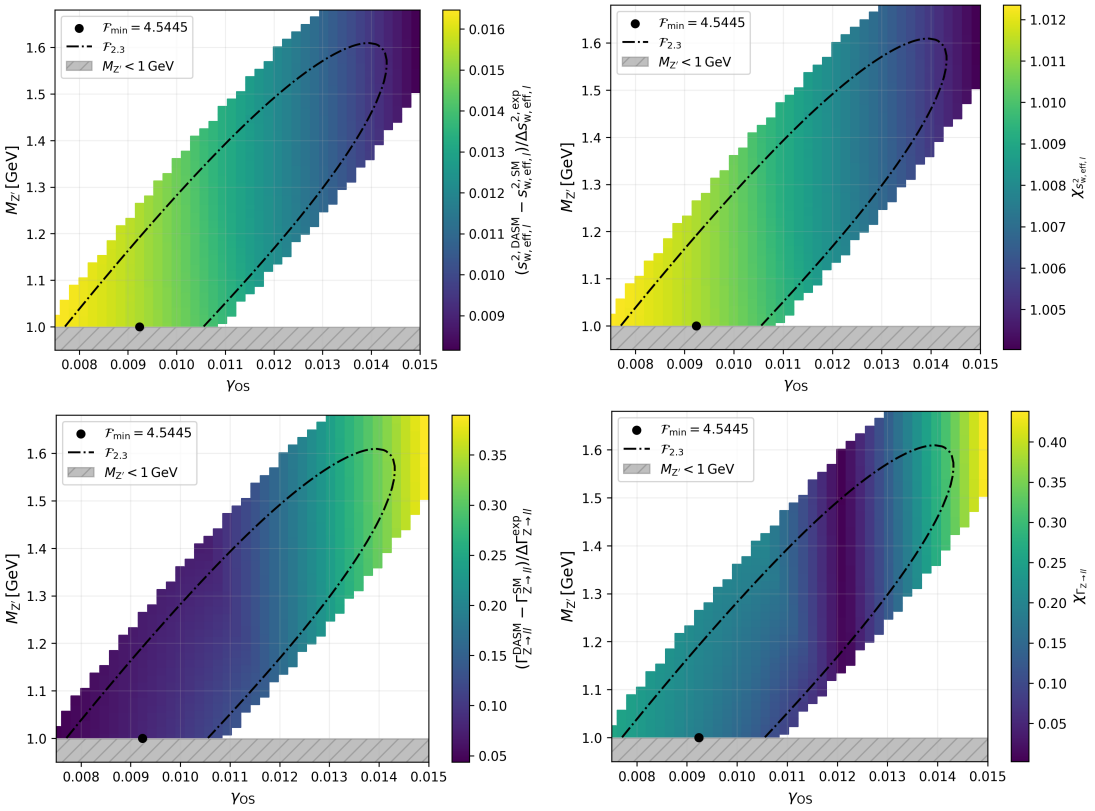

Figure 5.24.: The differences of the pull values between the DASM and the SM for $s^{2,\text{DASM}}_{\text{w,eff},l}$ (upper left) and $\Gamma^{\text{DASM}}_{\text{Z}\to ll}$ (lower left) and the contributions $\chi_{\mathcal{O}_i}$, $\mathcal{O}_i = s^2_{\text{w,eff},l}, \Gamma_{\text{Z}\to ll}$, to $\mathcal{F}$ (right column) in the vicinity of the minimum for fit scenario 1.

the SM limit, i.e. one would expect $\alpha' \to 0.2$, $\lambda_{12} \to \pi$, and $M_\text{h} \to 1\,\text{GeV}$. This parameter configuration would lead to the maximally allowed (within the BSM Higgs sector parameter space) increase of M^{DASM}_W. This behaviour is observed for α' and[27] λ_{12}. However, the value of the BSM Higgs mass does not follow this expectation. At the location of the minimum the value of M_h is close to, but not at, its lower limit of $M_\text{h} = 1\,\text{GeV}$. This indicates that in the region of the minimum, the potential increase of M^{DASM}_W is too small to compensate for the extra cost that is added to $\mathcal{F}$ for $M_\text{h} \to 1\,\text{GeV}$ by the remaining POs (mainly originating from a decrease of $\Gamma^{\text{DASM}}_{\text{Z}\to ll}$, see Fig. 5.21).
In summary, the minimization in fit scenario 1 is dominantly driven by minimizing the tension between prediction and measurement for $(g-2)_\mu$ which singles out a preferred direction in the γ_{OS}–$M_{\text{Z}'}$ plane. Furthermore, for $M_{\text{Z}'} < M_\text{Z}$, small values of γ_{OS} are preferred in the comparison of predictions and measured value for

[27] Note that, for the given values of α' and M_h, λ_{12} is at its upper limit set by the perturbative constraint on λ_1.

	DASM scenario 2	SM
$\mathcal{F}_{\text{min}}$	3.8734 ± 0.0001	7.7490
$\gamma_{\text{OS}} \times 10^3$	$5.85^{+4.54}_{-2.30}$	–
$M_{\text{Z}'}\,[\,\text{GeV}]$	$1^{+0.94}_{-0}$	–
α'	$0.2^{+0}_{-0.2}$	–
λ_{12}	$0.34^{+0.04}_{-0.34}$	–
$M_{\text{h}}\,[\,\text{GeV}]$	$5.25^{+9995}_{-4.25}$	–
θ_{r}	$0.0009^{+1.5699}_{-0.0009}$	–
$m_{\nu_4}\,[\,\text{TeV}]$	$10^{+0}_{-9.9}$	–
$M_{\text{H}}\,[\,\text{GeV}]$	125.25 ± 0.17	125.25
$M_{\text{Z}}\,[\,\text{GeV}]$	91.188 ± 0.002	91.1876
$m_{\text{t}}\,[\,\text{GeV}]$	172.9 ± 0.7	172.5
$\Delta\alpha^5_{\text{had}}$	0.02767 ± 0.00007	0.02768
α_{s}	0.1178 ± 0.001	0.1179

Table 5.4.: The minimum of $\mathcal{F}$ and the corresponding parameter values in the DASM (middle) and in the SM (right) in fit scenario 2.

M_{W}. This pushes the location of the minimum towards the lowest possible value of γ_{OS}, in the direction dictated by $(g-2)_\mu$. In the vicinity of the minimum, the remaining two considered POs $s^2_{\text{w,eff},l}$ and $\Gamma_{\text{Z}\to ll}$ vary only slightly compared to the respective experimental uncertainties. Thus, they do not contribute significantly to the precise determination of the location of the minimum or the respective $\mathcal{F}_{2.3}$ contour.

5.5.4.2. Fit scenario 2: $a_\mu^{\text{SM}} = a_{\mu,\text{lattice}}^{\text{SM}}$

In fit scenario 2, the found minimum value $\mathcal{F}_{\text{min}} = 3.8734 \pm 0.0001$ within the DASM is, again, significantly lower than the respective value $\mathcal{F}_{\text{SM}} = 7.7490$ within the SM. The uncertainty of $\mathcal{F}_{\text{min}}$ is determined via a comparison with the respective value in the hybrid scheme $\mathcal{F}^{\text{hybrid,conv}}_{\text{min}} = 3.8733$, after proper scheme conversion of γ. In addition, the minimization was repeated in the hybrid renormalization scheme to test the renormalization-scheme dependence of the obtained minimum and a similar value of $\mathcal{F}^{\text{hybrid}}_{\text{min}} = 3.8731$ was obtained.
Due to the significantly reduced tension between the prediction and the measured value for a_μ within the SM for fit scenario 2, $\mathcal{F}_{\text{SM}}$ is closer to $\mathcal{F}_{\text{min}}$ than in fit scenario 1. All details on the location of the found minimum of $\mathcal{F}$ are given in Tab. 5.4. The minimum of fit scenario 2 is located at $\lambda_1 = 0.257$, i.e. close to its perturbativity limit. A variation of the parameters c_{g} and c_{s} in the range 10^2–10^4

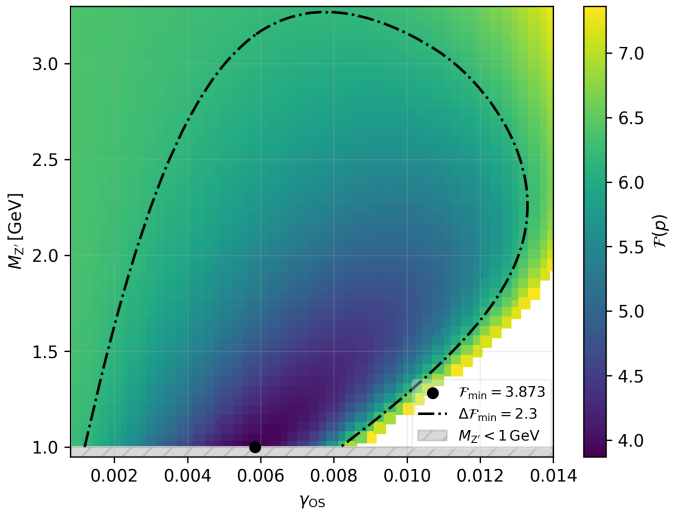

Figure 5.25.: The location of the minimum (black dot), the $\mathcal{F}_{2.3}$ contour (black dashed line), and the results for the scan of the vicinity of the minimum (coloured squares) in the γ_{OS}–$M_{Z'}$ plane in fit scenario 2.

shows only a negligible effect on the results obtained for the minimum and the $\mathcal{F}_{2.3}$ contour in the γ–$M_{Z'}$ plane. Thus, we choose $c_g = c_s = 10^4$ here.
In fit scenario 2 the minimum is, compared to fit scenario 1, located at an even smaller value of the gauge-boson mixing angle of $\gamma_{OS} = 0.0059^{+0.005}_{-0.002}$. The mass of the Z′ boson is at its lower limit[28] $M_{Z'} = 1^{+0.94}_{-\underline{0}}$ GeV. For the Higgs-sector parameters one finds $\alpha' = 0.2^{+\underline{0}}_{-\underline{0.2}}$, $\lambda_{12} = 0.34^{+0.04}_{-\underline{0.34}}$, and $M_h = 5.25^{+\underline{9995}}_{-\underline{4.25}}$ GeV. Thus, as in fit scenario 1, the mass hierarchy $M_H = M_h^{SM}, M_h < M_h^{SM}$ is preferred. Again, α' and λ_{12} are at the maximum[29] values of the available parameter space, i.e. they have the maximum distance to their respective SM-limit values, and the BSM Higgs-boson mass is found to minimize the tension between predictions and measurements when it is close to, but not exactly at, its lower bound of 1 GeV. However, all three BSM Higgs parameters are only very loosely constrained by the fit, which is reflected by their large uncertainties. This is even more extreme for the BSM parameters introduced in the fermion sector. We find the BSM fermion mass at its upper limit $m_{\nu_4} = 10^{+\underline{0}}_{-\underline{9.9}}$ TeV and a small value of $\theta_r = 0.0009^{+\underline{1.5699}}_{-\underline{0.0009}}$ for the BSM mixing angle. Both are, however, practically unconstrained by the fit. Finally, we remark that all uncertainties for the SM-like input parameters agree with their measurement uncertainties used in the construction of $\mathcal{F}$.
In Fig. 5.25 the result of the minimization of $\mathcal{F}$ with minimal value $\mathcal{F}_{min}$ (black point), the corresponding $\mathcal{F}_{2.3}$ contour (black dashed line), and the respective re-

[28] Here, underlined values lie at extreme values at the borders of the allowed parameter space.
[29] Similar to fit scenario 1, for the given values of α' and M_h, λ_{12} is at its upper limit set by the perturbativity constraint on λ_1.

$\mathcal{O}_i$	$\mathcal{O}_{\text{min},i}^{\text{DASM}}$	$\chi_{\mathcal{O}_i}$	$\chi_{\mathcal{O}_i,\text{SM}}$
a_μ	$1.165920508 \times 10^{-3}$	0.12	1.69
M_W	80.3591 GeV	1.49	1.95
$s^2_{\text{w,eff},l}$	0.23158	1.01	1.0
$\Gamma_{\text{Z}\to ll}$	83.9755 MeV	0.31	0.35

Table 5.5.: Values of the PO predictions $\mathcal{O}_{\text{min},i}^{\text{DASM}}$ at the location of the minimum in fit scenario 2. Further, the respective values of the $\chi_{\mathcal{O}_i}$ are given for the DASM and the SM case.

sults obtained by the scan in the vicinity of the minimum are shown. Again, the white region corresponds to an area with $\mathcal{F}(p) > \mathcal{F}_\text{min} + 3.5$, which we do not display in colour here to have a more detailed representation of the remaining (more interesting) scan results.
As mentioned above, the minimum is located close to the perturbativity limit of λ_1. This can lead to non-vanishing contributions of $\mathcal{P} \neq 0$ contributing to the found minima in the scan of the vicinity of the location of the minimum. For our choice of $c_\text{g} = c_\text{s} = 10^4$ the additional cost introduced by $\mathcal{P}$ is of $\mathcal{O}(10^{-6})$ in the entire scan range and, thus, negligible compared to the theoretical uncertainty of $\mathcal{F}_\text{min}$.
The $\mathcal{F}_{2.3}$ contour is bounded from below by the constraint $M_{\text{Z}'} > 1\,\text{GeV}$ and reaches up to values of $M_{\text{Z}'} \approx 3.27\,\text{GeV}$. Further, the scan indicates that the predictions might agree even better with data for smaller values[30] of $M_{\text{Z}'} < 1\,\text{GeV}$. The values for the gauge-boson mixing angle that can be reached within the $\mathcal{F}_{2.3}$ contour are within $[0.0012, 0.0133]$.
Starting from the position of the minimum, there is a strong increase of $\mathcal{F}$ for increasing values of γ_OS, compared to the overall scale set by $\mathcal{F}_\text{min}$. However, in contrast to fit scenario 1, there is only a moderate increase when leaving the region marked by the $\mathcal{F}_{2.3}$ contour in the opposite direction ($\gamma_\text{OS} \to 0$). This is directly related to the difference in the used SM predictions for a_μ in the two fit scenarios, simply reflecting that the SM prediction, and, thus, the SM limit $\gamma_\text{OS} \to 0$, provides a significantly better description of the data in fit scenario 2. Finally, we want to highlight that within the given $\mathcal{F}_{2.3}$ contour, one finds a rather narrow valley-shaped area (blue region) tied to the location of the minimum, that provides the best agreement between measurements and predictions. This valley-shaped region singles out the same direction in the γ_OS–$M_{\text{Z}'}$ plane that was found to minimize the tension between predictions and measurements of a_μ (see lower-right plot of Fig. 5.14).
We list the values of the POs at the location of the minimum and the respective values of the $\chi_{\mathcal{O}_i}$ within the DASM (at the location of the minimum) and within the SM in Tab. 5.5. To further investigate the results of the minimization, we

[30] However, similar to the situation for fit scenario 1, our approximations done in the derivations of the POs do not allow us to explore this region of the parameter space properly.

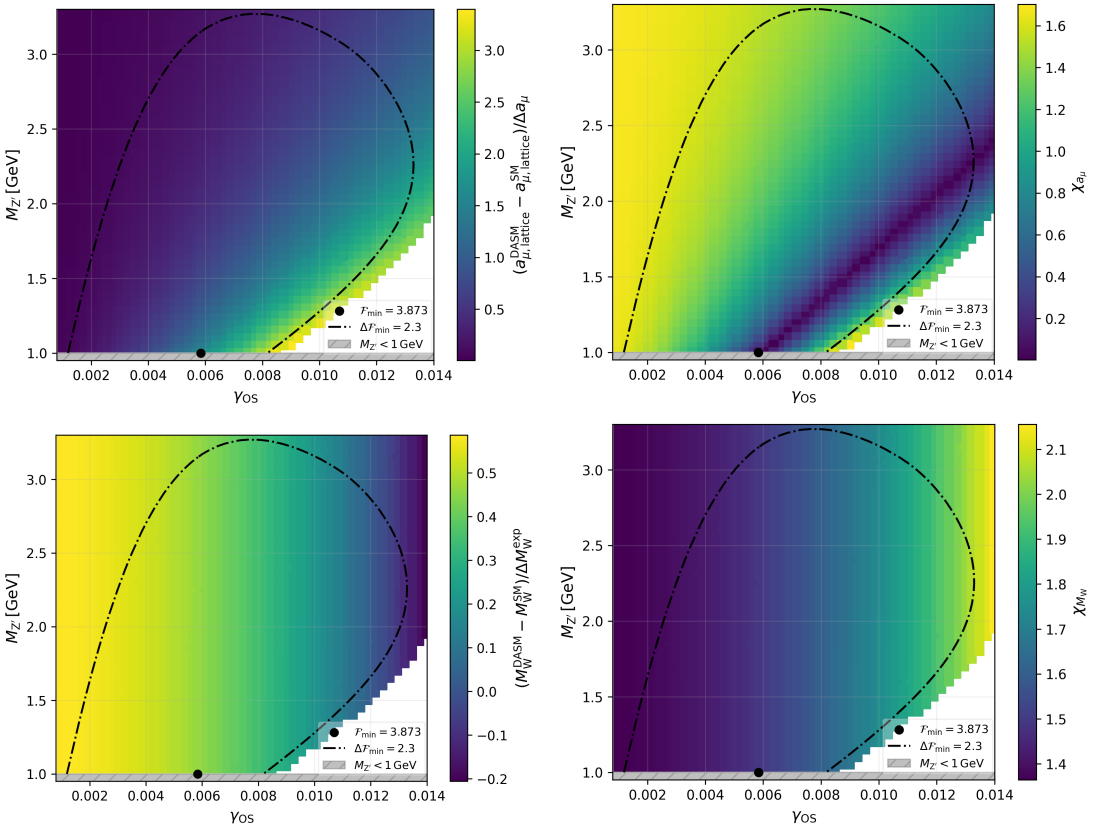

Figure 5.26.: The differences of the pull values between the DASM and the SM for $a_{\mu,\text{lattice}}^{\text{DASM}}$ (upper left) and $M_{\text{W}}^{\text{DASM}}$ (lower left) and the corresponding contributions $\chi_{\mathcal{O}_i}$ to $\mathcal{F}$ (right column) in the vicinity of the minimum for fit scenario 2.

give the differences between the pull values for the considered POs in the DASM and SM and the corresponding contributions $\chi_{\mathcal{O}_i}$ in the left and right columns of Figs. 5.26 and 5.27, respectively.

In the upper-left plot of Fig. 5.26 one finds a strong increase of the a_μ prediction within the DASM for increasing values of γ_{OS} (at the right side of the $\mathcal{F}_{2.3}$ contour) for values of $M_{\text{Z}'} < 2\,\text{GeV}$, which leads to a strong increase of the respective contributions χ_{a_μ} to $\mathcal{F}$. These contributions dominantly determine the $\mathcal{F}_{2.3}$ contour in this part of the parameter space. For decreasing $\gamma_{\text{OS}} \to 0$, $a_{\mu,\text{lattice}}^{\text{DASM}}$ slowly approaches its respective SM value leading to a comparably moderate increase of χ_{a_μ}. As expected by the previous discussion, there is a distinct direction (blue area, right plot) in the γ_{OS}–$M_{\text{Z}'}$ plane where the predictions show very good agreement with the data, giving rise to the valley-shaped area mentioned previously.

The difference between the DASM and SM pull values for M_{W} (lower left) and the values of $\chi_{\mathcal{O}_{M_{\text{W}}}}$ (lower right) are shown in the lower row of Fig. 5.26. For large parts of the scanned parameter space $M_{\text{W}}^{\text{DASM}}$ (lower-left plot in Fig. 5.26) is larger

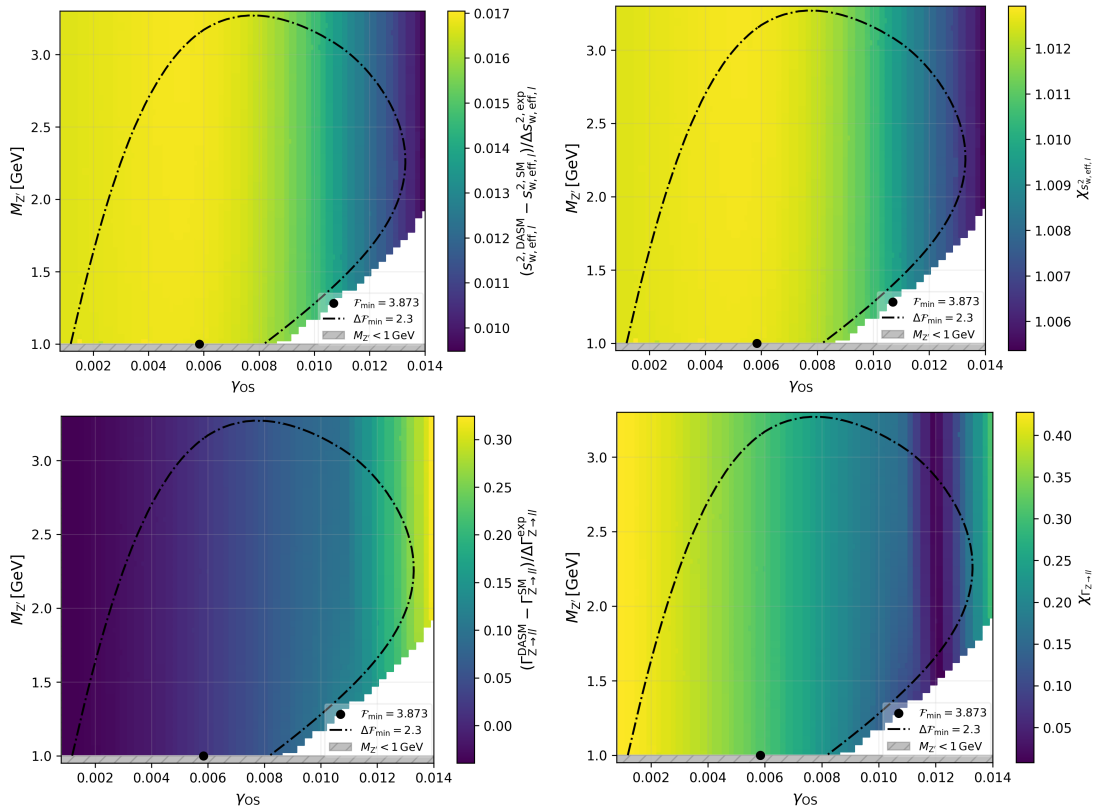

Figure 5.27.: The differences of the pull values between the DASM and the SM for $s^{2,\mathrm{DASM}}_{\mathrm{w,eff},l}$ (upper left) and $\Gamma^{\mathrm{DASM}}_{\mathrm{Z}\to ll}$ (lower left) and the corresponding contributions $\chi_{\mathcal{O}_i}$ to $\mathcal{F}$ (right column) in the vicinity of the minimum for fit scenario 2.

than its respective counterpart in the SM, i.e. closer to its measured value. However, as expected from the discussion given in Sect. 5.4.1, for large enough values of γ_{OS} the DASM prediction $M_{\mathrm{W}}^{\mathrm{DASM}}$ is lower than its SM counterpart, leading to an increase of the respective contributions $\chi_{M_{\mathrm{W}}}$ (lower-right plot in Fig. 5.26) to $\mathcal{F}$ compared to its corresponding SM value. Further, we want to emphasize that for fit scenario 2, $\chi_{M_{\mathrm{W}}}$ provides in the SM (see Tab. 5.5) the largest contribution to $\mathcal{F}$, and leads to the dominant contributions that determine the $\mathcal{F}_{2.3}$ contour for increasing values of γ_{OS} in the direction dictated by a_μ. Finally, we note that, due to contributions from the Higgs sector extension that lead to an increase of the predicted value, $M_{\mathrm{W}}^{\mathrm{DASM}}$ shows, at the location of the minimum, better agreement with data than the respective SM prediction (see Tab. 5.5).
In contrast to $a_{\mu,\mathrm{lattice}}^{\mathrm{DASM}}$ and $M_{\mathrm{W}}^{\mathrm{DASM}}$ the Z-pole observables $s^{2,\mathrm{DASM}}_{\mathrm{w,eff},l}$ and $\Gamma^{\mathrm{DASM}}_{\mathrm{Z}\to ll}$ (see left column of Fig. 5.27) show only small variations with respect to the corresponding experimental uncertainties in the entire fit range. Starting from the location of the minimum, the agreement between their predictions and the respective measurements increases (decreases) with increasing (decreasing) values of γ_{OS}, but

show only little sensitivity to variations of $M_{Z'}$ within the shown region. Similarly to fit scenario 1, $\Gamma^{\text{DASM}}_{Z\to ll}$ precisely agrees with the corresponding measured value for $\gamma_{\text{OS}} \approx 0.012$. For further increasing values of γ_{OS} the prediction for $\Gamma_{Z\to ll}$ further increases and consequently the values of $\chi_{\Gamma_{Z\to ll}}$ increase.
In summary, in fit scenario 2 the minimization is, similar to fit scenario 1, dominantly driven by minimizing the tension between the predictions and the measured value for a_μ. This yields a distinct direction in the γ_{OS}–$M_{Z'}$ plane where the prediction and the measured value show perfect agreement. Within this direction the fit prefers the smallest possible value for γ_{OS}. This maximizes the level of agreement between the predictions and the measured value for M_{W} within the area preferred by $(g-2)_\mu$. In the vicinity of the minimum the remaining two POs $s^2_{\text{w,eff},l}$ and $\Gamma_{Z\to ll}$ do not contribute significantly to the precise determination of the location of the minimum or the respective $\mathcal{F}_{2.3}$ contour.

5.5.4.3. Summary and comparison of the fit results

For both fit scenarios the DASM can provide significantly better agreement between theory predictions and experimental results for the considered POs. This is reflected by the significantly lower values of $\mathcal{F}_{\text{min,s1}} = 4.54$ and $\mathcal{F}_{\text{min,s2}} = 3.87$ obtained within the two scenarios, respectively, compared to the corresponding SM values of $\mathcal{F}_{\text{SM,s1}} = 30.70$ and $\mathcal{F}_{\text{SM,s2}} = 7.75$. To test the renormalization-scheme dependence of the results, the minimization was repeated using the hybrid renormalization scheme instead of the OS scheme in the two fit setups. The values $\mathcal{F}^{\text{hybrid}}_{\text{min,s1}} = 4.54$ and $\mathcal{F}^{\text{hybrid}}_{\text{min,s2}} = 3.87$ were found for the minima in the two fit scenarios, showcasing a negligible dependence of the result on the renormalization scheme.
In both fit scenarios, small values of $\gamma_{\text{OS}} = \mathcal{O}(10^{-3})$ and $M_{Z'} = 1\,\text{GeV}$ are preferred. For the precise determination of the γ_{OS}–$M_{Z'}$ region preferred by the minimization, a_μ plays a major role. It singles out a specific direction in the γ_{OS}–$M_{Z'}$ plane which resolves the tension between the respective predictions and the measured value of a_μ.
For $M_{Z'} < M_{\text{Z}}$ the W-boson mass prediction shows the highest level of agreement for the smallest possible value of γ_{OS}. Therefore, in the γ_{OS}–$M_{Z'}$ region preferred by a_μ, the minimum is located at the lowest possible value for γ_{OS}. Note that the significantly smaller discrepancy between $a^{\text{SM}}_{\mu,\text{lattice}}$ and a^{exp}_μ, compared to the discrepancy between $a^{\text{SM}}_{\mu,e^+e^-}$ and a^{exp}_μ, allows for smaller values of γ_{OS} in fit scenario 2 compared to fit scenario 1, i.e. the value of γ_{OS} at the location of the minimum is closer to its SM limit ($\gamma_{\text{OS}} \to 0$) in fit scenario 2. Additionally, M_{W} yields an important constraint for the determination of the respective $\mathcal{F}_{2.3}$ contour in the γ_{OS}–$M_{Z'}$ plane, especially for increasing values of γ_{OS} in the direction dictated by a_μ.
Finally, for all parameter configurations found by the respective scans over the vicinities of the minima, both $s^{2,\text{DASM}}_{\text{w,eff},l}$ and $\Gamma^{\text{DASM}}_{Z\to ll}$ vary only slightly compared to

the respective experimental uncertainties and an equally good agreement between the respective predictions and measurements as in the SM case is found at the minima. Thus, their impact on the minimization of $\mathcal{F}$ and the determination of the $\mathcal{F}_{2.3}$ contour in the γ_{OS}–$M_{\mathrm{Z}'}$ plane is small in either fit scenario.
The DASM prediction for a_μ depends only slightly on the remaining BSM parameters originating from the Higgs and fermion sectors. Their preferred values are mainly determined via the remaining three POs. For both fit scenarios, the mass hierarchy $M_{\mathrm{H}} = M_{\mathrm{h}}^{\mathrm{SM}}$, $M_{\mathrm{h}} < M_{\mathrm{h}}^{\mathrm{SM}}$, i.e. a light BSM Higgs boson, is preferred. In the determination of the precise values of the BSM Higgs-sector parameters at the location of the minimum, M_{W} plays an important role. In both investigated scenarios, the BSM Higgs-sector parameters lead to an increase of $M_{\mathrm{W}}^{\mathrm{DASM}}$, bringing it closer to its experimental counterpart. Thus, even though the preferred gauge-sector parameter configuration leads to an increase in the tension between $M_{\mathrm{W}}^{\mathrm{DASM}}$ and $M_{\mathrm{W}}^{\mathrm{exp}}$, with the help of the BSM Higgs sector one ultimately finds better agreement between its measurement and the prediction at the location of the minimum compared to the SM case in both fit scenarios. However, in either fit scenario the BSM Higgs-sector parameters remain widely unconstrained by the investigated POs.
In the investigated parameter regions, the impact of the BSM fermion-sector parameters on the considered POs is negligible. Thus, they remain practically unconstrained by the fit, as is also pointed out by the respective values for their 1σ uncertainty intervals.

5.5.5. Outlook

The results of this first analysis on the phenomenological implications of the various SM extensions introduced by the DASM clearly show that the DASM is an interesting and promising candidate in the search for new physics. In order to obtain a more sophisticated and more complete picture of the predictive power of the DASM and its phenomenological implications, we list several desirable additions for future analyses below.
To gain an even better insight into the exact implications of the gauge-sector extension introduced by the DASM, we propose the following future analyses:

- One should include the possibility for very light masses of the Z' boson $M_{\mathrm{Z}'} < 1\,\mathrm{GeV}$ in order to explore this promising part of the parameter space. In either of the two investigated setups—scenario 1 or scenario 2—our analysis suggests that masses of the Z' boson below the lower limit of $M_{\mathrm{Z}'} > 1\,\mathrm{GeV}$ are preferred. This lower bound is introduced to ensure the validity of certain approximations used in the derivations of the POs, which rely on the fact that the masses of external leptons are small compared to the mass of the Z' boson. Additionally, in the case $M_{\mathrm{Z}'} \leq m_\mu - m_\mathrm{e}$ the possibility of invisibly decaying Z' radiation opens up an additional decay channel in muon decay. This yields further NLO BSM contributions to the prediction of the mass of the W boson performed in Sect. 5.4.1, which have to be taken into account in respective analyses.

- Invisible Z'-radiation effects will, even for $M_{\mathrm{Z}'} \geq 1\,\mathrm{GeV}$, affect the LEP observables at NLO in the BSM effects. Similarly to the virtual BSM corrections, contributions originating from real Z' radiation lead to $\mathcal{O}(s_\gamma^2)$ effects in the two LEP POs considered in this work. Therefore, having the results from our analyses performed in Sects. 5.4.3-5.5.4 in mind, the respective contributions to $\Gamma_{\mathrm{Z}\to ll}^{\mathrm{DASM}}$ and $s_{\mathrm{w,eff},l}^{2,\mathrm{DASM}}$ are expected to be small in the phenomenologically preferred parameter regions (where $\gamma = \mathcal{O}(10^{-3})$) and are neglected in the presented analyses. However, taking into account the exact experimental setup used for the LEP measurements, a sophisticated analysis dedicated to a more correct theoretical treatment of these additional real-radiation effects should be performed to ensure that they are correctly included in the respective predictions in future analyses.

- There seem to be very powerful limits, especially for small gauge-boson masses of $M_{\mathrm{Z}'} < 10\,\mathrm{GeV}$, on certain γ–$M_{\mathrm{Z}'}$ combinations obtained from direct searches of neutral BSM gauge bosons at the NA64 [124], BaBar [125], and FASER [126] experiments that should be taken into account in future analyses. Unfortunately, their description of the chosen underlying theoretical setup is rather blurry, i.e. the exact interpretation of their reported results is not clear to us. A careful study is needed to understand how the reported limits translate into constraints on DASM parameters.

- To obtain a more complete picture, further POs such as additional Z-boson branching ratios, aiming to test the gauge-sector extension of the DASM at an even higher level of precision, should be included in the analyses.

With our choice of investigated POs the main focus of the analysis lies in exploring the phenomenological implications of the gauge-sector extension of the DASM. This is also reflected in the fact that the remaining BSM parameters of the Higgs and fermion sectors are widely unconstrained by the analysis. Thus, to further investigate the Higgs- and fermion-sector extensions of the DASM we propose for future analyses:

- To obtain a more precise estimate for the BSM Higgs-sector parameters, studies on branching ratios of the SM-like Higgs boson, or even more subtle predictions, such as a full prediction for the $S \to 4$ fermions branching ratio, where S denotes the SM-like Higgs boson of h and H, should be included in future analyses. For instance, even though the decay width of the SM-like Higgs boson is not known precisely, in case its decay into two BSM Higgs bosons is kinematically allowed, the resulting partial decay width can be used to get a first, rough upper limit[31] on λ_{12}.

- The lower bound of $m_{\nu_4} > 100\,\text{GeV}$ was introduced to avoid the unphysical artifacts, i.e. the threshold effects discussed in Sect. 5.3, in the minimization procedure. These artifacts originate from neglecting the unstable nature of decaying particles. Even though our analysis is not sensitive to the exact value of m_{ν_4} (see Sects. 5.4.1–5.4.5 and 5.5.4), it is desirable to cure these artifacts in future analyses. This can, e.g., be achieved by introducing a complex mass for ν_4 via the complex-mass scheme.

- In certain regions of the parameter space, the additional fermion of the dark sector ν_4 can be a stable particle[32]. A dedicated DM analysis should be performed within the DASM to see whether ν_4 provides a promising DM candidate, i.e. if the DASM offers potential explanations for the existence of DM.

Finally, the DASM introduces an additional gauge boson, a BSM Higgs boson, and a dark fermion. A dedicated study on their possible decays should be performed. This will give first implications for possible direct searches at modern high-precision experiments.

[31] This rough estimate is, e.g., obtained by simply demanding that this partial decay width does not exceed the upper experimental limit of the total decay width of the SM-like Higgs boson.

[32] This can, e.g., be achieved by taking $\theta_\text{r} \to 0$, where in our collider approximation the only non-vanishing interaction of ν_4 is given by $Z'\bar{\nu}_4\nu_4$.

6. Summary

There are several observations, such as the existence of DM or the matter–antimatter asymmetry in the visible universe that imply that the SM cannot be the complete theory describing Nature. Thus, it should rather be seen as an effective theory of some more fundamental model. In the pursuit of finding solutions for some of the open questions of modern HEP, many promising theories, like SUSY models, were developed. However, to this day there exists no evidence for the realization of any of these models in Nature. One promising ansatz in the search for possible new physics is to investigate the phenomenological implications of promising, but rather simple and generic extensions of the SM. Testing the predictions of these extensions with high precision shows whether they can address some of the open questions without destroying the astonishing predictive power that the SM shows for numerous collider measurements. This might offer first hints on the structure of possible new physics.

In the first part of this work we formulated the DASM. The DASM extends the SM by a rather generic dark sector. This dark sector is a singlet with respect to the SM gauge group, but comprises a $U(1)_\mathrm{d}$ gauge symmetry. The SM part of the theory is a singlet under this additional gauge group. The full gauge group of the DASM is given by $SU(3)_\mathrm{C} \times SU(2)_\mathrm{W} \times U(1)_\mathrm{Y} \times U(1)_\mathrm{d}$. In addition to the gauge field corresponding to the $U(1)_\mathrm{d}$, the DASM introduces a new complex Higgs field ρ to the scalar sector, which develops a non-vanishing vev. The Higgs field ρ carries only charge of the $U(1)_\mathrm{d}$. Consequently, the gauge group of the dark sector is spontaneously broken. This results in two new massive bosons, one Higgs boson and a Z' boson. Furthermore, right-handed SM-like neutrinos, as well as a Dirac fermion that carries charge of the $U(1)_\mathrm{d}$, are introduced in the DASM. Thus, the DASM uses the field-strength tensor of the weak hypercharge as well as the mass operator of the SM-like Higgs doublet, which are the only two gauge-invariant and renormalizable operators present in the SM, to open two portals to its dark sector. Additionally, the right-handed parts of the SM-like neutrinos provide a third portal to the dark sector.

We set up the theoretical framework for the DASM and formulate the theory in terms of the fields that correspond to mass eigenstates. Further, we give explicit results for the full Lagrangian of the DASM in R_ξ gauge. To this end, we introduce

a "collider approximation" for the neutrino sector extension which is well suited for studies of collider phenomenology. In this collider approximation, the DASM introduces two additional free parameters in the gauge sector, three free parameters in the Higgs sector, and two additional input parameters in the neutrino sector. Making use of the masses of the new particles and the mixing angles introduced in the Higgs, gauge, and neutrino sectors, we defined a particularly intuitive and experimentally easily accessible set of input parameters suitable for studies of the phenomenological implications of the DASM.
To be able to derive NLO predictions for POs within the DASM, we set up a complete renormalization of the DASM at NLO. For one, we defined a proper OS renormalization scheme—based on physical S-matrix elements—for the newly introduced mixing angles. This is of particular interest, since mixing angles are often introduced to parameterize BSM models, and there seems to be no agreement on their proper OS renormalization in the literature. We give explicit results for the OS renormalization constants of the gauge-, Higgs-, and fermion-sector mixing angles within the DASM. The suggested OS renormalization scheme for the mixing angles has various desirable properties [81]:

- The OS renormalization conditions for the mixing angles are based on S-matrix elements leading to gauge-independent renormalization constants.
- The resulting OS mixing-angle renormalization constants have smooth limits for extreme values of the respective mixing angle.
- Predictions for observables based on the OS renormalization scheme are stable in the degeneracy limit of the masses of the respective mixing particles.
- Employing complete OS renormalization for all mass-related parameters leads to a cancellation of all tadpole contributions in predictions for observables. Therefore, the presented OS predictions do not depend on the treatment of the tadpoles.
- The proposed OS renormalization for the gauge-sector mixing angle γ leads to a process-independent renormalization constant $\delta\gamma_{\mathrm{OS}}$.

For mixing angles connected to kinetic mixing, such as the mixing angle γ introduced in the gauge sector of the DASM, we are not aware of any complete OS renormalization proposed in the literature (previously to our work [38]). Therefore, the here presented OS renormalization can be seen as a proposal for the OS renormalization of gauge-sector mixing angles. As an alternative to the OS renormalization we give the corresponding $\overline{\mathrm{MS}}$ renormalization constants for all introduced mixing angles explicitly. $\overline{\mathrm{MS}}$ renormalization schemes are symmetric in the mixing fields and, by definition, process independent. However, $\overline{\mathrm{MS}}$ renormalization for mixing angles can lead to perturbative instabilities in certain regions of the parameter space and, in general, introduces a dependence on the tadpole

treatment in predictions for observables.
Finally, we performed a first phenomenological analysis of the DASM to investigate the effects of its various newly introduced features on POs. Due to the detailed studies of Higgs singlet extensions, which introduce Higgs sector extensions similar to the one of the DASM, the focus of our analysis was to investigate the phenomenological implications of the gauge-sector extension. To this end, we consider four POs: the mass of the W boson derived from muon decay, the anomalous magnetic moment of the muon, the leptonic effective weak mixing angle, and the leptonic partial decay width of the Z boson. We derived NLO predictions for these POs within the DASM. Assuming BSM contributions to be small we add for each PO the difference between the NLO DASM and NLO SM predictions to the respective state-of-the-art SM prediction to obtain sufficiently precise predictions that match the precision of the respective measurements.
The SM predictions for the leptonic effective weak mixing angle and the leptonic partial decay width of the Z boson agree with their respective measurements within their experimental 1σ uncertainties. The SM prediction for the mass of the W boson agrees with the corresponding experimental world average within 2σ. Note that, the world average used in our studies does not include the CDF measurement [7] since it is not compatible with other measurements of the W-bosons mass [8]. However, we want to remark that there exist regions in the parameter space of the DASM that lead to agreement between its predictions for the W-boson mass and the CDF measurement. For the anomalous magnetic moment of the muon currently two different SM predictions are present. They are based on different approaches for the determination of the hadronic vacuum polarization, either via a data-driven approach ($a_{\mu,e^+e^-}^{\mathrm{SM}}$) [4] or via lattice QCD ($a_{\mu,\mathrm{lattice}}^{\mathrm{SM}}$) [5]. The two approaches lead to a 5.1σ and a 1.7σ difference between SM prediction and measurement, respectively. Due to this large discrepancy, we included both scenarios in our studies. The dependences of these predictions on the new parameters were investigated in detail. All four POs only loosely depend on the additional parameters introduced by the Higgs- and neutrino-sector extensions and they are insensitive to the sign of the gauge-sector mixing angle.
A simultaneous fit of all four POs was performed to determine the parameter configuration that minimizes the tension between theory predictions and data. To this end, a χ^2-like likelihood function $\mathcal{F}$ was minimized within the perturbative region of the parameter space. For the two investigated scenarios, using either $a_{\mu,e^+e^-}^{\mathrm{SM}}$ or $a_{\mu,\mathrm{lattice}}^{\mathrm{SM}}$ for the derivation of $(g-2)_\mu$, we find the minimum values $\mathcal{F}_{\mathrm{min,s1}} = 4.54$ and $\mathcal{F}_{\mathrm{min,s2}} = 3.87$, respectively. The corresponding SM values in the two scenarios are given by $\mathcal{F}_{\mathrm{SM,s1}} = 30.70$ and $\mathcal{F}_{\mathrm{SM,s2}} = 7.75$. This shows that in both scenarios a significantly better agreement between data and predictions can be achieved within the DASM than for the SM case. In either scenario, the DASM can provide perfect agreement between predictions and measurement of $(g-2)_\mu$. Simultaneously the agreement between measurement and prediction for the W-boson mass is slightly better than in the SM and the predictions for the leptonic effective weak

mixing angle and the leptonic partial decay width show an equally good agreement with their respective measurements as in the SM case. In both scenarios, small values of the gauge-boson mixing angle $\gamma = \mathcal{O}(10^{-3})$ are preferred. Furthermore, both minima are located at the lower limit of $M_{Z'} = 1\,\text{GeV}$, which was imposed to guarantee the validity of the approximations performed in the derivations of the considered POs. As expected, the remaining BSM parameters remain widely unconstrained in our analysis.

This first analysis shows that the DASM remains a promising candidate to parameterize and identify possible new physics. However, to fully explore the predictive power of the DASM, further analyses have to be performed. Considering the results of our parameter fit, future analyses should avoid approximations that restrict the viable parameter space to $M_{Z'} > 1\,\text{GeV}$. This would reveal whether even lower masses of the Z′ boson can lead to even better agreement between measurements and predictions.
To set the cornerstone for direct searches at any HEP experiments, a detailed study of the decays of the new physics particles predicted by the DASM should be performed. Furthermore, the obvious next step for future analyses is to take more EW POs as well as limits obtained from direct Z′-boson searches performed, e.g. at the NA64 [124], BaBar [125], and FASER [126] experiments, into account. To obtain a more precise estimate of the Higgs-sector parameters additional POs sensitive to the Higgs-sector extension—such as predictions for branching ratios of the SM-like Higgs boson—should be considered. If kinematically allowed, even the decay of the SM-like Higgs boson into two BSM Higgs bosons could be used to obtain a first rough upper limit on λ_{12}. Finally, a dedicated DM analysis should be performed within the DASM to investigate whether the DASM might offer a possible explanation for the origin of DM.

Appendices

A. Cross sections within perturbation theory

In theoretical HEP, one of the main interests lies in determining precise predictions for cross sections of scattering events. In this thesis, we make use of perturbation theory to compute predictions. To this end, we expand the investigated observables in the coupling constants, which are assumed to be small. Here, we briefly describe the perturbative approach, closely following Refs. [51, 52].
In quantum field theory any scattering process can be described by the so-called S-matrix. The S-matrix quantifies the transition between the (possibly multi-particle) incoming state $|i\rangle$ and the final state $|f\rangle$. Splitting the Lagrangian in a free part $\mathcal{L}_0$ (monomials with up to two fields) and an interaction part $\mathcal{L}_\mathrm{I}$ (monomials with more than two fields)

$$\mathcal{L} = \mathcal{L}_0 + \mathcal{L}_\mathrm{I}, \tag{A.1}$$

the S-matrix element is, assuming asymptotically free initial and final states[1], given by the time-evolution operator in the interaction picture

$$S = \mathrm{T}\left[\exp\left\{\mathrm{i}\int \mathrm{d}^4x \mathcal{L}_\mathrm{I}\right\}\right], \tag{A.2}$$

where T denotes the time-ordering operator. The corresponding transition matrix element $\mathcal{M}_{fi}$ is defined via

$$\langle f|\, S\, |i\rangle = \langle f|i\rangle + \mathrm{i}(2\pi)^4\delta^{(4)}(p_i - p_f)\mathcal{M}_{fi}, \tag{A.3}$$

where the first term on the right side describes the scenario where no interaction takes place. Further, $p_{i/f}$ denote the total initial- and final-state four-momenta, respectively, the delta function ensures four-momentum conservation, and $|i\rangle$ and $|f\rangle$ are assumed to be asymptotically free states. Within perturbation theory, the S-matrix element can be related to so-called Feynman diagrams. Feynman diagrams are built of propagators (described by $\mathcal{L}_0$) and vertices (described by

[1] It is assumed that all interactions happen in a finite time interval and that the states are free of interactions for asymptotic times $t \to \pm\infty$.

$\mathcal{L}_{\mathrm{I}}$), which can be translated into analytical expressions via the Feynman rules. For $2 \to n$ particle scattering of unpolarized initial-state particles the absolute square of $\mathcal{M}_{fi}$ is related to the desired interaction cross section via

$$\mathrm{d}\sigma = \frac{1}{P\,\mathrm{F}(p_1,p_2)}\mathrm{d}\Phi(p_1,p_2,q_1,\ldots,q_n)|\mathcal{M}_{fi}|^2, \tag{A.4}$$

with $P = I_1! \times \cdots \times I_n!$, where I_j, $j = 1,\ldots,n$, is given by the number of identical final-state particles of type j, denoting the symmetry factor that has to be included to avoid double-counting. The flux factor for the incoming particles[2] is given by

$$\mathrm{F}(q_1,q_2) = 4\sqrt{(p_1p_2)^2 - m_1^2m_2^2}, \tag{A.5}$$

with the masses of the incoming particles m_1, m_2. The differential phase-space volume is defined via

$$\mathrm{d}\Phi(p_1,p_2,q_1,\ldots,q_n) = (2\pi)^4\delta^{(4)}\left(p_1+p_2-\sum_{i=1}^{n}q_i\right)\frac{\mathrm{d}^3\vec{q}_1}{2E_{q_1}(2\pi)^3}\cdots\frac{\mathrm{d}^3\vec{q}_n}{2E_{q_n}(2\pi)^3}, \tag{A.6}$$

where $E_{q_i} = \sqrt{m_{q_i}^2 + |\vec{q}_i|^2}$, $\vec{q}_i$, and q_i denote the energies as well as the three- and four-momenta of the final-state particles, respectively, and m_{q_i} is the mass of the final-state particle i. Further, for unpolarized scattering the squared matrix element $|\mathcal{M}_{fi}|^2$ has to be spin averaged over the initial-state particles and summed over all unresolved d.o.f. of the final-state particles. In the case of a particle decay, i.e. a $1 \to n$ process, the differential decay width is given by

$$\mathrm{d}\Gamma_{1\to f} = \frac{(2\pi)^4}{2E_pP}\delta^{(4)}\left(p-\sum_{i=1}^{n}q_i\right)\frac{\mathrm{d}^3\vec{q}_1}{2E_{q_1}(2\pi)^3}\cdots\frac{\mathrm{d}^3\vec{q}_n}{2E_{q_n}(2\pi)^3}|\mathcal{M}_{fi}|^2, \tag{A.7}$$

where $p = (E_p, \vec{p})$ is the four-momentum of the mother particle. For two massless particles in the final state Eqs. (A.4) and (A.7) simplify in the centre-of-mass frame to

$$\frac{\mathrm{d}\sigma_{2\to2}}{\mathrm{d}\Omega_{\mathrm{CM}}} = \frac{|\vec{q}_1|}{64\pi^2 s|\vec{p}_1|P}|\mathcal{M}_{fi}|^2, \qquad \frac{\mathrm{d}\Gamma_{1\to2}}{\mathrm{d}\Omega_{\mathrm{CM}}} = \frac{|\vec{q}_1|}{32\pi^2 m_p^2 P}|\mathcal{M}_{fi}|^2, \tag{A.8}$$

where $\sqrt{s} = (E_1 + E_2)$, with the energies of the initial-state particles E_1, E_2, m_p is the mass of the mother particle, and $|\vec{p}_1|$, $|\vec{q}_1|$ denote the magnitude of the three-momenta of the incoming and outgoing particles, respectively. Further, $\mathrm{d}\Omega_{\mathrm{CM}}$ is the solid angle in the CM frame defined by $\vec{q}_1$.

[2]Here, it is assumed that the incoming particles are (anti)parallel to each other.

B. Gauge transformations of the fields

Here we give the infinitesimal gauge transformations of the fields needed for the derivation of the Faddeev–Popov ghost Lagrangian in Sect. 3.2.3. As in the rest of this work, we adopt the conventions of Ref. [54] for the field-theoretical SM quantities here.
The infinitesimal gauge transformations of the gauge fields W_μ^a, B_μ, and C_μ read

$$\delta W_\mu^a = \partial_\mu \delta\theta^a + g_2 f^{abc} W_\mu^b \delta\theta^c, \qquad \delta B_\mu = \partial_\mu \delta\theta^{\mathrm{Y}}, \qquad \delta C_\mu = \partial_\mu \delta\theta^{\mathrm{C}}, \tag{B.1}$$

where the gauge-group parameters of the $SU(2)_{\mathrm{W}}$, $U(1)_{\mathrm{Y}}$, and $U(1)_{\mathrm{d}}$ gauge groups are given by $\delta\theta^a$, $\delta\theta^{\mathrm{Y}}$, and $\delta\theta^{\mathrm{C}}$, respectively. Similarly we find for the Higgs fields Φ and ρ

$$\delta\Phi = \left(-\frac{\mathrm{i}g_1}{2}\delta\theta^{\mathrm{Y}} + \frac{\mathrm{i}g_2\sigma_a}{2}\delta\theta^a \right)\Phi, \qquad \delta\rho = -\mathrm{i}e_{\mathrm{d}}\delta\theta^{\mathrm{C}}\rho. \tag{B.2}$$

Therefore, the infinitesimal gauge transformations for the fields corresponding to the gauge and scalar bosons of the DASM are given by

$$\delta W^\pm = \partial_\mu \delta\theta^\pm \pm \frac{ie}{s_{\mathrm{w}}} \left[W_\mu^\pm \left[c_{\mathrm{w}}(c_\gamma \delta\theta^{\mathrm{Z}} - s_\gamma \delta\theta^{\mathrm{Z}'}) - s_{\mathrm{w}}\delta\theta^{\mathrm{A}} \right] \right. \tag{B.3}$$

$$\left. + \left[s_{\mathrm{w}} A_\mu - c_{\mathrm{w}}(c_\gamma Z_\mu - s_\gamma Z'_\mu) \right] \delta\theta^\pm \right], \tag{B.4}$$

$$\delta A_\mu = \partial_\mu \delta\theta^{\mathrm{A}} + \mathrm{i}e \left(W_\mu^+ \delta\theta^- - W_\mu^- \delta\theta^+ \right), \tag{B.5}$$

$$\delta Z_\mu = \partial_\mu \delta\theta^{\mathrm{Z}} - \mathrm{i}e c_\gamma \frac{c_{\mathrm{w}}}{s_{\mathrm{w}}} \left(W_\mu^+ \delta\theta^- - W_\mu^- \delta\theta^+ \right), \tag{B.6}$$

$$\delta Z'_\mu = \partial \delta\theta^{\mathrm{Z}'} + \mathrm{i}e s_\gamma \frac{c_{\mathrm{w}}}{s_{\mathrm{w}}} \left(W_\mu^+ \delta\theta^- - W_\mu^- \delta\theta^+ \right), \tag{B.7}$$

$$\begin{aligned} \delta\phi^\pm = & \mp \mathrm{i}e\phi^\pm \left[\delta\theta^{\mathrm{A}} + \delta\theta^{\mathrm{Z}} \left[-c_{\mathrm{w}} s_\gamma \eta + \frac{s_{\mathrm{w}}^2 - c_{\mathrm{w}}^2}{2 s_{\mathrm{w}} c_{\mathrm{w}}} (c_\gamma - s_{\mathrm{w}} s_\gamma \eta) \right] \right. \\ & \left. - \delta\theta^{\mathrm{Z}'} \left[c_{\mathrm{w}} c_\gamma \eta + \frac{s_{\mathrm{w}}^2 - c_{\mathrm{w}}^2}{2 s_{\mathrm{w}} c_{\mathrm{w}}} (s_\gamma + s_{\mathrm{w}} c_\gamma \eta) \right] \right] \\ & \pm \frac{\mathrm{i}e}{2 s_{\mathrm{w}}} \left[v_2 + c_\alpha h + s_\alpha H \pm \mathrm{i} \left(c_x \chi - s_x \chi' \right) \right] \delta\theta^\pm, \end{aligned} \tag{B.8}$$

$$\begin{aligned}\delta h = & -\tilde{e}s_\alpha\left(c_\gamma\delta\theta^{\mathrm{Z}'}+s_\gamma\delta\theta^{\mathrm{Z}}\right)(c_x\chi'+s_x\chi)+\frac{ec_\alpha}{2s_{\mathrm{w}}c_{\mathrm{w}}}(c_x\chi-s_x\chi')\\ & \times\left[\delta\theta^{\mathrm{Z}}(c_\gamma-s_{\mathrm{w}}\eta s_\gamma)-\delta\theta^{\mathrm{Z}'}(s_\gamma+s_{\mathrm{w}}\eta c_\gamma)\right]+\frac{\mathrm{i}ec_\alpha}{2s_{\mathrm{w}}}\left(\phi^+\delta\theta^--\phi^-\delta\theta^+\right),\end{aligned} \tag{B.9}$$

$$\begin{aligned}\delta H = & \tilde{e}c_\alpha\left(c_\gamma\delta\theta^{\mathrm{Z}'}+s_\gamma\delta\theta^{\mathrm{Z}}\right)(c_x\chi+s_x\chi')+\frac{s_\alpha e}{2s_{\mathrm{w}}c_{\mathrm{w}}}(c_x\chi-s_x\chi')\\ & \times\left[\delta\theta^{\mathrm{Z}}(c_\gamma-s_{\mathrm{w}}\eta s_\gamma)-\delta\theta^{\mathrm{Z}'}(s_\gamma+s_{\mathrm{w}}\eta c_\gamma)\right]+\frac{\mathrm{i}es_\alpha}{2s_{\mathrm{w}}}\left(\phi^+\delta\theta^--\phi^-\delta\theta^+\right),\end{aligned} \tag{B.10}$$

$$\begin{aligned}\delta\chi = & \delta\theta^{\mathrm{Z}}\left[-\tilde{e}s_\gamma s_x(c_\alpha H-s_\alpha h+v_1)-\frac{ec_x}{2s_{\mathrm{w}}c_{\mathrm{w}}}(v_2+c_\alpha h+s_\alpha H)(c_\gamma-s_{\mathrm{w}}\eta s_\gamma)\right]\\ & +\delta\theta^{\mathrm{Z}'}\left[\frac{ec_x}{2s_{\mathrm{w}}c_{\mathrm{w}}}(v_2+c_\alpha h+s_\alpha H)(s_\gamma+s_{\mathrm{w}}\eta c_\gamma)-\tilde{e}c_\gamma s_x(c_\alpha H-s_\alpha h+v_1)\right]\\ & +\frac{ec_x}{2s_{\mathrm{w}}}\left(\phi^+\delta\theta^-+\phi^-\delta\theta^+\right),\end{aligned} \tag{B.11}$$

$$\begin{aligned}\delta\chi' = & \delta\theta^{\mathrm{Z}}\left[\frac{es_x}{2s_{\mathrm{w}}c_{\mathrm{w}}}(v_2+c_\alpha h+s_\alpha H)(c_\gamma-s_{\mathrm{w}}\eta s_\gamma)-\tilde{e}s_\gamma c_x(c_\alpha H-s_\alpha h+v_1)\right)\\ & -\delta\theta^{\mathrm{Z}'}\left[\frac{es_x}{2s_{\mathrm{w}}c_{\mathrm{w}}}(s_\gamma+s_{\mathrm{w}}\eta c_\gamma)(v_2+c_\alpha h+s_\alpha H)+\tilde{e}c_\gamma c_x(c_\alpha H-s_\alpha h+v_1)\right]\\ & -\frac{es_x}{2s_{\mathrm{w}}}\left(\phi^+\delta\theta^-+\phi^-\delta\theta^+\right),\end{aligned} \tag{B.12}$$

where we introduced the gauge-group parameters

$$\delta\theta^\pm=\frac{\delta\theta^1\mp i\delta\theta^2}{\sqrt{2}}, \tag{B.13}$$

$$\delta\theta^{\mathrm{A}}=ac_{\mathrm{w}}\delta\theta^{\mathrm{C}}+c_{\mathrm{w}}\delta\theta^{\mathrm{Y}}-s_{\mathrm{w}}\delta\theta^3, \tag{B.14}$$

$$\delta\theta^{\mathrm{Z}}=\left(ac_\gamma s_{\mathrm{w}}+s_\gamma\sqrt{1-a^2}\right)\delta\theta^{\mathrm{C}}+c_\gamma s_{\mathrm{w}}\delta\theta^{\mathrm{Y}}+c_\gamma c_{\mathrm{w}}\delta\theta^3, \tag{B.15}$$

$$\delta\theta^{\mathrm{Z}'}=\left(\sqrt{1-a^2}c_\gamma-as_\gamma s_{\mathrm{w}}\right)\delta\theta^{\mathrm{C}}-s_\gamma s_{\mathrm{w}}\delta\theta^{\mathrm{Y}}-s_\gamma c_{\mathrm{w}}\delta\theta^3. \tag{B.16}$$

With these explicit results for the infinitesimal gauge transformations it is straightforward to evaluate the infinitesimal variations of the gauge functionals (see Eq. (3.82)) needed for the calculation of the ghost Lagrangian given in Eq. (3.84).

C. Dimensional regularization

Going from LO calculations to higher-loop orders, loop integrals appear in calculations of observables. In general, these loop integrals can lead to UV and infrared (IR) divergences. The Kinoshita–Lee–Nauenberg [127, 128] theorem states that appearing IR divergences cancel in the calculation of sufficiently inclusive quantities. To address the appearing UV divergences a proper renormalization of the input parameters is needed.
To regularize appearing UV divergences, a regularization scheme is needed. In general, regularization schemes modify the underlying theory such that the UV divergences are mapped to well-defined expressions. However, they incorporate a certain limit, where the original theory is recovered. In this work, we use dimensional regularization [76,77], which is well suited for the regularization of UV divergences appearing in NLO calculations. In the following, we briefly sketch the main idea of dimensional regularization (for a more in-depth discussion see e.g. [129]). In dimensional regularization, appearing UV divergences are regularized by a shift of the space-time dimension $D = 4$ to arbitrary (complex) dimensions $D = 4 - 2\varepsilon$. In D dimensions the integration measure of the appearing loop integrals becomes

$$\int \frac{\mathrm{d}^4 q}{(2\pi)^4} \to \mu^{4-D} \int \frac{\mathrm{d}^D q}{(2\pi)^D}. \tag{C.1}$$

Here, a mass scale μ, the so-called reference scale of dimensional regularization, is introduced to keep the mass dimension of the integrals constant for any value of the space-time dimensions D.
For the consistency of the theory, all appearing four-vectors and other Lorentz covariants are analytically continued to $D \neq 4$ dimensions. In dimensional regularization, the space-time dimension D is chosen such that the integrals are well-defined. At NLO the UV divergences of the original theory are expressed as ε^{-1} poles. Further, the original theory is recovered in the limit $\varepsilon \to 0$. It is common to represent appearing UV divergences at NLO by the so-called standard 1-loop UV divergence of dimensional regularization

$$\Delta_{\mathrm{UV}} = \underbrace{\frac{2}{4-D}}_{=1/\varepsilon} - \gamma_{\mathrm{E}} + \log 4\pi, \tag{C.2}$$

where the Euler–Mascheroni constant γ_{E} is introduced. Finally, we want to emphasize that the correct treatment of γ_5 in D dimensions is non-trivial (see e.g. [54] for details). For NLO calculations, it is, however, sufficient to use the so-called naive γ_5 scheme [54], where γ_5 anticommutes with all generators of the Dirac algebra γ_μ, $\mu = 0, \ldots, D-1$. This scheme is implemented in the *FeynArts* and *FormCalc* packages, which are frequently used in the calculation of observables throughout this work.

D. $\overline{\text{MS}}$ renormalization constants of mixing angles

The results for the $\overline{\text{MS}}$ renormalization constants $\delta\gamma_{\overline{\text{MS}}}$, $\delta\alpha_{\overline{\text{MS}}}$, and $\delta\theta_{\text{r},\overline{\text{MS}}}$ are obtained from their respective OS results by keeping only terms proportional to the standard 1-loop UV divergence of dimensional regularization Δ_{UV} (see Sect. C). In this appendix, we give their explicit expressions in 't Hooft–Feynman gauge. In the PRTS, one finds

$$
\begin{aligned}
\delta\gamma_{\overline{\text{MS}}}^{\text{PRTS}} = \Delta_{\text{UV}}\Bigg\{ & \frac{\alpha_{\text{em}}\left[s_{2\gamma}\left(1-s_{\text{w}}^2\eta^2\right)+2s_{\text{w}}\eta c_{2\gamma}\right]}{16\pi c_{\text{w}}^2 s_{\text{w}}^2 M_{\text{ZZ}'-}^2}\sum_{l,u,d}\left[m_l^2+3(m_u^2+m_d^2)\right] \\
& - \frac{c_{\text{w}}^2 s_{\text{w}}^2 s_{2\gamma} s_{\theta_{\text{r}}}^2 \lambda_{12}^2 m_{\nu_4}^2 M_{\text{Z}}^2 M_{\text{Z}'}^2}{\alpha_{\text{em}}\pi^3 s_{2\alpha}^2 M_{\text{ZZ}'-}^2 M_{\text{Hh}-}^4} + \frac{1}{768\pi^3\alpha_{\text{em}} s_{\text{w}}^2 c_{\text{w}}^4 M_{\text{W}}^2}\Bigg\{\pi^2\alpha_{\text{em}}^2\Bigg\{\frac{2}{M_{\text{ZZ}'-}^2} \\
& \times\Big[c_{2\gamma}\Big(3c_{2\alpha}c_{\text{w}}^2 M_{\text{Hh}-}^2\Big[4s_{\text{w}}\eta M_{\text{W}}^2 - 2s_{\text{w}}c_{\text{w}}^2\eta M_{\text{ZZ}'+}^2 + s_{2\gamma}c_{\text{w}}^2 M_{\text{ZZ}'-}^2(s_{\text{w}}^2\eta^2 \\
& -1)\Big] - 2s_{\text{w}}\eta\big[3c_{\text{w}}^2 M_{\text{Hh}+}^2(2M_{\text{W}}^2 - c_{\text{w}}^2 M_{\text{ZZ}'+}^2) + 2c_{\text{w}}^4\left[M_{\text{ZZ}'+}^4 - 2M_{\text{Z}}^2 M_{\text{Z}'}^2\right] \\
& + 2c_{\text{w}}^2 M_{\text{ZZ}'+}^2 M_{\text{W}}^2(82s_{\text{w}}^2-1) + 48M_{\text{W}}^4\left(2c_{\text{w}}^2 s_{\text{w}}^2 + s_{\text{w}}^2\eta^2+1\right)\big]\Big) \\
& + s_{2\gamma}\Big(3c_{2\alpha}c_{\text{w}}^2 M_{\text{Hh}-}^2\left(s_{\text{w}}^2\eta^2-1\right)\left(c_{\text{w}}^2 M_{\text{ZZ}'+}^2 - 2M_{\text{W}}^2\right) \\
& - 3c_{\text{w}}^2 M_{\text{Hh}+}^2\left(s_{\text{w}}^2\eta^2-1\right)\left(c_{\text{w}}^2 M_{\text{ZZ}'+}^2 - 2M_{\text{W}}^2\right) + c_{\text{w}}^4 M_{\text{ZZ}'+}^4\left(s_{\text{w}}^2\eta^2-1\right) \\
& + 2c_{\text{w}}^2 M_{\text{ZZ}'+}^2 M_{\text{W}}^2\left[81s_{\text{w}}^2\eta^2 + 4s_{\text{w}}^2(5-23s_{\text{w}}^2) - 9\right] \\
& + 48M_{\text{W}}^4\left[2c_{\text{w}}^2\left(s_{\text{w}}^2\eta^2 - 2s_{\text{w}}^2+1\right) + s_{\text{w}}^4\eta^4 - 1\right]\Big)\Big] + 2s_{\text{w}}c_{\text{w}}^2\eta \\
& \times\Big(3c_{\text{w}}^2(M_{\text{Hh}+}^2 - M_{\text{ZZ}'+}^2) - 6c_{2\alpha}c_{2\gamma}^2 c_{\text{w}}^2 M_{\text{Hh}-}^2 + c_{4\gamma}c_{\text{w}}^2(3M_{\text{Hh}+}^2 - M_{\text{ZZ}'+}^2) \\
& + 4M_{\text{W}}^2(7c_{\text{w}}^2 - 75s_{\text{w}}^2 - 6)\Big) - \left[s_{4\gamma}c_{\text{w}}^4\left(s_{\text{w}}^2\eta^2-1\right)(3M_{\text{Hh}+}^2 - M_{\text{ZZ}'+}^2)\right]\Bigg\} \\
& + \frac{8s_{2\gamma}s_{\text{w}}^4 c_{\text{w}}^6\lambda_{12}^2 M_{\text{Z}}^2 M_{\text{Z}'}^2}{c_\alpha^2 s_\alpha^2 M_{\text{ZZ}'-}^2 M_{\text{Hh}-}^4}\Big[-3c_{2\alpha}M_{\text{Hh}-}^2(c_{\text{w}}^2 M_{\text{ZZ}'+}^2 + c_{2\gamma}c_{\text{w}}^2 M_{\text{ZZ}'-}^2 \\
& - 2M_{\text{W}}^2) + c_{2\gamma}c_{\text{w}}^2 M_{\text{ZZ}'-}^2(M_{\text{ZZ}'+}^2 - 3M_{\text{Hh}+}^2) - 3c_{\text{w}}^2 M_{\text{Hh}+}^2 M_{\text{ZZ}'+}^2
\end{aligned}
$$

$$+ 6M_{\text{Hh}+}^2 M_{\text{W}}^2 + c_{\text{w}}^2 M_{\text{ZZ}'+}^4 + 8M_{\text{ZZ}'+}^2 M_{\text{W}}^2 + 48c_{\text{w}}^2 M_{\text{Z}}^2 M_{\text{Z}'}^2 \Big] \Big\} \Big\}, \tag{D.1}$$

with the shorthands

$$M_{ij\pm}^2 \equiv M_i^2 \pm M_j^2, \qquad M_{ij\pm}^4 \equiv \left(M_{ij\pm}^2\right)^2, \tag{D.2}$$

for the $\overline{\text{MS}}$ renormalization constant of the gauge-boson mixing angle. Combining this with Eqs. (4.46), (4.47), and (4.48) it is straightforward to derive the explicit expressions for $\delta\gamma_{\overline{\text{MS}}}^{\text{FJTS}}$ and $\delta\gamma_{\overline{\text{MS}}}^{\text{GIVS}}$, as well.

For the Higgs mixing angle, the $\overline{\text{MS}}$-renormalization constant in the PRTS reads

$$\begin{aligned}
\delta\alpha_{\overline{\text{MS}}}^{\text{PRTS}} = \Delta_{\text{UV}} \Bigg\{ & \frac{\alpha_{\text{em}} s_{2\alpha} \Lambda_{\text{ZZ}'}^2}{32\pi M_{\text{W}}^2 M_{\text{Hh}-}^2 (\Lambda_{\text{ZZ}'}^2 - 2M_{\text{W}}^2)} \sum_{f=l,u,d} N_{C,f} \left[m_f^2 (M_{\text{Hh}+}^2 - 8m_f^2) \right] \\
& + \frac{s_{\theta_{\text{r}}}^2 \lambda_{12}^2 m_{\nu_4}^2 M_{\text{W}}^2 \left(2M_{\text{W}}^2 - \Lambda_{\text{ZZ}'}^2\right) \left(2c_{2\theta_{\text{r}}} m_{\nu_4}^2 - 6m_{\nu_4}^2 + M_{\text{Hh}+}^2\right)}{4\alpha_{\text{em}} \pi^3 s_\alpha c_\alpha \left(M_{\text{Hh}-}^2\right)^3 \Lambda_{\text{ZZ}'}^2} \\
& + \frac{1}{512\pi^3 M_{\text{W}}^4} \Bigg\{ \frac{\alpha_{\text{em}} \pi^2 M_{\text{W}}^2}{s_{\text{w}}^2 \Lambda_{\text{ZZ}'}^4} \Bigg(\frac{2 s_\alpha c_\alpha}{M_{\text{Hh}-}^2} \Big[2c_{4\alpha} M_{\text{Hh}-}^4 \Lambda_{\text{ZZ}'}^4 \\
& - 24 c_{2\alpha} M_{\text{Hh}+}^2 M_{\text{Hh}-}^2 \Lambda_{\text{ZZ}'}^4 + c_{4\gamma} M_{\text{ZZ}'-}^4 \Big[11 M_{\text{Hh}+}^4 + 48 M_{\text{ZZ}'+}^4 \\
& - 16 M_{\text{h}}^2 M_{\text{ZZ}'+}^2 + 4 M_{\text{H}}^2 M_{\text{h}}^2 - 32 M_{\text{h}}^2 M_{\text{W}}^2 + 96 M_{\text{W}}^4 \Big] + 4c_{2\gamma} \\
& \times \Big[11 M_{\text{ZZ}'+}^2 M_{\text{ZZ}'-}^2 M_{\text{Hh}+}^4 + 4 M_{\text{ZZ}'+}^2 M_{\text{ZZ}'-}^2 \left[M_{\text{H}}^2 M_{\text{h}}^2 + 8 M_{\text{W}}^2 \left(3M_{\text{W}}^2 - M_{\text{h}}^2\right) \right] \\
& + 16 \left[M_{\text{h}}^2 \left(M_{\text{Z}'}^6 - M_{\text{Z}}^6 \right) + 3 \left(M_{\text{Z}}^8 - M_{\text{Z}'}^8 \right) \right] \Big] + \left(11 M_{\text{Hh}+}^4 + 4 M_{\text{H}}^2 M_{\text{h}}^2 \right) \\
& \times \left(2 M_{\text{Z}}^2 M_{\text{ZZ}'+}^2 + M_{\text{Z}}^4 + 3 M_{\text{Z}'}^4 \right) + 16 M_{\text{h}}^2 \Big[8 M_{\text{Z}}^2 M_{\text{Z}'}^2 \left(M_{\text{ZZ}'+}^2 + M_{\text{W}}^2 \right) \\
& - 3 M_{\text{ZZ}'+}^4 \left(M_{\text{ZZ}'+}^2 + 2 M_{\text{W}}^2 \right) \Big] - 2 s_{\text{w}}^2 c_{\text{w}}^2 \Big[21 \left(M_{\text{ZZ}'+}^2 \right)^4 - 136 M_{\text{Z}}^2 M_{\text{Z}'}^2 M_{\text{ZZ}'+}^4 \\
& + 80 M_{\text{Z}}^4 M_{\text{Z}'}^4 \Big] + s_{\text{w}}^4 \Big[136 M_{\text{Z}}^2 M_{\text{Z}'}^2 M_{\text{ZZ}'+}^4 - 21 \left(M_{\text{ZZ}'+}^2 \right)^4 - 80 M_{\text{Z}}^4 M_{\text{Z}'}^4 \Big] \\
& + 96 M_{\text{W}}^4 \left(2 M_{\text{Z}}^2 M_{\text{ZZ}'+}^2 + M_{\text{Z}}^4 + 3 M_{\text{Z}'}^4 \right) + 3 \left(55 - 7 c_{\text{w}}^4 \right) \left(M_{\text{Z}}^8 + M_{\text{Z}'}^8 \right) \\
& + 6 M_{\text{Z}}^4 M_{\text{Z}'}^4 \left(5 + 11 c_{\text{w}}^4 \right) - 52 s_{\text{w}}^2 M_{\text{Z}}^2 M_{\text{Z}'}^2 (1 + c_{\text{w}}^2) \left(M_{\text{Z}}^4 + M_{\text{Z}'}^4 \right) \Big] \\
& - 16 s_{2\alpha} \Lambda_{\text{ZZ}'}^2 \Big[c_{2\gamma} M_{\text{ZZ}'-}^2 \left(M_{\text{ZZ}'+}^2 + 2 M_{\text{W}}^2 \right) + 2 M_{\text{W}}^2 M_{\text{ZZ}'+}^2 + M_{\text{Z}}^4 + M_{\text{Z}'}^4 \Big] \Bigg) \\
& + \frac{16 \lambda_{12}^2 M_{\text{W}}^2 s_{\text{w}}^2}{\alpha_{\text{em}} s_\alpha c_\alpha \left(M_{\text{Hh}-}^2 \right)^3} \Big[M_{\text{W}}^4 \Big[4 M_{\text{H}}^2 M_{\text{h}}^2 - 11 M_{\text{Hh}+}^4 \Big] - M_{\text{W}}^4 M_{\text{Hh}-}^2 \\
& \times \left[12 c_{2\alpha} M_{\text{Hh}+}^2 + c_{4\alpha} M_{\text{Hh}-}^2 \right] + 4 c_{2\gamma} c_{\text{w}}^4 M_{\text{Z}}^2 M_{\text{Z}'}^2 M_{\text{ZZ}'-}^2 M_{\text{Hh}+}^2 \\
& + 4 c_{\text{w}}^4 M_{\text{Z}}^4 M_{\text{Z}'}^2 M_{\text{Hh}+}^2 + 4 c_{\text{w}}^4 M_{\text{Z}}^2 M_{\text{Z}'}^4 \left(M_{\text{Hh}+}^2 - 12 M_{\text{Z}}^2 \right) \Big]
\end{aligned}$$

$$
\begin{aligned}
&+\frac{2\pi\lambda_{12}}{\Lambda^4_{\mathrm{ZZ}'}M^4_{\mathrm{Hh}-}}\Bigg[\frac{1}{c_\alpha s_\alpha}\Bigg[-2c_{6\alpha}M^4_{\mathrm{W}}M^4_{\mathrm{Hh}-}\Lambda^4_{\mathrm{ZZ}'}\\
&+c_{2\alpha}\Big[M^2_{\mathrm{ZZ}'-}\Big(M^2_{\mathrm{ZZ}'-}\Big[c_{4\gamma}\Big(M^4_{\mathrm{W}}M^4_{\mathrm{Hh}-}-16M^2_{\mathrm{Z}}M^2_{\mathrm{Z}'}\Big[c^4_{\mathrm{w}}M^4_{\mathrm{ZZ}'+}\\
&-c^2_{\mathrm{w}}M^2_{\mathrm{W}}M^2_{\mathrm{ZZ}'+}+4M^4_{\mathrm{W}}\Big]\Big)+8c_{6\gamma}c^2_{\mathrm{w}}M^2_{\mathrm{Z}}M^2_{\mathrm{Z}'}M^2_{\mathrm{ZZ}'-}\left(M^2_{\mathrm{W}}-2c^2_{\mathrm{w}}M^2_{\mathrm{ZZ}'+}\right)\Big]\\
&+4c_{2\gamma}\Big[M^4_{\mathrm{W}}M^2_{\mathrm{ZZ}'+}M^4_{\mathrm{Hh}-}-2c^2_{\mathrm{w}}M^2_{\mathrm{Z}}M^2_{\mathrm{Z}'}M^4_{\mathrm{ZZ}'-}\left(M^2_{\mathrm{W}}-2c^2_{\mathrm{w}}M^2_{\mathrm{ZZ}'+}\right)\Big]\Big)\\
&+2M^2_{\mathrm{W}}M^2_{\mathrm{Z}}M^2_{\mathrm{ZZ}'+}\left[M^2_{\mathrm{W}}M^4_{\mathrm{Hh}-}-8c^2_{\mathrm{w}}M^2_{\mathrm{Z}'}M^4_{\mathrm{ZZ}'-}\right]\\
&+4M^2_{\mathrm{Z}}M^2_{\mathrm{Z}'}M^4_{\mathrm{ZZ}'-}\left[c^4_{\mathrm{w}}\left(5M^4_{\mathrm{ZZ}'+}-4M^2_{\mathrm{Z}}M^2_{\mathrm{Z}'}\right)+16M^4_{\mathrm{W}}\right]\\
&+M^4_{\mathrm{W}}M^4_{\mathrm{Hh}-}\left(M^4_{\mathrm{Z}}+3M^4_{\mathrm{Z}'}\right)\Big]+4M^2_{\mathrm{Z}}M^2_{\mathrm{Z}'}M^4_{\mathrm{ZZ}'-}\Big(c^4_{\mathrm{w}}\Big[5M^4_{\mathrm{ZZ}'+}-4M^2_{\mathrm{Z}}M^2_{\mathrm{Z}'}\Big]\\
&-4c^4_{\mathrm{w}}\left(M^2_{\mathrm{ZZ}'+}\left[c_{4\gamma}M^2_{\mathrm{ZZ}'+}+c_{6\gamma}M^2_{\mathrm{ZZ}'-}\right]-c_{2\gamma}M^2_{\mathrm{ZZ}'+}M^2_{\mathrm{ZZ}'-}\right)\\
&+16c_{4\gamma}M^4_{\mathrm{W}}-16M^4_{\mathrm{W}}\Big)\Big]-8\frac{c_\alpha}{s_\alpha}c_{8\gamma}c^4_{\mathrm{w}}M^2_{\mathrm{Z}}M^2_{\mathrm{Z}'}\left(M^2_{\mathrm{ZZ}'-}\right)^4\Big]\Big\}\Bigg\},
\end{aligned}
\tag{D.3}
$$

with the respective colour factor for the fermions $N_{C,f}$ and the shorthands

$$
\Lambda^2_{\mathrm{ZZ}'}=M^2_{\mathrm{ZZ}'+}+M^2_{\mathrm{ZZ}'-}c_{2\gamma},\qquad \Lambda^4_{\mathrm{ZZ}'}\equiv\left(\Lambda^2_{\mathrm{ZZ}'}\right)^2. \tag{D.4}
$$

In combination with Eqs. (4.65), (4.66), and (4.67) the explicit expressions for $\delta\alpha^{\mathrm{FJTS}}_{\overline{\mathrm{MS}}}$ and $\delta\alpha^{\mathrm{GIVS}}_{\overline{\mathrm{MS}}}$ can easily be derived. Finally, the $\overline{\mathrm{MS}}$-renormalization constant for θ_{r} in the PRTS is given by

$$
\begin{aligned}
\delta\theta^{\mathrm{PRTS}}_{\mathrm{r},\overline{\mathrm{MS}}}=\frac{\Delta_{\mathrm{UV}}\lambda^2_{12}s^2_{\mathrm{w}}s_{\theta_{\mathrm{r}}}c_{\theta_{\mathrm{r}}}}{64\pi^3\alpha_{\mathrm{em}}c^2_\alpha s^2_\alpha(M^2_{\mathrm{H}}-M^2_{\mathrm{h}})^2}\Bigg\{&56c^2_{\mathrm{w}}M^2_{\mathrm{Z}}M^2_{\mathrm{Z}'}\\
&+2m^2_{\nu_4}s^2_{\theta_{\mathrm{r}}}\left[3c^2_{\mathrm{w}}c_{2\gamma}(M^2_{\mathrm{Z}'}-M^2_{\mathrm{Z}})-3c^2_{\mathrm{w}}(M^2_{\mathrm{Z}}+M^2_{\mathrm{Z}'})+10M^2_{\mathrm{W}}\right]\Bigg\}.
\end{aligned}
\tag{D.5}
$$

Similarly to the cases above, the respective expressions for $\delta\theta^{\mathrm{FJTS}}_{\mathrm{r},\overline{\mathrm{MS}}}$ and $\delta\theta^{\mathrm{GIVS}}_{\mathrm{r},\overline{\mathrm{MS}}}$ can be obtained from (D.5) using Eqs. (4.80), (4.81), and (4.82).

E. Derivation of the covariance matrix

The only relevant correlations needed in our analysis are between $\Gamma_{Z\to ll}$, $s^2_{w,\mathrm{eff},l}$, and M_Z. Their correlation coefficients are obtained from the correlation matrix given in Tab. 2.13 of Ref. [118]. To this end, we make use of the relations Eqs. (5.75) and (5.80) as well as (see e.g. [123])

$$\hat{V}_{kg} = \sum_{i,j} \frac{\partial y_k}{\partial x_i} \frac{\partial y_g}{\partial x_j}\bigg|_{x=\bar{x}} \hat{U}_{ij}, \tag{E.1}$$

where $\hat{U}$ is the covariance matrix for the set of pseudo-observables $x = \{M_Z, \Gamma_Z, \sigma^0_{had}, R^0_l, A^{0,l}_{FB}\}$, with their respective best fit values $\bar{x}$ given in Ref. [118], and $\hat{V}$ is the respective covariance matrix for the set of pseudo-observables $y = \{M_Z, \Gamma_Z, \sigma^0_{had}, \Gamma_{Z\to ll}, s^2_{w,\mathrm{eff},l}\}$ we are interested in. Inverting the covariance matrix $\hat{V}$ of this subsystem will give the respective values of (V^{-1}_{ij}), $i,j = 3,4,5$, used in our analysis (see Eq. (5.87)). To obtain the correct result for the inverse of the covariance matrix, one has to invert the full covariance matrix[1] $\hat{V}$, including the respective entries that account for the presence of Γ_Z and σ^0_{had}. The explicit values of the inverse of the covariance matrix read

$$(V^{-1})_{11} = \frac{1}{(\Delta M_W)^2} = 6.9444 \times 10^3\,\mathrm{GeV}^{-2}, \tag{E.2}$$

$$(V^{-1})_{22,e^+e^-} = \frac{1}{(\Delta a^{SM}_{\mu,e^+e^-})^2 + (\Delta a^{exp}_{\mu})^2} = 4.16493 \times 10^{18}, \tag{E.3}$$

$$(V^{-1})_{22,\mathrm{lattice}} = \frac{1}{(\Delta a^{SM}_{\mu,\mathrm{lattice}})^2 + (\Delta a^{exp}_{\mu})^2} = 2.60146 \times 10^{18}, \tag{E.4}$$

$$(V^{-1})_{33} = 4.08712 \times 10^8\,\mathrm{GeV}^{-2}, \tag{E.5}$$

$$(V^{-1})_{44} = 3.19361 \times 10^6, \tag{E.6}$$

[1] Note that this procedure reflects the situation where we do not have any knowledge about the predictions for Γ_Z and σ^0_{had} within the DASM and, thus, have to scale their respective theory uncertainties to infinity (after adding them in quadrature to the respective experimental errors).

$$(V^{-1})_{55} = \frac{1}{(\Delta M_{\mathrm{Z}})^2} = 2.28271 \times 10^5\,\mathrm{GeV}^{-2}, \tag{E.7}$$

$$(V^{-1})_{34} = 2.20856 \times 10^6\,\mathrm{GeV}^{-1}, \tag{E.8}$$

$$(V^{-1})_{35} = 8.65289 \times 10^4\,\mathrm{GeV}^{-1}, \tag{E.9}$$

$$(V^{-1})_{45} = 4.78144 \times 10^4\,\mathrm{GeV}^{-1}, \tag{E.10}$$

$$(V^{-1})_{66} = \frac{1}{(\Delta M_S)^2} = 34.6021\,\mathrm{GeV}^{-2}, \tag{E.11}$$

$$(V^{-1})_{77} = \frac{1}{(\Delta m_{\mathrm{t}})^2} = 2.04082\,\mathrm{GeV}^{-2}, \tag{E.12}$$

$$(V^{-1})_{88} = \frac{1}{(\Delta(\Delta\alpha^5_{\mathrm{had}}))^2} = 2.04082 \times 10^8, \tag{E.13}$$

$$(V^{-1})_{99} = \frac{1}{(\Delta\alpha_{\mathrm{s}})^2} = 10^6, \tag{E.14}$$

where, as already mentioned above, we used the values given in Tab. 2.13 of Ref. [118] for the determination of $(V^{-1})_{ij}$, $i, j = 3, 4, 5$. For the respective entries of the remaining SM-like input parameters as well as M_{W}, we make use of their experimental uncertainties $\Delta\mathcal{O}_i$, $\mathcal{O}_i \in \{M_{\mathrm{W}}, M_S, m_{\mathrm{t}}, \Delta\alpha^5_{\mathrm{had}}, \alpha_{\mathrm{s}}\}$, where S denotes the SM-like Higgs boson of h and H, taken from Ref. [16]. Further, for a_μ, we add the respective theoretical uncertainty given in Eqs. (5.43) or (5.44) in quadrature to the experimental uncertainty given in Eq. (5.45) to obtain the square of its total uncertainty $(\Delta a_\mu)^2$ used in V^{-1}. All remaining entries of V^{-1} are zero.

F. Feynman rules of the DASM

In the following, we give the Feynman rules of the DASM in the 't Hooft–Feynman gauge. To keep the expressions compact we do not give their full analytic dependence on the input parameters. The full dependence on the input parameters can be obtained with the help of Eqs. (3.28), (3.68), (3.69), and (3.81). All momenta are chosen to be incoming. Note that we do not explicitly list the Feynman rules for QCD, since they are equivalent to their counterpart in the SM (see e.g. [51,54]).

Propagators

Here we list the propagators for fields. They read:

- for scalar fields $S = h,\, H,\, \chi,\, \chi',\, \phi^{\pm}$,

  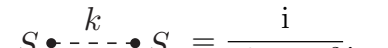

  $$= \frac{\mathrm{i}}{k^2 - M_S^2},$$

  with $M_\chi = M_{\mathrm{Z}}$, $M_{\chi'} = M_{\mathrm{Z}'}$ and $M_{\phi^\pm} = M_{\mathrm{W}}$.

- for gauge fields $V = A, Z, Z', W^{\pm}$,

  

  $$= \frac{-\mathrm{i} g_{\mu\nu}}{k^2 - M_V^2}.$$

- for ghost fields $G = u^A, u^Z, u^{Z'}, u^{\pm}$,

  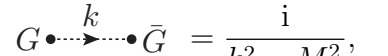

  $$= \frac{\mathrm{i}}{k^2 - M_G^2},$$

  with $M_{u^A} = 0, M_{u^Z} = M_{\mathrm{Z}}, M_{u^{Z'}} = M_{\mathrm{Z}'}$, and $M_{u^\pm} = M_{\mathrm{W}}$.

- for fermion fields $F = u_i, d_i, l_i, \nu_i, \nu_4$, $i = 1, 2, 3$,

  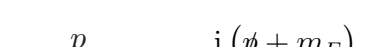

  $$= \frac{\mathrm{i}\left(\not{p} + m_F\right)}{p^2 - m_F^2}.$$

Vertices

In the following we list the Feynman rules for the vertices in the DASM.

VVV vertex:

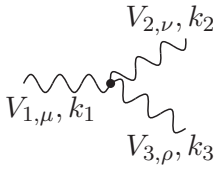

$$= \mathrm{i}eC \left[g_{\mu\nu} \left(k_1 - k_2\right)_\rho + g_{\mu\rho} \left(k_3 - k_1\right)_\nu + g_{\nu\rho} \left(k_2 - k_3\right) \right],$$

with the values

$V_1V_2V_3$	AW^+W^-	ZW^+W^-	$Z'W^+W^-$
C	1	$-\frac{c_\gamma c_\mathrm{w}}{s_\mathrm{w}}$	$\frac{s_\gamma c_\mathrm{w}}{s_\mathrm{w}}$

VVVV vertex:

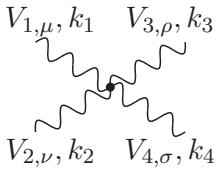

$$= \mathrm{i}e^2C \left[2g_{\mu\nu}g_{\rho\sigma} - g_{\mu\sigma}g_{\nu\rho} - g_{\mu\rho}g_{\nu\sigma} \right],$$

with the values

$V_1V_2V_3V_4$	$W^+W^+W^-W^-$	W^+W^-AZ	W^+W^-ZZ	W^+W^-AZ'
C	$\frac{1}{s_\mathrm{w}^2}$	$\frac{c_\gamma c_\mathrm{w}}{s_\mathrm{w}}$	$-\frac{c_\gamma^2 c_\mathrm{w}^2}{s_\mathrm{w}^2}$	$-\frac{s_\gamma c_\mathrm{w}}{s_\mathrm{w}}$

$V_1V_2V_3V_4$	W^+W^-ZZ'	$W^+W^-Z'Z'$	W^+W^-AA
C	$\frac{c_\gamma s_\gamma c_\mathrm{w}^2}{s_\mathrm{w}^2}$	$-\frac{s_\gamma^2 c_\mathrm{w}^2}{s_\mathrm{w}^2}$	-1

$V\bar{F}F$ vertex:

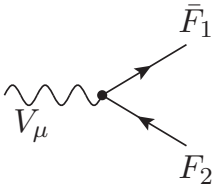

$$= \mathrm{i}e\gamma_\mu \left(\mathrm{C_L}\omega_\mathrm{L} + \mathrm{C_R}\omega_\mathrm{R}\right),$$

with the values

$V\bar{F}_1F_2$	$A\bar{f}_if_j$	$Z\bar{f}_if_j$	$W^+\bar{u}_id_j$	$W^-\bar{d}_ju_i$
$\mathrm{C_L}$	$-Q_f\delta_{ij}$	$\frac{c_\gamma}{s_\mathrm{w}c_\mathrm{w}}(1-\eta s_\mathrm{w}t_\gamma)\left(I^3_\mathrm{W}-\frac{s_\mathrm{w}(s_\mathrm{w}-\eta t_\gamma)}{1-\eta s_\mathrm{w}t_\gamma}Q_f\right)\delta_{ij}$	$\frac{1}{\sqrt{2}s_\mathrm{w}}V_{ij}$	$\frac{1}{\sqrt{2}s_\mathrm{w}}V^\dagger_{ji}$
$\mathrm{C_R}$	$-Q_f\delta_{ij}$	$-\frac{c_\gamma(s_\mathrm{w}-\eta t_\gamma)}{c_\mathrm{w}}Q_f\delta_{ij}-\frac{\tilde{e}s_\gamma s^2_{\theta_\mathrm{r}}}{e}\delta_{ij}\delta_{i3}\delta_{f\nu}$	0	0

$V\bar{F}_1F_2$	$Z'\bar{f}_if_j$	$W^+\bar{\nu}_il_j$	$W^-\bar{l}_j\nu_i$
$\mathrm{C_L}$	$-\frac{c_\gamma}{s_\mathrm{w}c_\mathrm{w}}\left(t_\gamma+\eta s_\mathrm{w}\right)\left(I^3_\mathrm{W}-\frac{s_\mathrm{w}(s_\mathrm{w}t_\gamma+\eta)}{t_\gamma+\eta s_\mathrm{w}}Q_f\right)\delta_{ij}$	$\frac{1}{\sqrt{2}s_\mathrm{w}}\delta_{ij}$	$\frac{1}{\sqrt{2}s_\mathrm{w}}\delta_{ij}$
$\mathrm{C_R}$	$\frac{c_\gamma(t_\gamma s_\mathrm{w}+\eta)}{c_\mathrm{w}}Q_f\delta_{ij}-\frac{\tilde{e}c_\gamma s^2_{\theta_\mathrm{r}}}{e}\delta_{ij}\delta_{i3}\delta_{f\nu}$	0	0

$V\bar{F}_1F_2$	$Z\bar{\nu}_4\nu_4$	$Z\bar{\nu}_{4/3}\nu_{3/4}$	$Z'\bar{\nu}_4\nu_4$	$Z'\bar{\nu}_{4/3}\nu_{3/4}$
C_L	$-\frac{\tilde{e}s_\gamma}{e}$	0	$-\frac{\tilde{e}c_\gamma}{e}$	0
C_R	$-\frac{\tilde{e}s_\gamma c^2_{\theta_\mathrm{r}}}{e}$	$\frac{\tilde{e}s_\gamma s_{\theta_\mathrm{r}}c_{\theta_\mathrm{r}}}{e}$	$-\frac{\tilde{e}c_\gamma c^2_{\theta_\mathrm{r}}}{e}$	$\frac{\tilde{e}c_\gamma s_{\theta_\mathrm{r}}c_{\theta_\mathrm{r}}}{e}$

$S\bar{F}F$ vertex:

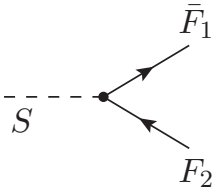

$$= ie\left(C_{\mathrm{L}}\omega_{\mathrm{L}} + C_{\mathrm{R}}\omega_{\mathrm{R}}\right),$$

with the values

$S\bar{F}_1F_2$	$h\bar{f}f$	$H\bar{f}f$	$\chi\bar{f}f$	$\chi'\bar{f}f$
C_{L}	$-\frac{c_\alpha m_{f,i}}{2M_{\mathrm{W}}s_{\mathrm{w}}}\delta_{ij}$	$-\frac{s_\alpha m_{f,i}}{2M_{\mathrm{W}}s_{\mathrm{w}}}\delta_{ij}$	$-2\mathrm{i}I^3_{\mathrm{W},f}\frac{c_\gamma c_{\mathrm{w}} M_{\mathrm{Z}} m_{f,i}}{2s_{\mathrm{w}}M^2_{\mathrm{W}}}\delta_{ij}$	$2\mathrm{i}I^3_{\mathrm{W},f}\frac{s_\gamma c_{\mathrm{w}} M_{\mathrm{Z}'} m_{f,i}}{2M^2_{\mathrm{W}}s_{\mathrm{w}}}\delta_{ij}$
C_{R}	$-\frac{c_\alpha m_{f,i}}{2M_{\mathrm{W}}s_{\mathrm{w}}}\delta_{ij}$	$-\frac{s_\alpha m_{f,i}}{2M_{\mathrm{W}}s_{\mathrm{w}}}\delta_{ij}$	$2\mathrm{i}I^3_{\mathrm{W},f}\frac{c_\gamma c_{\mathrm{w}} M_{\mathrm{Z}} m_{f,i}}{2s_{\mathrm{w}}M^2_{\mathrm{W}}}\delta_{ij}$	$-2\mathrm{i}I^3_{\mathrm{W},f}\frac{s_\gamma c_{\mathrm{w}} M_{\mathrm{Z}'} m_{f,i}}{2M^2_{\mathrm{W}}s_{\mathrm{w}}}\delta_{ij}$

$S\bar{F}_1F_2$	$h\bar{\nu}_4\nu_4$	$h\bar{\nu}_4\nu_3$	$h\bar{\nu}_3\nu_4$	$H\bar{\nu}_4\nu_4$	$H\bar{\nu}_4\nu_3$	$H\bar{\nu}_3\nu_4$
C_{L}	$\frac{s_\alpha s^2_{\theta_{\mathrm{r}}} m_{\nu_4}}{v_1 e}$	0	$\frac{s_\alpha s_{\theta_{\mathrm{r}}} c_{\theta_{\mathrm{r}}} m_{\nu_4}}{v_1 e}$	$-\frac{c_\alpha s^2_{\theta_{\mathrm{r}}} m_{\nu_4}}{v_1 e}$	0	$-\frac{c_\alpha s_{\theta_{\mathrm{r}}} c_{\theta_{\mathrm{r}}} m_{\nu_4}}{v_1 e}$
C_{R}	$\frac{s_\alpha s^2_{\theta_{\mathrm{r}}} m_{\nu_4}}{v_1 e}$	$\frac{s_\alpha s_{\theta_{\mathrm{r}}} c_{\theta_{\mathrm{r}}} m_{\nu_4}}{v_1 e}$	0	$-\frac{c_\alpha s^2_{\theta_{\mathrm{r}}} m_{\nu_4}}{v_1 e}$	$-\frac{c_\alpha s_{\theta_{\mathrm{r}}} c_{\theta_{\mathrm{r}}} m_{\nu_4}}{v_1 e}$	0

$S\bar{F}_1F_2$	$\chi\bar{\nu}_4\nu_4$	$\chi\bar{\nu}_4\nu_3$	$\chi\bar{\nu}_3\nu_4$	$\chi'\bar{\nu}_4\nu_4$	$\chi'\bar{\nu}_4\nu_3$
C_{L}	$\frac{\mathrm{i}s_x s^2_{\theta_{\mathrm{r}}} m_{\nu_4}}{v_1 e}$	0	$\frac{\mathrm{i}s_x s_{\theta_{\mathrm{r}}} c_{\theta_{\mathrm{r}}} m_{\nu_4}}{v_1 e}$	$\frac{\mathrm{i}c_x s^2_{\theta_{\mathrm{r}}} m_{\nu_4}}{v_1 e}$	0
C_{R}	$-\frac{\mathrm{i}s_x s^2_{\theta_{\mathrm{r}}} m_{\nu_4}}{v_1 e}$	$-\frac{\mathrm{i}s_x s_{\theta_{\mathrm{r}}} c_{\theta_{\mathrm{r}}} m_{\nu_4}}{v_1 e}$	0	$-\frac{\mathrm{i}s_x s^2_{\theta_{\mathrm{r}}} m_{\nu_4}}{v_1 e}$	$-\frac{\mathrm{i}c_x s_{\theta_{\mathrm{r}}} c_{\theta_{\mathrm{r}}} m_{\nu_4}}{v_1 e}$

$S\bar{F}_1F_2$	$\chi'\bar{\nu}_3\nu_4$	$\phi^+\bar{u}_i d_j$	$\phi^-\bar{d}_j u_i$	$\phi^+\bar{\nu}_i l_j$	$\phi^-\bar{l}_j\nu_i$
C_{L}	$\frac{\mathrm{i}c_x s_{\theta_{\mathrm{r}}} c_{\theta_{\mathrm{r}}} m_{\nu_4}}{v_1 e}$	$\frac{m_{u,i}}{\sqrt{2}s_{\mathrm{w}}M_{\mathrm{W}}}V_{ij}$	$-\frac{m_{d,i}}{\sqrt{2}s_{\mathrm{w}}M_{\mathrm{W}}}V^\dagger_{ji}$	0	$-\frac{m_{f,i}}{\sqrt{2}M_{\mathrm{W}}s_{\mathrm{w}}}\delta_{ij}$
C_{R}	0	$-\frac{m_{d,i}}{\sqrt{2}s_{\mathrm{w}}M_{\mathrm{W}}}V_{ij}$	$\frac{m_{u,i}}{\sqrt{2}s_{\mathrm{w}}M_{\mathrm{W}}}V^\dagger_{ji}$	$-\frac{m_{f,i}}{\sqrt{2}M_{\mathrm{W}}s_{\mathrm{w}}}\delta_{ij}$	0

SSSS vertex:

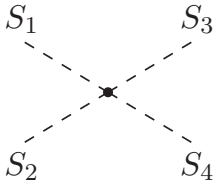

$$= -\frac{\mathrm{i}e^2\left(c_\alpha^2 M_\mathrm{h}^2 + s_\alpha^2 M_\mathrm{H}^2\right)}{4 s_\mathrm{w}^2 M_\mathrm{W}^2} C_1 + \mathrm{i}\lambda_{12} C_2$$

$$+ \frac{48\mathrm{i}s_\mathrm{w}^2 \lambda_{12}^2 M_\mathrm{W}^2 \left(s_\alpha^2 M_\mathrm{h}^2 + c_\alpha^2 M_\mathrm{H}^2\right)}{e^2 \left(M_\mathrm{h}^2 - M_\mathrm{H}^2\right)^2} C_3,$$

with the values

$S_1S_2S_3S_4$	$hhhh$	$hhhH$	$hhHH$	$hHHH$	$HHHH$	$HH\phi^+\phi^-$	$hh\phi^+\phi^-$
C_1	$3c_\alpha^4$	$3c_\alpha^3 s_\alpha$	$3c_\alpha^2 s_\alpha^2$	$3c_\alpha s_\alpha^3$	$3s_\alpha^4$	s_α^2	c_α^2
C_2	$-3s_{2\alpha}^2$	$\frac{3s_{4\alpha}}{2}$	$-\frac{1+3c_{4\alpha}}{2}$	$-\frac{3s_{4\alpha}}{2}$	$-3s_{2\alpha}^2$	$-2c_\alpha^2$	$-2s_\alpha^2$
C_3	$-t_\alpha^2$	t_α	-1	$\frac{1}{t_\alpha}$	$-\frac{1}{t_\alpha^2}$	0	0

$S_1S_2S_3S_4$	$Hh\phi^+\phi^-$	$HH\chi'\chi'$	$HH\chi'\chi$	$HH\chi\chi$	$Hh\chi'\chi'$
C_1	$s_\alpha c_\alpha$	$s_\alpha^2 s_x^2$	$-s_\alpha^2 s_x c_x$	$s_\alpha^2 c_x^2$	$c_\alpha s_\alpha s_x^2$
C_2	$s_{2\alpha}$	$-1 + c_{2\alpha}c_{2x}$	$c_{2\alpha}s_{2x}$	$-1 - c_{2x}c_{2\alpha}$	$-s_{2\alpha}c_{2x}$
C_3	0	$-\frac{c_x^2}{3s_\alpha^2}$	$-\frac{s_{2x}}{6s_\alpha^2}$	$-\frac{s_x^2}{3s_\alpha^2}$	$\frac{c_x^2}{3c_\alpha s_\alpha}$

$S_1S_2S_3S_4$	$Hh\chi'\chi$	$Hh\chi\chi$	$hh\chi'\chi'$	$hh\chi'\chi$	$hh\chi\chi$
C_1	$-s_\alpha c_\alpha s_x c_x$	$c_\alpha s_\alpha c_x^2$	$c_\alpha^2 s_x^2$	$-c_\alpha^2 s_x c_x$	$c_\alpha^2 c_x^2$
C_2	$-s_{2\alpha}s_{2x}$	$s_{2\alpha}c_{2x}$	$-1 - c_{2\alpha}c_{2x}$	$-c_{2\alpha}s_{2x}$	$-1 + c_{2\alpha}c_{2x}$
C_3	$\frac{s_{2x}}{3s_{2\alpha}}$	$\frac{s_x^2}{3s_\alpha c_\alpha}$	$-\frac{c_x^2}{3c_\alpha}$	$-\frac{s_{2x}}{6c_\alpha^2}$	$\frac{s_{2x}^2}{c_\alpha^2}$

$S_1S_2S_3S_4$	$\phi^+\phi^+\phi^-\phi^-$	$\phi^+\phi^-\chi'\chi'$	$\phi^+\phi^-\chi'\chi$	$\phi^+\phi^-\chi\chi$	$\chi\chi\chi'\chi'$	$\chi'\chi'\chi'\chi'$
C_1	2	s_x^2	$-s_xc_x$	c_x^2	$\frac{3}{4}s_{2x}^2$	$3s_x^4$
C_2	0	$-2c_x^2$	$-s_{2x}$	$-2s_x^2$	$-\frac{1-3c_{4x}}{2}$	$-3s_{2x}^2$
C_3	0	0	0	0	$-\frac{s_{2x}^2}{s_{2\alpha}^2}$	$\frac{c_x^4}{c_\alpha^2 s_\alpha^2}$

$S_1S_2S_3S_4$	$\chi\chi\chi\chi$	$\chi'\chi\chi\chi$	$\chi'\chi'\chi'\chi$
C_1	$3c_x^4$	$-3c_x^3s_x$	$-3c_xs_x^3$
C_2	$-3s_{2x}^2$	$-\frac{3}{2}s_{4x}$	$\frac{3}{2}s_{4x}$
C_3	$-\frac{4s_x^4}{s_{2\alpha}^2}$	$-\frac{s_x^3c_x}{s_\alpha^2c_\alpha^2}$	$-\frac{s_xc_x^3}{s_\alpha^2c_\alpha^2}$

VSS vertex:

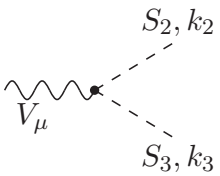

$$= i\left(eC_1 + \tilde{e}C_2\right)\left(k_2 - k_3\right)_\mu ,$$

with the values

$V_1S_2S_3$	$W^\pm\phi^\mp h$	$W^\pm\phi^\mp H$	$W^\pm\phi^\mp\chi$	$W^\pm\phi^\mp\chi'$
C_1	$\mp\frac{c_\alpha}{2s_\mathrm{w}}$	$\mp\frac{s_\alpha}{2s_\mathrm{w}}$	$-\frac{\mathrm{i}M_\mathrm{Z}c_\gamma c_\mathrm{w}}{2M_\mathrm{W}s_\mathrm{w}}$	$\frac{\mathrm{i}M_{\mathrm{Z}'}c_\mathrm{w}s_\gamma}{2M_\mathrm{W}s_\mathrm{w}}$
C_2	0	0	0	0

$V_1S_2S_3$	$A\phi^+\phi^-$	$Z\phi^+\phi^-$	$Z'\phi^+\phi^-$	$Z\chi h$
C	-1	$\frac{\eta s_\mathrm{w}s_\gamma + c_\gamma(c_\mathrm{w}^2 - s_\mathrm{w}^2)}{2c_\mathrm{w}s_\mathrm{w}}$	$\frac{s_\mathrm{w}(\eta c_\gamma + s_\mathrm{w}s_\gamma) - s_\gamma c_\mathrm{w}^2}{2c_\mathrm{w}s_\mathrm{w}}$	$-\frac{\mathrm{i}M_\mathrm{Z}c_\alpha c_\gamma(c_\gamma - \eta s_\mathrm{w}s_\gamma)}{2M_\mathrm{W}s_\mathrm{w}}$
C_2	0	0	0	$-\frac{\mathrm{i}M_{\mathrm{Z}'}s_\alpha s_\gamma^2 c_\mathrm{w}}{M_\mathrm{W}}$

$V_1S_2S_3$	$Z\chi H$	$Z\chi' h$	$Z\chi' H$
C_1	$-\frac{\mathrm{i}M_\mathrm{Z}c_\gamma s_\alpha(c_\gamma-\eta s_\mathrm{w}s_\gamma)}{2M_\mathrm{W}s_\mathrm{w}}$	$\frac{\mathrm{i}M_{\mathrm{Z}'}c_\alpha s_\gamma c_\gamma(1-\eta s_\mathrm{w}t_\gamma)}{2M_\mathrm{W}s_\mathrm{w}}$	$\frac{\mathrm{i}M_{\mathrm{Z}'}s_\alpha s_\gamma c_\gamma(1-\eta s_\mathrm{w}t_\gamma)}{2M_\mathrm{W}s_\mathrm{w}}$
C_2	$\frac{\mathrm{i}M_{\mathrm{Z}'}c_\alpha s_\gamma^2 c_\mathrm{w}}{M_\mathrm{W}}$	$-\frac{\mathrm{i}M_\mathrm{Z}s_\alpha s_\gamma c_\gamma c_\mathrm{w}}{M_\mathrm{W}}$	$\frac{\mathrm{i}M_\mathrm{Z}c_\alpha s_\gamma c_\gamma c_\mathrm{w}}{M_\mathrm{W}}$

$V_1S_2S_3$	$Z'\chi h$	$Z'\chi' h$	$Z'\chi H$
C_1	$\frac{\mathrm{i}M_\mathrm{Z}c_\alpha c_\gamma^2(\eta s_\mathrm{w}+t_\gamma)}{2M_\mathrm{W}s_\mathrm{w}}$	$-\frac{\mathrm{i}M_{\mathrm{Z}'}c_\alpha s_\gamma(s_\gamma+\eta s_\mathrm{w}c_\gamma)}{2M_\mathrm{W}s_\mathrm{w}}$	$\frac{\mathrm{i}M_\mathrm{Z}s_\alpha c_\gamma^2(\eta s_\mathrm{w}+t_\gamma)}{2M_\mathrm{W}s_\mathrm{w}}$
C_2	$-\frac{\mathrm{i}M_{\mathrm{Z}'}s_\alpha s_\gamma c_\gamma c_\mathrm{w}}{M_\mathrm{W}}$	$-\frac{\mathrm{i}M_\mathrm{Z}s_\alpha c_\gamma^2 c_\mathrm{w}}{M_\mathrm{W}}$	$\frac{\mathrm{i}M_{\mathrm{Z}'}c_\alpha s_\gamma c_\gamma c_\mathrm{w}}{M_\mathrm{W}}$

$V_1S_2S_3$	$Z'\chi' H$
C_1	$-\frac{\mathrm{i}M_{\mathrm{Z}'}s_\alpha s_\gamma(s_\gamma+c_\gamma\eta s_\mathrm{w})}{2M_\mathrm{W}s_\mathrm{w}}$
C_2	$\frac{\mathrm{i}M_\mathrm{Z}c_\alpha c_\gamma^2 c_\mathrm{w}}{M_\mathrm{W}}$

SVV vertex:

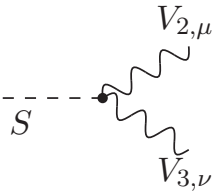

$$= ig_{\mu\nu}\left(eC_1 + \tilde{e}C_2\right),$$

with the values

$S_1V_2V_3$	hZZ	HZZ	hZZ'
C_1	$\frac{c_\alpha M_\mathrm{W}(\eta s_\gamma s_\mathrm{w}+c_\gamma)^2}{c_\mathrm{w}^2 s_\mathrm{w}}$	$\frac{s_\alpha M_\mathrm{W}(c_\gamma-\eta s_\gamma s_\mathrm{w})^2}{c_\mathrm{w}^2 s_\mathrm{w}}$	$\frac{c_\alpha M_\mathrm{W}\left[s_{2\gamma}(\eta^2 s_\mathrm{w}^2-1)-2\eta s_\mathrm{w}c_{2\gamma}\right]}{2c_\mathrm{w}^2 s_\mathrm{w}}$
C_2	$-2v_1\tilde{e}s_\alpha s_\gamma^2$	$2v_1\tilde{e}c_\alpha s_\gamma^2$	$-v_1\tilde{e}s_\alpha s_{2\gamma}$

$S_1V_2V_3$	HZZ'	$hZ'Z'$	$HZ'Z'$
C_1	$\frac{s_\alpha M_\mathrm{W}\left[s_{2\gamma}(\eta^2 s_\mathrm{w}^2-1)-2\eta s_\mathrm{w}c_{2\gamma}\right]}{2c_\mathrm{w}^2 s_\mathrm{w}}$	$\frac{c_\alpha M_\mathrm{W}(s_\gamma+\eta s_\mathrm{w}c_\gamma)^2}{c_\mathrm{w}^2 s_\mathrm{w}}$	$\frac{s_\alpha M_\mathrm{W}(s_\gamma+\eta s_\mathrm{w}c_\gamma)^2}{c_\mathrm{w}^2 s_\mathrm{w}}$
C_2	$v_1\tilde{e}c_\alpha s_{2\gamma}$	$-2v_1\tilde{e}s_\alpha c_\gamma^2$	$2v_1\tilde{e}c_\alpha c_\gamma^2$

$S_1V_2V_3$	hW^+W^-	HW^+W^-	$\phi^\pm W^\mp A$	$\phi^\pm W^\mp Z$	$\phi^\pm W^\mp Z'$
C_1	$\frac{c_\alpha M_\mathrm{W}}{s_\mathrm{w}}$	$\frac{s_\alpha M_\mathrm{W}}{s_\mathrm{w}}$	$-M_\mathrm{W}$	$\frac{M_\mathrm{W}(\eta s_\gamma - s_\mathrm{w} c_\gamma)}{c_\mathrm{w}}$	$\frac{M_\mathrm{W}(\eta c_\gamma + s_\gamma s_\mathrm{w})}{c_\mathrm{w}}$
C_2	0	0	0	0	0

SSS vertex:

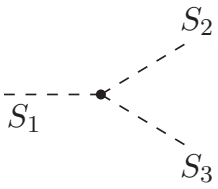

$$= \frac{\mathrm{i}e}{2 s_\mathrm{w} M_\mathrm{W}} C_1 + \frac{4\mathrm{i} s_\mathrm{w} \lambda_{12} M_\mathrm{W}}{e\,(M_\mathrm{h}^2 - M_\mathrm{H}^2)} C_2,$$

with the values

$S_1S_2S_3$	HHh	Hhh	hhh	HHH
C_1	$-s_\alpha^2 c_\alpha\,(2M_\mathrm{H}^2 + M_\mathrm{h})$	$-\,(M_\mathrm{H}^2 + 2M_\mathrm{h}^2)\, s_\alpha c_\alpha^2$	$-3M_\mathrm{h}^2 c_\alpha^3$	$-3M_\mathrm{H}^2 s_\alpha^3$
C_2	$-c_\alpha\,(2M_\mathrm{H}^2 + M_\mathrm{h}^2)$	$s_\alpha\,(M_\mathrm{H}^2 + 2M_\mathrm{h}^2)$	$-3 s_\alpha t_\alpha M_\mathrm{h}^2$	$\frac{3M_\mathrm{H}^2 c_\alpha}{t_\alpha}$

$S_1S_2S_3$	$\phi^+\phi^- h$	$\phi^+\phi^- H$	$\chi'\chi' h$	$\chi\chi h$	$\chi'\chi' H$	$\chi\chi H$
C_1	$-M_\mathrm{h}^2 c_\alpha$	$-M_\mathrm{H}^2 s_\alpha$	$-M_\mathrm{h}^2 c_\alpha s_x^2$	$M_\mathrm{h}^2 c_\alpha c_x^2$	$M_\mathrm{H}^2 s_\alpha s_x^2$	$-M_\mathrm{H}^2 s_\alpha c_x^2$
C_2	0	0	$\frac{-M_\mathrm{h}^2 c_x^2}{c_\alpha}$	$-\frac{M_\mathrm{h}^2 s_x^2}{c_\alpha}$	$\frac{M_\mathrm{H}^2 c_x^2}{s_\alpha}$	$\frac{M_\mathrm{H}^2 s_x^2}{s_\alpha}$

$S_1S_2S_3$	$\chi\chi' h$	$\chi\chi' H$
C_1	$\frac{M_\mathrm{h}^2 s_{2x} s_\alpha^2}{2c_\alpha}$	$\frac{M_\mathrm{H}^2 s_{2x} s_\alpha}{2}$
C_2	$-\frac{M_\mathrm{h}^2 s_{2x}}{2c_\alpha}$	$\frac{M_\mathrm{H}^2 s_{2x}}{2s_\alpha}$

SSVV vertex:

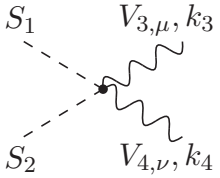

$$= \mathrm{i}\left(e^2 C_1 + \tilde{e}^2 C_2\right) g_{\mu\nu},$$

with the values

$S_1S_2V_2V_3$	$hhZZ$	$hhZ'Z$	$hhZ'Z'$	$HHZZ$
C_1	$\frac{c_\alpha^2(c_\gamma-\eta s_\mathrm{w} s_\gamma)^2}{2c_\mathrm{w}^2 s_\mathrm{w}^2}$	$\frac{c_\alpha^2\left[2\eta s_\mathrm{w} c_{2\gamma}+s_{2\gamma}(1-\eta^2 s_\mathrm{w}^2)\right]}{4c_\mathrm{w}^2 s_\mathrm{w}^2}$	$\frac{c_\alpha^2(s_\gamma+\eta s_\mathrm{w} c_\gamma)^2}{2c_\mathrm{w}^2 s_\mathrm{w}^2}$	$\frac{s_\alpha^2(c_\gamma-\eta s_\mathrm{w} s_\gamma)^2}{2c_\mathrm{w}^2 s_\mathrm{w}^2}$
C_2	$2s_\alpha^2 s_\gamma^2$	$s_\alpha s_{2\gamma}$	$2s_\alpha^2 c_\gamma^2$	$2c_\alpha^2 s_\gamma^2$

$S_1S_2V_2V_3$	$HHZ'Z$	$HHZ'Z'$	$HhZZ$
C_1	$-\frac{s_\alpha^2\left[2\eta s_\mathrm{w} c_{2\gamma}+s_{2\gamma}\left(1-\eta^2 s_\mathrm{w}^2\right)\right]}{4c_\mathrm{w}^2 s_\mathrm{w}^2}$	$\frac{s_\alpha^2(s_\gamma+\eta s_\mathrm{w} c_\gamma)^2}{2c_\mathrm{w}^2 s_\mathrm{w}^2}$	$\frac{s_{2\alpha}(\eta s_\mathrm{w} s_\gamma-c_\gamma)^2}{4s_\mathrm{w}^2 c_\mathrm{w}^2}$
C_2	$c_\alpha^2 s_{2\gamma}$	$2c_\alpha^2 c_\gamma^2$	$-s_{2\alpha}s_\gamma^2$

$S_1S_2V_2V_3$	$HhZ'Z$	$HhZ'Z'$	$\phi^+\phi^-AA$	$\phi^+\phi^-ZA$
C_1	$-\frac{s_{2\alpha}\left[2\eta s_\mathrm{w} c_{2\gamma}+s_{2\gamma}\left(1-\eta^2 s_\mathrm{w}^2\right)\right]}{8c_\mathrm{w}^2 s_\mathrm{w}^2}$	$\frac{s_{2\alpha}(s_\gamma+\eta s_\mathrm{w} c_\gamma)^2}{4c_\mathrm{w}^2 s_\mathrm{w}^2}$	2	$-\frac{\eta s_\mathrm{w} s_\gamma+s_\gamma\left(c_\mathrm{w}^2-s_\mathrm{w}^2\right)}{c_\mathrm{w} s_\mathrm{w}}$
C_2	$-s_{2\alpha}c_\gamma s_\gamma$	$-s_{2\alpha}c_\gamma^2$	0	0

$S_1S_2V_2V_3$	$\phi^+\phi^-Z'A$	$\phi^+\phi^-ZZ$	$\phi^+\phi^-Z'Z$
C_1	$\frac{s_\gamma\left(c_\mathrm{w}^2-s_\mathrm{w}^2\right)-\eta s_\mathrm{w} c_\gamma}{c_\mathrm{w} s_\mathrm{w}}$	$\frac{\left[\eta s_\mathrm{w} s_\gamma+c_\gamma\left(c_\mathrm{w}^2-s_\mathrm{w}^2\right)\right]^2}{2c_\mathrm{w}^2 s_\mathrm{w}^2}$	$\frac{2\eta s_\mathrm{w} c_{2\gamma}(c_\mathrm{w}^2-s_\mathrm{w}^2)-s_{2\gamma}\left[\left(c_\mathrm{w}^2-s_\mathrm{w}^2\right)^2-\eta^2 s_\mathrm{w}^2\right]}{4c_\mathrm{w}^2 s_\mathrm{w}^2}$
C_2	0	0	0

$S_1S_2V_2V_3$	$\phi^+\phi^-Z'Z'$	hhW^+W^-	HhW^+W^-	HHW^+W^-
C_1	$\frac{\left[\eta s_\mathrm{w} c_\gamma+s_\gamma\left(s_\mathrm{w}^2-c_\mathrm{w}^2\right)\right]^2}{2c_\mathrm{w}^2 s_\mathrm{w}^2}$	$\frac{c_\alpha^2}{2s_\mathrm{w}^2}$	$\frac{s_\alpha c_\alpha}{2s_\mathrm{w}}$	$\frac{s_\alpha^2}{2s_\mathrm{w}}$
C_2	0	0	0	0

$S_1S_2V_2V_3$	$\phi^+\phi^-W^+W^-$	$\chi\chi W^+W^-$	$\chi\chi' W^+W^-$	$\chi'\chi' W^+W^-$
C_1	$\frac{1}{2s_\mathrm{w}^2}$	$\frac{M_\mathrm{Z}^2 c_\gamma^2 c_\mathrm{w}^2}{2M_\mathrm{W}^2 s_\mathrm{w}^2}$	$-\frac{M_\mathrm{Z} M_{\mathrm{Z}'} s_\gamma c_\gamma c_\mathrm{w}^2}{2M_\mathrm{W}^2 s_\mathrm{w}^2}$	$\frac{M_{\mathrm{Z}'}^2 s_\gamma^2 c_\mathrm{w}^2}{2M_\mathrm{W}^2 s_\mathrm{w}^2}$
C_2	0	0	0	0

$S_1S_2V_2V_3$	$\chi\chi ZZ$	$\chi\chi Z'Z$	$\chi\chi Z'Z'$
C_1	$\frac{M_\mathrm{Z}^2 c_\gamma^4 (1-\eta s_\mathrm{w} t_\gamma)^2}{2M_\mathrm{W}^2 s_\mathrm{w}^2}$	$\frac{M_\mathrm{Z}^2 c_\gamma^2 \left[2\eta s_\mathrm{w} c_{2\gamma} + s_{2\gamma}\left(1-\eta^2 s_\mathrm{w}^2\right)\right]}{4M_\mathrm{W}^2 s_\mathrm{w}^2}$	$\frac{M_\mathrm{Z}^2 c_\gamma^2 (\eta s_\mathrm{w} c_\gamma + s_\gamma)^2}{2M_\mathrm{W}^2 s_\mathrm{w}^2}$
C_2	$\frac{2M_{\mathrm{Z}'}^2 s_\gamma^4 c_\mathrm{w}^2}{M_\mathrm{W}^2}$	$\frac{2M_{\mathrm{Z}'}^2 c_\gamma s_\gamma^3 c_\mathrm{w}^2}{M_\mathrm{W}^2}$	$\frac{2M_{\mathrm{Z}'}^2 c_\gamma^2 s_\gamma^2 c_\mathrm{w}^2}{M_\mathrm{W}^2}$

$S_1S_2V_2V_3$	$\chi'\chi ZZ$	$\chi'\chi Z'Z$
C_1	$\frac{M_\mathrm{Z} M_{\mathrm{Z}'} s_{2\gamma} (\eta s_\mathrm{w} s_\gamma - c_\gamma)^2}{4M_\mathrm{W}^2 s_\mathrm{w}^2}$	$\frac{M_\mathrm{Z} M_{\mathrm{Z}'} s_{2\gamma} \left[2\eta s_\mathrm{w} c_{2\gamma} + s_{2\gamma}\left(1-\eta^2 s_\mathrm{w}^2\right)\right]}{8M_\mathrm{W}^2 s_\mathrm{w}^2}$
C_2	$\frac{2M_\mathrm{Z} M_{\mathrm{Z}'} s_\gamma^3 c_\gamma c_\mathrm{w}^2}{M_\mathrm{W}^2}$	$\frac{2M_\mathrm{Z} M_{\mathrm{Z}'} s_\gamma^2 c_\gamma^2 c_\mathrm{w}^2}{M_\mathrm{W}^2}$

$S_1S_2V_2V_3$	$\chi'\chi Z'Z'$	$\chi'\chi' ZZ$
C_1	$-\frac{M_\mathrm{Z} M_{\mathrm{Z}'} s_{2\gamma} (s_\gamma + \eta s_\mathrm{w} c_\gamma)^2}{4M_\mathrm{W}^2 s_\mathrm{w}^2}$	$\frac{M_{\mathrm{Z}'} s_\gamma^2 (\eta s_\mathrm{w} s_\gamma - c_\gamma)^2}{2M_\mathrm{W}^2 s_\mathrm{w}^2}$
C_2	$\frac{2M_\mathrm{Z} M_{\mathrm{Z}'} c_\gamma^3 s_\gamma c_\mathrm{w}^2}{M_\mathrm{W}^2}$	$\frac{2M_\mathrm{Z}^2 c_\gamma^2 s_\gamma^2 c_\mathrm{w}^2}{M_\mathrm{W}^2}$

$S_1S_2V_2V_3$	$\chi'\chi' Z'Z$	$\chi'\chi' Z'Z'$
C_1	$\frac{M_\mathrm{Z} M_{\mathrm{Z}'} s_{2\gamma} \left[2\eta s_\mathrm{w} c_{2\gamma} + s_{2\gamma}\left(1-\eta^2 s_\mathrm{w}^2\right)\right]}{8M_\mathrm{W}^2 s_\mathrm{w}^2}$	$\frac{M_{\mathrm{Z}'}^2 s_\gamma^2 c_\gamma^2 (t_\gamma + \eta s_\mathrm{w})^2}{2M_\mathrm{W}^2 s_\mathrm{w}^2}$
C_2	$\frac{2M_\mathrm{Z} M_{\mathrm{Z}'} c_\gamma^2 s_\gamma^2 c_\mathrm{w}^2}{M_\mathrm{W}^2}$	$\frac{2M_\mathrm{Z}^2 c_\gamma^4 c_\mathrm{w}^2}{M_\mathrm{W}^2}$

$S_1S_2V_2V_3$	$h\phi^\mp W^\pm A$	$H\phi^\mp W^\pm A$	$\chi\phi^\mp W^\pm A$	$\chi'\phi^\mp W^\pm A$	$h\phi^\mp W^\pm Z$
C_1	$-\frac{c_\alpha}{2s_\mathrm{w}}$	$-\frac{s_\alpha}{2s_\mathrm{w}}$	$\mp\frac{\mathrm{i}M_\mathrm{Z} c_\gamma c_\mathrm{w}}{2M_\mathrm{W} s_\mathrm{w}}$	$\pm\frac{\mathrm{i}M_{\mathrm{Z}'} s_\gamma c_\mathrm{w}}{2M_\mathrm{W} s_\mathrm{w}}$	$\frac{c_\alpha(\eta s_\gamma - s_\mathrm{w} c_\gamma)}{2c_\mathrm{w} s_\mathrm{w}}$
C_2	0	0	0	0	0

$S_1S_2V_2V_3$	$h\phi^\mp W^\pm Z'$	$H\phi^\mp W^\pm Z$	$H\phi^\mp W^\pm Z'$	$\chi\phi^\mp W^\pm Z$
C_1	$\frac{c_\alpha(\eta c_\gamma + s_\mathrm{w} s_\gamma)}{2c_\mathrm{w} s_\mathrm{w}}$	$\frac{s_\alpha(\eta s_\gamma - s_\mathrm{w} c_\gamma)}{2c_\mathrm{w} s_\mathrm{w}}$	$\frac{s_\alpha(\eta c_\gamma + s_\mathrm{w} s_\gamma)}{2c_\mathrm{w} s_\mathrm{w}}$	$\pm\frac{\mathrm{i}M_\mathrm{Z} c_\gamma(\eta s_\gamma - s_\mathrm{w} c_\gamma)}{2M_\mathrm{W} s_\mathrm{w}}$
C_2	0	0	0	0

$S_1S_2V_2V_3$	$\chi\phi^{\mp}W^{\pm}Z'$	$\chi'\phi^{\mp}W^{\pm}Z$	$\chi'\phi^{\mp}W^{\pm}Z'$
C_1	$\pm\frac{\mathrm{i}M_{\mathrm{Z}}c_\gamma(\eta+s_{\mathrm{w}}t_\gamma)}{2M_{\mathrm{W}}s_{\mathrm{w}}}$	$\pm\frac{\mathrm{i}M_{\mathrm{Z}'}s_\gamma(c_\gamma s_{\mathrm{w}}-\eta s_\gamma)}{2M_{\mathrm{W}}s_{\mathrm{w}}}$	$\mp\frac{\mathrm{i}M_{\mathrm{Z}'}s_\gamma c_\gamma(\eta+s_{\mathrm{w}}t_\gamma)}{2M_{\mathrm{W}}s_{\mathrm{w}}}$
C_2	0	0	0

$S\bar{G}G$ vertex:

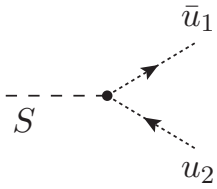

$= \mathrm{i}eC_1 + \mathrm{i}\tilde{e}C_2,$

with the values

$S\bar{u}_1u_2$	$h\bar{u}^Zu^Z$	$h\bar{u}^{Z'}u^{Z'}$	$H\bar{u}^Zu^Z$
C_1	$-\frac{M_{\mathrm{Z}}^2c_\alpha c_\gamma(c_\gamma-\eta s_\gamma s_{\mathrm{w}})}{2M_{\mathrm{W}}s_{\mathrm{w}}}$	$-\frac{M_{\mathrm{Z}'}^2c_\alpha s_\gamma(s_\gamma+\eta s_{\mathrm{w}}c_\gamma)}{2M_{\mathrm{W}}s_{\mathrm{w}}}$	$\frac{M_{\mathrm{Z}}^2c_\gamma s_\alpha(\eta s_\gamma s_{\mathrm{w}}-c_\gamma)}{2M_{\mathrm{W}}s_{\mathrm{w}}}$
C_2	$\frac{M_{\mathrm{Z}}M_{\mathrm{Z}'}c_{\mathrm{w}}s_\alpha s_\gamma^2}{M_{\mathrm{W}}}$	$\frac{M_{\mathrm{Z}}M_{\mathrm{Z}'}c_\gamma^2s_\alpha c_{\mathrm{w}}}{M_{\mathrm{W}}}$	$-\frac{M_{\mathrm{Z}}M_{\mathrm{Z}'}c_\alpha s_\gamma^2c_{\mathrm{w}}}{M_{\mathrm{W}}}$

$S\bar{u}_1u_2$	$\chi\bar{u}^{\pm}u^{\pm}$	$\chi'\bar{u}^{\pm}u^{\pm}$	$\phi^{\pm}\bar{u}^{\pm}u^A$	$\phi^{\pm}\bar{u}^{\pm}u^Z$
C_1	$\mp\mathrm{i}\frac{M_{\mathrm{Z}}c_{\mathrm{w}}c_\gamma}{2s_{\mathrm{w}}}$	$\pm\mathrm{i}\frac{M_{\mathrm{Z}'}s_\gamma c_{\mathrm{w}}}{2s_{\mathrm{w}}}$	M_{W}	$M_{\mathrm{W}}\left[\frac{(s_{\mathrm{w}}^2-c_{\mathrm{w}}^2)}{2s_{\mathrm{w}}c_{\mathrm{w}}}\left(c_\gamma-s_{\mathrm{w}}\eta s_\gamma\right)-s_{\mathrm{w}}s_\gamma\eta\right]$
C_2	0	0	0	0

$S\bar{u}_1u_2$	$\phi^{\pm}\bar{u}^{\pm}u^{Z'}$	$\phi^{\pm}\bar{u}^Zu^{\mp}$	$\phi^{\pm}\bar{u}^{Z'}u^{\mp}$	$h\bar{u}^{\pm}u^{\pm}$
C_1	$-M_{\mathrm{W}}\left[\frac{(s_{\mathrm{w}}^2-c_{\mathrm{w}}^2)}{2s_{\mathrm{w}}c_{\mathrm{w}}}\left(s_\gamma+s_{\mathrm{w}}\eta c_\gamma\right)+s_{\mathrm{w}}c_\gamma\eta\right]$	$-\frac{M_{\mathrm{Z}'}^2s_\gamma c_{\mathrm{w}}}{2M_{\mathrm{W}}s_{\mathrm{w}}}$	$\frac{M_{\mathrm{Z}}^2c_{\mathrm{w}}c_\gamma}{2M_{\mathrm{W}}s_{\mathrm{w}}}$	$-\frac{c_\alpha M_{\mathrm{W}}}{2s_{\mathrm{w}}}$
C_2	0	0	0	0

$S\bar{u}_1u_2$	$H\bar{u}^{\pm}u^{\pm}$	$h\bar{u}^Zu^{Z'}$	$h\bar{u}^{Z'}u^Z$	$H\bar{u}^Zu^{Z'}$
C_1	$-\frac{s_\alpha M_{\mathrm{W}}}{2s_{\mathrm{w}}}$	$\frac{M_{\mathrm{Z}}^2c_\alpha c_\gamma(s_\gamma+\eta c_\gamma s_{\mathrm{w}})}{2M_{\mathrm{W}}s_{\mathrm{w}}}$	$\frac{M_{\mathrm{Z}'}^2c_\alpha s_\gamma(c_\gamma-\eta s_\gamma s_{\mathrm{w}})}{2M_{\mathrm{W}}s_{\mathrm{w}}}$	$\frac{M_{\mathrm{Z}}^2c_\gamma s_\alpha(s_\gamma+\eta s_{\mathrm{w}}c_\gamma)}{2M_{\mathrm{W}}s_{\mathrm{w}}}$
C_2	0	$\frac{M_{\mathrm{Z}}M_{\mathrm{Z}'}c_\gamma s_\alpha s_\gamma c_{\mathrm{w}}}{M_{\mathrm{W}}}$	$\frac{M_{\mathrm{Z}}M_{\mathrm{Z}'}c_\gamma s_\alpha s_\gamma c_{\mathrm{w}}}{M_{\mathrm{W}}}$	$-\frac{M_{\mathrm{Z}}M_{\mathrm{Z}'}c_\alpha c_\gamma s_\gamma c_{\mathrm{w}}}{M_{\mathrm{W}}}$

$S\bar{u}_1u_2$	$H\bar{u}^{Z'}u^Z$	$H\bar{u}^{Z'}u^{Z'}$
C_1	$\frac{M_{Z'}^2 s_\alpha s_\gamma (c_\gamma - \eta s_\gamma s_w)}{2M_W s_w}$	$-\frac{M_{Z'}^2 s_\alpha s_\gamma (s_\gamma + \eta c_\gamma s_w)}{2M_W s_w}$
C_2	$-\frac{M_Z M_{Z'} c_\alpha c_\gamma s_\gamma c_w}{M_W}$	$-\frac{M_Z M_{Z'} c_\alpha c_\gamma^2 c_w}{M_W}$

V$\bar{\text{G}}$G vertex:

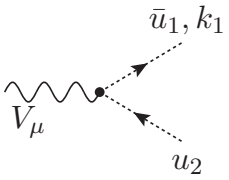

$$= \mathrm{i}ek_{1,\mu}C,$$

with the values

$V\bar{u}_1u_2$	$A\bar{u}^\pm u^\pm$	$W^\pm\bar{u}^A u^\mp$	$W^\mp\bar{u}^\mp u^A$	$Z\bar{u}^\pm u^\pm$	$Z'\bar{u}^\pm u^\pm$
C	± 1	± 1	± 1	$\mp\frac{c_\gamma c_w}{s_w}$	$\mp\frac{s_\gamma c_w}{s_w}$

$V\bar{u}_1u_2$	$W^\pm\bar{u}^Z u^\mp$	$W^\pm\bar{u}^{Z'} u^\mp$	$W^\mp\bar{u}^\mp u^Z$	$W^\mp\bar{u}^\mp u^{Z'}$
C	$\mp\frac{c_\gamma c_w}{s_w}$	$\pm\frac{s_\gamma c_w}{s_w}$	$\mp\frac{c_\gamma c_w}{s_w}$	$\mp\frac{s_\gamma c_w}{s_w}$

German Summary

Die gegenwärtige Theorie der Hochenergiephysik ist das sogenannte Standard Modell der Teilchenphysik (SM). In der Vergangenheit wurde Übereinstimmung zwischen zahlreichen sehr präzisen Messungen an Beschleunigerexperimenten und den entsprechenden Vorhersagen des SMs gefunden. Trotz dieser erstaunlichen Vorhersagekraft des SMs gibt es einige Beobachtungen, wie beispielsweise die im sichtbaren Universum beobachtete Materie-Antimaterie Asymmetrie oder die Existenz von Dunkler Materie, die es nicht erklären kann. Auch haben Neutrinos, im Widerspruch zu den Erkenntnissen, die aus Messungen moderner Experimente geschlossen werden konnten, im SM keine Masse.
Diese unerklärten Phänomene zeigen, dass das SM nicht die ultimative Theorie, die der Natur zugrunde liegt, sein kann. Mit der Entdeckung eines Higgs-Bosons [1, 2] am LHC im Jahre 2012 wurde das letzte Teilchen, das vom SM vorhergesagt wird, gefunden. Da trotz immenser Bemühungen seitdem keine neuen Elementarteilchen entdeckt wurden, ist die Suche nach kleinsten Abweichungen zwischen hochpräzisen Messungen und ebenso präzisen Theorievorhersagen des SMs und seiner Erweiterungen der vielversprechendste Weg, um Hinweise auf die Struktur von neuer Physik zu bekommen.
In dieser Arbeit wird die sogenannte „Dark Abelian Sector Model“(DASM) Erweiterung des SMs definiert. Das DASM erweitert die Eichgruppe des SMs um eine weitere, spontan gebrochene, $U(1)_\mathrm{d}$ Eichsymmetrie. Das SM ist ein Singulett unter der $U(1)_\mathrm{d}$. Zusätzlich zum massebehafteten neutralen Z′-Eichboson, das zum entsprechenden Eichfeld der $U(1)_\mathrm{d}$ gehört, führt das DASM noch ein weiteres Higgs-Boson und ein Dirac-Fermion ein, die beide ausschließlich Ladung der $U(1)_\mathrm{d}$ tragen, sowie ungeladene SM-artige rechts-händige Neutrinos. Das SM besitzt zwei Operatoren – den Higgsmassenoperator $\Phi^\dagger\Phi$ und den Feldstärketensor der schwachen Hyperladung – die eichinvariant sind und eine Massendimension < 4 haben. Die durch das DASM eingeführten Erweiterungen des SM nutzen diese beiden Operatoren, um zwei Portale zu einem möglichen dunklen Sektor, der unter dem SM ungeladen ist, zu öffnen. Die Existenz der rechts-händigen SM-artigen Neutrinos und des zusätzlichen Fermions erlaubt es zudem, ein drittes Portal zwischen dem SM und dem dunklen Sektor zu öffnen.
In der vorgelegten Arbeit erarbeiten wir das DASM vollständig und bringen es

in eine Form, die das Berechnen von Vorhersagen erleichtert. Des Weiteren definieren wir intuitive und experimentell gut messbare Inputparameter für das DASM. Dafür ersetzen wir die ursprünglichen Parameter der Lagrangedichte soweit möglich durch die Massen der neuen Teilchen und Mischungswinkel, die die Änderungen der Kopplungsstärken der entsprechenden SM-artigen Teilchen im Vergleich zu ihren jeweiligen SM-Werten parametrisieren. Für den Higgssektor wählen wir die Masse $M_{\mathrm{h}'}$ des neuen Higgs-Bosons, den Mischungswinkel α des Higgssektors, und die skalare Selbstkopplung λ_{12} als Inputparameter für die drei neu eingeführten freien Parameter. Im Eichsektor wählen wir die Masse $M_{\mathrm{Z}'}$ des neuen Eichbosons und den Mischungswinkel γ des Eichsektors als neue Inputparameter. Im Fermionsektor wählen wir die Masse m_{ν_4} des neuen Fermions und den Mischungswinkel θ_{r} des fermionischen Sektors. Mit dieser Wahl der Inputparameter definieren wir daraufhin auf nächstführender Ordnung ein „*On-Shell*-Renormierungsschema“ und geben zusätzlich die Ergebnisse der Renormierungskonstanten der Mischungswinkel für $\overline{\mathrm{MS}}$-Renormierung explizit an.
Wir nutzen diese Renormierungsschemata, um eine erste Analyse der phänomenologischen Implikationen der DASM-Erweiterungen durchzuführen. Dafür betrachten wir vier elektroschwache Präzessionsobservablen (PO): Die Masse des W-Bosons, errechnet über den Myonenzerfall, das anomale magnetische Moment des Myons, den leptonischen effektiven schwachen Mischungswinkel, und die leptonische Zerfallsbreite des Z-Bosons. Mithilfe eines simultanen Fits dieser PO finden wir Regionen des DASM-Parameterraumes, die die große Diskrepanz zwischen Messung und Vorhersage des anomalen magnetischen Moments des Myons verschwinden lassen und gleichzeitig zu einer Übereinstimmung der Vorhersagen und Messungen der anderen drei PO führen, die ähnlich gut wie die respektive Übereinstimmung im SM ist. Somit beschreibt das DASM die untersuchten Daten in diesen Bereichen signifikant besser als das SM und bleibt damit eine vielversprechende Erweiterung für die Suche nach neuer Physik. Für weiterführende Untersuchungen wäre es interessant, wenn weitere PO mit in diese Analyse aufgenommen werden, um ein noch besseres und ganzheitlicheres Verständnis für die phänomenologischen Implikationen der DASM-Erweiterung zu bekommen und zu untersuchen, ob das DASM beispielsweise mögliche Erklärungen für den Ursprung Dunkler Materie liefern kann.

Bibliography

[1] ATLAS Collaboration, G. Aad, et al., *Observation of a new particle in the search for the Standard Model Higgs boson with the ATLAS detector at the LHC*, *Phys. Lett. B* **7**16 (2012) 1–29, [arXiv:1207.7214].

[2] CMS Collaboration, S. Chatrchyan, et al., *Observation of a New Boson at a Mass of 125 GeV with the CMS Experiment at the LHC*, *Phys. Lett. B* **7**16 (2012) 30–61, [arXiv:1207.7235].

[3] **M**uon g-2 Collaboration, D. P. Aguillard et al., *Measurement of the Positive Muon Anomalous Magnetic Moment to 0.20 ppm*, *Phys. Rev. Lett.* **1**31 (2023) 161802, [arXiv:2308.06230].

[4] T. Aoyama et al., *The anomalous magnetic moment of the muon in the Standard Model*, *Phys. Rept.* **8**87 (2020) 1–166, [arXiv:2006.04822].

[5] S. Borsanyi et al., *Leading hadronic contribution to the muon magnetic moment from lattice QCD*, *Nature* **5**93 (2021) 51–55, [arXiv:2002.12347].

[6] M. Awramik, M. Czakon, A. Freitas, and G. Weiglein, *Precise prediction for the W-boson mass in the standard model*, *Phys. Rev. D* **6**9 (2004) 053006, [hep-ph/0311148].

[7] **C**DF Collaboration, C. Hays, *High precision measurement of the W-boson mass with the CDF II detector*, *PoS* **I**CHEP2022 (2022) 898.

[8] **L**HC-TeV MW Working Group Collaboration, S. Amoroso et al., *Compatibility and combination of world W-boson mass measurements*, *Eur. Phys. J. C* **8**4 (2024) 451, [arXiv:2308.09417].

[9] I. Brivio and M. Trott, *The Standard Model as an Effective Field Theory*, *Phys. Rept.* **7**93 (2019) 1–98, [arXiv:1706.08945].

[10] V. Silveira and A. Zee, *Scalar Phantoms*, *Phys. Lett. B* **1**61 (1985) 136–140.

[11] V. Barger, P. Langacker, M. McCaskey, M. Ramsey-Musolf, and G. Shaughnessy, *Complex Singlet Extension of the Standard Model*, *Phys. Rev. D* **7**9 (2009) 015018, [arXiv:0811.0393].

[12] D. O'Connell, M. J. Ramsey-Musolf, and M. B. Wise, *Minimal Extension of the Standard Model Scalar Sector*, *Phys. Rev. D* **7**5 (2007) 037701, [hep-ph/0611014].

[13] R. M. Schabinger and J. D. Wells, *A Minimal spontaneously broken hidden sector and its impact on Higgs boson physics at the CERN Large Hadron Collider*, *Phys. Rev. D* **7**2 (2005) 093007, [hep-ph/0509209].

[14] T. D. Lee, *A Theory of Spontaneous T Violation*, *Phys. Rev. D* **8** (1973) 1226–1239.

[15] G. C. Branco, et al., *Theory and phenomenology of two-Higgs-doublet models*, *Phys. Rept.* **5**16 (2012) 1–102, [arXiv:1106.0034].

[16] Particle Data Group Collaboration, R. Workman, et al., *Review of Particle Physics*, *PTEP* **2**022 (2022) 083C01.

[17] G. Chalons, D. Lopez-Val, T. Robens, and T. Stefaniak, *The Higgs singlet extension at LHC Run 2*, *PoS* **DIS**2016 (2016) 113, [arXiv:1606.07793].

[18] M. Pospelov, *Secluded U(1) below the weak scale*, *Phys. Rev. D* **8**0 (2009) 095002, [arXiv:0811.1030].

[19] H. Davoudiasl, H.-S. Lee, and W. J. Marciano, *Dark Side of Higgs Diphoton Decays and Muon g-2*, *Phys. Rev. D* **8**6 (2012) 095009, [arXiv:1208.2973].

[20] M. Cadeddu, N. Cargioli, F. Dordei, C. Giunti, and E. Picciau, *Muon and electron g-2 and proton and cesium weak charges implications on dark Z_d models*, *Phys. Rev. D* **1**04 (2021) L011701, [arXiv:2104.03280].

[21] K. Sakurai, F. Takahashi, and W. Yin, *Singlet extensions and W boson mass in light of the CDF II result*, *Phys. Lett. B* **8**33 (2022) 137324, [arXiv:2204.04770].

[22] W.-Z. Feng and P. Nath, *Cogenesis in a universe with vanishing $B - L$ within a gauged $U(1)_x$ extension*, *Phys. Lett. B* **7**31 (2014) 43–50, [arXiv:1312.1334].

[23] J. Heeck, *Unbroken B – L symmetry*, *Phys. Lett. B* **7**39 (2014) 256–262, [arXiv:1408.6845].

[24] M. Sajjad Athar et al., *Status and perspectives of neutrino physics*, *Prog. Part. Nucl. Phys.* **1**24 (2022) 103947, [arXiv:2111.07586].

[25] X. G. He, G. C. Joshi, H. Lew, and R. R. Volkas, *New Z' phenomenology*, *Phys. Rev. D* **43** (1991) R22–R24.

[26] K. S. Babu, C. F. Kolda, and J. March-Russell, *Implications of generalized Z - Z' mixing*, *Phys. Rev. D* **57** (1998) 6788–6792, [hep-ph/9710441].

[27] S. Gopalakrishna, S. Jung, and J. D. Wells, *Higgs boson decays to four fermions through an abelian hidden sector*, *Phys. Rev. D* **78** (2008) 055002, [arXiv:0801.3456].

[28] B. Holdom, *Oblique electroweak corrections and an extra gauge boson*, *Phys. Lett. B* **259** (1991) 329–334.

[29] Z. Trócsányi, *Super-weak force and neutrino masses*, *Symmetry* **12** (2020) 107, [arXiv:1812.11189].

[30] Z. Péli and Z. Trócsányi, *Precise prediction for the mass of the W boson in gauged U(1) extensions of the standard model*, arXiv:2305.11931.

[31] M. P. Bento, H. E. Haber, and J. a. P. Silva, *Tree-level Unitarity in $SU(2)_L \times U(1)_Y \times U(1)_{Y'}$ Models*, arXiv:2306.01836.

[32] M. Algueró, J. Matias, A. Crivellin, and C. A. Manzari, *Unified explanation of the anomalies in semileptonic B decays and the W mass*, *Phys. Rev. D* **106** (2022) 033005, [arXiv:2201.08170].

[33] Z. Chen, K. Ye, and M. Zhang, *Asymmetric dark matter with a spontaneously broken U(1)': Self-interaction and gravitational waves*, *Phys. Rev. D* **107** (2023) 095027, [arXiv:2303.11820].

[34] Z. Péli and Z. Trócsányi, *Exclusion bounds for neutral gauge bosons*, arXiv:2402.14786.

[35] K. N. Abazajian, *Sterile neutrinos in cosmology*, *Phys. Rept.* **711-712** (2017) 1–28, [arXiv:1705.01837].

[36] A. Boyarsky, M. Drewes, T. Lasserre, S. Mertens, and O. Ruchayskiy, *Sterile neutrino Dark Matter*, *Prog. Part. Nucl. Phys.* **104** (2019) 1–45, [arXiv:1807.07938].

[37] A. L. Foguel, G. M. Salla, and R. Z. Funchal, *(In)Visible signatures of the minimal dark abelian gauge sector*, *JHEP* **12** (2022) 063, [arXiv:2209.03383].

[38] S. Dittmaier, J. Rehberg, and H. Rzehak, *Renormalization of a Standard Model extension with a Dark Abelian Sector and predictions for the W-boson mass*, *JHEP* **01** (2024) 037, [arXiv:2308.07845].

[39] O. W. Greenberg, *Spin and Unitary Spin Independence in a Paraquark Model of Baryons and Mesons*, *Phys. Rev. Lett.* **1**3 (1964) 598–602.

[40] M. Y. Han and Y. Nambu, *Three Triplet Model with Double SU(3) Symmetry*, *Phys. Rev.* **1**39 (1965) B1006–B1010.

[41] H. Fritzsch, M. Gell-Mann, and H. Leutwyler, *Advantages of the Color Octet Gluon Picture*, *Phys. Lett. B* **4**7 (1973) 365–368.

[42] S. L. Glashow, *Partial Symmetries of Weak Interactions*, *Nucl. Phys.* **2**2 (1961) 579–588.

[43] S. Weinberg, *A Model of Leptons*, *Phys. Rev. Lett.* **1**9 (1967) 1264–1266.

[44] A. Salam, *Elementary Particle Theory*, *Almyuist and Wiksell, Stockholm (1968).*

[45] S. L. Glashow, J. Iliopoulos, and L. Maiani, *Weak Interactions with Lepton-Hadron Symmetry*, *Phys. Rev. D* **2** (1970) 1285–1292.

[46] P. W. Higgs, *Broken symmetries, massless particles and gauge fields*, *Phys. Lett.* **1**2 (1964) 132–133.

[47] P. W. Higgs, *Broken Symmetries and the Masses of Gauge Bosons*, *Phys. Rev. Lett.* **1**3 (1964) 508–509.

[48] F. Englert and R. Brout, *Broken Symmetry and the Mass of Gauge Vector Mesons*, *Phys. Rev. Lett.* **1**3 (1964) 321–323.

[49] P. W. Higgs, *Spontaneous Symmetry Breakdown without Massless Bosons*, *Phys. Rev.* **1**45 (1966) 1156–1163.

[50] T. W. B. Kibble, *Symmetry Breaking in Non-Abelian Gauge Theories*, *Phys. Rev.* **1**55 (1967) 1554–1561.

[51] M. Böhm, A. Denner, and H. Joos, *Gauge theories of the electroweak interaction*. Vieweg+Teubner Verlag, 2001.

[52] M. D. Schwartz, *Quantum Field Theory and the Standard Model*. Cambridge University Press, 3, 2014.

[53] M. E. Peskin and D. V. Schroeder, *An Introduction to quantum field theory*. CRC Press, 1995.

[54] A. Denner and S. Dittmaier, *Electroweak Radiative Corrections for Collider Physics*, *Phys. Rept.* **8**64 (2020) 1–163, [arXiv:1912.06823].

[55] N. Cabibbo, *Unitary Symmetry and Leptonic Decays*, *Phys. Rev. Lett.* **1**0 (1963) 531–533.

[56] M. Kobayashi and T. Maskawa, *CP Violation in the Renormalizable Theory of Weak Interaction*, *Prog. Theor. Phys.* **4**9 (1973) 652–657.

[57] Z. Maki, M. Nakagawa, and S. Sakata, *Remarks on the unified model of elementary particles*, *Prog. Theor. Phys.* **2**8 (1962) 870–880.

[58] B. Pontecorvo, *Neutrino Experiments and the Problem of Conservation of Leptonic Charge*, *Zh. Eksp. Teor. Fiz.* **5**3 (1967) 1717–1725.

[59] **S**NO Collaboration, Q. R. Ahmad et al., *Measurement of the rate of $\nu_e + d \to p + p + e^-$ interactions produced by $8B$ solar neutrinos at the Sudbury Neutrino Observatory*, *Phys. Rev. Lett.* **8**7 (2001) 071301, [nucl-ex/0106015].

[60] **S**uper-Kamiokande Collaboration, Y. Fukuda et al., *Evidence for oscillation of atmospheric neutrinos*, *Phys. Rev. Lett.* **8**1 (1998) 1562–1567, [hep-ex/9807003].

[61] **K**ATRIN Collaboration, M. Aker et al., *Direct neutrino-mass measurement with sub-electronvolt sensitivity*, *Nature Phys.* **1**8 (2022) 160–166, [arXiv:2105.08533].

[62] **P**lanck Collaboration, N. Aghanim et al., *Planck 2018 results. VI. Cosmological parameters*, *Astron. Astrophys.* **6**41 (2020) A6, [arXiv:1807.06209]. [Erratum: Astron.Astrophys. 652, C4 (2021)].

[63] T. S. van Albada, J. N. Bahcall, K. Begeman, and R. Sancisi, *The Distribution of Dark Matter in the Spiral Galaxy NGC-3198*, *Astrophys. J.* **2**95 (1985) 305–313.

[64] M. Pospelov and J. Pradler, *Big Bang Nucleosynthesis as a Probe of New Physics*, *Ann. Rev. Nucl. Part. Sci.* **6**0 (2010) 539–568, [arXiv:1011.1054].

[65] S. Profumo, L. Giani, and O. F. Piattella, *An Introduction to Particle Dark Matter*, *Universe* **5** (2019) 213, [arXiv:1910.05610].

[66] D. Clowe, et al., *A direct empirical proof of the existence of dark matter*, *Astrophys. J. Lett.* **6**48 (2006) L109–L113, [astro-ph/0608407].

[67] A. D. Sakharov, *Violation of CP Invariance, C asymmetry, and baryon asymmetry of the universe*, *Pisma Zh. Eksp. Teor. Fiz.* **5** (1967) 32–35.

[68] S. M. Carroll, *The Cosmological constant*, *Living Rev. Rel.* **4** (2001) 1, [astro-ph/0004075].

[69] L. Altenkamp, M. Boggia, and S. Dittmaier, *Precision calculations for $h \to WW/ZZ \to 4$ fermions in a singlet extension of the Standard Model with* Prophecy4f, *JHEP* **0**4 (2018) 062, [arXiv:1801.07291].

[70] D. Ross and M. Veltman, *Neutral currents and the Higgs mechanism*, *Nuclear Physics B* **9**5 (1975) 135–147.

[71] M. J. G. Veltman, *Limit on Mass Differences in the Weinberg Model*, *Nucl. Phys. B* **1**23 (1977) 89–99.

[72] S. Dittmaier and H. Rzehak, *Electroweak renormalization based on gauge-invariant vacuum expectation values of non-linear Higgs representations. Part I. Standard Model*, *JHEP* **0**5 (2022) 125, [arXiv:2203.07236].

[73] S. Dittmaier and H. Rzehak, *Electroweak renormalization based on gauge-invariant vacuum expectation values of non-linear Higgs representations. Part II. Extended Higgs sectors*, *JHEP* **0**8 (2022) 245, [arXiv:2206.01479].

[74] B. W. Lee and J. Zinn-Justin, *Spontaneously Broken Gauge Symmetries Part 3: Equivalence*, *Phys. Rev. D* **5** (1972) 3155–3160.

[75] C. Grosse-Knetter and R. Kögerler, *Unitary gauge, Stueckelberg formalism and gauge invariant models for effective lagrangians*, *Phys. Rev. D* **4**8 (1993) 2865–2876, [hep-ph/9212268].

[76] G. 't Hooft and M. J. G. Veltman, *Regularization and Renormalization of Gauge Fields*, *Nucl. Phys. B* **4**4 (1972) 189–213.

[77] C. G. Bollini and J. J. Giambiagi, *Lowest order divergent graphs in nu-dimensional space*, *Phys. Lett. B* **4**0 (1972) 566–568.

[78] M. Böhm, H. Spiesberger, and W. Hollik, *On the One-Loop Renormalization of the Electroweak Standard Model and Its Application to Leptonic Processes*, *Fortsch. Phys.* **3**4 (1986) 687–751.

[79] A. Denner, *Techniques for the Calculation of Electroweak Radiative Corrections at the One-Loop Level and Results for W-physics at LEP 200*, *Fortschr. Phys.* **4**1 (1993) 307–420.

[80] J. Fleischer and F. Jegerlehner, *Radiative Corrections to Higgs-boson Decays in the Weinberg-Salam Model*, *Phys. Rev. D* **2**3 (1981) 2001–2026.

[81] A. Denner, S. Dittmaier, and J.-N. Lang, *Renormalization of mixing angles*, *JHEP* **1**1 (2018) 104, [arXiv:1808.03466].

[82] A. Denner, J.-N. Lang, and S. Uccirati, *NLO electroweak corrections in extended Higgs Sectors with RECOLA2*, *JHEP* **0**7 (2017) 087, [arXiv:1705.06053].

[83] S. Dittmaier, S. Schuhmacher, and M. Stahlhofen, *Integrating out heavy fields in the path integral using the background-field method: general formalism*, *Eur. Phys. J. C* **81** (2021) 826, [arXiv:2102.12020].

[84] S. Dittmaier, *Electric charge renormalization to all orders*, *Phys. Rev. D* **103** (2021) 053006, [arXiv:2101.05154].

[85] S. Weinberg, *The Quantum Theory of Fields*, vol. 2. Cambridge University Press, 1996.

[86] A. Denner, G. Weiglein, and S. Dittmaier, *Application of the background field method to the electroweak standard model*, *Nucl. Phys. B* **440** (1995) 95–128, [hep-ph/9410338].

[87] T. Robens and T. Stefaniak, *Status of the Higgs Singlet Extension of the Standard Model after LHC Run 1*, *Eur. Phys. J. C* **75** (2015) 104, [arXiv:1501.02234].

[88] T. Hahn, *Generating Feynman diagrams and amplitudes with FeynArts 3*, *Comput. Phys. Commun.* **140** (2001) 418–431, [hep-ph/0012260].

[89] Wolfram Research, Inc., "Mathematica, Version 14.0." Champaign, IL, 2024.

[90] A. Alloul, N. D. Christensen, C. Degrande, C. Duhr, and B. Fuks, *FeynRules 2.0 - A complete toolbox for tree-level phenomenology*, *Comput. Phys. Commun.* **185** (2014) 2250–2300, [arXiv:1310.1921].

[91] A. Denner, S. Dittmaier, and L. Hofer, *Collier: a fortran-based Complex One-Loop Library in Extended Regularizations*, *Comput. Phys. Commun.* **212** (2017) 220–238, [arXiv:1604.06792].

[92] A. Denner and S. Dittmaier, *Reduction of one loop tensor five point integrals*, *Nucl. Phys. B* **658** (2003) 175–202, [hep-ph/0212259].

[93] A. Denner and S. Dittmaier, *Reduction schemes for one-loop tensor integrals*, *Nucl. Phys. B* **734** (2006) 62–115, [hep-ph/0509141].

[94] A. Denner and S. Dittmaier, *Scalar one-loop 4-point integrals*, *Nucl. Phys. B* **844** (2011) 199–242, [arXiv:1005.2076].

[95] G. Knippen, *(L)oopTools-like (In)terface for (C)ollier*, *private code* (2017).

[96] T. Hahn and M. Perez-Victoria, *Automatized one loop calculations in four-dimensions and D-dimensions*, *Comput. Phys. Commun.* **118** (1999) 153–165, [hep-ph/9807565].

[97] H. Dembinski and P. Ongmongkolkul et al., *scikit-hep/iminuit*, *https://doi.org/10.5281/zenodo.3949207* (Dec, 2020).

[98] F. James and M. Roos, *Minuit: A System for Function Minimization and Analysis of the Parameter Errors and Correlations*, *Comput. Phys. Commun.* **1**0 (1975) 343–367.

[99] C. Sturm, B. Summ, and S. Uccirati, *Electroweak corrections to $g + g \to H_{l,h}$ and $H_{l,h} \to \gamma + \gamma$ in the Higgs-singlet extension of the Standard model*, *JHEP* **1**1 (2023) 113, [arXiv:2212.11835].

[100] A. Denner, S. Dittmaier, M. Roth, and D. Wackeroth, *Predictions for all processes $e^+e^- \to 4$ fermions $+\gamma$*, *Nucl. Phys. B* **5**60 (1999) 33–65, [hep-ph/9904472].

[101] A. Denner, S. Dittmaier, M. Roth, and L. H. Wieders, *Electroweak corrections to charged-current $e^+e^- \to 4$ fermion processes: Technical details and further results*, *Nucl. Phys. B* **7**24 (2005) 247–294, [hep-ph/0505042]. [Erratum: Nucl.Phys.B 854, 504–507 (2012)].

[102] A. Denner and S. Dittmaier, *The Complex-mass scheme for perturbative calculations with unstable particles*, *Nucl. Phys. B Proc. Suppl.* **1**60 (2006) 22–26, [hep-ph/0605312].

[103] **M**uLan Collaboration, D. M. Webber et al., *Measurement of the Positive Muon Lifetime and Determination of the Fermi Constant to Part-per-Million Precision*, *Phys. Rev. Lett.* **1**06 (2011) 041803, [arXiv:1010.0991].

[104] A. Sirlin, *$\mathcal{O}(\alpha^2)$ corrections to muon lifetime, m_W, and m_Z in the $\mathrm{SU}(2)_L \times \mathrm{U}(1)$ theory*, *Phys. Rev. D* **2**9 (Jan, 1984) 89–95.

[105] W. F. L. Hollik, *Radiative Corrections in the Standard Model and their Role for Precision Tests of the Electroweak Theory*, *Fortsch. Phys.* **3**8 (1990) 165–260.

[106] M. S. Chanowitz, M. A. Furman, and I. Hinchliffe, *Weak Interactions of Ultraheavy Fermions*, *Phys. Lett. B* **7**8 (1978) 285.

[107] M. Consoli, W. Hollik, and F. Jegerlehner, *The Effect of the Top Quark on the M_W-M_Z Interdependence and Possible Decoupling of Heavy Fermions from Low-Energy Physics*, *Phys. Lett. B* **2**27 (1989) 167–170.

[108] F. Jegerlehner, *The anomalous magnetic moment of the muon*, vol. 226. Springer, 2008.

[109] L. L. Foldy and S. A. Wouthuysen, *On the Dirac theory of spin 1/2 particle and its nonrelativistic limit*, *Phys. Rev.* **7**8 (1950) 29–36.

[110] J. S. Schwinger, *On Quantum electrodynamics and the magnetic moment of the electron*, *Phys. Rev.* **7**3 (1948) 416–417.

[111] R. Jackiw and S. Weinberg, *Weak interaction corrections to the muon magnetic moment and to muonic atom energy levels*, *Phys. Rev. D* **5** (1972) 2396–2398.

[112] I. Bars and M. Yoshimura, *Muon magnetic moment in a finite theory of weak and electromagnetic interaction*, *Phys. Rev. D* **6** (1972) 374–376.

[113] *LEP design report: v.1 The LEP injector chain.* Report. CERN, Geneva, 1983. By the LEP Injector Study Group.

[114] **A**LEPH Collaboration, D. Decamp et al., *ALEPH: A detector for electron-positron annnihilations at LEP*, *Nucl. Instrum. Meth. A* **2**94 (1990) 121–178. [Erratum: Nucl.Instrum.Meth.A 303, 393 (1991)].

[115] **D**ELPHI Collaboration, P. A. Aarnio et al., *The DELPHI detector at LEP*, *Nucl. Instrum. Meth. A* **3**03 (1991) 233–276.

[116] **L**3 Collaboration, B. Adeva et al., *The Construction of the L3 Experiment*, *Nucl. Instrum. Meth. A* **2**89 (1990) 35–102.

[117] **O**PAL Collaboration, K. Ahmet et al., *The OPAL detector at LEP*, *Nucl. Instrum. Meth. A* **3**05 (1991) 275–319.

[118] **A**LEPH, DELPHI, L3, OPAL, SLD, LEP Electroweak Working Group, SLD Electroweak Group, SLD Heavy Flavour Group Collaboration, S. Schael et al., *Precision electroweak measurements on the Z resonance*, *Phys. Rept.* **4**27 (2006) 257–454, [hep-ex/0509008].

[119] F. J. Dyson, *The Radiation theories of Tomonaga, Schwinger, and Feynman*, *Phys. Rev.* **7**5 (1949) 486–502.

[120] F. J. Dyson, *The S matrix in quantum electrodynamics*, *Phys. Rev.* **7**5 (1949) 1736–1755.

[121] M. Awramik, M. Czakon, A. Freitas, and G. Weiglein, *Complete two-loop electroweak fermionic corrections to* $\sin^2\theta^{lept}_{eff}$ *and indirect determination of the Higgs boson mass*, *Phys. Rev. Lett.* **9**3 (2004) 201805, [hep-ph/0407317].

[122] I. Dubovyk, A. Freitas, J. Gluza, T. Riemann, and J. Usovitsch, *Complete electroweak two-loop corrections to Z boson production and decay*, *Phys. Lett. B* **7**83 (2018) 86–94, [arXiv:1804.10236].

[123] G. Cowan, *Statistical data analysis.* Oxford University Press, 1998.

[124] **N**A64 Collaboration, Y. M. Andreev et al., *Search for Light Dark Matter with NA64 at CERN*, *Phys. Rev. Lett.* **1**31 (2023) 161801, [arXiv:2307.02404].

[125] **B**aBar Collaboration, J. P. Lees et al., *Search for Invisible Decays of a Dark Photon Produced in e^+e^- Collisions at BaBar*, *Phys. Rev. Lett.* **1**19 (2017) 131804, [arXiv:1702.03327].

[126] **F**ASER Collaboration, H. Abreu et al., *Search for dark photons with the FASER detector at the LHC*, *Phys. Lett. B* **8**48 (2024) 138378, [arXiv:2308.05587].

[127] T. Kinoshita, *Mass singularities of Feynman amplitudes*, *J. Math. Phys.* **3** (1962) 650–677.

[128] T. D. Lee and M. Nauenberg, *Degenerate Systems and Mass Singularities*, *Phys. Rev.* **1**33 (1964) B1549–B1562.

[129] J. C. Collins, *Renormalization: An Introduction to Renormalization, the Renormalization Group and the Operator-Product Expansion*. Cambridge University Press, 1984.

Acknowledgments

As I approach the end of this journey, I am deeply grateful for the support I received during the past five years.

Stefan, thank you for giving me the opportunity to collaborate with you on this research project. The past five years have been an interesting and memorable time that I will think of many times in the future. Thanks for all the support and advice along the way! Last but not least I would like to mention our ongoing table football rivalry, which I'm eagerly looking forward to continue whenever I am around!

Thank you, Heidi, for all the support and help on the project, especially whenever physics did not seem to make any sense anymore.

I have had many great group members and office mates. In no particular order, I especially want to mention José Lüis H., Max R., Jan S., Lillot H., and Stefan R. All of you were a big part of this journey. Thank you for all the support. Further, I want to thank José Lüis H., Sebastian S., and Maria D. for all the proofreading and the many ("insightful") discussions on any topics.

A big thanks to the whole 8th floor of the physics high rise for all the interesting and sometimes also "spannenden" discussions on everything apart of physics, and thank you for having some wild opinions on random topics Mathieu P., Sebastian S., Robin B., and Max S. It was a great pleasure listening! However, there is no doubt in my mind that a bear will win against a tiger.

Finally, I want to thank Ali K., my family, and all the other people from outside of physics who supported me along this journey!